



UNIVERSITÉ
University of Namur
DE NAMUR

Institutional Repository - Research Portal Dépôt Institutionnel - Portail de la Recherche

researchportal.unamur.be

THESIS / THÈSE

DOCTOR OF SCIENCES

Effect of doping, coating and electrolytic environment on the photocatalytic and photoelectrochemical activity of metal oxide semiconducting materials

Wang, YingYing

Award date:
2020

Awarding institution:
University of Namur

[Link to publication](#)

General rights

Copyright and moral rights for the publications made accessible in the public portal are retained by the authors and/or other copyright owners and it is a condition of accessing publications that users recognise and abide by the legal requirements associated with these rights.

- Users may download and print one copy of any publication from the public portal for the purpose of private study or research.
- You may not further distribute the material or use it for any profit-making activity or commercial gain
- You may freely distribute the URL identifying the publication in the public portal ?

Take down policy

If you believe that this document breaches copyright please contact us providing details, and we will remove access to the work immediately and investigate your claim.



University of Namur

Faculté des Sciences

DEPARTEMENT DE CHIMIE

Laboratoire de Chimie des Matériaux Inorganiques

**Effect of doping, coating and electrolytic environment on the
photocatalytic and photoelectrochemical activity of metal oxide semiconducting
materials**

Yingying WANG

Dissertation présentée par

Yingying Wang

En vue de l'obtention du grade

De Docteur en Sciences

Composition du jury :

Prof. Alexandru Vlad (UCLouvain)

Prof. Yujia Zeng (SZU, China)

Prof. Olivier Deparis (UNamur)

Dr. Luca Fusaro (UNamur)

Prof. Alain Krief (UNamur, Membre invité)

Prof. Bao-Lian SU (UNamur, Promoteur)

August 2020

Université de Namur
FACULTE DES SCIENCES

Rue de Bruxelles 61—5000 NAMUR
Tél. 081/72 54 10—Fax. 081/72 45 30

**Effect of doping, coating and electrolytic environment on the
photocatalytic and photoelectrochemical activity of metal oxide semiconducting
materials**

Yingying WANG

Abstract:

Photocatalytic/photoelectrochemical water splitting under solar light irradiation is considered as a prospective technology to support the sustainable and renewable H₂ economy. Extensive efforts have been devoted to the conversion of solar energy into H₂ production by PC/PEC water splitting. However, the process of PC/PEC for H₂ production is still with low efficiency. The design and optimization of both photocatalyst materials and PC/PEC systems to achieve high efficiency and stability for H₂ production under solar light are urgently in need but full of challenge. TiO₂ based photocatalysts with high chemical stability and excellent photocatalytic properties have great potential for solar-to-H₂ conversion. To conquer the challenges of the large band gap and rapid recombination of photogenerated electron-hole pairs in TiO₂, non-metal doping method emerges to be economic, facile and effective on boosting the visible light activity. In this thesis, we firstly synthesized the carbon doped and coated TiO₂ by the “one pot” hydrolysis of TiCl₄ in glucose solution approach. The synergistic effect of carbon doping and coating of TiO₂ to significantly boost textural, optical and electronic properties and photocurrent of TiO₂ for high performance visible light H₂ production from water splitting has been comprehensively investigated. Carbon doping can significantly inhibit the phase transformation of the Titania material from anatase to rutile, thus increasing its thermal stability while carbon coating can suppress the grain aggregation of TiO₂. The synergy of carbon doping and coating however, not only ensures an enhanced narrowing effect of the electronic band gap of TiO₂ thus extending the absorbance to the visible or even near-infrared (NIR) regions, but also promotes dramatically the separation of electron-hole pairs. Owing to these synergistic effects, the carbon coated and doped TiO₂ shows much superior photocatalytic activity for both degradation of organics and PC/PEC water splitting under solar light illumination. Secondly, the carbon composed Ti_nO_{2n-1} ($2 \leq n \leq 9$) were obtained in the process of carbon coating and doping TiO₂ at high temperature. The influence factors, formation mechanism of the growth of

Ti_nO_{2n-1} and the followed performance of PEC water splitting were further investigated. Except studies on the effects of photocatalysts or photoanode materials on photocatalytic activity, the studies on how electrolytic species in PEC system especially additives such as sacrificial reagents (SRs) and electrolyte cations/anions affect the photocatalytic activity of different photocatalysts including TiO_2 are also carried out. The electrolytic parameters are fine-tuned to optimize the efficiency of PEC water splitting. The main target of third part work is to provide the improved understanding of optimizing the electrolytic environments to achieve high efficiency of PEC water splitting over different photocatalysts such as TiO_2 , WO_3 , Fe_2O_3 , $BiVO_4$, $ZnFe_2O_4$, $ZnCr_2O_4$ and $LaFeO_3$.

Thesis presented for the award of the degree of Doctor in Sciences

August 2020

Promoteur: Prof. Bao-Lian SU

Université de Namur
FACULTE DES SCIENCES

Rue de Bruxelles 61—5000 NAMUR
Tél. 081/72 54 10—Fax. 081/72 45 30

**Effet du dopage, du revêtement et de l'environnement électrolytique sur la
l'activité photocatalytique et photoélectrochimique des matériaux semi-conducteurs à
base d'oxydes de métaux**

Yingying Wang

Résumé :

La décomposition photocatalytique/photo-électrochimique de l'eau sous irradiation solaire pour la production d'hydrogène est considérée comme une technologie prospective pour soutenir une économie H₂ durable. Des efforts importants ont été consacrés à la conversion de l'énergie solaire pour la production d'H₂ par la décomposition photocatalytique (PC)/photoélectrochimique (PEC) de l'eau. Cependant, le processus de PC/PEC pour la production d'H₂ reste encore peu efficace. La conception de matériaux photocatalyseurs et de systèmes PC/PEC plus performants pour atteindre une efficacité et une stabilité élevées dans la production d'H₂ sous lumière solaire répondent à des besoins urgents et constituent également des défis. Les photocatalyseurs à base de TiO₂ ayant une grande stabilité chimique et d'excellentes propriétés photocatalytiques représentent un grand potentiel pour la conversion de l'énergie solaire en H₂. Pour réduire la largeur de bande interdite électronique et la recombinaison des paires électron-trou photogénérées dans le TiO₂, le dopage non métallique s'avère efficace, facile et aussi économique pour stimuler son activité dans la zone de lumière visible. Dans cette thèse, nous avons tout d'abord synthétisé le TiO₂ dopé et revêtu de carbone par une méthode "one-pot" via l'hydrolyse simultanée de TiCl₄ en solution de glucose. L'effet synergique des dopage et revêtement au carbone de TiO₂ pour augmenter de manière significative les propriétés texturées, optiques et électroniques et le photocourant de TiO₂ pour la production de H₂ dans la zone de lumière visible de haute performance à partir de la décomposition de l'eau a été étudié de manière exhaustive. Le dopage au carbone peut inhiber de manière significative la transformation de phase du matériau d'oxyde de Titane de l'anatase au rutile, augmentant ainsi sa stabilité thermique, et le revêtement de carbone peut supprimer l'agrégation des grains de TiO₂. Cette synergie garantit non seulement un meilleur effet de réduction de la bande interdite électronique du TiO₂, étendant ainsi l'absorbance aux régions visibles ou même proches de l'infrarouge (NIR), mais favorise aussi considérablement la séparation des paires électron-trou. Le TiO₂ dopé et revêtu de carbone présente donc une

activité photocatalytique bien supérieure pour la dégradation des matières organiques et la décomposition de l'eau PC/PEC sous éclairage solaire. Ensuite, le composite carbone/Ti_nO_{2n-1} ($2 \leq n \leq 9$) a été obtenu avec le même processus à haute température. Les facteurs d'influence, le mécanisme de formation de la croissance de Ti_nO_{2n-1} et les performances de la décomposition de l'eau par PEC ont été étudiés plus en détail. Enfin, une étude sur les effets de différentes espèces électrolytiques dans le système PEC, en particulier les substances additives telles que les agents sacrifiants, les cations/anions électrolytiques et les températures de la solution sur l'activité photocatalytique d'une large série de matériaux semiconducteurs tels que TiO₂, WO₃, Fe₂O₃, BiVO₄, ZnFe₂O₄, ZnCr₂O₄ et LaFeO₃ a également été réalisée. L'objectif principal de la troisième partie des travaux est de mieux comprendre l'effet des environnements électrolytiques pour obtenir une efficacité élevée de la décomposition de l'eau par PEC.

Thesis presented for the award of the degree of Doctor in Sciences

August 2020

Promoteur: Prof. Bao-Lian SU

Table of Contents

CHAPTER 1	8
Introduction.....	8
1.1 Overview.....	9
1.2 Basic principles for PC/PEC water splitting	11
1.2.1 PC water splitting.....	11
1.2.2 PEC water splitting	13
1.2.3 Efficiency of PC/PEC water Splitting.....	15
1.3 Strategies to improve the PC/PEC efficiency.....	16
1.3.1 Non-metal doping in TiO ₂	16
1.3.2 Carbon coating in TiO ₂	57
1.3.3 The effect of electrolytic environments on PC/PEC water splitting	60
1.4 Summary	66
References.....	68
CHAPTER 2	79
Objectives and Scientific Strategy	79
2.1 Objectives.....	80
2.1.1 Synergy of carbon doping and coating in TiO ₂ for enhanced photocatalysis and photoelectrochemical performance of TiO ₂	81
2.1.2 Magnéli (Ti _n O _{2n-1}) materials for PEC water splitting.....	82
2.1.3 Impact of electrolytic environment on the PEC performance of metal oxides	82
2.2 Scientific strategy.....	82
2.2.1 Materials synthesis.....	82
2.2.2 Chemicals.....	83
2.2.3 Characterization and instruments.....	84
2.2.4 Evaluation of photocatalytic activity	86
References.....	88
CHAPTER 3	90
Synergistic effects of carbon doping and coating of TiO ₂ with exceptional photocurrent enhancement for high performance H ₂ production from water splitting	90
3.1 Introduction.....	92
3.2 Experimental	93
3.2.1 Materials Synthesis	93
3.2.2 Materials characterization	93
3.2.3 Photocatalytic test of the degradation of dye pollutant	94
3.2.4 Electrochemical and Photoelectrochemical measurement	95
3.2.5 Photocatalytic H ₂ production performance	95
3.3 Results and discussions	96
3.3.1 Crystalline structure and textural properties	97
3.3.2 Surface elemental analysis	102
3.3.3 Optical properties	104

3.3.4 Photocatalytic & Photoelectrochemical activity	105
3.4 Conclusions.....	112
References.....	112
Supplementary information	115
CHAPTER 4	135
A novel synthesis of carbon composed two-dimensional Ti_nO_{2n-1} for PEC water splitting	135
4.1 Introduction.....	137
4.2 Materials and methods	138
4.2.1 Preparation of Ti_nO_{2n-1} materials	138
4.2.2 Materials characterization	138
4.2.3 Photoelectrochemical measurement.....	139
4.3 Result and discussion	139
4.3.1 Synthesis of carbon composed Ti_nO_{2n-1} materials	139
4.3.2 The influence factors on the growth of Magnéli materials	143
4.3.3 Crystal structures of two-dimensional Ti_nO_{2n-1} ($3 \leq n \leq 9$) materials	145
4.3.4 Photoelectrochemical activity	145
4.4 Conclusion	155
References.....	157
Supplementary information	158
CHAPTER 5	160
Impact of electrolytic environments on solar light PEC water splitting over different metal oxide semiconductors	160
5.1 Introduction.....	162
5.2 Materials and Methods.....	163
5.3 Result and discussion	165
5.3.1 Characterization of photoelectrodes.....	165
5.3.2 Effect of different electrolyte environments on PEC water splitting performance	167
5.4 Conclusion	175
References.....	177
Supplementary information	179
CHAPTER 6	191
Conclusions and Perspectives	191
6.1 Conclusions.....	192
6.2 Perspectives.....	195
<i>List of papers</i>	198
<i>Acknowledgements</i>	199

CHAPTER 1.

Introduction

1.1 Overview

The major energy sources for people's survival and development still root in non-renewable fossil fuels, which are petroleum, coal, betumes, natural gas, shale oil, etc. Such unsustainable energy consumption also results in environmental deterioration such as air and water contamination and global warming. Therefore, alternative clean energy sources are urgently through needed. [1-4] Since solar energy is abundantly available and clean, it has become the key to alleviate the energy crisis and environmental issues among all renewable energy resources (biomass, wind, geothermal, marine, etc.). [4, 5] On the other hand, H₂ is one of the most promising energy carrier since it is one of the most abundant elements in earth. Due to its cleanliness, plentiful quantity and high energy efficiency, H₂ plays a crucial role in driving modern energy system for sustainable development of society. Thus, converting solar energy into usable and storable form particularly like H₂ in a both economically and environmentally friendly way is highly desirable. [6-8]

Since Honda and Fujishima first used Titania photoanodes for decomposing water into H₂ and oxygen in 1972, photocatalytic water splitting using functional semiconductor photocatalysts has long been studied as the potential route for H₂ production using solar light. [9-12] In the past decades, other types of metal oxide semiconductors have been also subsequently developed as photocatalysts or photoelectrodes to increase the efficiency of PC/PEC water splitting. [13-18] Considering the efficiency and stability in the liquid media, TiO₂ still remains the most attractive and investigated photocatalyst. It is well-known that TiO₂ has strong photocatalytic activity, superior chemical stability and high resistance against corrosion in the aqueous media, as well as nontoxicity and low cost. [19-23] Although the conversion efficiency of TiO₂ has been improved successfully after important efforts during last decade, the solar-to-hydrogen efficiency of most TiO₂ based materials is around 1-2%, which still remains at a very low level. [24, 25] The first reason is that due to the large electronic bandgap of TiO₂, it only absorbs ultraviolet light (about 3-5% of total solar light), the utilization of solar light has thus vastly been restricted. On the other hand, pure TiO₂ photocatalyst suffered from the fast recombination of photoexcited electron-hole pairs, which drastically decreases the efficiency of photo-energy conversion. [26-29] Considerable efforts have been made to reduce the bandgap of TiO₂ to extend the light absorption to visible region by a series of approaches, such as coupling with narrow-bandgap materials, dye sensitization, and surface plasmonic treatment. In addition, one of the most developed modification strategies for enhancing the photocatalytic activity of TiO₂ employs metals especially noble metals, such as Ru, Rh, Au, Pd and Pt etc.

Introduction

With the assistance of these noble metals, the performance of TiO₂ in photocatalytic H₂ or O₂ evolution is improved owing to the lowered activation energy and increased electron donor concentration.^[30-38] Unfortunately, all metal-compounded TiO₂ materials have problems on thermal stability and the increased recombination centres of the charge carriers.^[39, 40] The lifetime of photogenerated charge carriers is an important issue and needs to be improved.^[26, 40-43] Furthermore, the above-mentioned noble metals are costive and can cause the secondary water contamination. Thus, on account of effectively sustainable development of H₂ production in industry, the utilization of noble metals is highly undesirable.^[26, 44, 45] The research attention has therefore been shifted to non-metal doping for tuning the electronic, chemical and photocatalytic properties of TiO₂. Sato et al. initially reported the photocatalytic activity of nitrogen doped TiO₂ with the absorption band around 450 nm. The substitutional doping of nitrogen was believed to result in the electronic band-gap narrowing of TiO₂.^[46] Then Asahi et al. revealed the enhanced photocatalytic activity of nitrogen doped TiO₂ in the form of TiO_{2-xN_x}, attributed to its absorption capacity of visible light (> 460 nm).^[47] Afterwards, other non-metal (such as C, S, B, P, halogens) doped TiO₂ have also been found to be photoactive under visible light.^[48-59] Non-metal doping can alter the electronic structure of TiO₂ by introducing localized states in the electronic bandgap and also reconstruct the surface structure of TiO₂ which facilitates the charge transfer.^[60-64] In this first chapter, the specific band gap tuning and the possible origin of visible light activity of non-metal doped TiO₂ will be discussed. Different doping pathways and recent advancements including the basic concepts, the developed mechanisms and some breakthroughs on non-metal doped TiO₂ for PC/PEC water splitting are also summarized. Specially, the carbon can not only be doped in TiO₂ but also be coated in TiO₂. Both can boost photocatalytic activity of TiO₂.^[65, 66] Carbon coating can effectively hinder the phase transformation from anatase to rutile and improve the thermal stability of TiO₂.^[67] Meanwhile, due to the good conductivity of carbon, the mass transfer and charge separation can also be improved.^[67] The carbon coated TiO₂ shows much superior photocatalytic activity for both degradation of organics and photocatalytic/photoelectrochemical (PEC) water splitting under visible light.^[67] Thus, the research on coating in TiO₂ is further highlighted.

Besides, the “surface back-reaction (SBR)” effect caused by the regeneration of H₂O from produced H₂ and O₂ on the surface of photocatalysts combined with the problem of fast recombination of electron/hole pairs highly hinder the H₂ production from pure water splitting. Most semiconductors even with narrow band gap (< 3 eV) such as WO₃, Fe₂O₃, BiVO₄, LaFeO₃ could not effectively decompose water into H₂ and O₂ in simple aqueous suspension system.

Introduction

The sacrificial reagents (SRs) can effectively work as hole scavengers, separating the photoexcited electrons and holes and preventing oxygen formation as well as the followed SBR. Various compounds such as organic methanol, EDTA (ethylenediaminetetraacetate), amines or inorganic Na₂S/Na₂SO₃, NaI/NaIO₃ and some ions species, Fe³⁺, Ce³⁺ and CN⁻ have been proved to increase the efficiency of H₂ production. [68, 69] For PEC water splitting, the electrolytic condition essentially affects the process of H₂ production. Electrolytic parameters, such as temperature, pH, ionic strength, cations species and SRs have significant impacts on the interface catalysis which determines PEC performance. The PEC activities of photoanodes remarkably varies in different electrolytes. [70-73] The electrolytic parameters can be fine-tuned to optimize the efficiency of PEC water splitting for photoanodes based on different metal oxides. Generally, compared to developing various photocatalysts, researches about the effects of electrolytic environments on PEC performance are very limited. Therefore, the specific effects of different electrolytic parameters on PEC behaviour are briefly summarized based on recent progress on optimization and selection of SRs and electrolytes for H₂ production from PC/PEC water splitting.

1.2 Basic principles for PC/PEC water splitting

1.2.1 PC water splitting

Photocatalytic water splitting is used to decompose water into its constituent, H₂ and dioxygen using a photocatalyst irradiated by natural or simulated sunlight as shown in Fig. 1.1. During this process, the photon energy is absorbed and converted into chemical energy, which is very similar to the process occurring in the photosynthesis of green plants. Therefore, photocatalytic water splitting is considered as an artificial photosynthesis for H₂ production.

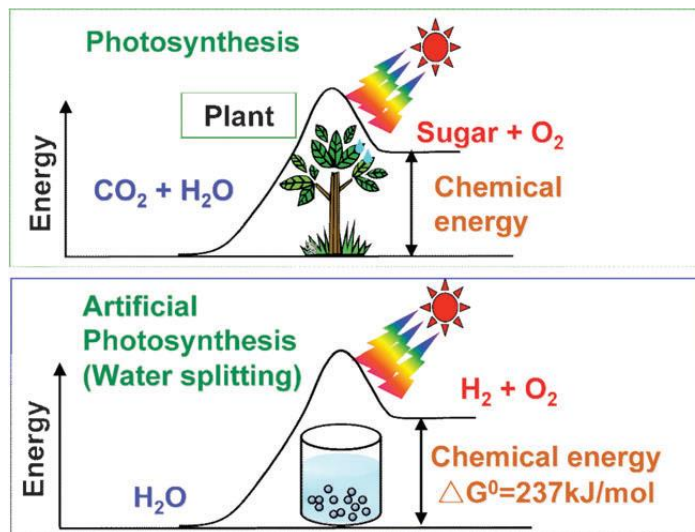
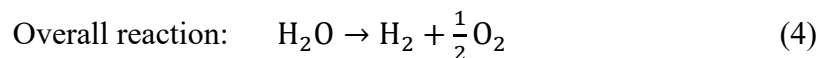
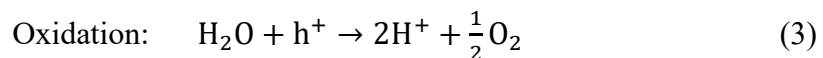
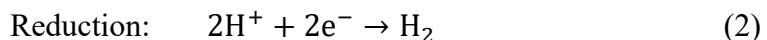


Fig. 1.1. Photosynthesis by green plants and photocatalytic water splitting as an artificial photosynthesis. Reprinted with permission from ref [74]. Copyright 2009 Royal Society of Chemistry.

In the photocatalytic system, when the photocatalysts are irradiated by sunlight, electron-hole pairs are generated on the surface of TiO_2 . The reaction can be expressed in eq. (1), as shown in Fig. 1.2.



These photoexcited electrons and holes react with protons (H^+) to produce H_2 and with H_2O to generate O_2 , respectively. (Fig. 1.2 (2) and (3)). The reduction (eq. 2) and oxidation (eq. 3) reactions are the basic principles for photocatalytic water splitting.



The overall water splitting reaction (eq.4) is an uphill reaction which involves positive change in Gibbs free energy (ΔG°) of 237 kJ/mol or 1.23 eV. To facilitate the oxidation-reduction reactions, the conduction band (CB) of the photocatalyst must be lower than the H^+/H_2 reduction potential (0V vs. NHE) and the valence band (VB) must be higher than the $\text{H}_2\text{O}/\text{O}_2$ oxidation potential (+1.23V vs. NHE). [74] The higher the VB energy position of the semiconductors, the lower the oxidizing power in water splitting reactions. The valence band maximum (VBM) of TiO_2 is mainly composed of oxygen 2p orbitals with a potential of approximately 2 V vs. NHE. While the conduction band minimum (CBM) is derived from titanium 3d orbitals and is more negative than 0 V vs. NHE. [40, 75] Therefore, the oxidation-

reduction potentials (OPR) of H^+/H_2 and $\text{H}_2\text{O}/\text{O}_2$ should be between the CBM and the VBM of TiO_2 .

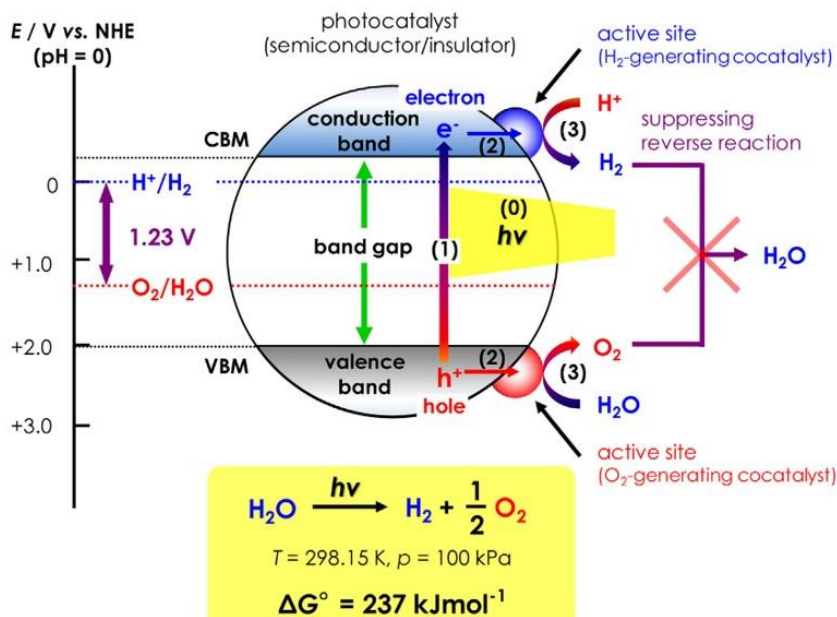


Fig. 1.2. Schematic illustrating a sequence of photocatalytic water splitting reactions by one-step excitation in a single photocatalyst. Reprinted with permission from ref [76]. Copyright 2013 Coordination Chemistry Reviews.

1.2.2 PEC water splitting

Fig. 1.3 presents the basic principles of conventional PEC water splitting system. PEC water splitting device consists of a light absorbing photoanode as working electrode, reference electrode and a counter electrode placed in the aqueous electrolyte solution. When the n-type TiO_2 works as the photoanode, the holes are accumulated at the interface between TiO_2 and the electrolyte solution which participate in the oxygen-evolution half-reaction (OER). Meanwhile the electrons are transferred to the counter electrode, for example the most widely used platinum electrode, through the conductive electrolyte medium involved subsequently in the H_2 -evolution half-reaction (HER). The protons and H_2O molecules adsorbed on electrodes will then be reduced and oxidized by electrons and holes, respectively, as expressed in eq.2 and 3. Generally, the overall reaction of PEC water splitting occurs in an electrochemical cell including two independent half-reactions, which consequently change the chemical composition of the system and respond to the interfacial potential difference at the corresponding electrodes. [77] Since the potentials of both working electrode and counter

electrode change depending on the influence of overall reaction of water splitting, the reference electrode with substantially stable composition is needed to standardize the potential of the whole system. The most acceptable reference electrodes considered as standard for zero potential are as follows:

NHE (Normal Hydrogen Electrode): potential of a platinum electrode in 1 M acid solution at 25°C

SHE (Standard Hydrogen Electrode): potential of a platinum electrode in a theoretical ideal solution (the current standard for zero potential for all temperatures)

RHE (Reversible Hydrogen Electrode): a practical hydrogen electrode whose potential depends on the pH of the solution at 25°C

In practical PEC measurements, hydrogen electrodes are not convenient to quote from an experimental standpoint. The common reference electrodes are the saturated calomel electrode (SCE), Hg/Hg₂Cl₂/ KCl (saturated in water) with potential of 0.244 V vs. RHE (pH = 0) and the silver-silver chloride electrode, Ag/AgCl/KCl (saturated in water) with a potential of 0.198 V vs. RHE (pH = 0).

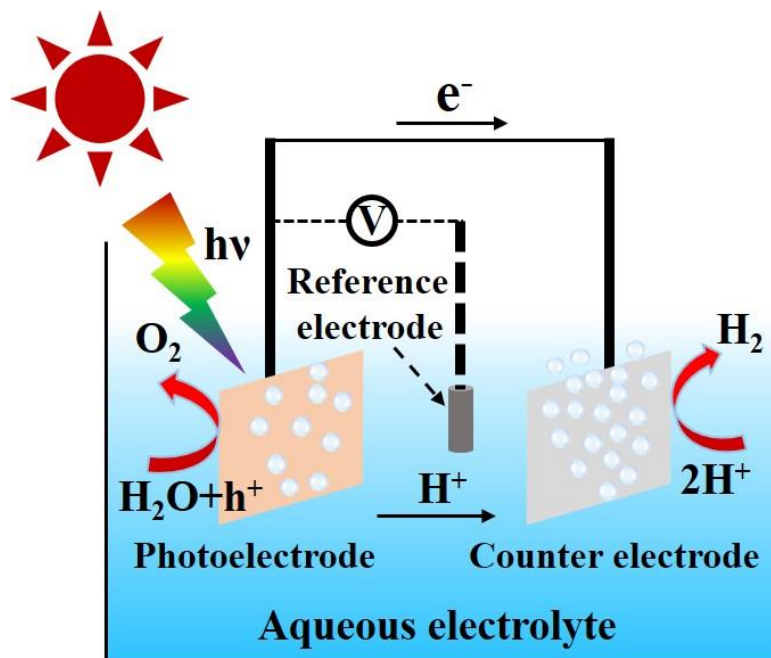


Fig. 1.3. Schematic of basic set up of PEC water splitting system.

An external voltage is applied between working electrode based on semiconductor materials and the reference electrode to equilibrate the Fermi level of the semiconductor and the work function of the metal counter electrode. By driving the electrode to more negative potentials,

the energy of the electrons is raised and reaches a level high enough to transfer into vacant electronic states on species in the electrolyte. When a flow of electrons takes place from electrode to solution, a reduction current occurs. In reverse, the energy of the electrons is lowered after imposing a more positive potential, and electrons in the electrolyte will prefer a certain energy on the electrode and will transfer there. The flow of electrons from solution to electrode is an oxidation current. In this case, the transfer of the electrons within the working electrode can be controlled by manipulating the potential of the working electrode with respect to the reference. And electrons transfer to the counter electrode and charges separation as well as water splitting reactions can be assured at the same time.

1.2.3 Efficiency of PC/PEC water Splitting

The solar to H₂ conversion efficiency (STH) is generally used to describe the H₂ production efficiency of photocatalytic water splitting. STH efficiency is the ratio of the “H₂-energy output” to the “solar energy input” at 25 °C, which can be described in equation 5. [78]

$$STH = \left[\frac{(mmol\ H_2\ /s)*(237\ kJ/mol)}{P_{total}\ (mW/cm^2)*Area\ (cm^2)} \right]_{AM\ 1.5G} \quad (5)$$

Where P_{total} represents the power density (mW/cm²) of incident simulated sunlight (AM1. 5G). For PEC water splitting, the numerator is the product of photocurrent density (j_{sc}) at zero bias (short-circuit photocurrent), the thermodynamic voltage required for water splitting (1.23 V), and the faradic efficiency (η_F), as expressed in Eq.6.

$$STH = \left[\frac{|j_{sc}\ (mA/cm^2)|*(1.23V)*\eta_F}{P_{total}\ (mW/cm^2)} \right]_{AM1.5G} \quad (6)$$

To know the contribution of light of different wavelengths region to STH efficiency, the NREL standard spectrum of AM1.5G as solar spectrum is analysed in Fig. 1.4. Quantum efficiency (QE) represents the characteristic photon conversion efficiency, which is defined as the percentage of generated electrons and incident photons under light irradiation with a specific wavelength. With a QE of 100%, the entire UV photons accounts for a maximum theoretical STH efficiency of only 3.3%, light ≤ 600 nm (2.07 eV) results in 17.8%. While up to 1000 nm (1.23 eV), the STH efficiency can be calculated to be ~48% (using a single semiconductor). The fact clearly reveals that the visible light makes the major contribution to STH efficiency, indicating the significance of improving the visible-light activity of photocatalysts.

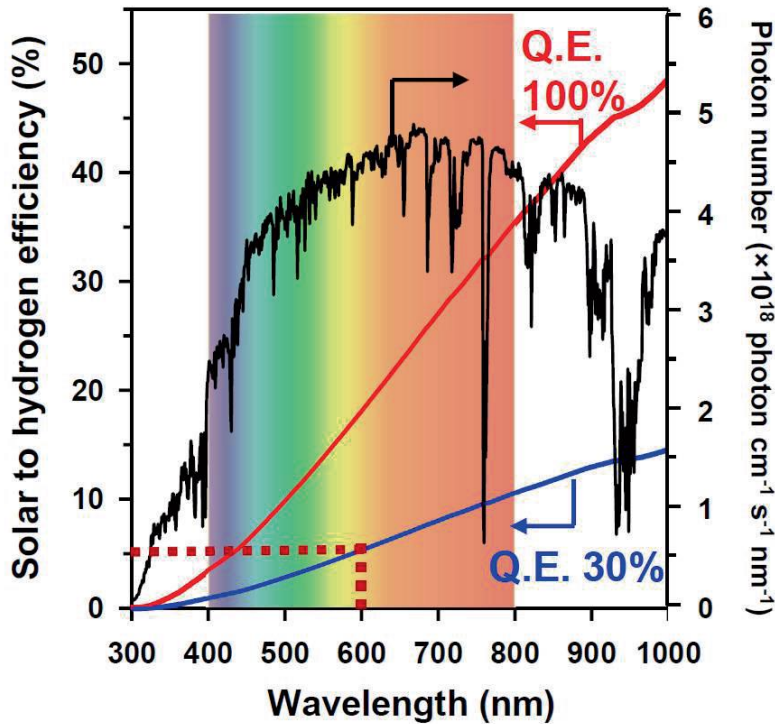


Fig. 1.4. Photon number of AM 1. 5G as a function of wavelength and theoretical efficiency for solar-to- H₂ integrated from a low wavelength to respective wavelength at a QE's of 100 and 30%. Reprinted with the permission from ref [79]. Copyright 2011 De Gruyter.

The incident photon-to-current efficiency (IPCE) is typically described as the ratio of photocurrent collected to incident photon flux. The IPCE is one of the most important diagnostic values obtained from a chronoamperometry (potentiostatic) measurement. The STH efficiency can be ideally estimated from the integration of the IPCE data over the solar spectrum. The IPCE can be given as a function of wavelength (λ) as shown in Eq.7.

$$\text{IPCE}(\lambda) = \frac{\text{electrons/cm}^2/\text{s}}{\text{photons/cm}^2/\text{s}} = \frac{|j_{ph}(\text{mA/cm}^2)| * 1239.8(\text{V}*\text{nm})}{P_{mono}(\text{mW/cm}^2) * \lambda(\text{nm})} \quad (7)$$

Where 1239.8 V*nm is the product of h (Planck's constant) and c (the speed of light), and the P_{mono} is the calibrated illumination power intensity of the monochromatic light.

1.3 Strategies to improve the PC/PEC efficiency

1.3.1 Non-metal doping in TiO₂

PC/PEC water splitting under solar light is a desired candidate technology for solving energy and environment issues in the future. TiO₂ is known as one of the most excellent UV-light driven photocatalysts over time. Non-metal doping is an effective strategy for the band gap

Introduction

engineering of TiO₂ to achieve visible-light activity. Actually, most non-metal doped TiO₂ materials have been applied in the degradation of organics, which can be regarded as essential instructions for the PC/PEC water splitting. To better guide our research work, we summarize the non-metal doped TiO₂ for photocatalytic H₂ production from different perspectives. Numerous non-metal doped TiO₂ photocatalysts have been reported to be active under visible light. The possible origins of visible light absorption and the followed photocatalysis have been discussed. Non-metal doping allows the formation of localized states in the band gap of TiO₂ contributing to its visible range electronic transitions. Impurity states such as N 2p, C 2p, S 2p lie above the VB of TiO₂ or mix with O 2p uplifting the VB. Cationic doping such as I⁷⁺, S⁴⁺, P⁵⁺ may behave as electron trap sites forming a sub band below the CB of TiO₂. The defect states of oxygen vacancies and Ti³⁺ resulting from non-metal doping are located above the VB and below the CB of TiO₂, respectively. Various synthetic methods of non-metal doped TiO₂ are also presented in detail in this chapter. Most importantly, we describe the creative work on non-metal doped TiO₂ for enhanced PC/PEC water splitting in recent years. The innovations on synthesis protocols, morphologies and the proposed mechanisms of the improved photocatalysis will be illustrated. Nitrogen is the first attempted non-metal dopant in TiO₂ and is still the most popular and adoptable one. The C-, B-, S- and P-doped TiO₂ systems are successively developed to increase the efficiency of photocatalytic H₂ production. The halogens have also shown their great potential in the modification of the electronic band gap structure of TiO₂ as well as in boosting the H₂ generation under visible light. The processes for photocatalytic/PEC water splitting such as photon absorption, charge carriers separation and transport can be enhanced by the non-metal doping, which all contribute to the final increased photocatalytic efficiency for water splitting. Even though the photocatalytic activity of TiO₂ has been remarkably improved by non-metal doping, the non-metal doped TiO₂ for water splitting is still at the early stage. The systematic studies of the relationship between properties of non-metal doped TiO₂ (e. g. dopant concentration and distribution, phase structure, morphology, surface area) and photocatalytic performance are rarely reported. In these experimental studies of photocatalytic/PEC water splitting over non-metal doped TiO₂ photocatalysts, the sacrificial agents and the assisted noble metals are also widely employed for reaching a high H₂ production rate. Moreover, the research on single element doped TiO₂ might reach its bottleneck, the co-doping strategy has been thus applied to further increase the photocatalytic efficiency for water splitting. Earth-abundant cocatalysts like C₃N₄, graphite oxide can be considered to be loaded in the non-metal doped TiO₂ system to alternatives of noble metals. The development of low-cost and high effective photocatalysts is still a great

challenge. We believe that the non-metal doped TiO₂ for photocatalytic/PEC water splitting under solar light will play an important role in the economic and environmental-friendly H₂ production.

1.3.1.1 Band structure of TiO₂

Electronic Band gap (Eg) of the pure semiconductor refers to the energy difference between the valence band maximum (VBM) and the lowest conduction band minimum (CBM). Only if the semiconductors are excited by photons with energy ($h\nu$) equal to or higher than Eg, electrons in VB can be excited to CB. More specifically, as shown in Fig. 1.5, the CBM and VBM of TiO₂ with both anatase and rutile phases consisted of “d” orbitals of titanium and “p” orbital of oxygen, which correspond respectively to the lowest unoccupied molecular orbitals (LUMO) and the highest occupied molecular orbitals (HOMO).^[75, 80]

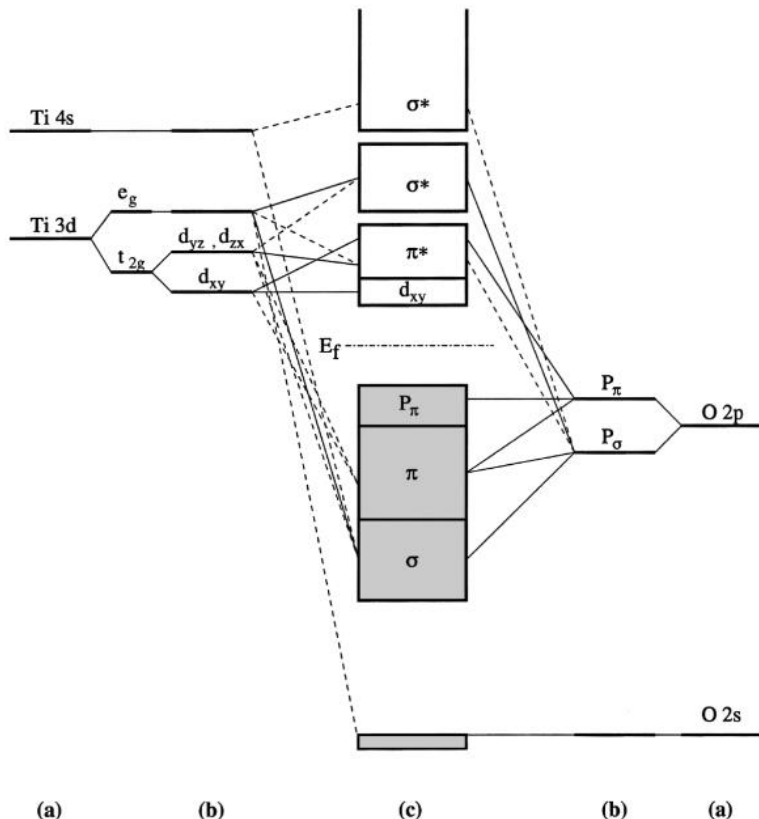


Fig. 1.5. Molecular orbital diagram of TiO₂ with both anatase and rutile phases (a) atomic levels, (b) crystal-field split levels, and (c) final interaction states. The thin-solid and dashed lines represent large and small contributions, respectively. Reprinted with permission from ref [80]. Copyright 2000 American Physical Society.

Titanium oxide has three kinds of crystalline phases, which are named as anatase, brookite and

rutile. Since the brookite TiO_2 is not easy to prepare in the laboratory, the other two forms have been mostly studied in photocatalysis applications. Fig. 1.6 shows the crystalline structures of TiO_2 in the form of TiO_6 octahedrons with each Ti^{4+} cation surrounded by six O^{2-} anions. Both anatase and rutile phases have tetragonal structures and the octahedron chains but in zigzag and linear forms respectively. The anatase TiO_2 has a lower density comparing to that of rutile one (3.9 versus 4.25 g/cm^3) and thus could have larger specific surface area.

The electronic band gap is determined by the crystalline structure which results in the slight difference in the band gap between anatase and rutile phase (3.2 versus 3.0 eV). Anatase TiO_2 is considered to be more photoactive not only owing to its special structure but also to its around 0.1 eV higher fermi level than that of rutile phase.^[81, 82] Pristine TiO_2 whatever anatase or rutile phase only responds to UV light because of their electronic large band gap ($3\text{-}3.2 \text{ eV}$). To achieve the photoactive TiO_2 under visible light, the electronic band gap modulation is necessary by doping other elements or other modification methods.^[83\text{-}86]

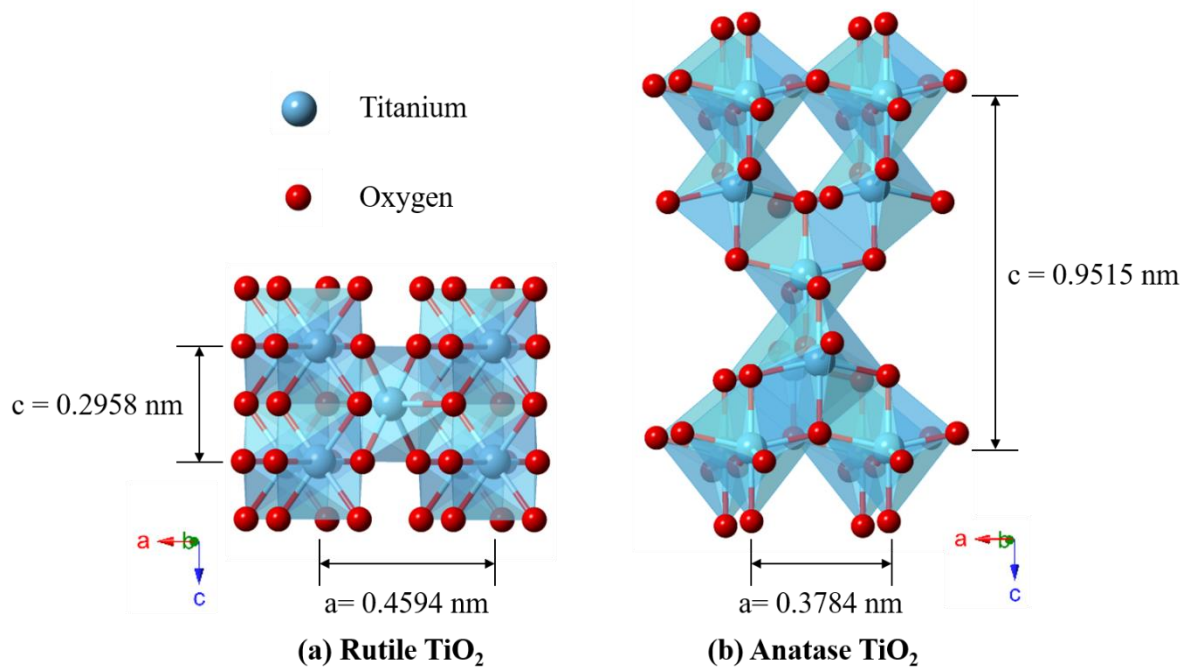


Fig. 1.6. TiO_6 polyhedra for the (a) rutile TiO_2 and (b) anatase TiO_2 .

1.3.1.2 Electronic Band gap engineering for visible light absorption

The photon absorption induces the excitation of electrons from the VB to the CB of TiO_2 . The absorption efficiency of solar light mainly depends on the band gap structure of TiO_2 . The pure TiO_2 only absorbs UV light due to its large band gap while the non-metal doping in TiO_2 photocatalysts with visible-light activity. Considerable works have proven the electronic band

Introduction

gap narrowing of TiO₂ by non-metal doping for photocatalysis as summarized in table 1.

Table 1. Summary of band gap narrowing of TiO₂ by non-metal doping reported in recent years

Dopant	Concentration	Maximum absorption wavelength	Band gap	Application	Reference
N	-	570 nm	2.17 eV	Dye photodegradation	[87]
N	-	520 nm	2.4 eV	Photodegradation of gaseous toluene	[88]
N	1.53 at%	550 nm	2.25 eV	Dye photodegradation	[89]
N	-	570 nm	2.17 eV	H ₂ production	[90]
N	1.08 at%	520 nm	2.38 eV	PEC water splitting	[91]
N	2 wt%	440 nm	2.87 eV	Dye photodegradation	[92]
N	-	500 nm	2.5 eV	Dye photodegradation	[93]
N	0.44 at%	550 nm	2.25 eV	Dye photodegradation and H ₂ production	[94]
N	-	575 nm	2.15 eV	Photoconversion of CO	[95]
C	2.3 at%	471 nm	2.63 eV	PEC water splitting	[96]
C	-	559 nm	2.22 eV	PEC water splitting	[97]
C	-	564 nm	2.2 eV	PEC water splitting	[98]
C	-	540 nm	2.3 eV	Photodegradation of 4-chlorophenol	[99]
C	4 at%	477 nm	2.6 eV	H ₂ production	[100]
C	-	540 nm	2.3 eV	Photodegradation of gaseous toluene	[101]
C	-	460 nm	2.69 eV	Photodegradation of microcystin-LR	[102]
C	-	519 nm	2.39 eV	Oxidative destruction Of NO	[103]
C	-	459 nm	2.7 eV	Photodegradation of microcystin-LR	[104]
C	-	438 nm	2.83 eV	Lithium Ion Batteries	[105]

Introduction

C	-	464 nm	2.67 eV	Dye photodegradation	[106]
C	0.7 wt%	466 nm	2.66 eV	Photodegradation of nonylphenol	[107]
N and C	-	471 nm	2.63 eV	NO oxidation	[108]
N and C	-	460 nm	2.7 eV	Photodegradation of phenol	[109]
N and C	-	564 nm	2.2 eV	PEC water splitting	[110]
B	-	431 nm	2.88 eV	Photodegradation of 4-chlorophenol	[111]
B	0.25 wt%	432 nm	2.87 eV	Dye photodegradation	[112]
B	2.74 at%	426 nm	2.91 eV	Dye photodegradation	[113]
B	-	559 nm	2.22 eV	Dye photodegradation	[114]
B	0.9 wt%	429 nm	2.89 eV	Photodegradation of endocrine	[115]
N and B	N: 1.3 at% B: 0.7 at%	445 nm	2.72 eV	Photodegradation of byproducts	[116]
S	-	490 nm	2.53 eV	Photodegradation of phenol	[117]
S	-	575 nm	2.16 eV	Photodegradation of quinoline	[118]
S	3 wt%	450 nm	2.76 eV	PEC water splitting	[119]
S	-	541 nm	2.29 eV	Dye photodegradation	[120]
S	-	496 nm	2.5 eV	Dye photodegradation	[121]
S	-	530 nm	2.34 eV	PEC water splitting	[122]
S	-	438 nm	2.83 eV	H ₂ production	[53]
S	-	429 nm	2.89 eV	Dye photodegradation	[123]
N and S	N: 1 at% S: 0.78 at%	585 nm	2.12 eV	Photodegradation of escherichia coli	[124]
C and S	C: 2.38 wt% S: 0.45 wt%	485 nm	2.56 eV	Dye photodegradation	[125]
N, C	-	464 nm	2.67 eV	Photodegradation of	[126]

Introduction

and S				gaseous toluene	
P	1.57 at%	411 nm	3.02 eV	Dye photodegradation	[127]
P	0.96 at%	411 nm	3.02 eV	PEC water splitting	[128]
P	10 wt%	460 nm	2.7 eV	Photodegradation of phenol	[129]
P	6.61 at%	428 nm	2.9 eV	PEC water splitting	[130]
P	-	411 nm	3.02 eV	Dye photodegradation and PEC water splitting	[131]
F	8.01 at%	451 nm	2.75 eV	H ₂ production	[132]
F and N	F: 6.25 at% N: 6.25 at%	564 nm	2.2 eV	H ₂ production	[133]
F and N	F: 1.7 wt% N: 3.59 wt%	444 nm	2.79 eV	Dye photodegradation	[134]
F and S	F: 2.1 at% S: 0.8 at%	510 nm	2.43 eV	Dye photodegradation	[135]
F and B	-	459 nm	2.7 eV	PEC water splitting and dye photodegradation	[52]
F and P	-	460 nm	2.7 eV	Photodegradation of Atrazine	[136]
N, B and F	N: 1.71 at% B: 2.67 at% F: 1.58 at%	451 nm	2.75 eV	Dye photodegradation	[137]
Cl	-	415 nm	2.99 eV	Dye photodegradation	[138]
C and Cl	-	441 nm	2.81 eV	Dye photodegradation	[139]
I	-	441 nm	2.81 eV	Photodegradation of phenol	[140]
I	4 at%	564 nm	2.2 eV	Photodegradation of 4-chlorophenol	[141]
I	7 wt%	459 nm	2.7 eV	Photodegradation of gaseous acetone	[142]

Introduction

I	3.52 at%	443 nm	2.8 eV	PEC water splitting	[143]
I	10 wt%	413 nm	3 eV	CO ₂ photoreduction	[144]
N and Br	0.3 wt% Br	431 nm	2.88 eV	H ₂ production	[145]
Cl and Br	Cl: 0.9 at% Br: 1.8 at%	435 nm	2.85 eV	H ₂ production	[146]

There are three main mechanisms proposed to account for visible light absorption of TiO₂ when using non-metal doped TiO₂ as shown in Fig. 1.7, which are as follows:

Type 1: A new valence band (VB) is located above the valence band maximum (VBM) of TiO₂ resulting in the lowered excitation energy. Electrons are generated from the doping level to the conduction band (CB) of TiO₂ under visible light irradiation. The new uplifted VB can be originated from different kinds of impurity states. Asahi et al. and some other groups claimed that the new VB is from the mixed states of O 2p with the 2p states of dopants such as N, C and B as shown in Fig. 1.7a. [47, 147-149] Umebayashi et al. presented the red shift in the absorption edge of S-doped TiO₂ caused by mixing the S 3p states with the VB of O 2p. [63] Recently, other researchers stated the presence of isolated impurity states of non-metal above the VB of TiO₂ (Fig. 1.7b). [150-153] Livraghi reported that the isolated states generated by single-atom nitrogen centers played an essential role in the visible light absorption and charge transport (Fig. 1.7c). [154] Ihara et al. suggested that the visible light absorption could be originated from oxygen defect sites in the form of NO species generated by the nitrogen doping, rather than from the nitrogen states itself. [155] Thus it is also possible that the new VB be derived from the oxygen vacancy related defect levels. Oxygen vacancies as shown in Fig. 1.7d have already been proved to be the prevalent defects in semiconductor materials, which narrow the electronic bandgap and promote electron-hole separation. [156] The localized oxygen vacancy states in the lattice of TiO₂ created by non-metal doping can effectively expand the visible light absorption range. However, the states of oxygen vacancy are still under debate. Some researchers proposed this kind of states should be situated above the VB of TiO₂, [150, 157, 158] while others stated that it should be located below the CB of TiO₂. [159, 160]

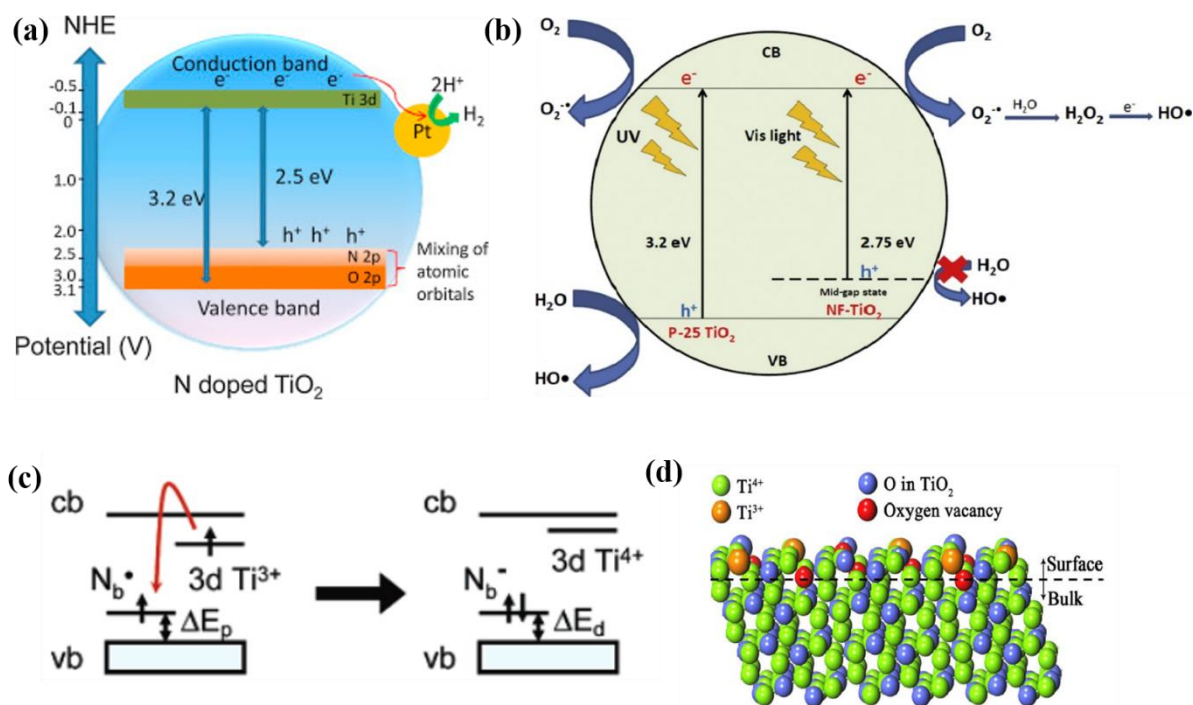


Fig. 1.7. Schematic illustration of (a) band gap reduction by N 2p orbital mixing in TiO₂ with Pt nanoparticles as co-catalysts for the generation of H₂, reprinted with permission from ref [147], Copyright 2015 Elsevier; (b) band gap structure of N-doped TiO₂ photocatalyst, reprinted with permission from ref [151], Copyright 2014 Elsevier; (c) electronic band structure modifications resulting from the interactions between doped N and Ti³⁺ (oxygen vacancy) defects, reprinted with permission from ref [154], copyright 2006 American Physical Society; (d) surface defects in TiO₂, reprinted with permission from ref [156], copyright 2018 Royal Society of Chemistry.

Type 2: A new sub band is formed below the conduction band minimum (CBM) resulting in a lowered band energy of TiO₂. The photo-excited electrons from the VB will be trapped in the sub band facilitating electrons transfer under visible light. This sub band could be consisted of Ti³⁺ 3d states created by non-metal doping during the vacuum calcination process as shown in Fig. 1.8a and b.^[161-165] Ti³⁺ self-doped TiO₂ known as black TiO₂ has been demonstrated to be responsible for visible-light absorption, which is attributed to the introduction of new sub band below the CBM.^[24, 166, 167] Another statement that the sub band might be originated from cations of non-metal elements was also proposed. Su et al. have reported the new states of I⁷⁺ from the IO₄⁻ group located below the CBM of TiO₂ and suggested that the photoexcitation from the VB of TiO₂ to the surface IO₄⁻ is responsible for the visible-light response of the I-doped TiO₂ as shown in Fig. 1.8c^[142] The transition level of S⁴⁺ is also found to be below the

CBM of TiO_2 which induces electron emissions from O 2p to the impurity energy level (S^{4+}) under visible light as illustrated in Fig. 1.8d. [168, 169]

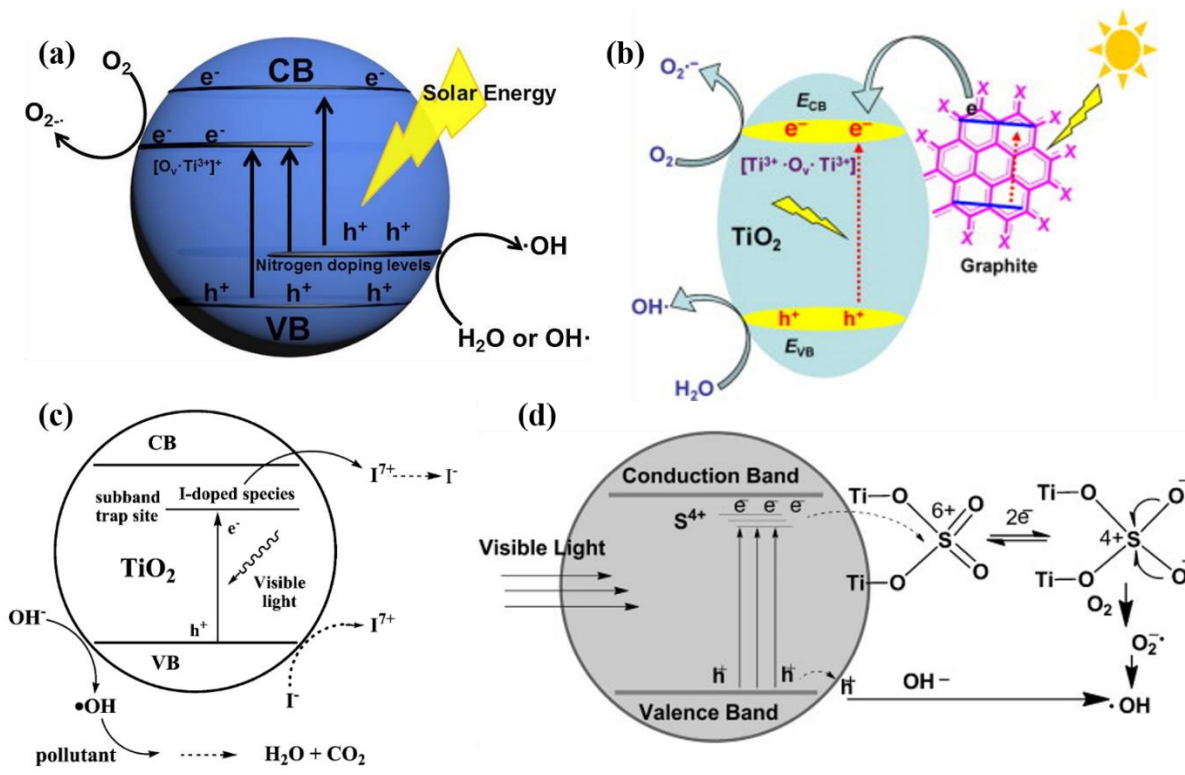


Fig. 1.8. Schematic illustration of (a) proposed mechanism of Ti^{3+} and N co-doped TiO_2 , reprinted with permission from ref [161], Copyright 2016 Elsevier; (b) mechanism of photo-degradation over Ti^{3+} and carbon co-doped catalyst, reprinted with permission from ref [163], copyright 2014 Elsevier; (c) proposed photocatalytic mechanisms over I-TiO₂, reprinted with permission from ref[142], copyright 2016 American Chemical Society; (d) charge transfer process in S-TiO₂ for degradation of phenol, reprinted with permission from ref [169], copyright 2014 Elsevier.

Type 3: The visible light absorption of TiO_2 can also be resulted from the interplay of type 1 and 2. The extent of red shift to visible light region in TiO_2 will be enhanced due to the synergistic effect. The most common situation for this case is co-doping with non-metal impurities and the in-situ created Ti^{3+} in TiO_2 as shown in Fig. 1.9a. [170-172] Electrons can be injected from the impurity level to Ti^{3+} 3d level more easily because of the significantly narrowed band gap. Ti^{3+} can trap these electrons and prolong the lifetime of photo-induced electron-hole pairs and hinder their recombination as illustrated in Fig. 1.9b. [161] Besides, co-doping with different non-metal elements can be another solution for tuning the band structure

of both VB and CB of TiO_2 . [173-176]

In addition to the above three types of doping effects for electronic band gap narrowing, some researchers proposed that visible light absorption is in fact originated from the existence of colour centers in the band structure of doped TiO_2 rather than from the band gap narrowing as shown in Fig. 1.9c and d. [177-179] The colour center also known as F-center (from the original German Farbe which means color), is a type of crystallographic defect caused by oxygen vacancies filled with unpaired electrons, which tend to absorb visible light. The electrons in the oxygen vacancies can also reduce the adjacent Ti^{4+} into Ti^{3+} species. [180]

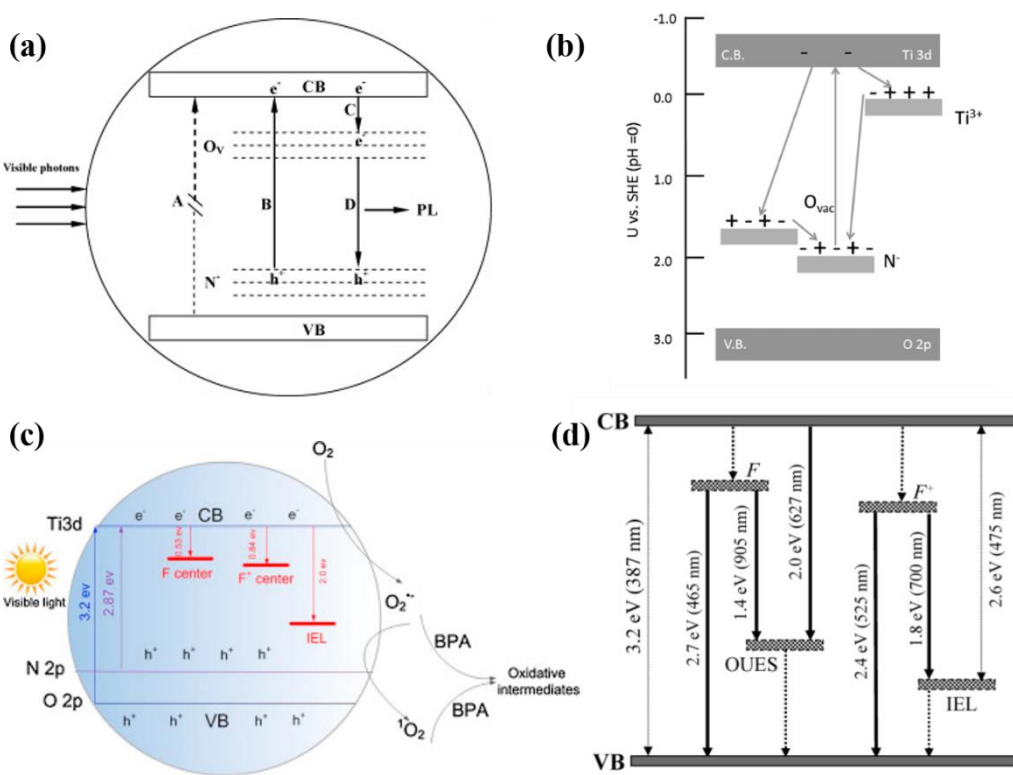


Fig. 1.9. Schematic illustration of (a) electron transfer process over N-doped TiO_2 nanocrystals under visible light irradiation, reprinted with permission from ref [172], copyright 2008 Elsevier; (b) visible light excitation of N-F co-doped TiO_2 and refilling of empty N states by electron transfer from either Ti^{3+} or O vacancy, reprinted with permission from ref [174], copyright 2014 American Physical Society; (c) Band gap structure of N-F co-doped TiO_2 under visible light irradiation, reprinted with permission from ref [175], copyright 2016 Elsevier; (d) proposed structural model of energy states that exist between the VB and CB of TiO_2 , reprinted with permission from ref [178], copyright 2005 American Chemical Society.

Due to the redox potential of non-metal elements and oxygen-deficient synthesis condition, the

oxygen vacancies and Ti^{3+} colour centre are easily formed during the doping process resulting in visible light activity. In short, all these localized states in non-metal doped TiO_2 can be responsible for the visible light activity as summarized in Fig. 1.10.

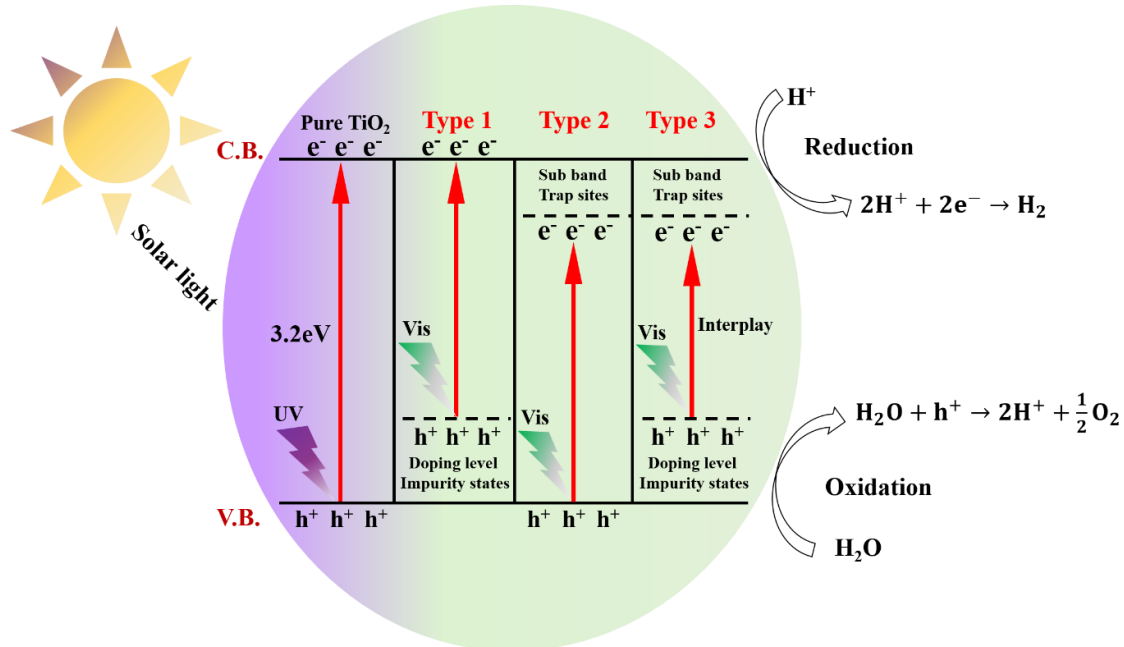


Fig. 1.10. Schematic of basic mechanisms of photocatalytic water splitting over non-metal doped TiO_2 photocatalysts.

1.3.1.3 Synthetic strategies of non-metal doped TiO_2

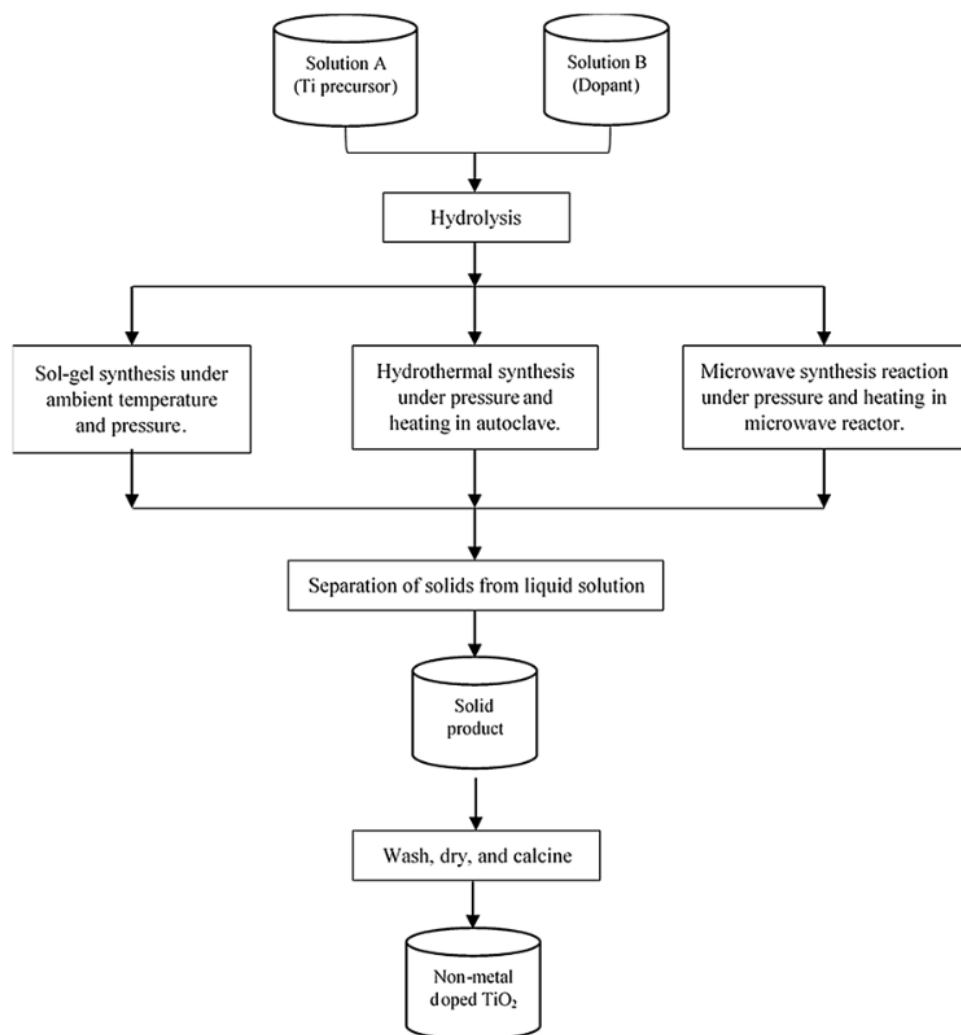
The photocatalytic activity of TiO_2 is closely related to the crystalline phase, particle size, morphology, specific surface area, doping amount and forms, which are dependent on the preparation methods. To understand the relationship between synthetic strategies and the performance of TiO_2 , the main doping approaches are summarized as follows:

1.3.1.3a Wet chemical methods

The wet-chemical fabrications such as sol-gel method, hydrothermal method, and microwave-assisted method are widely explored to prepare various non-metal (N, C, S, B, P and Halogens) doped TiO_2 . The benefits are mainly derived from the easy manoeuvrability and controllability in the doping level and particle sizes by simple variations in the experimental conditions, such as hydrolysis rate, solution pH and solvent systems.^[181-183] These three synthesis methods are very similar as shown in Fig. 1.11. The sol-gel method of doping TiO_2 is normally operated at ambient temperature and pressure while the hydrothermal way is usually carried out in an autoclave keeping at a specific temperature. The microwave-assisted method is often combined

Introduction

with the sol-gel or hydrothermal methods using a microwave reactor to speed up the formation of the products during the doping process. In a representative preparation procedure, the solution A is formed by titanium precursors such as titanium isopropoxide (TIP) [184], tetrabutylorthotitanate (TBOT) [185], and titanium tetrachloride [186] in their solvent. As summarized in table 2, amine [187, 188], ammonia [189, 190] and urea [191-193] are commonly used as precursors for nitrogen doping. For carbon doping, there are abundant organic compounds serving as the carbon sources such as methanol [194], cellulose [195, 196], glucose [197-200] and chitosan, etc. The sulfuric acid or sulfate precursors, thiourea have been applied as sulfur sources. [201-203] The B and P sources are normally provided by boric acid [113, 204, 205] and phosphorous acid [127, 131, 206] or phosphate [127, 131] respectively. The researches on halogen elements doping other than F in TiO₂ are relatively rare. The fluorine doping typically uses ammonium fluoride [207, 208], chlorine dopant usually comes from the residuals from chloroform [209] and the iodine doping mostly employs iodic acid. [140, 210]



Introduction

Fig. 1.11. Sol-gel, hydrothermal, and microwave-assisted methods for doping of non-metal onto TiO₂ photocatalyst. Reprinted with the permission from ref [183]. Copyright 2017 Springer Berlin Heidelberg.

Table 2. A short overview of Non-metal doped TiO₂ by wet-growth methods

Dopant	Doping procedure	Titanium precursors	Dopant precursors	Ref
N	Sol-gel	Titanium isopropoxide	Urea	[211]
		Tetrabutyl titanate	Urea	[212]
		Titanium tetra-n-butoxide	Urea	[213]
		Titanium tetrachloride	Ammonia	[214]
		Titanium butoxide	Nitric acid	[215]
		Titanium butoxide	Ammonium nitrate	[216]
	Hydrothermal method	Ti-peroxo complex	Urea	[217]
		Titanium isopropoxide	Chitosan	[218]
		Tetrabutyl titanate	Urea	[219]
		Titanium isopropoxide	N-Methyl-2-pyrrolidone	[220]
		Titanium tetrachloride	Ammonia	[221]
		Titanium tetra-isopropoxide	Ammonia	[222]
C	Microwave-assisted method	P25 TiO ₂	Ammonium chloride	[223]
		P25 TiO ₂	Ammonium phosphatediabasic	[224]
		P25 TiO ₂	Ammonia	[225]
		Anatase TiO ₂	Guanidine hydrochloride	[226]
	Sol-gel	Titanium butoxide	Cellulose	[227]
		Titanium tetrachloride	Melamine borate	[227]
		Tetrabutyl titanate	Hexadecyl trimethylammonium bromide	[228]
		TiO ₂	Methanol	[194]
		Titanium butoxide	Self-doping	[99]

Introduction

		Titanium isopropoxide	Cellulose	[195]
B	Hydrothermal method	Titanium isopropoxide	Methoxyethane	[229]
		Titanium n-butoxide	Chitosan	[230]
		Tetrabutyl titanate	Polystyrene	[106]
		Tetrabutyl titanate	Fructose	[231]
		Titanium Sulfide	Fructose	[232]
Microwave-assisted method				
		Titanium tetraisopropoxide	Self-doping	[233]
S	Sol-gel	Titanium butoxide	Boric acid	[234]
		Tetrabutyl titanate	Boric acid	[235]
	Hydrothermal	Titanium tetrafluoride	Boric acid	[236]
		Titanium diboride	Self-doping	[237]
	Microwave-assisted method	Titanium isopropoxide	Boric acid	[238]
P	Sol-gel	Titanium isopropoxide	Sulfuric acid	[239]
		Titanium butoxide	Thiourea	[240]
		Titanium tetraisopropoxide	Thiourea	[241]
	Hydrothermal	Tetrabutyl orthotitanate	Thiourea	[135]
		Tetrabutyl titanate	Potassium persulfate	[169]
F	Sol-gel	Titanium tetraisopropoxide, Titanium tetrachloride	Cyclohexyl phosphin	[129]
		Titanium butoxide	Phosphoric acid	[242]
		Titanium isopropoxide	Phosphoric acid	[206]
	Hydrothermal	Tetrabutyl titanate	Hypophosphorus acid	[243]
		N-tetrabutyl titanate	Phosphoric acid	[244]
		Tetrabutyl titanate	Hypophosphorous acid	[245]
	Sol-gel	Titanium isopropoxide	Trifluoroacetic acid	[246, 247]
	Hydrothermal	Etrabutyl orthotitanate	Ammonia fluoride	[135]

		Titanium tetrafluoride	Self-doping	[248]
		Ti plates	Hydrogen fluoride	[54]
Cl	Hydrothermal	Titanium tetrachloride	Chloroform	[138, 139]
I	Sol-gel	Tetrabutyl titanate	Iodic acid	[210, 249]
	Hydrothermal	Titanium tetrafluoride	Iodic acid	[250]
		P25 TiO ₂	Iodic acid	[144]
		Titanium isopropoxide	Iodic acid	[251]

1.3.1.3b One-step thermal treatment

The one-step thermal treatment involves three specific approaches which are as follows:

1. Chemical vapor deposition of TiO₂ in gas atmospheres with doping species. [97, 252-260]
2. Physical deposition such as sputtering and pulsed laser deposition of TiO₂ or Ti related targets with mixture of carrier gas and doping species as the reactive gas. [47, 148, 261-266]
3. Incomplete oxidizing compounds with Ti and doping elements. [148, 172, 267-272]

Compared to the hydrothermal process, one-step thermal treatment can be simple, versatile, scalable and fast. Specially, the approaches 1 and 2 are frequently used for non-metal doped TiO₂ especially for thin films with high purity and conformal morphology. [263, 273-276]

Considering the commonality on gas phase doping in TiO₂ of thermal treatment and physical deposition, the overview of non-metal doping by approaches 1-2 is given in table 3.

The approach 3 is facile and normally used for N, C and S doping by incomplete oxidation of inorganic compounds such as TiN [172, 268], TiC [148, 270] and TiS₂ [63, 267]. However, the doping concentration is hard to control even by managing the calcination conditions such as temperature, duration, gas flow, ramping rate and cooling rate. Thus the improvement on vis-photoactivity of the doped TiO₂ by such approach is very limited.

Table 3. A Summary of non-metal doping in TiO₂ by one-step thermal treatment

Dopant	Synthesis routes	Gas/impurity sources
N	Thermal treatment of TiO ₂ in N ₂ or NH ₃ flow or mixed with urea at high temperature. [91, 133, 188, 277-284]	N ₂ , NH ₃ , NO, urea, hydrazine, tertbutylamine
	CVD growth from vapor of TiO ₂ precursor and	

Introduction

	<p>nitrogen source like NH₃, hydrazine, NO, tertbutylamine. [285-290]</p> <p>Sputtering or electron-beam evaporation using TiO₂ target under gas flow containing N₂. [47, 263, 291-297]</p> <p>PLD using TiO₂ with TiN targets in oxygen /nitrogen gas mixture. [261, 266, 298-301]</p>	
C	<p>Calcination TiO₂ under CO or acetylene gas flow. [55, 97, 302-307]</p> <p>PLD using TiC target under Ar or using TiO₂ target under CH₄ flow. [265, 308, 309]</p> <p>Sputtering using TiO₂ under CO or CO₂ gas flow or Co-sputtering using TiO₂ and graphite as target. [310-312]</p>	CO, CO ₂ , CH ₄ , acetylene (C ₂ H ₂), and graphite
B	<p>CVD from mixed gases of TiO₂ precursor and diborane or vapor of borate, boric acid and boron. [256, 258, 259, 313-315]</p> <p>Co-sputtering of Ti and TiB₂ in a plasma of Ar and O₂ gases. [316]</p>	Diborane, borate, boric acid and boron
S	<p>Calcination TiO₂ at high temperature under H₂S flux or sulfur vapor. [254, 255, 317, 318]</p> <p>CVD of TiO₂ or vapor produced by TiO₂ precursor and thiourea or disulfide as volatile sulfur source. [319-321]</p> <p>PLD using TiS₂ target in air. [322]</p> <p>Co-sputtering of Ti and TiB₂ in a plasma of Ar and O₂ gases. [316]</p>	H ₂ S, S, thiourea ([CH ₃) ₃ C]S ₂)
P	CVD of TiO ₂ precursor and vapor gases from phosphphoric acid, triethyl phosphate and Sodium hypophosphite. [130, 260, 323, 324]	HPO ₃ , NaH ₂ PO ₂ , (C ₂ H ₅ O) ₃ PO
Halogens	CVD: The t-butylfluoride and pentafluoropropionic acid are commonly used as F precursor to produce vapor gas. [324, 325]	F: C ₄ H ₉ F, CF ₃ CF ₂ COOH

1.3.1.3c Other methods

Table 4 presents a list of synthesis of non-metal doped TiO₂ made by methods other than above-mentioned methods. Anodization method is used to synthesize non-metal-doped TiO₂ nanotubes with a unique structure, high specific area and high absorption ability. The anodic oxidation of the Ti foil in electrolytes containing non-metal precursors can achieve one-step doping. [326, 327]

In principle, all species including H₂ can be incorporated into TiO₂ by ion implantation technique. It seems that the dopant content and location can be adjusted by the parameters of implanter including the fluence and the energy. The defects in TiO₂ produced by ion bombardment can be annealed out afterwards. However, the ion scattering still results in inhomogeneous dopant distribution in the presupposed depth. Even with high-energy accelerators (operating at 50-1000 keV), the implantation depth is limited to micrometers. Moreover, the whole set of ion implanter is complicated, thus the doping by ion implantation stays at the preliminarily stage.

Up to present, the plasma modification way is only applied for the nitrogen doping in TiO₂ by using N₂ or NH₃ as the N sources. [328, 329] The interstitial doping is favoured by N₂-plasma treatment whereas substitutional N doping with oxygen vacancies is preferred by reductive NH₃-plasma treatment. N-plasma surface modification has effectively enhanced the photocatalytic activity of TiO₂ without any damage on its structure. [328, 330]

Table 4. Non-metal doped TiO₂ by other methods

Dopant	Doping method	Titanium precursors	Dopant precursors	Ref
N	Anodization	Ti foil	Urea	[331]
B, N	Anodization	Ti foil	NH ₄ F, boricacid	[332]
C	Anodization	Ti plates	Graphene Oxide Quantum Dots	[333]
C	Anodization	Ti foil	Ethylene glycol	[334]
S	Anodization		Sulfuric acid	[335]
N	Ion implantation	As-prepared TiO ₂	N ions	[336]

Introduction

C, N	Coimplantation	As-prepared TiO ₂	N and C ions	[337]
B	Ion implantation	As-prepared TiO ₂	B ions	[338]
S	Ion implantation	As-prepared TiO ₂	S ions	[339]
N	Plasma treatment	Titanium tetraisopropoxide	N ₂	[340]
N	Plasma treatment	As-prepared TiO ₂	N ₂	[341]
N	Plasma treatment	As-prepared TiO ₂	NH ₃	[342]

1.3.1.4 Advance in non-metal doped TiO₂ for PC/PEC water splitting

In this part, we present recent progress on non-metal doping in TiO₂ in the terms of synthesis protocols, morphologies, PC/PEC activity for H₂ production and proposed mechanisms. Table 5 summarizes the performance of non-metal doped TiO₂ developed in recent years for PC / PEC water splitting. The relevant parameters including the dopant content, light sources, type and concentration of liquid media (electrolyte or scavenger solution) are listed in the table. The noble metals such as Pt and Pd are employed as assisted co-catalysts.

Table 5. Summary of important developments on non-metal doped TiO₂ photocatalysts for water splitting.

Photocatalyst	Co-catalyst	Light sources	Electrolyte or scavenger solution	H ₂ evolution rate or QE	Ref.
N-Anatase TiO ₂ sheets	1 wt% Pt	300W Xe lamp with the wavelength of 420-770 nm	0.01 M NaOH and 3 mM terephthalic acid	81 μmol h ⁻¹ m ⁻²	[90]
N- Anatase TiO ₂	1.3 wt% Pt	300W Xe lamp with the	Mixed solution of methanol	140 μmol h ⁻¹ g ⁻¹	[343]

Introduction

		wavelength \geq 400 nm	and water (1:3)		
N- Anatase TiO ₂	3 wt% In and 2 wt% Pd	8 pieces of ordinary day light lamps (36W*8)	Mixed solution of methanol and water (1:4)	75 $\mu\text{mol h}^{-1}\text{g}^{-1}$	[344]
N- Anatase TiO ₂ NTs		Simulated solar light (AM 1.5)	1M KOH	1.26%	[345]
N-TiO ₂ Anatase nanofibers	1 wt% Pt	Six pieces of UV lamps (3W*6)	Mixed solution of ethanol and water (1:3)	2250 $\mu\text{mol h}^{-1}\text{g}^{-1}$	[346]
N- Anatase TiO ₂ sheet	0.5 wt% Pt	350W Xe lamp with the wavelength \geq 420 nm	Mixed solution of methanol and water (1:4)	865 $\mu\text{mol h}^{-1}\text{g}^{-1}$	[347]
5 wt% N-Anatase TiO ₂ nano rice grain		150W Xe lamp as solar light simulator	0.5 M Na ₂ SO ₄	0.8%	[348]
N-Anatase and Rutile TiO ₂	Graphite oxide	500W Xe lamp of visible light	Mixed solution of methanol and water (1:10)	112 $\mu\text{mol h}^{-1}\text{g}^{-1}$	[349]
4.33 at%N-Anatase TiO ₂ film		300W Xe lamp	Mixed solution of methanol and water (1:10)	4500 $\mu\text{mol h}^{-1}\text{m}^{-2}$	[350]
1.12wt%N-Anatase TiO ₂ /Au	Au	150W solar light simulator	Mixed solution of methanol and water (1:9)	79 $\mu\text{mol h}^{-1}\text{g}^{-1}$	[351]
2.08 at% N-Anatase TiO ₂ nanobelts	0.5 wt% Pt	300W Xe lamp with the wavelength of 420-800 nm	Mixed solution of methanol and water (1:4)	670 $\mu\text{mol h}^{-1}\text{g}^{-1}$	[352]

Introduction

0.44 at% N-Anatase TiO ₂ grains	0.6 wt% Pt	350W Xe lamp with the wavelength \geq 420 nm	Mixed solution of methanol and water (1:3)	55 $\mu\text{mol h}^{-1}\text{g}^{-1}$	[94]
N-Anatase TiO ₂	2 wt% Gd	10 AM to 3 PM artificial solar light by 150 W Xe lamp	Mixed solution of methanol and water (1:19)	10764 $\mu\text{mol h}^{-1}\text{g}^{-1}$	[353]
C-Anatase TiO ₂	0.4 wt % Pt	A 300W solar simulator equiped with filter (520 \pm 46 nm)	1M KOH	8.5%	[98]
4 at% C-Anatase TiO ₂	Au/CdS with 1wt% Pt	300W Xe lamp with the wavelength \geq 420 nm	Mixed solution of Na ₂ S (0.05 M) and Na ₂ SO ₃ (0.1 M)	433.2 $\mu\text{mol h}^{-1}\text{g}^{-1}$	[354]
3.62wt% C-Rutile and Anatase TiO ₂		300W Xe lamp with the wavelength > 280 nm	Mixed solution of methanol and water (1:4)	27.9 $\mu\text{mol h}^{-1}\text{g}^{-1}$	[56]
21wt% C-Anatase TiO ₂		A 300 W Xe lamp as a full spectrum solar simulator	10 vol % TEOA	33.04 $\mu\text{mol h}^{-1}\text{g}^{-1}$	[355]
C-Anatase TiO ₂ on TiC		300W Xe lamp with the wavelength > 400 nm	Mixed solution of methanol and water (1:5)	279.23 $\mu\text{mol h}^{-1}\text{g}^{-1}$	[272]
C-Anatase TiO ₂	g-C ₃ N ₄	300W Xe lamp (\geq 420 nm)	Mixed solution of Triethanolamine and water (1:9) with 1	1147 $\mu\text{mol h}^{-1}\text{g}^{-1}$	[356]

Introduction

			mg/ml chloroplatinic acid (H_2PtCl_6)		
C-N-Anatase TiO_2		450W Xe lamp with the wavelength ≥ 420 nm	Mixed solution of methanol and water (1:3)	81.8 $\mu\text{mol h}^{-1}\text{g}^{-1}$	[357]
1.1 at% B- Anatase TiO_2	1 wt% Pt	-	Mixed solution of methanol and water (1:9) and 0.33mM $AgNO_3$	780 $\mu\text{mol h}^{-1}\text{g}^{-1}$	[237]
10 wt% B- Anatase TiO_2	0.6 wt% Pt	Simulated solar light by Xe lamp (300 W)	Mixed solution of methanol and water (1:19)	11.8 mmol $\text{h}^{-1}\text{g}^{-1}$	[162]
B-N-Anatase TiO_2	1 wt% Pd	125W Hg medium pressure lamp (UV-vis excitation)	1M Fructose solution	500 $\mu\text{mol h}^{-1}\text{g}^{-1}$	[358]
S-Rutile TiO_2 core-shell structure	0.5 wt% Pt	AM 1.5 simulated solar light	Mixed solution of methanol and water (1:4)	258 $\mu\text{mol h}^{-1}\text{g}^{-1}$	[255]
S-Anatase TiO_2 nanotubes	CuO/ Cu_2O	500W Xe lamp with the wavelength of 400-500 nm	Mixed solution of methanol and water (1:4)	7.5 mmol $\text{h}^{-1}\text{g}^{-1}$	[359]
S-Anatase TiO_2 nanopillars		AM1.5G with bandpass filter(λ $= 400$ nm)	Mixed solution of methanol and water (1:4)	163.9 $\mu\text{mol h}^{-1}\text{g}^{-1}$	[53]
3.4 at% S- Anatase /Rutile TiO_2 on carbon		300W Xe lamp with the wavelength $>$	Mixed solution of methanol and water (1:9)	333 $\mu\text{mol h}^{-1}\text{g}^{-1}$	[360]

Introduction

substrate		400nm			
0.08at%N-3.8 at% S-Anatase /Rutile TiO ₂	V ₂ O ₅ with 1 wt% Pt	125W high pressure Hg lamp with the wavelength > 400nm	Mixed solution of methanol and water (1:9)	3200 μmol h ⁻¹ g ⁻¹	[361]
F-Rutile TiO ₂		400W Hg high pressure lamp	Mixed solution of methanol and water (1:5. 5)	113 μmol h ⁻¹ g ⁻¹	[362]
5wt% F-Anatase /Rutile TiO ₂	1 wt% Pt	300W Xe lamp with the wavelength of 350-400 nm	Mixed solution of methanol and water (1:4)	22 mmol h ⁻¹ g ⁻¹	[363]
6.9 wt% F-Anatase TiO ₂ nanosheets		300W Xe lamp with the wavelength > 400 nm	1M Na ₂ SO ₄ solution	18270 μmol h ⁻¹ g ⁻¹	[59]
6.25 at% N-F-Anatase TiO ₂		400W Xe lamp with the wavelength > 400 nm	Mixed solution of 0.1 M Na ₂ SO ₄ and 0. 1 M Na ₂ S	57 μmol h ⁻¹ g ⁻¹	[133]
3DOM N-Br-Anatase TiO ₂		350W Xe lamp with the wavelength ≥ 420 nm	Mixed solution of triethanolamine and water (1:9)	2247 μmol h ⁻¹ g ⁻¹	[145]
Cl-Br-Anatase /Rutile TiO ₂	0.3 wt% Pt	450W Hg high pressure lamp	2M Na ₂ CO ₃	467 μmol h ⁻¹ g ⁻¹	[146]

1.3.1.4a Nitrogen doping

Nitrogen doped TiO₂ is one of the most promising and investigated photocatalyst system for H₂ production under visible light irradiation. [61, 155, 364, 365] In general, the substitutional N 2p

Introduction

impurity states are localized above the top of the O 2p valence contributing to the band-gap narrowing.^[366, 367] While interstitial N atoms bind to O lattice ions in the form of NO species, the resulted new energy states lie above the VB of TiO₂, and thus the excitation energy is shifted towards visible region.^[154, 188, 367] High doping concentration of nitrogen leads to the formation of stoichiometric oxynitrides or nitrides, resulting in a red shift of the absorption edges. Some of key findings of N-TiO₂ for H₂ production are presented in the following section.

Compared to conventionally N doped single-wall TiO₂ nanotubes (N-SW-TiO₂ NTs), the surface area, smoothness and orderliness of the N-DW-TiO₂ NTs (N doped double-wall TiO₂ nanotubes) were improved.^[368-370] N-DW-TiO₂ NTs were prepared by a facile two steps anodization method using the NH₄F both for etching and *in situ* N doping source. As shown in Fig. 1.12, the photocurrent density on the N-DW-TiO₂ NTs is higher throughout the potential window and reaches to a high value of 1.51 mA/cm² at 1.23 V vs RHE, 136% higher than that on N-SW-TiO₂ NTs. The N-DW-TiO₂ NTs show a maximum photon-to-H₂ efficiencies of 1.26% at 0.5 V vs RHE which is 2.7 times higher than that of N-SW-TiO₂ NTs (Fig. 1.12g). The maximum IPCE value of N-DW-TiO₂ NTs is 56% at 390 nm, which is three times higher than that of N-SW-TiO₂ NTs (Fig. 1.12h). Apparently, the photocatalytic efficiency is highly improved by the double wall structure of TiO₂. In other words, the nitrogen doping in DW-TiO₂ NTs can be more effective for PEC water splitting.

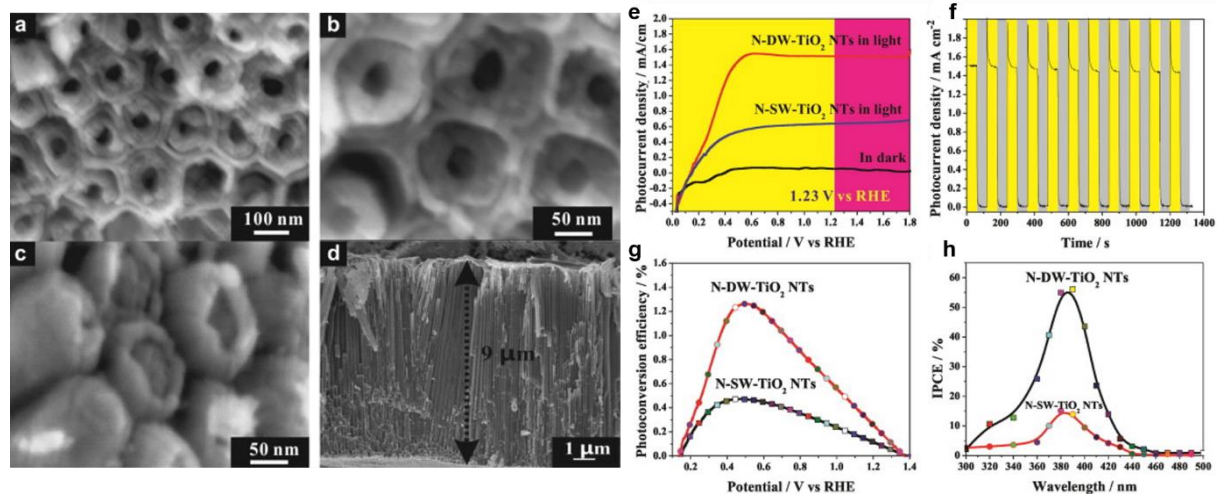


Fig. 1.12. (a, b) Top-view SEM image, (c) Bottom-view SEM image and (d) Side-view SEM image of N-DW-TiO₂ NTs; (e) linear-sweep voltammograms collected with a scan rate of 5 mV/s in dark and under illumination; (f) amperometric I-t curves at an applied potential of 1.23 v RHE under illumination with 60 s light on/off cycles; (g) photoconversion efficiency as a function of applied potential; (h) IPCE spectra in the region of 300-500 nm at 1.23 v

Introduction

RHE. Reproduced with the permission from ref [345]. Copyright 2011 Elsevier.

Bio-inspired fabrication of nitrogen doped TiO₂ by using a living mussel (*Cristaria plicata*) as cradle has first been reported by Xie *et al.*. As presented in Fig. 1.13a, the tablets consisted with amorphous TiO₂ precursor with a diameter of 10 mm and thickness of 1-2 mm were implanted into the mussel's body as a pearl nucleus. After 15~90 days of mineralization, the TiO₂ tablets were wrapped thin layers of nacre. The nitrogen doped TiO₂ (bm-TiO₂) in the shape of nanospherical clusters were obtained followed by washing and heat treatments. The H₂ production rate of pristine TiO₂ is almost zero under visible light, whereas the H₂ production rate of the bm-TiO₂ increases up to 55 μmol h⁻¹g⁻¹ as shown in Fig. 1.13e. Apparently, visible-light efficiency of TiO₂ is improved by the nitrogen doping with the special assistance from *Cristaria plicata*. The interstitial nitrogen doping in TiO₂ is confirmed by the XPS (inset: Fig. 1.13f). The N concentration is calculated to be 0.44 at% based on the XPS result. The valence-band XPS spectra of TiO₂ samples are shown in Fig. 1.13g (inset), compared to pristine TiO₂, the main absorption onset in the VB of bm-TiO₂ is located at 1.0 eV and the band tail blue-shifts towards the vacuum level approximately 0.6 eV. The band gap shift is attributed to the presence of the lattice defects which further confirms the interstitial nitrogen doping in TiO₂. Nitrogen doping in TiO₂ by mimicking natural pearl process in a living mussel is very innovative but still in its early stage, this approach extends the chemical methodologies for fabrication functional N-doped oxide materials.

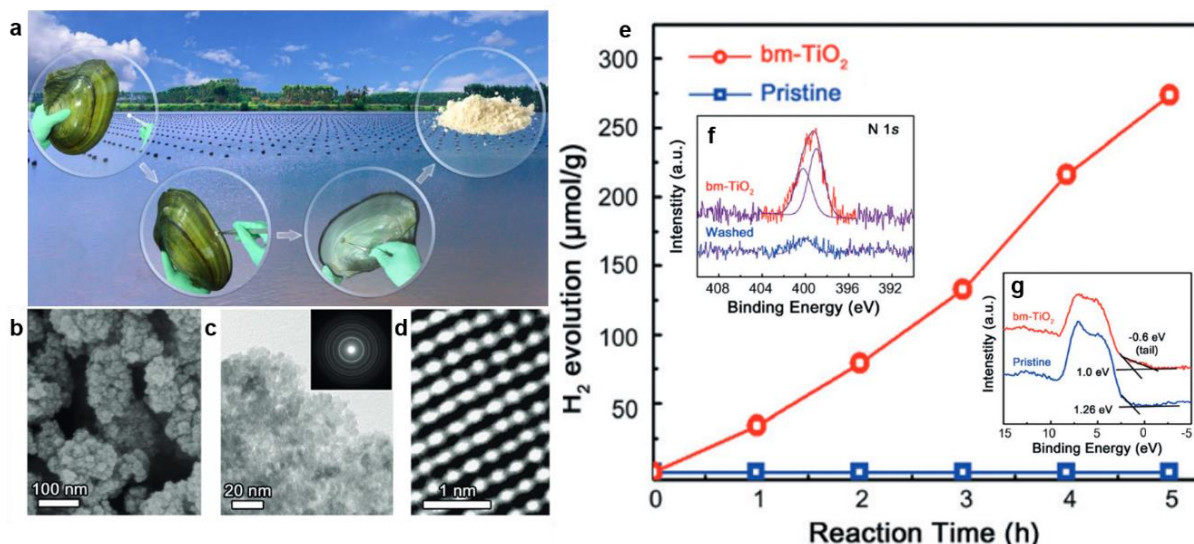


Fig. 1.13. (a) The flowchart of TiO₂ mineralization processes in living mussels; (b) SEM image of bm-TiO₂ nanoparticles mineralized in mussel for 90 days; (c) TEM image of bm-

Introduction

TiO₂ nanoparticles and the corresponding diffraction rings of SAED pattern(inset); (d) A HR-TEM image of bm-TiO₂ revealing the fringes of (101) planes; (e) H₂ evolved under visible light after photocatalytic water reduction using TiO₂ samples; (f) N 1s XPS spectra of bm-TiO₂ nanocrystals; (g) Valence-band XPS spectra of TiO₂ samples. Reproduced with the permission from ref [94]. Copyright 2016 German Chemical society.

Another creative idea is to incorporate dopants into TiO₂ with distinctively dominant facets. Most anatase TiO₂ crystals are dominated by the thermodynamically stable {101} facets while the TiO₂ with dominant {001} facets are more reactive.^[371, 372] The nitrogen doped TiO₂ with dominant {001} facet was first fabricated by the hydrothermal treatment of titanium nitride (TiN) in hydrofluoric acid (HF).^[90] The H₂ evolution rates of N-TiO₂ are 1483 and 81 $\mu\text{mol}\cdot\text{h}^{-1}\cdot\text{m}^{-2}$ under 220-770 nm and 420-770 nm, respectively. While the H₂ evolution rates of pure TiO₂ ({001} dominant facet) and N-TiO₂ (without preferential {001} facets) are 1333 and 38 $\mu\text{mol}\cdot\text{h}^{-1}\cdot\text{m}^{-2}$ under 220-770 nm. However, no obvious H₂ production is detected in the presence of TiO₂ ({001} dominant facet) and N-TiO₂ (without preferential {001} facets) under visible light. It can be concluded that nitrogen doped anatase TiO₂ sheets with dominant {001} facets have much superior activity for H₂ production under visible light. This work can also be extended to other non-metal doped anatase TiO₂ sheets with dominant {001} facets.

The surface heterojunction composed of both {001} and {101} facets has also been considered to enhance the photoefficiency of TiO₂. The N-doped TiO₂ nanobelts with a co-exposed (101) and (001) facets were hydrothermally synthesized. As shown in Fig. 1.14, compared to the pure TiO₂, the N-doped TiO₂ samples exhibit stronger absorption indicating enhanced the visible-light activity due to the nitrogen doping. The H₂ evolution rate increases as the nitrogen doping content under visible light ($400 \text{ nm} < \lambda < 800 \text{ nm}$). The H₂ production rate of TiO₂ nanobelts with 2.08 at% N is $670 \mu\text{mol h}^{-1} \text{ g}^{-1}$ which is much higher than the values obtained with other N-doped TiO₂ nanobelts with a single facet exposed.^[347, 373] The surface heterojunction in TiO₂ not only promotes the water molecule disintegration but also improves the ability of the charge separation. In addition, the result of cycling tests on the 2.08-N-TiO₂ (Fig. 1.14c) shows no obvious decrease for H₂ production displaying a satisfactory stability. The TiO₂ nanobelts show higher photocurrent response with an increasing N content. Due to the existence of surface heterojunction, the electrons in (001) are attracted immediately to (101) and transferred to the active reaction sites to combine with H⁺ to release H₂. Conversely, the holes are attracted immediately from (101) to (001) which has a better capability of promoting these holes to react with OH⁻ to form hydroxyl radicals (OH•). The N-doped TiO₂ nanobelts with co-exposed two

dominant surfaces of (101) and (001) facets exhibit significantly enhanced photocatalytic activities.

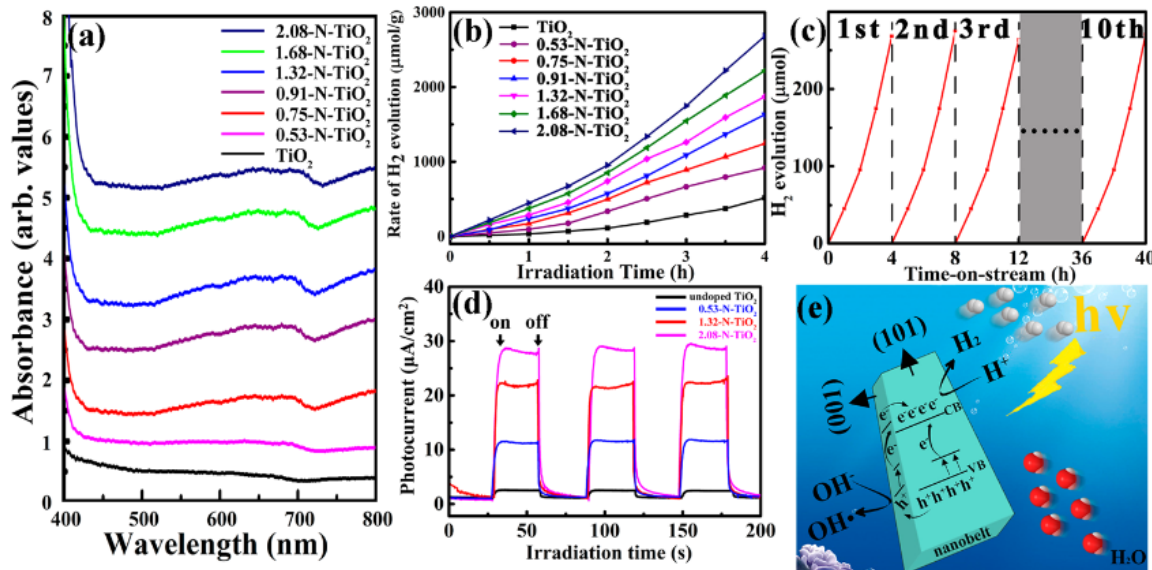


Fig. 1.14. (a) UV-vis diffuse reflectance (DR) spectra of the samples; (b) H₂ production rates of the products; (c) Cycling stability results of photocatalytic H₂ production over 2.08-N-TiO₂ sample; (d) Photocurrent responses under illumination ($\lambda > 400$ nm) of undoped TiO₂ nanobelts, 0.53-N-TiO₂ nanobelts, 1.32-N-TiO₂ nanobelts, and 2.08-N-TiO₂ nanobelts; (e) Diagram of the charge shift process in N-doped TiO₂ nanobelt. Reprinted with the permission from ref [352]. Copyright 2016 American Chemical Society.

1.3.1.4b Boron doping

Boron with a small ionic radius can be incorporated at oxygen sites more easily which gives rise to mid electronic gap states. On the other hand, the interstitial boron present in the form of B^{o+} ($\sigma \leq 3$) behaves as the electron donor. The enhanced charge transfer could be attributed to the synergistic action of both doping types. The active Ti³⁺ species can also be induced by the boron doping resulting in self-doped TiO₂ (TiO_{2-x}).

A series of B-TiO_{2-x} with photocatalysts was prepared via sol-gel synthesis method using boric acid as boron source.^[201] As shown in Fig. 1.15, with increased dopant concentration, the intensity of peak at 191.8 eV ascribed to interstitial B becomes stronger. The two major peaks of Ti 2p_{3/2} and Ti 2p_{1/2} are shifted to the lower binding energy, indicating the formation of Ti³⁺ species.^[374, 375] The ESR signal of Ti³⁺ at a g-value of 1.98729 gradually increases with increasing doping amount of B from 2% to 10%. The concentration of Ti³⁺ species is estimated to be ca. 30 μmol/g in the 10% B-TiO_{2-x} sample. The H₂ evolution rate generally is observed

Introduction

to increase with increasing the content of dopant B. Particularly, the B-TiO_{2-x} with 10 wt% B has the highest rate of 11.8 mmol h⁻¹g⁻¹ which is 3.5 times of that of a commercial P25. In addition, B-TiO_{2-x} exhibited a high stability since no obvious drop in H₂ production rate was observed after 42 h photocatalytic reaction including 21 cycling tests. It has been concluded that the interstitial B doping not only leads to the formation of abundant and stable Ti³⁺ species but also favours the lattice disorder of B-TiO_{2-x} photocatalysts. Therefore, two groups of mid-gap states are formed, which result in a significant reduction of the band gap. The band gap engineering can promote the photogenerated electron mobility and provide the B-O-Ti³⁺ structure as trapping sites to prevent electron-pairs from recombination, which ultimately enhances the solar-light photocatalytic activity of B-TiO_{2-x} toward H₂ production water splitting.

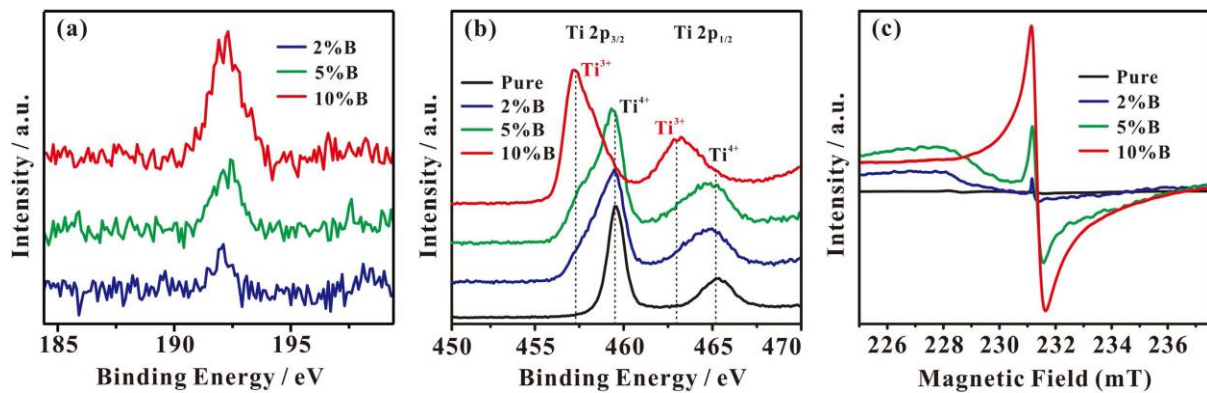


Fig. 1.15. (a) B 1s and (b) Ti 2p XPS spectra of B-TiO_{2-x} samples with different B doping;(c) ESR spectra of B-TiO_{2-x} samples with different B doping, measured at 295K; Reprinted with the permission from ref [162]. Copyright 2016 Nature.

Furthermore, the location of heteroatoms in TiO₂ is supposed to influence the photocatalytic reaction preferences towards electron reduction or hole oxidation. By controlling the spatial distribution of boron from the core to the shell within a microsphere, the effect of the heteroatoms on modulating H₂ and oxygen evolution was investigated. The Fig. 1.16a illustrates the boron distribution-dependent electronic structures, the core part has the intrinsic band gap which is independent on the chemical states of boron. While the VBM of the shell containing interstitial boron is inclined to shift downwards due to the band bending effect originating from the existence of B^{σ+} and Ti³⁺. Thus, the holes from the lowered VB of TiO₂ in the shell have a stronger oxidative power than those from the VB of TiO₂ in the core. The TiO₂ with boron in the core shows a 4-fold improvement in H₂ evolution compared to the TiO₂ with

boron in the shell. Conversely, the boron-containing shell leads to a 4.5-fold improvement in oxygen evolution compared to the shell with a boron gradient. The photocatalytic reaction preference is thus switched to the oxygen producing reactions by doping boron in the shell. The microsphere of TiO_2 with boron in the shell shows the typical electron conduction behavior of TiO_2 . Whereas with concentrated boron in the core, a cooperative conduction of electron and $\text{B}^{\sigma+}$ ions is observed but only at the first scan indicating the high diffusion capability of boron derived by the electric field. This work clearly advances the designing and constructing of efficient photocatalysts by spatial heteroatom engineering.

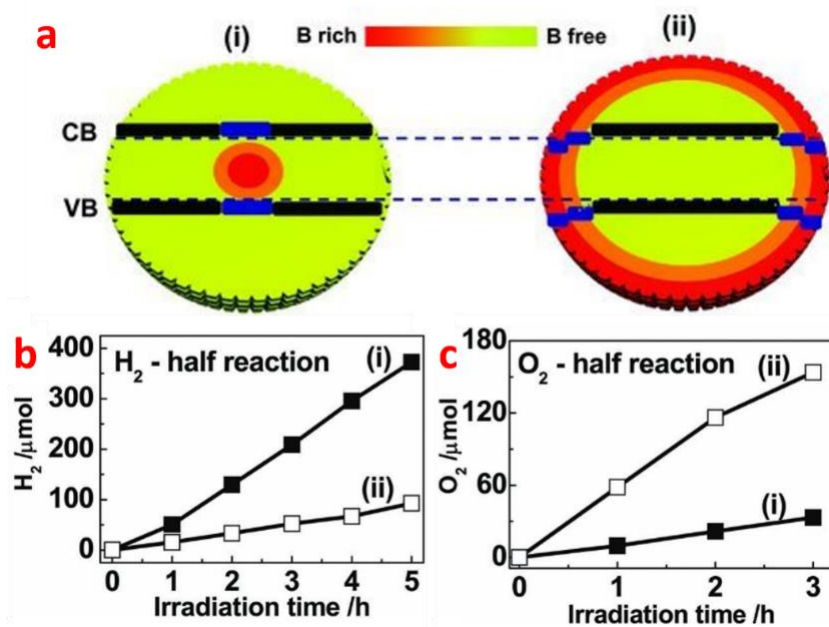


Fig. 1.16. a) The dependence of spatial electronic structures on the distribution of boron within the TiO_2 microspheres, the bands in the boron containing areas are highlighted in blue; i) TiO_2 microspheres with a boron-free shell and ii) TiO_2 microspheres with a boron-containing shell; b) Photocatalytic H_2 evolution from 1wt% Pt loaded TiO_2 microsphere photocatalysts in the presence of methanol as an electron donor; c) Photocatalytic oxygen evolution from the TiO_2 microsphere photocatalysts in the presence of AgNO_3 as a hole donor. Reproduced with the permission from ref [237]. Copyright 2012 German Chemical society.

Since both nitrogen and boron dopants can promote the photocatalytic activity, the N and B co-doped TiO_2 has synergistic effect in which the N atoms improve the absorption efficiency of visible light and the B atoms inhibit the TiO_2 crystallite growth, boosting the charge separation of photogenerated electron-hole pairs. [376-378] The N-B co-doped TiO_2 has been further

Introduction

demonstrated to contain extrinsic defects of $(NOB)^{\cdot}$ species in addition to the $(NiO)^{\cdot}$ species which commonly exist in the N-doped TiO_2 . The $(NOB)^{\cdot}$ species are supposed to be based on the bonding of both interstitial N and B atoms to the same lattice oxygen ion. The $(NOB)^{\cdot}$ can easily trap one electron leading to the $(NOB)^{\cdot\cdot}$ diamagnetic center which lies at approximately 0.4 eV above the VB of TiO_2 contributing to the visible light activity.^[379] Liu et al. reported a red anatase TiO_2 with B and N co-doping for full spectrum solar energy conversion. The pre-doped interstitial boron weakens the surrounding Ti-O bonds and thus improve the solubility of nitrogen in TiO_2 resulting in significantly narrowed band gap of TiO_2 down to 1.94 eV. This red TiO_2 based photoanode shows a good PEC activity for water splitting under visible light.^[380] The sol-gel method synthesized B and N co-doped TiO_2 with Pd as the cocatalyst shows a high H_2 production rate of $500 \mu\text{mol h}^{-1}\text{g}^{-1}$.^[358]

1.3.1.4c Sulphur doping

The sulphur doped TiO_2 has also been studied for visible-light photocatalysis. Because S has a similar electron structure with O but with a larger ionic radius, introducing of sulfur into TiO_2 lattice could significantly modify the electronic structures of TiO_2 .^[240, 254, 381, 382] The sulphur has more than one oxidation states such as S^{2+} , S^{4+} or S^{6+} in TiO_2 playing a multi-type doping effect on photocatalytic reactions. The in-situ S-doped TiO_2 nanopillars were synthesized by a facile one step thermal treatment of titanyl sulfate hydrated heating up to 500, 600, 700, and 800°C denoted as T500, T600, T700 and T800, respectively.^[53] The pure anatase TiO_2 transforms into rutile at 600 °C while the S-doped TiO_2 maintains at anatase phase at 700 °C resulting in the higher crystallinity and less surface defects of anatase TiO_2 . The morphology of TiO_2 nanopillars with diameter of around 3μm can be observed obviously by the SEM and TEM presented in Fig. 1.17a, b. With calcination temperatures increasing, the doping content of S element decreases gradually as revealed by the XPS spectra (Fig. 1.17c). The T700 sample calcined at phase transition temperature shows the highest photocatalytic H_2 evolution rate of $163.9 \mu\text{mol h}^{-1}\text{g}^{-1}$. The introduction of S in TiO_2 highly promotes the photocatalytic performance, which is attributed to the improvement in the anatase crystallinity and photon utilization.

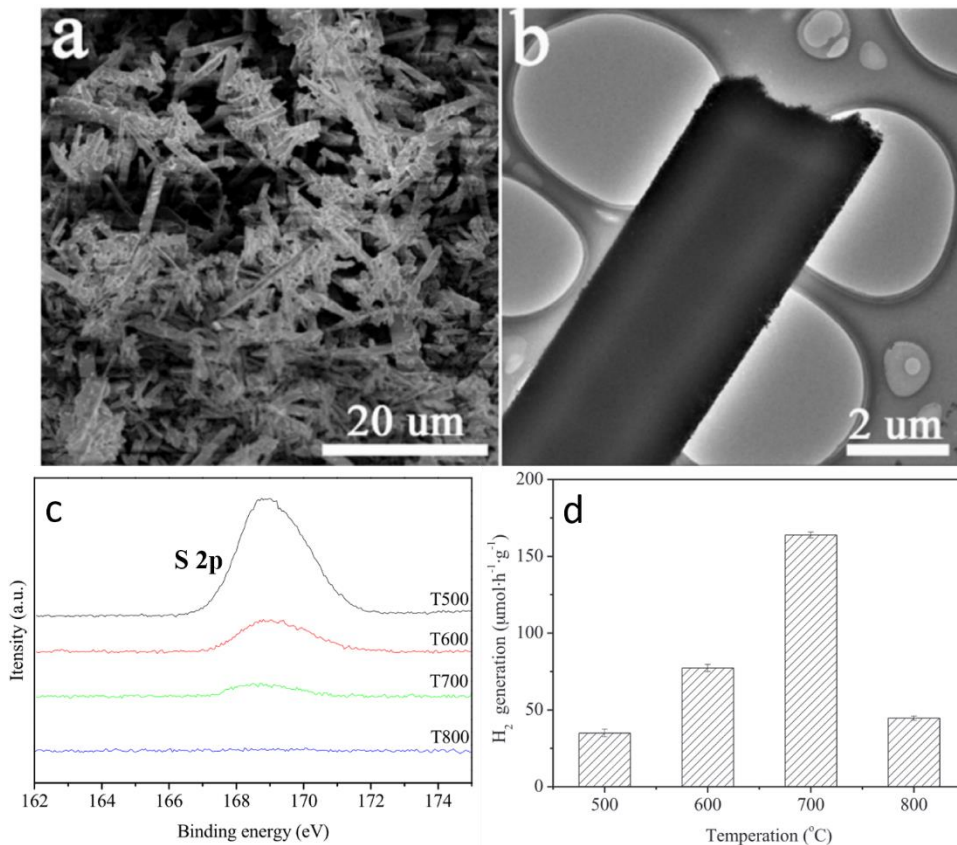


Fig. 1.17. SEM (a), TEM (b) images of S-doped TiO₂ prepared at 700 °C calcinations; (c) The XPS spectra of S 2p for samples prepared at 500, 600, 700 and 800 °C calcinations, respectively; (d)Visible-light photocatalytic H₂ evolution of samples. Reproduced with the permission from ref [53]. Copyright 2015 Elsevier.

Modification of rutile TiO₂ for water splitting is common due to its chemical inertness which is, however, a desired merit to achieve photostability. The unique S-doped rutile TiO₂ with core-shell structure was obtained by reduction TiO₂ with molten Al and the following sulfidation in the H₂S gas as shown in Fig. 1.18. As H₂S reduces the phase transition energy from anatase to rutile, the anatase TiO₂ can completely transform into the rutile allotrope at a relatively low temperature like 600 °C. Meanwhile, these S²⁻ anions occupy the oxygen vacancies and introduce new electronic transitions from the S 3p orbitals to the Ti 3d orbitals during the sulfuration process. The band gap can be further narrowed with the by-product of Ti³⁺. The S-doped rutile TiO₂ (R'-TiO₂-S) shows nearly 30-folds improvement over pristine rutile TiO₂ in photocatalytic water-splitting activity. And the PEC measurement of R'-TiO₂-S photoelectrode shows a high STH efficiency of 1.67% (Fig. 1.18c). The R'-TiO₂-S also impressively enhances the IPCE value in both UV region (300-380 nm) and visible region (400-580 nm). The upward shift of Fermi level in the shell of S-doped TiO₂ is supposed to bend

Introduction

the band edge of TiO_2 and to facilitate the charge separation at the interface of S-doped shell part and the electrolyte. In conclusion, the S and Ti^{3+} doping level extend the light absorption to the visible and even to near-infrared region, which result in the significantly improved photocatalytic/PEC activity.

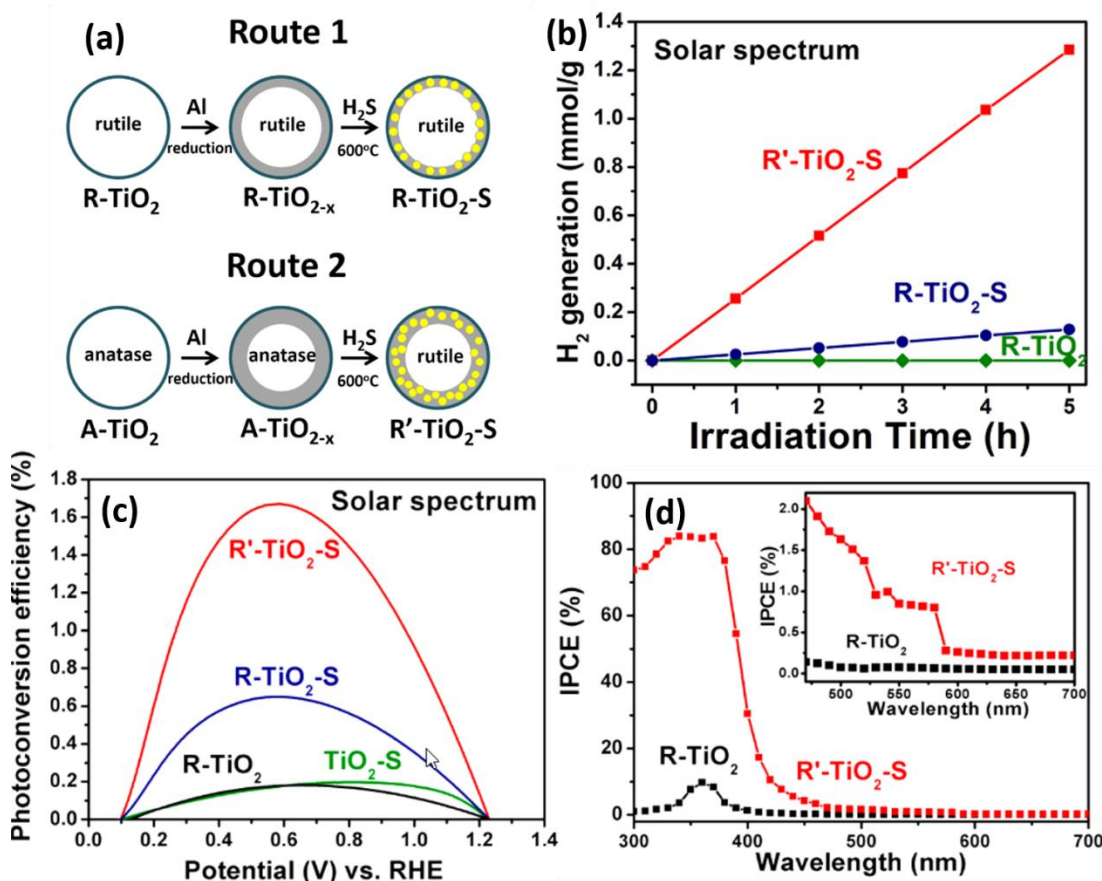


Fig. 1.18. (a) Two schematic synthetic routes of rutile TiO_2 with sulfided surface; (b) Photocatalytic water splitting for H_2 generation in the presence of different photocatalysts; (c) photoconversion efficiency as a function of applied potential; (d) IPCE spectra in the region of 300-700 nm at 0.65 Vs RHE; Inset: IPCE spectra in the region of 420-700 nm. Reproduced with the permission from ref [255]. Copyright 2013 American Chemical Society.

The formation of defect states in non-metal doped TiO_2 is inevitable during the synthesizing process. Defects like oxygen vacancies and Ti interstitial can act as active sites to boost photocatalytic reaction as mentioned above. However, these dopant-induced defects also have a negative effect on photocatalytic activity due to the charge carrier trapping and recombination sites. The balance between the two aspects is crucial for optimization of the photoactivity. [61, 383-385] The laminated defect controlled S-doped TiO_2 on carbon substrate ($\text{LDC-S-TiO}_2/\text{C}$) was

Introduction

synthesized involving an S impregnation of Ti_3C_2 MXenes followed by two-step oxidation processes. After the second time oxidation, the excess carbon is reduced while the defects concentration is increased as shown in Fig. 1.19a. The undoped laminated TiO_2 ($\text{L-TiO}_2/\text{C}$) is taken as a reference sample. The charge-transfer efficiency under visible light can be estimated by the measurement of transient photocurrent density (TPC) under visible light as shown in Fig. 1.19b. Apparently, $\text{LDC-S-TiO}_2/\text{C}$ with further oxidation achieves the highest photoinduced current density, about two times as that of $\text{L-S-TiO}_2/\text{C}$ (0.135 mA cm^{-2} Vs 0.062 mA cm^{-2}). The sulfur doping might be responsible for the reduced Gibbs free energy ΔG of water splitting, accelerating the carrier-transfer step and H_2 release. The $\text{LDC-S-TiO}_2/\text{C}$ shows 17-fold and 48-fold improvements on H_2 generation rates under full-spectrum light and visible light comparing to undoped TiO_2 . In addition, the porous carbon substrate can work as the co-catalyst and provide more active sites. This novel strategy shed a new insight for designing effective S-doped TiO_2 for solar energy conversion.

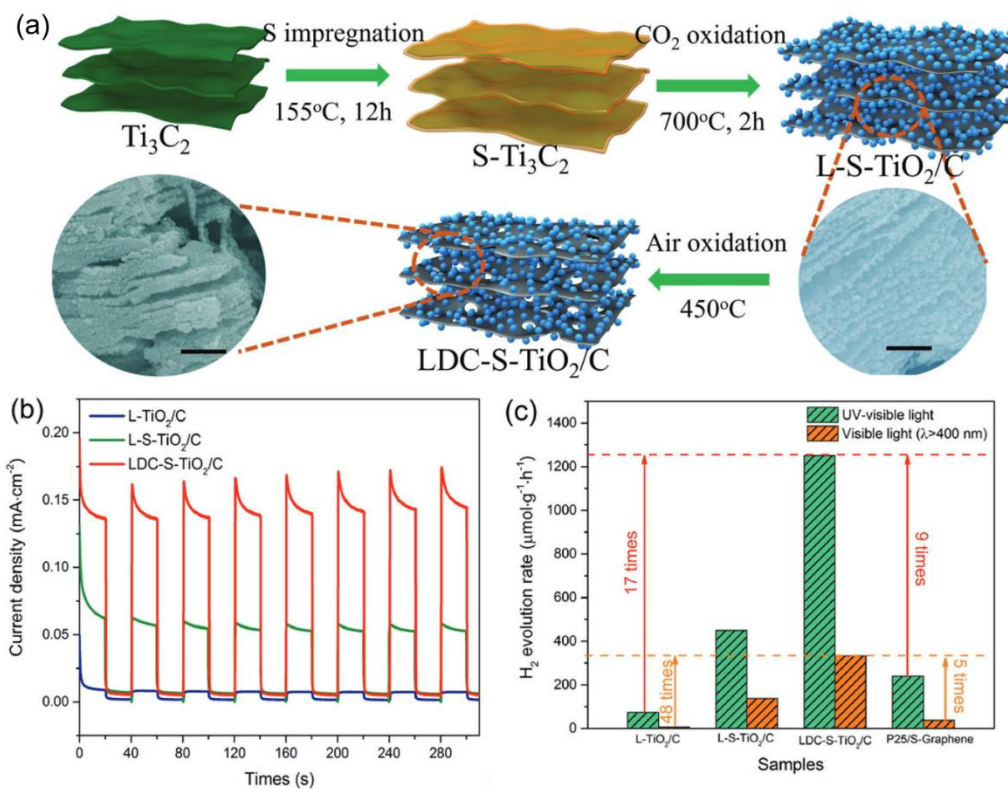


Fig. 1.19. (a) The schematic diagram of synthesis of $\text{LDC-S-TiO}_2/\text{C}$. All scale bars are 500 nm; (b) Transient photocurrent density (TPC) response of $\text{L-TiO}_2/\text{C}$, $\text{L-S-TiO}_2/\text{C}$, and $\text{LDC-S-TiO}_2/\text{C}$; (c) Average photocatalytic H_2 evolution rates over different samples; Reproduced with the permission from ref [360]. Copyright 2018 German Chemical society.

1.3.1.4d Phosphorus doping

In the case of phosphorus doping, two kinds of possible states including cationic (P^{5+}) and anionic (P^{3-}) exist in TiO_2 . The P^{5+} state originates from the substitution of the Ti^{4+} site accompanied with the release of an electron and the increased electrical conductivity. Since the ionic radius of P^{5+} is smaller than that of Ti^{4+} , the P incorporation into TiO_2 lattice with a Ti-O-P bond is more feasible. The hybridization of Ti 2p and P 2p orbits can lead to a narrowing of the electronic band gap of TiO_2 by forming new donor states below the CB of TiO_2 . On the contrary, the substitution occurring on the O^{2-} site conducts to the formation of P^{3-} state and the simultaneous neutralization of an electron in the system. The presence of P^{3-} state decreases the charge carrier density and may promote the electron-hole recombination. Besides, the commonly applied impurity sources contain phosphorous with positive valence such as phosphoric acid or phosphate. It is difficult to restore P species from oxidation states to P^{3-} even under the reducing atmosphere. Thus the enhanced photocatalytic activity is mostly driven by the dominant P^{5+} in TiO_2 .^[260, 386, 387] The P cation-doped TiO_2 for PEC water splitting was first reported by Li et al. The hierarchical TiO_2 nanotube photonic crystals (TiO_2 NTPC) were prepared by two-step electrochemical anodization. The P was then loaded into TiO_2 NTPC (P- TiO_2 NTPC) by CVD process using NaH_2PO_2 as the phosphorus source. Fig. 1.20a shows the hierarchically periodical nanoring structure of P- TiO_2 NTPC with an average diameter of 150 nm. A computer-simulated finite-difference time-domain (FDTD) procedure was conducted (Fig. 1.20a right part). The top layer of photonic nanoring shows strong electric field intensity, indicating the light harvesting in these nanorings. The optical absorption was significantly enhanced in the region of 400-500 nm. The red shift of the band gap to 2.90 eV can be attributed to the formation of new donor states below the CB of TiO_2 . The PEC performance of P- TiO_2 NTPC is superior and the photocurrent density value for P- TiO_2 NTPC presents a 140% increase compared to that of undoped TiO_2 under solar light. The photoconversion efficiency is improved by the P doping in TiO_2 under both UV and visible light. Apparently, the combination of P cation doping with the unique photonic nanostructures of TiO_2 NTPCs effectively heighten the PEC property under solar light.

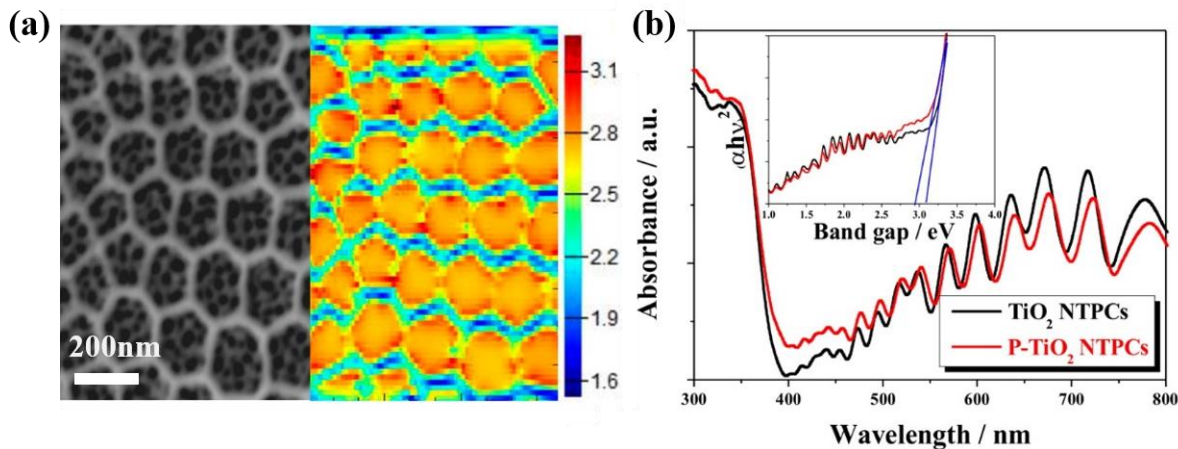


Fig. 1.20. (a) High-resolution SEM image of top photonic porous layer of P-TiO₂ NTPC and corresponding FDTD simulation of light intensity enhancement on top surface of P-TiO₂ NTPC; (b) Diffuse reflectance UV-vis absorption spectra and the band gap measurement from Tauc plot analysis (inset); Reproduced with the permission from ref [130]. Copyright 2016 American Chemical Society.

The dual-doping of P⁵⁺ and P³⁻ in TiO₂ has also been reported by employing PH₃ treatment at a low temperature (300 °C) for improving the PEC performance of TiO₂ nanorods. Consequently, three doping species such as Ti³⁺, P⁵⁺, and P³⁻ are observed. The incorporation with these ions in TiO₂ leads to the enhanced optical absorption with the colour change from white to yellow as presented in Fig. 1.21a. On the other hand, the PH₃ treatment increases the density of various surface states, especially like the P³⁻ states which facilitate the charge recombination. However, compensated with the positive effect of P⁵⁺ and Ti³⁺, PH₃-treated TiO₂ still has large carrier density resulting in faster transport and longer lifetimes of photogenerated electrons. The photocurrent of photoelectrode based on PH₃ treated TiO₂ is 5 times higher than that of pristine one (1.8 mA/cm² vs 0.35 mA/cm²) under solar light as shown in Fig. 1.21b. This facile PH₃ annealing strategy for P doping is effective for improving the photoactivity of TiO₂ and allows the further optimization on other semiconductor materials.

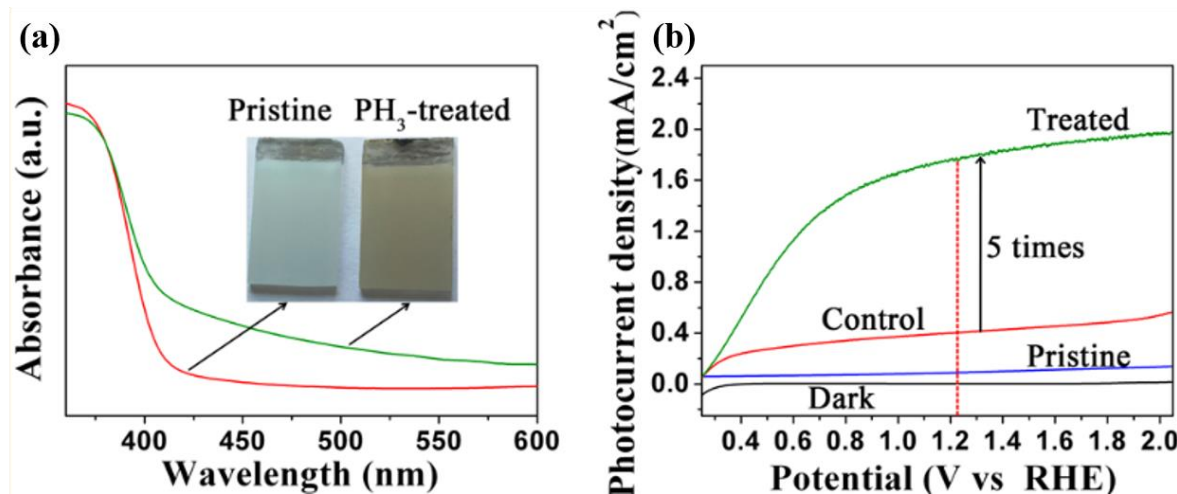


Fig. 1.21. (a) Absorption spectra of rutile TiO_2 nanorod arrays before and after PH_3 treatment; (b) Photocurrent response of rutile TiO_2 nanorod arrays. Reproduced with the permission from ref [388]. Copyright 2016 American Chemical Society.

1.3.1.4e Halogen doping

In recent years, the doping of halogen (F, Cl, Br, I) has triggered a new area of research on TiO_2 photocatalyst. The halogen doped TiO_2 samples exhibit an enhanced photocatalytic activity under both UV and visible light. The ionic radius of halogens and oxygen increases in the order $\text{F} < \text{O} < \text{Cl} < \text{Br} < \text{I}$ (i. e., 1.19, 1.4, 1.81, 1.96, and 2.20 Å, respectively, at a six-coordinate site). [389] In terms of ionic size, F atoms are in favour of substitution at O sites, which promote the formation of oxygen vacancies like F and F^- centers and lower the CB edge of TiO_2 . While I atoms prefer to be inserted at Ti sites existing as oxidation states like $\text{I}^{5+}/\text{I}^{7+}$. [58, 140, 246, 390] These halogen atoms highly improve the photogenerated electron mobility and inhibit the rapid recombination of electron-hole pairs. Both F and I doped TiO_2 electrodes show enhanced photoelectric conversion efficiency for dye sensitized solar cells under simulated sunlight. [391-395] Specially, it is well known that all the halogens form acids when bonded to H_2 . The surface acidification by halogens doping increases the adsorption of reactant polar molecules that boosts photocatalytic reactions on the catalyst surface. [146, 396] Zhang et al. [362] prepared the fluorine-doped TiO_2 using anhydrous hydrogen fluoride (AHF) via vapor-phase fluorination at low temperature. Due to the presence of the electronegative fluorine atoms, F- TiO_2 has more active sites on the surface. Thus the adsorption of hydroxyl radicals on the TiO_2 is remarkably increased by the surface fluorination, which is closely relevant to photocatalytic properties. The F- TiO_2 reveals highly enhanced photocatalytic H_2 evolution rate of 113.1 $\mu\text{mol/h}$ which is two

times higher than that of pure TiO_2 ($51.2 \mu\text{mol}/\text{h}$) under UV light irradiation.^[363]

The F^- can be selectively doped on $\{001\}$ facets of anatase TiO_2 using HF etching of TiO_2 nanosheets with co-exposed $\{001\}$ and $\{101\}$ facets.^[59] Since the photoinduced holes are transferred to $\{001\}$ facets, these Ti^{3+} states and oxygen vacancies introduced in $\{001\}$ facets by F-doping dramatically accelerate the transportation of holes and reduce the recombination of electron/hole pairs as illustrated in Fig. 1.22. Consequently, the H_2 production rate of the as-prepared sample under the visible-light illumination is remarkably increased to $18.27 \text{ mmol g}^{-1} \text{ h}^{-1}$ and the quantum efficiency is up to 21.6% at $\lambda = 420 \text{ nm}$. Apparently, doping F on $\{001\}$ facets of TiO_2 is an effective strategy for improving the spatial separation of photogenerated carriers as well as the photocatalytic water splitting.

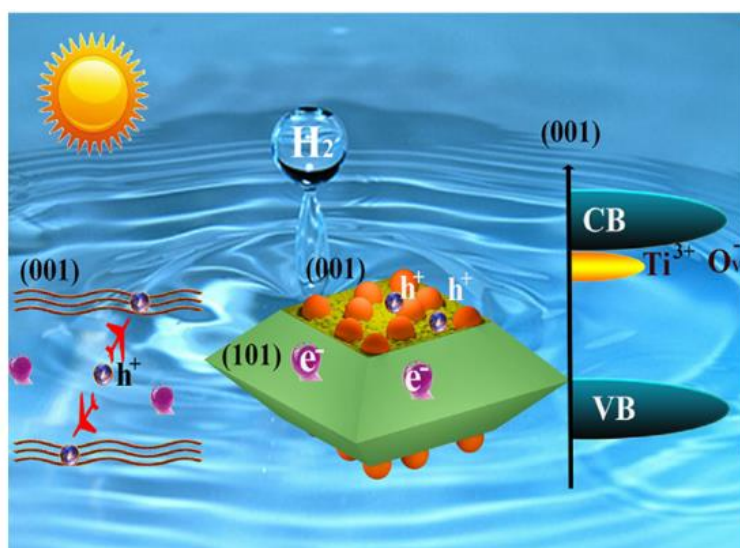


Fig. 1.22. Mechanism of F^- Selective Etching and Doping on $\text{TiO}_2 \{001\}$ for H_2 production.

Reprinted with the permission from ref [59]. Copyright 2018 American Chemical Society.

Other halogens (Cl, Br, I) modified TiO_2 photocatalysts were mostly used in the degradation of organics. The mono-doped TiO_2 with other halogens (Cl, Br, I) for enhanced photocatalytic/PEC water splitting has not been reported. Co-doping of Cl and Br in TiO_2 was conducted by hydrothermal synthesis.^[146] The TiO_2 is transformed into rutile phase as the doping amount of Br increases. The Cl^- and Br^- co-doped TiO_2 with mixed anatase/rutile phases shows the highest H_2 production rate but only under UV light. It is clear that N 2p impurity levels induced by N dopant in TiO_2 locate above the VB of TiO_2 , halogens co-doping with N can be an effective way for visible light-driven photocatalysts. The hierarchical honeycomb Br-, N-co-doped TiO_2 catalyst was firstly fabricated by one-step hydrothermal treatment of

massive TiO_2 with cetyltrimethylammonium bromide (CTAB) and melamine serving as Br and N sources. The N dopant tends to act as the acceptor, while the doped Br atoms incline to occupy Ti sites acting as the donor. The Br-N can form donor-acceptor pairs narrowing the electronic band gap of TiO_2 to 2.88 eV as shown in Fig. 1.23a. In photocatalytic reactions, as illustrated in Fig. 1.23b, the holes on the N acceptor levels could passivate the same amount of electrons on the Br donor levels. Therefore, the efficient charge separation is achieved and the lifetime of electron-hole pairs is prolonged. The Br-N co-doped TiO_2 exhibits much higher H_2 generation rate of $2247 \mu\text{mol h}^{-1}\text{g}^{-1}$ under visible light, comparing to single Br- or N-doped TiO_2 (0 or $63 \mu\text{mol h}^{-1}\text{g}^{-1}$). The strategy of co-doping with halogens and other non-metal like N shows its great potential for H_2 production.

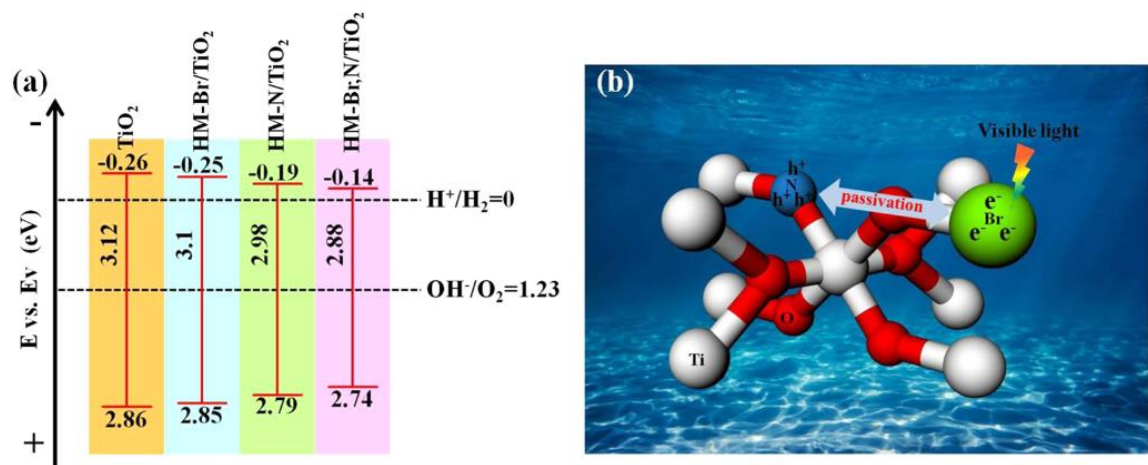


Fig. 1.23. Energy diagram showing the positions of valence and conduction bands of TiO_2 , HM-Br/TiO₂, HM-N/TiO₂, and HM-Br, N/TiO₂; (b) Schematic for the passivation effect of Br-N donor-acceptor pairs in HM-Br, N/TiO₂. Reprinted with the permission from ref [145].

Copyright 2018 American Chemical Society.

1.3.1.4f Carbon doping

Carbon, as a common non-metallic material, has a large electron-storage capacity, superior charge-transfer and good permeability into TiO_2 . Various theoretical and experimental works have focused on the study of the visible light absorption properties of carbon doped TiO_2 . [397, 398] Carbon doping widens the region of absorption light and sensitizes white TiO_2 by affecting the electronic environments for Ti cations and O anions. As dopant and sensitizer, carbon dramatically improves the photocatalytic activity of TiO_2 in the visible-light region. [103, 106, 107, 399-402] The C-modified TiO_2 samples were obtained from the pyrolysis of hydrothermally

Introduction

synthesized TiO₂-sucrose composites.^[65] The C-TiO₂ exhibited high photocatalytic activity for the H₂ evolution under simulated solar light irradiation. The H₂ production is as high as 1.25 mL h⁻¹ from 0.002 g of catalyst after 6 h of irradiation. The PL intensity of C doped TiO₂ is significantly faded compared to that of pure TiO₂, which implies the suppressed recombination of photogenerated electron-holes. The carbon modification may cause the formation of oxygen vacancies that trap electrons and facilitate efficient electron-hole separation. Due to the doping or surface modification effect of carbon in TiO₂, the PC / PEC H₂ production from water splitting is highly enhanced. For example, photoanode of carbon doped TiO₂ nanowire arrays exhibited a ~70% enhancement of photocurrent density comparing to that of photoanode based on the pristine TiO₂.^[403]

A new strategy for preparing highly carbon-doped TiO₂ (HC-TiO₂) at low temperature has been developed by employing Ti₃C₂ MXene as the precursor. As shown in Fig. 1.24, the multangular flower-like morphology composes of tightly aggregated nanorods with a diameter dimension of 35 ± 10 nm. The small size of these nanorods is beneficial to the carrier diffusion during the photocatalytic reaction. The HC-TiO₂ with a high carbon content (20 wt%) red-shifts the absorption edges of TiO₂. The impurity levels above the VBM promote the transfer rate of photogenerated electrons. Apparently, the HC-TiO₂ shows remarkably higher photocurrent which is 8 times as that of P25 (Fig. 1.24c). The HC-TiO₂ also exhibits higher H₂ evolution rate of 33.04 $\mu\text{mol h}^{-1}\text{g}^{-1}$ while the pure P25 only has a production rate of 3.41 $\mu\text{mol h}^{-1}\text{g}^{-1}$. This work enriched the synthesis method of C-doped TiO₂ from 2D MXene based materials.

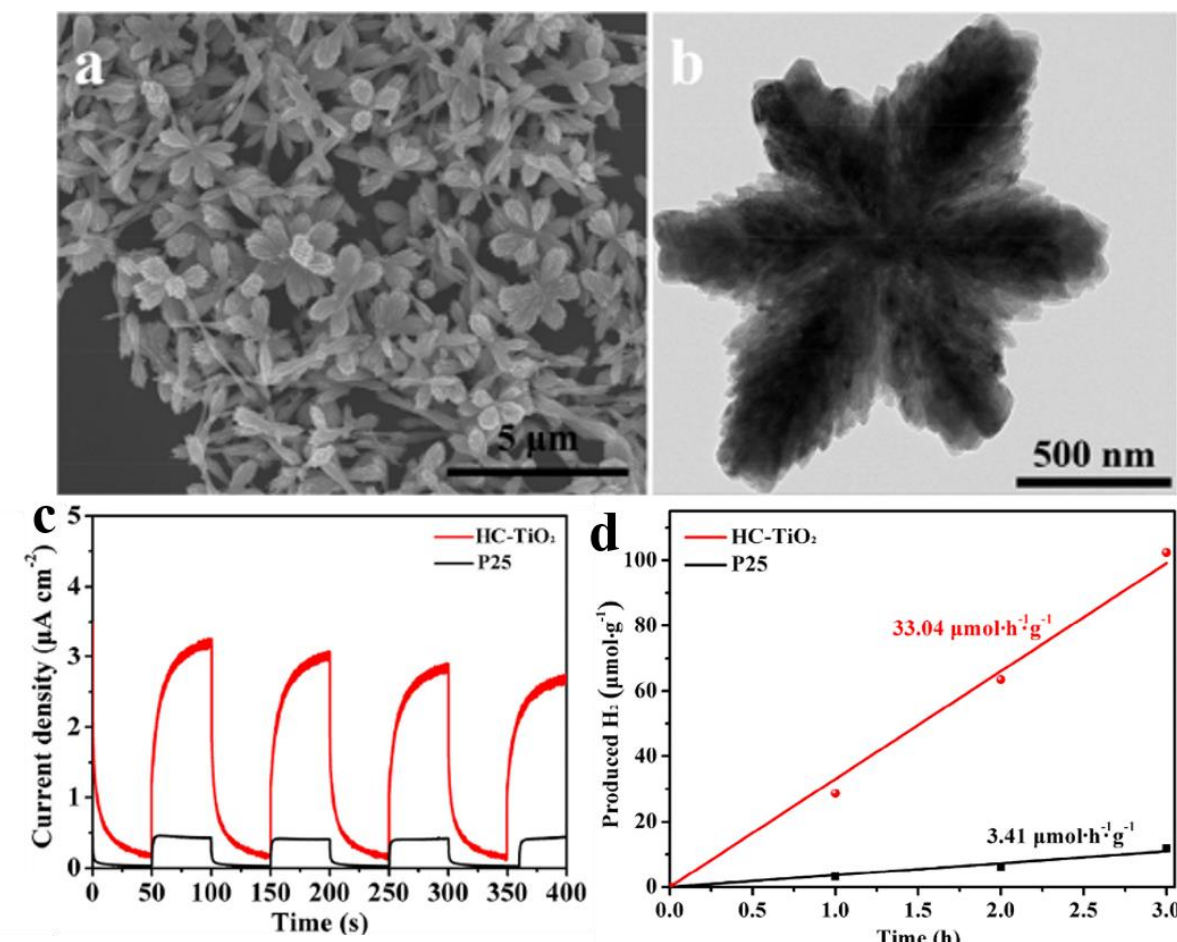


Fig. 1.24. (a) SEM and (b) TEM of as-prepared HC-TiO₂; (c) Transient photocurrent responses and (d) H₂ evolution plots under simulated sunlight irradiation of as-prepared HC-TiO₂ and P25. Reproduced with the permission from ref [355]. Copyright 2018 American Chemical Society.

Novel core-shell structure with large specific surface area and enhanced light absorption has also been reported to have intensively improved photocatalytic activity.^[404-406] The carbon doped TiO₂ with core-shell structure was also synthesized by oxidizing TiC in air at 350 °C for 30, 60, 90, 120, and 180 min, denoted as TC1-TC5 respectively, as shown in Fig. 1.25a. All the TiC@C-TiO₂ samples possess higher photocatalytic activity for water splitting than P25 under visible light irradiation as shown in Fig. 1.25a₁ and b₁. The photoelectron transmission and the followed catalytic reactions in the core-shell structured C-doped TiO₂ are affected by the annealing conditions. In general, heating treatments under various temperatures for different durations influence the specific surface area and the thickness of core and shell parts as well as the dopant concentration in TiC@C-TiO₂. The photostability of TC2 is further ensured by cycling photocatalytic tests under 6 h of visible illumination (Fig. 1.25c₁). Moreover, the

Introduction

TiC@C-TiO₂ core-shell samples show almost the same H₂ evolution with or without Pt cocatalyst presented in Fig. 1.25d₁. Therefore, the TiC not only provides the carbon dopant source, but also acts as a good support for TiO₂ photocatalyst. The carbon impurity effectively narrows the band gap of TiO₂ and enhances the light absorption. The photoelectron transfer is also fastened in the presence of the TiC phase and the recombination rate of charge carriers is thus inhibited. Due to the synergistic effect of the carbon dopant and the inner TiC, photocatalytic property of TiO₂ for water splitting is highly improved.

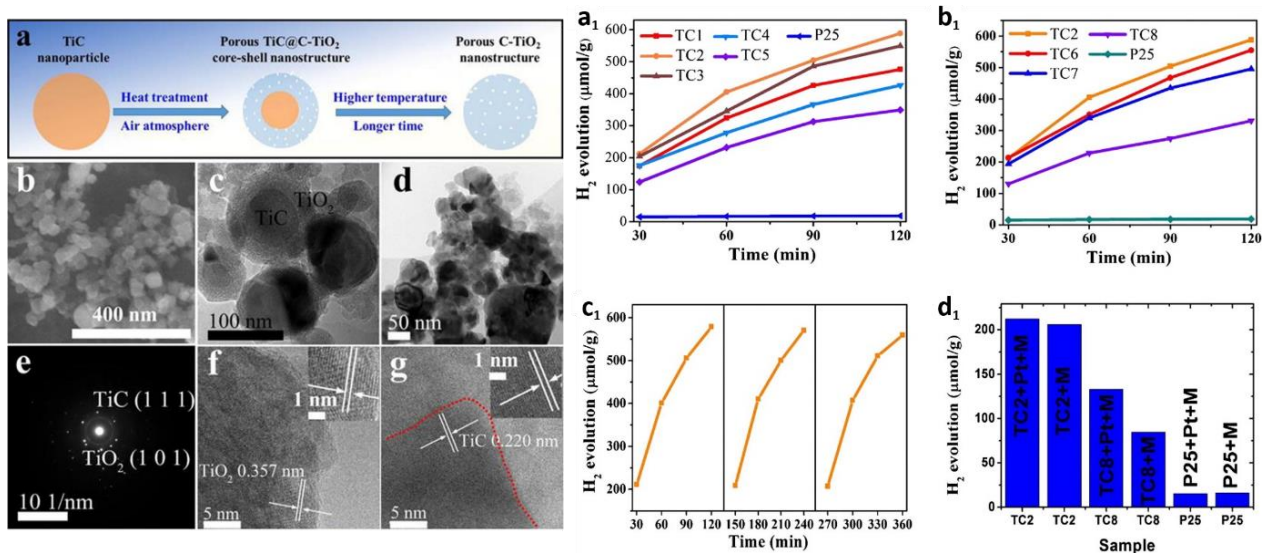


Fig. 1.25. (a) The prepared procedure of TiC@C-TiO₂ core-shell nanostructure and C-TiO₂ materials; (b) SEM image of TC2; TEM image of (c) TC2, TiC@C-TiO₂ core-shell nanostructure and (d) C-TiO₂ materials; (e) SAED pattern of prepared TC2, TiC@C-TiO₂ core-shell nanostructure material; HR-TEM images of (f) C-TiO₂ shell and (g) TiC core; (a₁) (b₁) Photocatalytic H₂ evolution of P25 and the as-synthesized samples under visible light irradiation; (c₁) Cycling test of TC2 for 6 h under visible light irradiation, and (d₁) photocatalytic H₂ production with or without Pt co-catalyst under 30 min visible light irradiation. Reproduced with the permission from ref [272]. Copyright 2017 Elsevier.

The Z-scheme photocatalytic system with heterojunction between two different semiconductors mimics the natural photosynthesis of green plants known as Z-scheme process is widely employed for PC / PEC water splitting. The heterojunction plays as an electron mediator facilitating charge transporting and separation.^[354] The heterojunctions of C-doped TiO₂ with other visible light sensitive photocatalysts were also investigated. Yun et al.^[354] deposited the Au@CdS core-shell structure on 0.04 at% C-doped TiO₂ (TiO_{1.96}C_{0.04}) with the

Introduction

help of UV light irradiation. This combination denoted as CdS/Au/TiO_{1.96}C_{0.04} gives rise to the reduction potential of protons and the ability of charge separation due to the Z-scheme mechanism. The novel system of CdS/Au/TiO_{1.96}C_{0.04} produces a H₂ amount approximately 4 times higher than CdS/Au/TiO₂ without the carbon doping under visible light irradiation. The heterostructure of C-doped TiO₂ with g-C₃N₄ was also reported with improved light absorption and lower charge recombination rate which are beneficial to photocatalytic reactions.^[356] The photocatalysts of C-TiO₂/g-C₃N₄ exhibit superior visible light activity with the highest H₂ generation rate of 1.15 mmol h⁻¹g⁻¹. The apparent quantum efficiency of C-TiO₂/g-C₃N₄ photocatalysts is significantly increased to 6.2% under 420 nm irradiation, compared to 2.6% of the pristine g-C₃N₄.

1.3.2 Carbon coating in TiO₂

Except doping, carbon can also be coated in TiO₂ resulting enhanced visible light absorption as well as photocatalytic activity of TiO₂.^[407, 408] The first effect of carbon coating is to suppress the phase transformation from anattas to rutile.^[164, 409, 410] For example, pure amorphous TiO₂ would undergo phase transformation from anatase to rutile started around 600 °C as shown in Fig. 1.26a. However, anatase phase still dominated in TiO₂ when calcination temperature increased up to 800 °C with carbon coating as shown in Fig. 1.26b and even to higher temperature (1100 °C) as shown in Fig. 1.26c. The suppression degree of the phase transformation depended on the amount of carbon coated.^[409] Due to the phase suppression, both the thermal stability and crystallinity of TiO₂ photocatalyst increase largely which is helpful for both the photocatalytic stability and activity of TiO₂.^[411, 412] The coated carbon can also enhance the light absorption properties of TiO₂ which are often determined by the UV-vis absorption spectra.^[67] As dye sensitizer, carbon highly increases the light absorption of TiO₂ especially under visible light.^[413, 414]

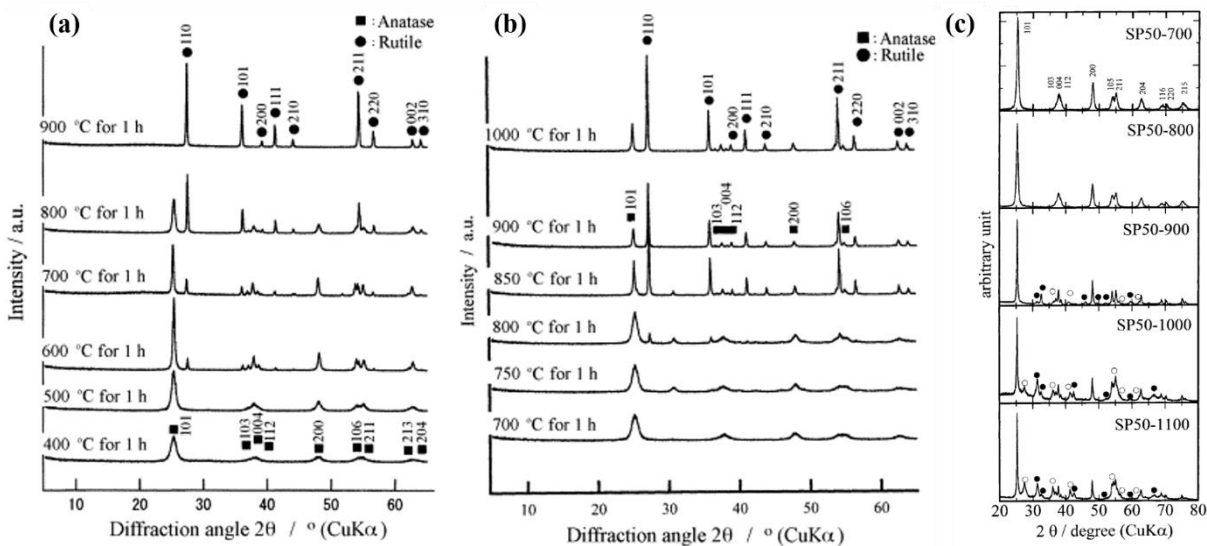


Fig. 1.26. Changes in X-ray diffraction pattern of (a) pure TiO_2 sample, (b) carbon coated TiO_2 , reprinted with permission from ref [409], copyright 2003 Elsevier; (c) another type of carbon coated TiO_2 (SP50-calcination temperature, black circle: anatase phase, white circle: rutile phase), reprinted with permission from ref [410], copyright 2002 Royal Society of Chemistry.

Furthermore, the coated carbon layer around TiO_2 can effectively promote the charge transfer and suppress the recombination of photogenerated electron-hole pairs as illustrated in Fig. 1.27a. Upon the irradiation, the photoexcited electrons transfer on the surface of carbon and facilitate the spatial separation of electrons and holes (Fig. 1.27b). The coated carbon in TiO_2 in the form of carbon layer (Fig. 1.27c) or carbon shell (Fig. 1.27d) can trap and accumulate electrons.^[164, 415] The intimate interface between carbon layer or shell and TiO_2 can work as a bridge for electrons transfer promoting photocatalytic reactions. Therefore, the carbon coated TiO_2 photocatalysts show enhanced photocatalytic activity for H_2 production.

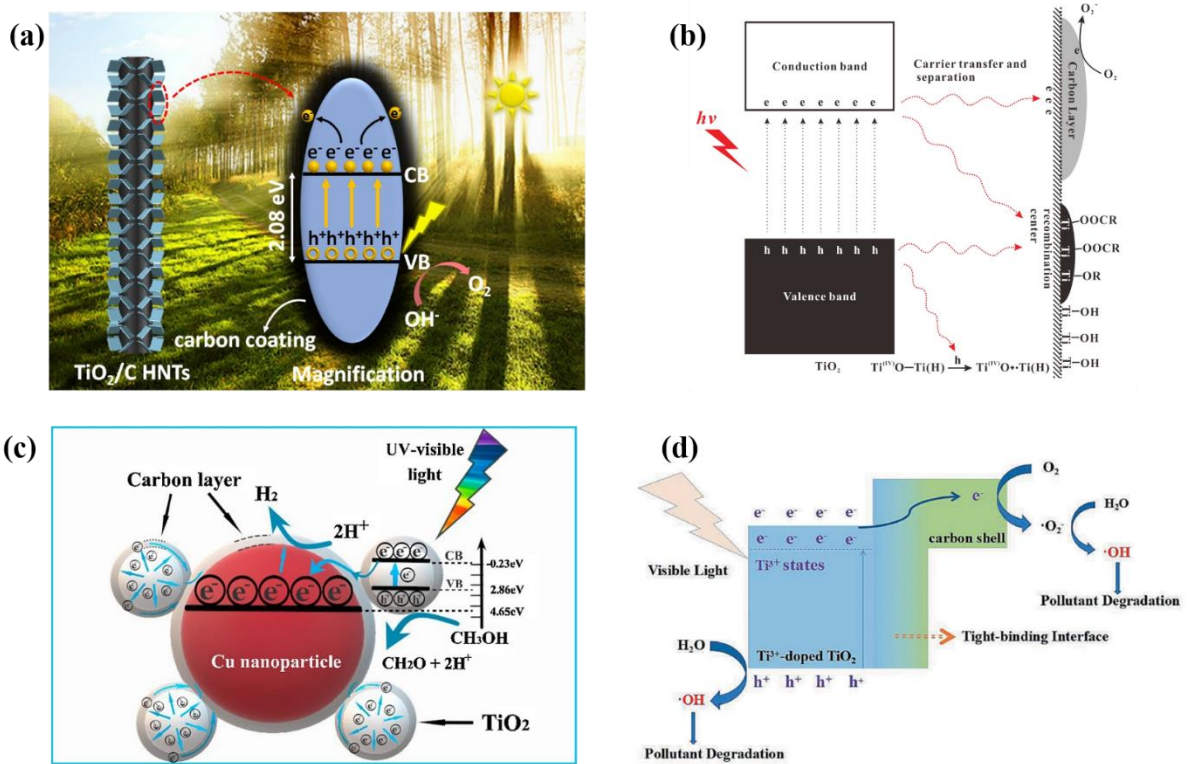


Fig. 1.27. Schematic of the photocatalytic mechanism of (a) carbon coated TiO₂ hierarchical nanotube (TiO₂/C HNTs) under full solar spectrum light, reprinted with permission from ref [67], copyright 2019 Elsevier; (b) carbon-coated TiO_{2-x} photocatalyst upon visible-light irradiation, reprinted with permission from ref [416], copyright 2018 American Chemical Society; (c) carbon coated Cu-TiO₂ nanocomposite system, reprinted with permission from ref [417], copyright 2019 Elsevier; (d) carbon coated TiO₂ with Ti³⁺ doping, reprinted with permission from ref [418], copyright 2019 Taylor and Francis.

As shown in Fig. 1.28a, the photocatalytic H₂ production of carbon coated TiO₂ nano-dendrites (C-TiO₂ NDs) achieves 2.9 and 4.1 times higher than TiO₂ nanobelts (TiO₂ NBs) and TiO₂ nanorods (TiO₂ NRs), respectively. The photocurrent density of another type of carbon doped TiO₂ (TTC) is much higher than pristine TiO₂ sample (Fig. 1.28b) under visible light which directly confirms enhanced the separation of electron/hole pairs and electron transfer process. The carbon coated TiO₂ nanotubes (TNTs) is also found to be more active than pristine TNTs for photocatalytic H₂ production as shown in Fig. 1.28c. Clearly, the carbon coating successfully enhances the activity of TiO₂ for PC / PEC water splitting. In fact, the carbon doping in TiO₂ might occur in carbon coating process even though the observation of carbon doping in carbon coated TiO₂ is very challenging. The dual effect of both carbon doping and coating is rarely reported. The synergy of carbon doping and coating in TiO₂ would be more interesting than pure carbon doping in TiO₂ and pure carbon coating in TiO₂.

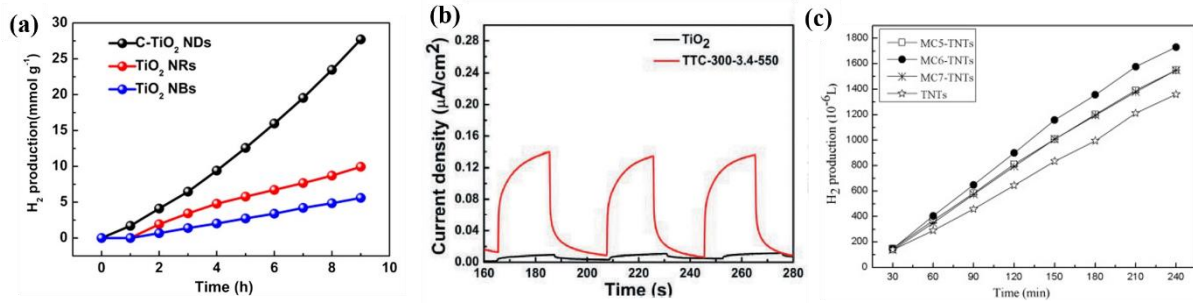


Fig. 1.28. (a) Photocatalytic H₂ production over carbon coated TiO₂ nano-dendrites (C-TiO₂ NDs), TiO₂ nanorods (TiO₂ NRs) and TiO₂ nanobelts (TiO₂ NBs) under UV light, reprinted with permission from ref [419], copyright 2020 Elsevier; (b) Transient photocurrent response of carbon coated TiO₂ under visible light (TTC-300-3.4-550), reprinted with permission from ref [418], copyright 2019 Taylor and Francis; (c) photocatalytic H₂ evolution by process of film catalysts over samples of carbon coated TiO₂ nanotubes (TNTs) calcined at 500 °C, 600 °C and 700 °C (named as MC5-TNTs, MC6-TNTs, MC7-TNTs, respectively) under full solar spectrum illumination, reprinted with permission from ref [420], copyright 2011 Elsevier.

1.3.3 The effect of electrolytic environments on PC/PEC water splitting

Until now, most efforts devoted to PEC cells field mainly focus on developing applicable photoelectrode materials to achieve high STH efficiency. On the contrary, little attention have been paid to study the PEC performance for water splitting under practical conditions. In electrochemical systems, all reactions occur through a medium, the electrolyte which contains dissolved mobile ions supporting current flow. The properties of the electrolyte such as temperature, pH, ionic strength and conductivity are critically important to charge transport across the interface between the electrodes and the electrolyte in any electrochemical experiment.

1.3.3.1 Effect of anion and cation species

Electrolyte anions are often reported to affect the performance of water oxidation (WO) by affecting the proton transfer processes or acting as electron donors. Electrolytes with efficient proton-accepting properties (e.g., NO₃⁻, ClO₄⁻) can dramatically boost photocurrent densities.^[421, 422] For example, CoBi/BiVO₄ electrodes exhibited two time higher photocurrent density in sodium borate than that in sodium sulfate.^[423] Electrolytes with different cations (Li⁺, Na⁺, Li⁺, Rb⁺, Cs⁺) were also found to influence on PEC water splitting. The mechanism remains unclear and might be related to interaction with H₂O/OH_{ad} and compensation for surface

defects. [424-426] The influence of cations on PEC water splitting also depends on different photoanode materials. WO_3 photoanode was reported to obtain highest WO efficiency with K^+ in acidic electrolytes [70] while Ni/NiO_x catalysts preferred Li^+ for WO reactions. [427] The photocurrents of TiO_2 electrodes in strong alkaline electrolytes and BiVO_4 electrodes in medium basic borate electrolytes decrease in sequence: $\text{Li}^+ > \text{K}^+ > \text{Na}^+$. [428] Combining with anion species, cations may affect the water splitting process differently. The effects of cations in the electrolyte on PEC water splitting especially on the half reaction of H_2 production are still under debate.

1.3.3.2 Effect of pH

The pH value of electrolytes affects the performance of PEC cells differently over different photoanodes. For example, Ahmed et al found that high pH values substantially improve the photocatalytic activity of photocatalyst made by nanohybrid carbon nanotubes@ TiO_2 nanoribbons (CNTs@TNRs). [71] In base medium, if OH^- ions are the main conductive species, increased pH value can increase electrical conductivity and the ion mobility of electrolyte. Zhang et al reported that with increasing pH, the H_2 production and quantum yield (QY) over $\text{Ru}/(\text{CuAg})_{0.15}\text{In}_{0.3}\text{Zn}_{1.4}\text{S}_2$ photocatalyst decreased significantly, and at pH = 2 the catalyst achieved a production rate 2.7 times higher than at pH = 4 under visible light irradiation. And lower PH can also affect the consuming of electron donors or SRs. [429]

1.3.3.3 Effect of temperature

The properties of photoanode materials are very sensitive to the temperature of electrolytic environment. The band gap of a semiconductor reduces as the temperature increases, the number of absorbed protons increases largely, and the amount of photogenerated electron/holes pairs and the followed photocurrent density increase. The dependence of the bandgap with temperature (T) is given by the Varshni model as shown in Eq. (15)

$$E_g(T) = E_0 - \alpha T^2 / (\alpha + \beta) \quad (15)$$

Where E_0 is the bandgap of the given materials at 0 K, α is the limit of gap energy when $T \rightarrow \infty$, β is supposed to be related to the Debye temperature. [430, 431]

Meanwhile, as increasing temperature in a certain range, for example 25 °C-100 °C, if liquid electrolytes are employed, the conductivity of a semiconductor increases rapidly followed by the improvement of charge carriers' mobility and the diffusion length. The lifetime of photogenerated electron/hole pairs is also prolonged by the increased temperature. Moreover,

the onset potential is shifted to lower potentials as the temperature increases, reducing the external applied potential. The main processes of overall PEC water splitting including photon absorption, the exciton separation and carrier diffusion/transport can all be improved by the increased temperature of electrolytic environment. Thus, the photocurrent density, the H₂ production rate as well as the energy conversion efficiency of PEC water splitting were highly increased. [432, 433]

1.3.3.4 The role of sacrificial reagents (SRs)

Although the photocatalytic splitting of water to H₂ has been regarded as promising approach in solving the energy crisis and much researches have been performed, the photocatalytic H₂ production from pure water remains a low efficiency process. This primarily is due to the high recombination rates of photogenerated electrons and holes, together with the regeneration of H₂O from produced H₂ and O₂ on the photocatalysts surface, which is called “surface back-reaction (SBR)”. Both not only lead to the low quantum efficiency of photocatalysis, but also inevitably reduce the amount of produced H₂ as well as the photocatalytic activity.

In order to achieve higher H₂ production efficiencies and to improve the light-to-hydrogen conversion, SRs are usually required to act as electron donors, which effectively consume holes and prevent the recombination of photogenerated electrons and holes on the semiconductor surface, at the same time restrain the process of the SBR. In general, the electron donors (or acceptors) played by sacrificial reagents (SRs) irreversibly react with photo-generated holes (or electrons), as shown in Fig. 1.29a, which enhances the charges separation and transfer and thus hinders the H₂O formation from H₂ and O₂. [434-436] The redox potentials of SRs are between the valence band and the conduction band of semiconductor photocatalysts. SRs as electron donors can consume the holes and prevent the recombination of photogenerated electrons / hole pairs as shown in Fig. 1.29b.

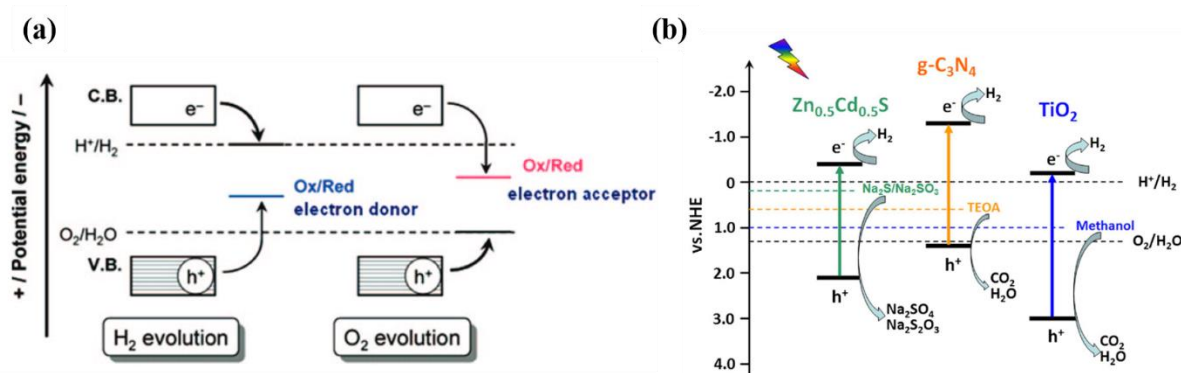


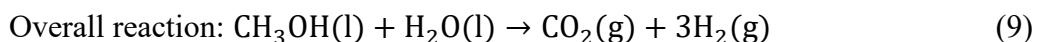
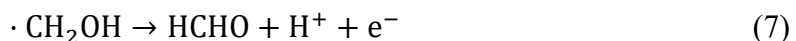
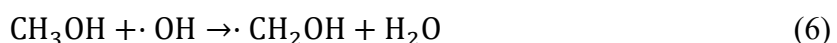
Fig. 1.29. (a) Photocatalytic reactions in the presence of sacrificial reagents. Reprinted with

Introduction

permission from ref [437]. Copyright 2010 American Chemical Society. (b) Scheme of the most suitable sacrificial reagents over different photocatalysts, reprinted with permission from ref [69], copyright 2017 Springer.

The addition of sacrificial molecules into water/photocatalysts suspension can remarkably improve the photoefficiency of water splitting. The photogenerated electrons or holes are scavenged by these molecules, which greatly depressed the charge carrier recombination. Common sacrificial electron donors include organic and inorganic ones. Organic compounds (hydrocarbon) such as alcohols^[438-443], organic acids^[444-447] and aldehydes^[448-451] are widely employed as electron donors to scavenge photo-generated holes for photocatalytic hydrogen generation. Lots of studies have observed that the effect on photocatalysts varies with different organic compounds SRs.^[444, 452] For example, by systemic investigated the photocatalytic H₂ production performance of TiO₂ in different SRs, Wang et al. confirmed that SRs with lower oxidation potentials and higher permittivity allowed for higher photocatalytic H₂ evolution rate over same photocatalyst.^[69] On the one hand, oxidation potential of SRs determines the ability of electron donation. SRs with lower oxidation potential mean that they can be more easily oxidized and more efficiently trap holes.

On the other hand, the interaction between SRs and photocatalyst surface determines the final availability of electron donors, which will increase and trap more holes with the increase of dielectric constant of the solvent.^[69] Among organic SRs, methanol is the mostly used. Because in comparison with other organic compounds, the H₂ evolution rate enhancement observed with methanol is mainly due to the decreased oxidation capacity and the increased permittivity. Methanol molecules as electron donors are oxidized in photocatalytic reactions, the hydrogen production process can be expressed as follows,^[435, 453-455]

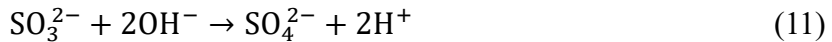


$$\Delta G^\circ = 16.1 \text{ kJ/mol}$$

The splitting energy for methanol/H₂O system is 0.7 eV and lower than that for water. In addition, the SBR effect is highly suppressed without the production of oxygen, hydrogen production is thus enhanced. Inorganic sacrificial reagents system such as S²⁻/SO₃²⁻^[455-461],

Introduction

$\text{Fe}^{3+}/\text{Fe}^{2+}$ [462-464], $\text{Ce}^{4+}/\text{Ce}^{3+}$ [465], I^-/IO_3^- [444], and CN^- [466] are normally used as electron donors/hole acceptors. These reductive ions are easily oxidized by photogenerated holes. For example, the reactions occur in the presence of $\text{S}^{2-}/\text{SO}_3^{2-}$ are described in equations. 10-14.



S^{2-} and SO_3^{2-} react with holes and can be oxidized into S_n^{2-} and $\text{S}_2\text{O}_3^{2-}$ respectively. Theoretically, they can work as sacrificial reagents independently. Since the S_n^{2-} can continue reacting with holes to form sulphur, adding SO_3^{2-} can prevent the further precipitation of sulphur and keep the reduction potential of the sacrificial reagents system. It has been proved that using $\text{S}^{2-}/\text{SO}_3^{2-}$ mixtures efficiently improved the H_2 production from water.^[467-470]

In practical application, SRs can differently affect photocatalysts. For example, $\text{Na}_2\text{S}/\text{Na}_2\text{SO}_3$, triethanolamine and methanol were found to be the most suitable SRs for $\text{Zn}_{0.5}\text{Cd}_{0.5}\text{S}$, g-C₃N₄, and TiO_2 , respectively as illustrated in Fig. 1.29b. The sacrificial reagents as electron donors have been vastly developed using various materials and play a key role in hydrogen production via the photocatalyzed water-splitting reaction. For better adjusting the electrolytic environment and optimizing the activity of photocatalysts, choosing a suitable SRs is crucial.

1.3.3.5 Band bending in electrolytes

When an n-type semiconductor is immersed in an aqueous electrolyte, electrons transfer across the semiconductor-liquid junction (SCLJ) until the electronic equilibration is reached, where the chemical potential of the electrons in the semiconductor (Fermi level) is equal to the redox potential (E_{redox}) in the electrolyte. The electric charge-transferring region from the semiconductor surface to the SCLJ is called space-charge region (SCR). The electric field between the semiconductor and the electrolyte shifts the energy-band edges of the semiconductor in the space-charge layer, which is known as band bending. Fig. 1.30 presents a schematic energy levels at the n-type semiconductor-electrolyte interfaces. When $E_F > E_{\text{redox}}$, as shown in Fig. 1.30b, the electrons transfer to the semiconductor side and the accumulation layer is formed resulting in downward bending of the band edges. When $E_F < E_{\text{redox}}$, electrons are depleted in the space-charge region that is therefore called depletion layer, and the energy bands bend upward as seen in Fig. 1.30c. If the concentration of electrons in the space-charge

region falls below the intrinsic level as shown in Fig. 1.30d, the depletion layer will become inversion layer and both these two layers contain positive charges. Fig. 1.30e presents the electrolytic double layer, the compact (Helmholtz) layer followed by the diffuse (Gouy-Chapman) layer on the electrolyte side. When the depletion layer or inversion layer is formed, the double layer is negative, filled with trapped electrons, adsorbed ions, solvent molecules, etc. Therefore, the potential decreases across the double layer due to $\Delta\varphi_{SC}$ in the space charge layer, $\Delta\varphi_H$ in Helmholtz layer, and $\Delta\varphi_G$ in Gouy layer. In the electrolyte with high ionic strength, the potential drop in double layer is normally much smaller than that in the space-charge region and the density of surface states (N_{ss}) on the semiconductor is low ($<10^{12} \text{ cm}^{-2}$). Therefore, $\Delta\varphi_{SC}$ dominates the change in potential and depends on the extent of band bending, which in turn influences the E_F of the semiconductor and the density of carriers on the surface. When the N_{ss} is high ($10^{13} - 10^{14} \text{ cm}^{-2}$), the potential drop, $\Delta\varphi_H$ and $\Delta\varphi_G$ are non-negligible, resulting in Fermi-level pinning effect which may boost the electron-holes recombination. Therefore, without contribution to charge separation in the semiconductor, the Fermi-level pinning effect is negative for PEC water splitting. [471-473] In brief, the band bending effect significantly enhances the electron-hole separation at the interface between semiconductor and electrolyte and thus depress the electron-hole pair recombination rate.

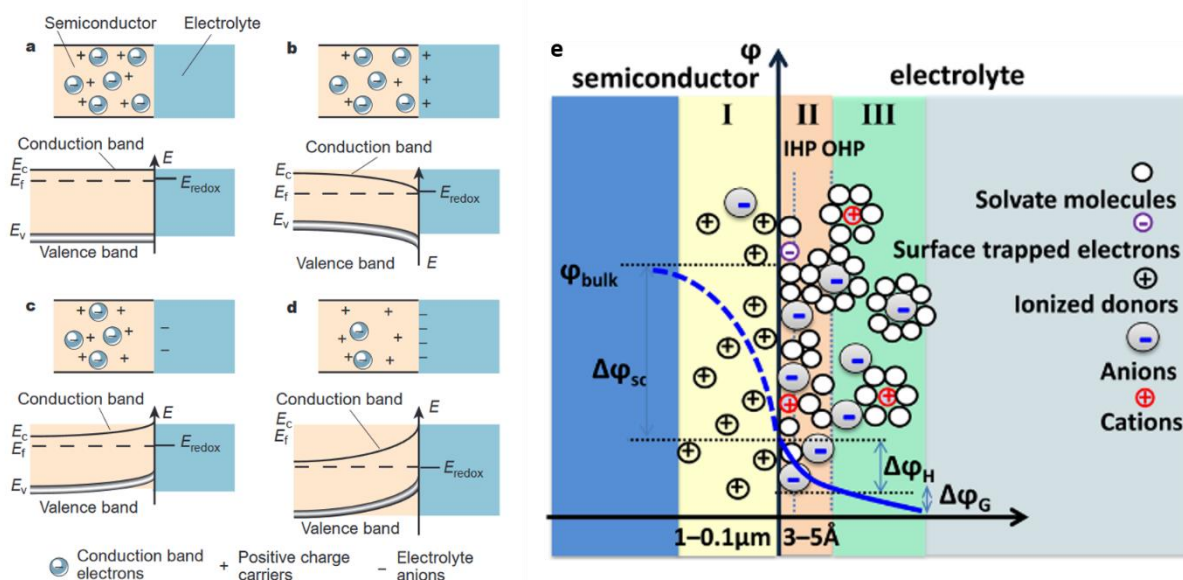


Fig. 1.30. Diagram of the electronic energy levels at the interface between the n-type semiconductor and an electrolyte(left): a, Flat band potential, where no space-charge layer exists in the semiconductor; b, accumulation layer; c, depletion layer; d, inversion layer. Reprinted with permission from ref [474]. Copyright 2016 American Chemical Society. e, the scheme of semiconductor-double layer interface (blue line) and the potential (φ) profile in the space charge layer ($\Delta\varphi_{SC}$) (I), Helmholtz layer ($\Delta\varphi_H$) (II), and Gouy layer ($\Delta\varphi_G$) (III).

Reprinted with permission from ref [436]. Copyright 2016 American Chemical Society.

Other important factors such as ionic strength effect the electrolytic conductivity, ionic mobility, charge transfer and stability of electrodes in PEC devices. The properties of both semiconductor and electrolytes influence the process of PEC water splitting. Concerning effects of above-mentioned electrolytic parameters on the performance of PEC water splitting, the comprehensive and comparative study is still missing. Understanding of this issue can be very helpful to develop new strategies to promote H₂ production from water splitting.

1.4 Summary

Photocatalytic/PEC water splitting under solar light is a desired candidate technology for solving energy and environment issues in the future. TiO₂ is known as one of the most excellent UV-light driven photocatalysts over time. Non-metal doping is an effective strategy for the electronic band gap engineering of TiO₂ to achieve visible-light activity. Actually, most non-metal doped TiO₂ materials have been applied in the degradation of organics, which can still be essential instructions for the photocatalytic/PEC water splitting. In this first chapter, we have summarized the non-metal doped TiO₂ for photocatalytic H₂ production from different perspectives. Numerous non-metal doped TiO₂ photocatalysts have been reported to be active under visible light. The possible origins of visible light absorption and the followed photocatalysis have been discussed. Non-metal doping allows the formation of localized states in the band gap of TiO₂ contributing to its visible range electronic transitions. Impurity states such as N 2p, C 2p, S 2p lie above the VB of TiO₂ or mix with O 2p uplifting the VB. We believe that the non-metal doped TiO₂ for photocatalytic/PEC water splitting under solar light will play an important role in the economic and environmental-friendly H₂ production. Specially, carbon can also be coated in TiO₂ in addition to carbon doping promoting the light utilization and charge transfer, leading to enhanced photocatalytic activity. The carbon coating in TiO₂ might accompany with carbon doping leading to dual or synergistic effect of carbon in TiO₂ on photocatalytic / PEC water splitting. Comparing to pure carbon doping or pure carbon coating, the synergy of carbon doping and coating in TiO₂ might result in more than doubled enhancement of photocatalytic performance. In addition, the defect states of oxygen vacancies resulted from non-metal doping located above the VB of TiO₂ or below the CB of TiO₂ also boost the visible-light response of TiO₂. The existence of large amount of oxygen vacancies in TiO₂ would stoichiometrically result in oxygen deficiency and phase changing of TiO₂ into

Introduction

titanium suboxides (Ti_nO_{2n-1}). The specific effect of oxygen deficiency on the photocatalytic / PEC performance of Ti_nO_{2n-1} materials might be interesting to investigate for the further application of Ti_nO_{2n-1} materials.

On the other hand, the SBR effect not only leads to the low quantum efficiency of photocatalysis, but also inevitably reduces the amount of H₂ production as well as the photocatalytic activity. In experimental studies of photocatalytic/PEC water splitting over different photocatalysts, the sacrificial agents are widely employed for reaching a high H₂ production rate. Addition of sacrificial reagents (SRs) such as methanol as the electron donor into water/photocatalysts suspension can improve the photoefficiency of H₂ production. The photogenerated holes are scavenged by these molecules, which greatly depress the charge carrier recombination. Without the production of oxygen, the SBR effect is highly suppressed. Specially, the electrolyte parameters (e.g., temperature, pH, anions and cations) affect the performance of PEC water splitting. The electrolytic properties can be well-tuned to maximize the charge transfer and mass-transport for efficient H₂ production. Therefore, the dopants, the preparation conditions, the SRs and the electrolytes can all manipulate the final efficiency of water splitting.

From the above discussion, it is clear that doping, coating, the modulation of electrolytic environment and the addition of sacrificial reagents can strongly influence the photocatalytic and photoelectrochemical performance of photocatalysts.

After this general introduction chapter, we will give the objectives and the scientific strategy of this PhD thesis in the second chapter. We will then present the synthesis of the carbon doped and coated TiO₂ by the “one pot” hydrolysis of TiCl₄ in glucose solution in third chapter. The effect of carbon doping and coating of TiO₂ on the textural, optical and electronic properties, photocurrent of TiO₂ and their photocatalytic and photoelectrochemical performances will be comprehensively investigated. In the fourth chapter, the carbon composed Ti_nO_{2n-1} ($2 \leq n \leq 9$) materials including bi-dimensional Magnéli materials will be prepared by the hydrolysis of TiCl₄ in glucose solution and calcined at high temperatures. The influence factors, formation mechanism of the growth of Ti_nO_{2n-1} and the followed performance of PEC water splitting will be deeply studied. In the fifth chapter, the studies on how electrolytic species in PEC system especially additives such as sacrificial reagents (SRs) and electrolyte cations/anions affect the photocatalytic activity of different photocatalysts including TiO₂ will be carried out. A series of metal oxide semiconducting materials such as TiO₂, WO₃, Fe₂O₃, BiVO₄, ZnFe₂O₄, ZnCr₂O₄ and LaFeO₃ will be studied. In the last chapter, general conclusions and perspectives for future research are given.

References

- [1] I. Dincer, Renew. Sust. Energ. Rev. 4 (2000) 157-175.
- [2] D. Dominković, I. Baćeković, A.S. Pedersen, G. Krajačić, Renew. Sust. Energ. Rev. 82 (2018) 1823-1838.
- [3] J.A. Foley, R. DeFries, G.P. Asner, C. Barford, G. Bonan, S.R. Carpenter, F.S. Chapin, M.T. Coe, G.C. Daily, H.K. Gibbs, Science 309 (2005) 570-574.
- [4] T.H. Oh, M. Hasanuzzaman, J. Selvaraj, S.C. Teo, S.C. Chua, Renew. Sust. Energ. Rev. 81 (2018) 3021-3031.
- [5] R. Foster, M. Ghassemi, A. Cota, Solar energy: renewable energy and the environment, CRC Press 2009, .
- [6] E. Kabir, P. Kumar, S. Kumar, A.A. Adelodun, K.-H. Kim, Renew. Sust. Energ. Rev. 82 (2018) 894-900.
- [7] K. Khanafer, K. Vafai, Renew. Energy 123 (2018) 398-406.
- [8] M. Ni, M.K. Leung, D.Y. Leung, K. Sumathy, Renew. Sust. Energ. Rev. 11 (2007) 401-425.
- [9] A. Fujishima, K. Honda, Nature 238 (1972) 37.
- [10] E. Miller, Energy Environ. Sci. 8 (2015) 2809-2810.
- [11] H. Döscher, J. Geisz, T. Deutsch, J. Turner, Energy Environ. Sci. 7 (2014) 2951-2956.
- [12] J. Wu, S. Huang, Z. Jin, J. Chen, L. Hu, Y. Long, J. Lu, S. Ruan, Y.-J. Zeng, J. Mater. Sci. 53 (2018) 16557-16566.
- [13] A. Kleiman-Shwarscstein, Y.-S. Hu, A.J. Forman, G.D. Stucky, E.W. McFarland, J. Phys. Chem. C 112 (2008) 15900-15907.
- [14] Y.-S. Hu, A. Kleiman-Shwarscstein, A.J. Forman, D. Hazen, J.-N. Park, E.W. McFarland, Chem. Mater. 20 (2008) 3803-3805.
- [15] G. Wang, Y. Ling, D.A. Wheeler, K.E. George, K. Horsley, C. Heske, J.Z. Zhang, Y. Li, Nano Lett. 11 (2011) 3503-3509.
- [16] T. Yang, J. Xue, H. Tan, A. Xie, S. Li, W. Yan, Y. Shen, J. Mater. Chem. A 6 (2018) 1210-1218.
- [17] D. Hong, G. Cao, X. Zhang, J. Qu, Y. Deng, H. Liang, J. Tang, Electrochim. Acta 283 (2018) 959-969.
- [18] Y. Fang, Y. Xu, X. Li, Y. Ma, X. Wang, Angew. Chem. 130 (2018) 9897-9901.
- [19] G. Wang, H. Wang, Y. Ling, Y. Tang, X. Yang, R.C. Fitzmorris, C. Wang, J.Z. Zhang, Y. Li, Nano Lett. 11 (2011) 3026-3033.
- [20] Z. Zhang, M.F. Hossain, T. Takahashi, Int. J. Hydrog. Energy 35 (2010) 8528-8535.
- [21] X. Chen, L. Liu, Y.Y. Peter, S.S. Mao, Science (2011) 1200448.
- [22] T. Butburee, Y. Bai, H. Wang, H. Chen, Z. Wang, G. Liu, J. Zou, P. Khemthong, G.Q.M. Lu, L. Wang, Adv. Mater. 30 (2018) 1705666.
- [23] Z. Wang, X. Li, H. Ling, C.K. Tan, L.P. Yeo, A.C. Grimsdale, A.I.Y. Tok, Small 14 (2018) 1800395.
- [24] H. Cui, W. Zhao, C. Yang, H. Yin, T. Lin, Y. Shan, Y. Xie, H. Gu, F. Huang, J. Mater. Chem. A 2 (2014) 8612-8616.
- [25] Z. Zhang, L. Zhang, M.N. Heddili, H. Zhang, P. Wang, Nano Lett. 13 (2012) 14-20.
- [26] J. Ran, J. Zhang, J. Yu, M. Jaroniec, S.Z. Qiao, Chem. Soc. Rev. 43 (2014) 7787-7812.
- [27] S.N.H. Jaafar, L.J. Minggu, K. Arifin, M.B. Kassim, W.R.D. Wan, Renew. Sust. Energ. Rev. 78 (2017) 698-709.
- [28] G. Ai, H. Li, S. Liu, R. Mo, J. Zhong, Adv. Funct. Mater. 25 (2015) 5706-5713.
- [29] H. Tong, S. Ouyang, Y. Bi, N. Umezawa, M. Oshikiri, J. Ye, Adv. Mater. 24 (2012) 229-251.
- [30] J. Yang, D. Wang, H. Han, C. Li, Acc. Chem. Res. 46 (2013) 1900-1909.
- [31] P. Roy, C. Das, K. Lee, R. Hahn, T. Ruff, M. Moll, P. Schmuki, J. Am. Chem. Soc. 133 (2011) 5629-5631.
- [32] K. Iwashina, A. Kudo, J. Am. Chem. Soc. 133 (2011) 13272-13275.
- [33] Y.-C. Pu, G. Wang, K.-D. Chang, Y. Ling, Y.-K. Lin, B.C. Fitzmorris, C.-M. Liu, X. Lu, Y. Tong, J.Z. Zhang, Nano Lett. 13 (2013) 3817-3823.
- [34] Z. Zhang, Y. Yu, P. Wang, ACS Appl. Mater. Interfaces 4 (2012) 990-996.
- [35] J. Yu, L. Qi, M. Jaroniec, J. Phys. Chem. C 114 (2010) 13118-13125.
- [36] Y. Yang, C.-H. Chang, H. Idriss, Appl. Catal. B 67 (2006) 217-222.
- [37] G.L. Chiarello, E. Selli, L. Forni, Appl. Catal. B 84 (2008) 332-339.
- [38] F. Wang, Y. Jiang, D.J. Lawes, G.E. Ball, C. Zhou, Z. Liu, R. Amal, ACS Catal. 5 (2015) 3924-3931.
- [39] W. Choi, A. Termin, M.R. Hoffmann, J. Phys. Chem. 98 (1994) 13669-13679.
- [40] Y. Gai, J. Li, S.-S. Li, J.-B. Xia, S.-H. Wei, Phys. Rev. Lett. 102 (2009) 036402.
- [41] T. Hisatomi, J. Kubota, K. Domen, Chem. Soc. Rev. 43 (2014) 7520-7535.
- [42] Y. Zhao, N. Hoivik, K. Wang, Nano Energy, 30 (2016) 728-744.
- [43] V. Kumaravel, S. Mathew, J. Bartlett, S.C. Pillai, Appl. Catal. B (2018).
- [44] C.C. McCrory, S. Jung, I.M. Ferrer, S.M. Chatman, J.C. Peters, T.F. Jaramillo, J. Am. Chem. Soc. 137 (2015) 4347-4357.
- [45] L. Preethi, R.P. Antony, T. Mathews, L. Walczak, C.S. Gopinath, Sci. Rep. 7 (2017) 14314.
- [46] S. Sato, Chem. Phys. Lett. 123 (1986) 126-128.

Introduction

- [47] R. Asahi, T. Morikawa, T. Ohwaki, K. Aoki, Y. Taga, *Science* 293 (2001) 269-271.
- [48] J. Zhang, Y. Wu, M. Xing, S.A.K. Leghari, S. Sajjad, *Energy Environ. Sci.* 3 (2010) 715-726.
- [49] A. Zaleska, *Recent Pat. Eng.* 2 (2008) 157-164.
- [50] R. Daghrir, P. Drogui, D. Robert, *Ind. Eng. Chem. Res.* 52 (2013) 3581-3599.
- [51] S. In, A. Orlov, R. Berg, F. García, S. Pedrosa-Jimenez, M.S. Tikhov, D.S. Wright, R.M. Lambert, *J. Am. Chem. Soc.* 129 (2007) 13790-13791.
- [52] H. Li, J. Xing, Z. Xia, J. Chen, *Electrochim. Acta* 139 (2014) 331-336.
- [53] Z. Xing, Z. Li, X. Wu, G. Wang, W. Zhou, *Int. J. Hydrot. Energy* 41 (2016) 1535-1541.
- [54] G. Wu, J. Wang, D.F. Thomas, A. Chen, *Langmuir* 24 (2008) 3503-3509.
- [55] I.S. Cho, C.H. Lee, Y. Feng, M. Logar, P.M. Rao, L. Cai, D.R. Kim, R. Sinclair, X. Zheng, *Nat. Commun.* 4 (2013) 1723.
- [56] S.K. Parayil, H.S. Kibombo, C.-M. Wu, R. Peng, J. Baltrusaitis, R.T. Koodali, *Int. J. Hydrot. Energy* 37 (2012) 8257-8267.
- [57] J. He, Q. Liu, Z. Sun, W. Yan, G. Zhang, Z. Qi, P. Xu, Z. Wu, S. Wei, *J. Phys. Chem. C* 114 (2010) 6035-6038.
- [58] G. Liu, Z. Chen, C. Dong, Y. Zhao, F. Li, G.Q. Lu, H.-M. Cheng, *J. Phys. Chem. B* 110 (2006) 20823-20828.
- [59] Y. Yang, K. Ye, D. Cao, P. Gao, M. Qiu, L. Liu, P. Yang, *ACS Appl. Mater. Interfaces* 10 (2018) 19633-19638.
- [60] G. Liu, Y. Zhao, C. Sun, F. Li, G.Q. Lu, H.M. Cheng, *Angew. Chem. Int. Ed.* 47 (2008) 4516-4520.
- [61] M. Batzill, E.H. Morales, U. Diebold, *Phys. Rev. Lett.* 96 (2006) 026103.
- [62] C. Di Valentin, G. Pacchioni, A. Selloni, S. Livraghi, E. Giannello, *J. Phys. Chem. B* 109 (2005) 11414-11419.
- [63] T. Umebayashi, T. Yamaki, H. Itoh, K. Asai, *Appl. Phys. Lett.* 81 (2002) 454-456.
- [64] H. Wang, J.P. Lewis, *J. Condens. Matter Phys.* 17 (2005) L209.
- [65] L. Zhao, X. Chen, X. Wang, Y. Zhang, W. Wei, Y. Sun, M. Antonietti, M.-M. Titirici, *Adv. Mater.* 22 (2010) 3317.
- [66] X. Cheng, H. Liu, Q. Chen, J. Li, P. Wang, *Carbon* 66 (2014) 450-458.
- [67] Z. Liang, X. Bai, P. Hao, Y. Guo, Y. Xue, J. Tian, H. Cui, *Appl. Catal. B* 243 (2019) 711-720.
- [68] X. Chen, S.S. Mao, *Chem. Rev.* 107 (2007) 2891-2959.
- [69] M. Wang, S. Shen, L. Li, Z. Tang, J. Yang, *J. Mater. Sci.* 52 (2017) 5155-5164.
- [70] J.C. Hill, K.-S. Choi, *J. Phys. Chem. C* 116 (2012) 7612-7620.
- [71] A.M. Ahmed, F. Mohamed, A.M. Ashraf, M. Shaban, A.A.P. Khan, A.M. Asiri, *Chemosphere* 238 (2020) 124554.
- [72] S. Guo, X. Zhao, W. Zhang, W. Wang, *Mater. Sci. Eng. B* 227 (2018) 129-135.
- [73] N.K. Biswas, (2017).
- [74] A. Kudo, Y. Miseki, *Chem. Soc. Rev.* 38 (2009) 253-278.
- [75] S. Agrawal, N.J. English, K.R. Thampi, J. MacElroy, *Phys. Chem. Chem. Phys.* 14 (2012) 12044-12056.
- [76] Y. Moriya, T. Takata, K. Domen, *Coord. Chem. Rev.* 257 (2013) 1957-1969.
- [77] A.J. Bard, L.R. Faulkner, J. Leddy, C.G. Zoski, *Electrochemical methods: fundamentals and applications*, Wiley New York, 1980.
- [78] Z. Chen, T.F. Jaramillo, T.G. Deutsch, A. Kleiman-Shwarscstein, A.J. Forman, N. Gaillard, R. Garland, K. Takanabe, C. Heske, M. Sunkara, *J. Mater. Res.* 25 (2010) 3-16.
- [79] K. Takanabe, K. Domen, *Green* 1 (2011) 313-322.
- [80] R. Asahi, Y. Taga, W. Mannstadt, A.J. Freeman, *Phys. Rev. B* 61 (2000) 7459.
- [81] A. Wold, *Chem. Mater.* 5 (1993) 280-283.
- [82] H.P. Maruska, A.K. Ghosh, *Sol. Energy* 20 (1978) 443-458.
- [83] G. Barolo, S. Livraghi, M. Chiesa, M.C. Paganini, E. Giannello, *J. Phys. Chem. C* 116 (2012) 20887-20894.
- [84] X. Li, D. Wang, G. Cheng, Q. Luo, J. An, Y. Wang, *Appl. Catal. B* 81 (2008) 267-273.
- [85] C. Xu, R. Killmeyer, M.L. Gray, S.U. Khan, *Appl. Catal. B* 64 (2006) 312-317.
- [86] M.G. Méndez-Medrano, E. Kowalska, A. Lehoux, A. Herissan, B. Ohtani, S. Rau, C. Colbeau-Justin, J.L. Rodriguez-Lopez, H. Remita, *J. Phys. Chem. C* 120 (2016) 25010-25022.
- [87] J. Wang, Z. Wang, H. Li, Y. Cui, Y. Du, *J. Alloys Compd.* 494 (2010) 372-377.
- [88] F. Dong, W. Zhao, Z. Wu, S. Guo, *J. Hazard. Mater.* 162 (2009) 763-770.
- [89] J. Wang, D.N. Tafen, J.P. Lewis, Z. Hong, A. Manivannan, M. Zhi, M. Li, N. Wu, *J. Am. Chem. Soc.* 131 (2009) 12290-12297.
- [90] G. Liu, H.G. Yang, X. Wang, L. Cheng, J. Pan, G.Q. Lu, H.-M. Cheng, *J. Am. Chem. Soc.* 131 (2009) 12868-12869.
- [91] S. Hoang, S. Guo, N.T. Hahn, A.J. Bard, C.B. Mullins, *Nano Lett.* 12 (2011) 26-32.
- [92] G.B. Soares, B. Bravin, C.M. Vaz, C. Ribeiro, *Appl. Catal. B* 106 (2011) 287-294.
- [93] V. Vaiano, O. Sacco, D. Sannino, P. Ciambelli, *Appl. Catal. B* 170 (2015) 153-161.
- [94] J. Xie, H. Xie, B.L. Su, Y.b. Cheng, X. Du, H. Zeng, M. Wang, W. Wang, H. Wang, Z. Fu, *Angew. Chem. Int. Ed.* 55 (2016) 3031-3035.

Introduction

- [95] Y.J. Hwang, S. Yang, H. Lee, *Appl. Catal. B* 204 (2017) 209-215.
- [96] C. Xu, R. Killmeyer, M.L. Gray, S.U. Khan, *Inorg. Chem.* 8 (2006) 1650-1654.
- [97] J.H. Park, S. Kim, A.J. Bard, *Nano Lett.* 6 (2006) 24-28.
- [98] S.K. Mohapatra, M. Misra, V.K. Mahajan, K.S. Raja, *J. Phys. Chem. C* 111 (2007) 8677-8685.
- [99] Y. Park, W. Kim, H. Park, T. Tachikawa, T. Majima, W. Choi, *Appl. Catal. B* 91 (2009) 355-361.
- [100] H.J. Yun, H. Lee, J.B. Joo, N.D. Kim, J. Yi, *Inorg. Chem.* 12 (2010) 769-772.
- [101] F. Dong, S. Guo, H. Wang, X. Li, Z. Wu, *J. Phys. Chem. C* 115 (2011) 13285-13292.
- [102] G. Liu, C. Han, M. Pelaez, D. Zhu, S. Liao, V. Likodimos, N. Ioannidis, A.G. Kontos, P. Falaras, P.S. Dunlop, *Nanotechnology* 23 (2012) 294003.
- [103] X. Wu, S. Yin, Q. Dong, C. Guo, H. Li, T. Kimura, T. Sato, *Appl. Catal. B* 142 (2013) 450-457.
- [104] V. Likodimos, C. Han, M. Pelaez, A.G. Kontos, G. Liu, D. Zhu, S. Liao, A.A. de la Cruz, K. O'Shea, P.S. Dunlop, *Ind. Eng. Chem. Res.* 52 (2013) 13957-13964.
- [105] S. Goriparti, E. Miele, M. Prato, A. Scarpellini, S. Marras, S. Monaco, A. Toma, G.C. Messina, A. Alabastri, F.D. Angelis, *ACS Appl. Mater. Interfaces* 7 (2015) 25139-25146.
- [106] J. Shao, W. Sheng, M. Wang, S. Li, J. Chen, Y. Zhang, S. Cao, *Appl. Catal. B* 209 (2017) 311-319.
- [107] Z. Noorimotlagh, I. Kazeminezhad, N. Jaafarzadeh, M. Ahmadi, Z. Ramezani, S.S. Martinez, J. Hazard. Mater. 350 (2018) 108-120.
- [108] V. Trevisan, A. Olivo, F. Pinna, M. Signoretto, F. Vindigni, G. Cerrato, C. Bianchi, *Appl. Catal. B* 160 (2014) 152-160.
- [109] J. Zhang, Z. Xing, J. Cui, Z. Li, S. Tan, J. Yin, J. Zou, Q. Zhu, W. Zhou, *Dalton Trans.* 47 (2018) 4877-4884.
- [110] X. Song, W. Li, D. He, H. Wu, Z. Ke, C. Jiang, G. Wang, X. Xiao, *Adv. Energy Mater.* (2018) 1800165.
- [111] J. Xu, Y. Ao, M. Chen, D. Fu, *J. Alloys Compd.* 484 (2009) 73-79.
- [112] X. Wang, M. Blackford, K. Prince, R.A. Caruso, *ACS Appl. Mater. Interfaces* 4 (2012) 476-482.
- [113] M. Szkoda, K. Siuzdak, A. Lisowska-Oleksiak, J. Karczewski, J. Ryl, *Inorg. Chem.* 60 (2015) 212-215.
- [114] G.G. Bessegato, J.C. Cardoso, M.V.B. Zanoni, *Catal. Today* 240 (2015) 100-106.
- [115] E.B. Simsek, *Appl. Catal. B* 200 (2017) 309-322.
- [116] W.H. Abdelraheem, M.K. Patil, M.N. Nadagouda, D.D. Dionysiou, *Appl. Catal. B* 241 (2019) 598-611.
- [117] S. Liu, X. Chen, J. Hazard. Mater. 152 (2008) 48-55.
- [118] E.M. Rockafellow, L.K. Stewart, W.S. Jenks, *Appl. Catal. B* 91 (2009) 554-562.
- [119] L. Randeniya, A. Murphy, I. Plumb, *J. Mater. Sci.* 43 (2008) 1389-1399.
- [120] M. Bayati, A. Moshfegh, F. Golestani-Fard, *Appl. Catal. A-Gen.* 389 (2010) 60-67.
- [121] R.G. Chaudhuri, S. Paria, *Dalton Trans.* 43 (2014) 5526-5534.
- [122] S.W. Shin, J.Y. Lee, K.-S. Ahn, S.H. Kang, J.H. Kim, *J. Phys. Chem. C* 119 (2015) 13375-13383.
- [123] X. Yan, K. Yuan, N. Lu, H. Xu, S. Zhang, N. Takeuchi, H. Kobayashi, R. Li, *Appl. Catal. B* 218 (2017) 20-31.
- [124] J. Rengifo-Herrera, E. Mielczarski, J. Mielczarski, N. Castillo, J. Kiwi, C. Pulgarin, *Appl. Catal. B* 84 (2008) 448-456.
- [125] S. Ivanov, A. Barylyak, K. Besaha, A. Bund, Y. Bobitski, R. Wojnarowska-Nowak, I. Yaremchuk, M. Kus-Liskiewicz, *Nanoscale Res. Lett.* 11 (2016) 140.
- [126] F. Dong, W. Zhao, Z. Wu, *Nanotechnology*, 19 (2008) 365607.
- [127] Y. Lv, L. Yu, H. Huang, H. Liu, Y. Feng, *J. Alloys Compd.* 488 (2009) 314-319.
- [128] X. Zhou, B. Jin, S. Zhang, H. Wang, H. Yu, F. Peng, *Inorg. Chem.* 19 (2012) 127-130.
- [129] M. Iwase, K. Yamada, T. Kurisaki, B. Ohtani, H. Wakita, *Appl. Catal. B* 140 (2013) 327-332.
- [130] Z. Li, Y. Xin, W. Wu, B. Fu, Z. Zhang, *ACS Appl. Mater. Interfaces* 8 (2016) 30972-30979.
- [131] X. Feng, P. Wang, J. Hou, J. Qian, Y. Ao, C. Wang, J. Hazard. Mater. 351 (2018) 196-205.
- [132] M. Xing, J. Zhang, B. Qiu, B. Tian, M. Anpo, M. Che, *Small*, 11 (2015) 1920-1929.
- [133] N. Kumar, U. Maitra, V.I. Hegde, U.V. Waghmare, A. Sundaresan, C. Rao, *Inorg. Chem.* 52 (2013) 10512-10519.
- [134] J. Cheng, J. Chen, W. Lin, Y. Liu, Y. Kong, *Appl. Surf. Sci.* 332 (2015) 573-580.
- [135] G. Yang, Z. Jiang, H. Shi, M.O. Jones, T. Xiao, P.P. Edwards, Z. Yan, *Appl. Catal. B* 96 (2010) 458-465.
- [136] J.A. Khan, C. Han, N.S. Shah, H.M. Khan, M.N. Nadagouda, V. Likodimos, P. Falaras, K. O'Shea, D.D. Dionysiou, *Environ. Eng. Sci.* 31 (2014) 435-446.
- [137] F.-t. Li, X.-j. Wang, Y. Zhao, J.-x. Liu, Y.-j. Hao, R.-h. Liu, D.-s. Zhao, *Appl. Catal. B* 144 (2014) 442-453.
- [138] H. Xu, Z. Zheng, L. Zhang, H. Zhang, F. Deng, *J. Solid State Chem.* 181 (2008) 2516-2522.
- [139] H. Xu, L. Zhang, *J. Phys. Chem. C* 114 (2010) 11534-11541.
- [140] X. Hong, Z. Wang, W. Cai, F. Lu, J. Zhang, Y. Yang, N. Ma, Y. Liu, *Chem. Mater.* 17 (2005) 1548-1552.
- [141] S. Tojo, T. Tachikawa, M. Fujitsuka, T. Majima, *J. Phys. Chem. C* 112 (2008) 14948-14954.
- [142] W. Su, Y. Zhang, Z. Li, L. Wu, X. Wang, J. Li, X. Fu, *Langmuir*, 24 (2008) 3422-3428.
- [143] A. Lisowska-Oleksiak, K. Szybowska, V. Jasulaitiené, *Electrochim. Acta* 55 (2010) 5881-5885.
- [144] S. Song, J. Tu, Z. He, F. Hong, W. Liu, J. Chen, *Appl. Catal. A-Gen.* 378 (2010) 169-174.

Introduction

- [145] C. Zhang, Y. Zhou, J. Bao, X. Sheng, J. Fang, S. Zhao, Y. Zhang, W. Chen, *ACS Appl. Mater. Interfaces* 10 (2018) 18796-18804.
- [146] H. Luo, T. Takata, Y. Lee, J. Zhao, K. Domen, Y. Yan, *Chem. Mater.* 16 (2004) 846-849.
- [147] B. Naik, S.Y. Moon, S.H. Kim, J.Y. Park, *Appl. Surf. Sci.* 354 (2015) 347-352.
- [148] L. Zhang, M.S. Tse, O.K. Tan, Y.X. Wang, M. Han, *J. Mater. Chem. A* 1 (2013) 4497-4507.
- [149] E.M. Samsudin, S.B.A. Hamid, *Appl. Surf. Sci.* 391 (2017) 326-336.
- [150] F. Peng, L. Cai, H. Yu, H. Wang, J. Yang, *J. Solid State Chem.* 181 (2008) 130-136.
- [151] C. Zhao, M. Pelaez, D.D. Dionysiou, S.C. Pillai, J.A. Byrne, K.E. O'Shea, *Catal. Today* 224 (2014) 70-76.
- [152] S.A. Ansari, M.M. Khan, M.O. Ansari, M.H. Cho, *New J. Chem.* 40 (2016) 3000-3009.
- [153] C.W. Dunnill, I.P. Parkin, *Dalton Trans.* 40 (2011) 1635-1640.
- [154] S. Livraghi, M.C. Paganini, E. Giamello, A. Selloni, C. Di Valentin, G. Pacchioni, *J. Am. Chem. Soc.* 128 (2006) 15666-15671.
- [155] T. Ihara, M. Miyoshi, Y. Iriyama, O. Matsumoto, S. Sugihara, *Appl. Catal. B* 42 (2003) 403-409.
- [156] W. Zhou, H. Fu, *Inorg. Chem. Front.* 5 (2018) 1240-1254.
- [157] H. Li, S. Yin, Y. Wang, T. Sekino, S.W. Lee, T. Sato, *J. Catal.* 297 (2013) 65-69.
- [158] A.K. Rumaiz, J. Woicik, E. Cockayne, H. Lin, G.H. Jaffari, S.I. Shah, *Appl. Phys. Lett.* 95 (2009) 262111.
- [159] X. Pan, M.-Q. Yang, X. Fu, N. Zhang, Y.-J. Xu, *Nanoscale* 5 (2013) 3601-3614.
- [160] I. Justicia, P. Ordejón, G. Canto, J.L. Mozos, J. Fraxedas, G.A. Battiston, R. Gerbasi, A. Figueras, *Adv. Mater.* 14 (2002) 1399-1402.
- [161] W. Fang, Y. Zhou, C. Dong, M. Xing, J. Zhang, *Catal. Today* 266 (2016) 188-196.
- [162] N. Feng, F. Liu, M. Huang, A. Zheng, Q. Wang, T. Chen, G. Cao, J. Xu, J. Fan, F. Deng, *Sci. Rep.* 6 (2016) 34765.
- [163] Y. Liu, M. Xing, J. Zhang, *Chinese J. Catal.* 35 (2014) 1511-1519.
- [164] G. Fu, P. Zhou, M. Zhao, W. Zhu, S. Yan, T. Yu, Z. Zou, *Dalton Trans.* 44 (2015) 12812-12817.
- [165] Y. Xiao, X. Yu, Y. Gao, J. Liu, Z. Li, *Catal. Commun.* 102 (2017) 1-4.
- [166] F. Zuo, L. Wang, P. Feng, *Int. J. Hydrog. Energy* 39 (2014) 711-717.
- [167] F. Amano, M. Nakata, A. Yamamoto, T. Tanaka, *J. Phys. Chem. C* 120 (2016) 6467-6474.
- [168] J.W. Zheng, A. Bhattcahrayya, P. Wu, Z. Chen, J. Highfield, Z. Dong, R. Xu, *J. Phys. Chem. C* 114 (2010) 7063-7069.
- [169] Y. Niu, M. Xing, B. Tian, J. Zhang, *Appl. Catal. B* 115 (2012) 253-260.
- [170] I. Milosevic, A. Jayaprakash, B. Greenwood, B. Van Driel, S. Rtimi, P. Bowen, *Nanomaterials* 7 (2017) 391.
- [171] G. Yang, Z. Jiang, H. Shi, T. Xiao, Z. Yan, *J. Mater. Chem.* 20 (2010) 5301-5309.
- [172] Z. Wu, F. Dong, W. Zhao, S. Guo, *J. Hazard. Mater.* 157 (2008) 57-63.
- [173] Y. Wu, M. Xing, J. Zhang, *J. Hazard. Mater.* 192 (2011) 368-373.
- [174] J.W. Hamilton, J.A. Byrne, P.S. Dunlop, D.D. Dionysiou, M. Pelaez, K. O'Shea, D. Synnott, S.C. Pillai, *J. Phys. Chem. C* 118 (2014) 12206-12215.
- [175] X. He, W.G. Aker, M. Pelaez, Y. Lin, D.D. Dionysiou, H.-m. Hwang, *J. Photochem. Photobiol. A* 314 (2016) 81-92.
- [176] Q. Wang, C. Chen, W. Ma, H. Zhu, J. Zhao, *Chem. Eur. J.* 15 (2009) 4765-4769.
- [177] N. Serpone, Is the band gap of pristine TiO₂ narrowed by anion-and cation-doping of titanium dioxide in second-generation photocatalysts?, ACS Publications, 2006.
- [178] D. Li, H. Haneda, S. Hishita, N. Ohashi, *Chem. Mater.* 17 (2005) 2596-2602.
- [179] J. Chen, L.-B. Lin, F.-Q. Jing, *J. Phys. Chem. Solids* 62 (2001) 1257-1262.
- [180] S. Hoang, S.P. Berglund, N.T. Hahn, A.J. Bard, C.B. Mullins, *J. Am. Chem. Soc.* 134 (2012) 3659-3662.
- [181] X. Qiu, C. Burda, *Chem. Phys.* 339 (2007) 1-10.
- [182] U. Akpan, B. Hameed, *Appl. Catal. A-Gen.* 375 (2010) 1-11.
- [183] M. Nasirian, Y. Lin, C. Bustillo-Lecompte, M. Mehrvar, *Int. J. Environ. Sci. Technol.* 15 (2018) 2009-2032.
- [184] A.-A. Salarian, Z. Hami, N. Mirzaei, S.M. Mohseni, A. Asadi, H. Bahrami, M. Vosoughi, A. Alinejad, M.-R. Zare, *J. Mol. Liq.* 220 (2016) 183-191.
- [185] X. Zhang, Y. Sun, X. Cui, Z. Jiang, *Int. J. Hydrog. Energy* 37 (2012) 1356-1365.
- [186] Y. Huang, W. Ho, S. Lee, L. Zhang, G. Li, J.C. Yu, *Langmuir* 24 (2008) 3510-3516.
- [187] Y.-C. Wu, L.-S. Ju, *J. Alloys Compd.* 604 (2014) 164-170.
- [188] J. Lynch, C. Giannini, J.K. Cooper, A. Lojudice, I.D. Sharp, R. Buonsanti, *J. Phys. Chem. C* 119 (2015) 7443-7452.
- [189] W. Qian, P.A. Greaney, S. Fowler, S.-K. Chiu, A.M. Goforth, J. Jiao, *ACS Sustain. Chem. Eng.* 2 (2014) 1802-1810.
- [190] B. Kosowska, S. Mozia, A.W. Morawski, B. Grzmil, M. Janus, K. Kałucki, *Sol. Energy Mater. Sol.* 88 (2005) 269-280.
- [191] Y. Nosaka, M. Matsushita, J. Nishino, A.Y. Nosaka, *Sci. Technol. Adv. Mater.* 6 (2005) 143.
- [192] J. Marques, T.D. Gomes, M.A. Forte, R.F. Silva, C.J. Tavares, *Catal. Today* 326 (2019) 36-45.

Introduction

- [193] J. Rengifo-Herrera, J. Kiwi, C. Pulgarin, J. Photochem. Photobiol. A 205 (2009) 109-115.
- [194] H.U. Lee, S.C. Lee, S.H. Choi, B. Son, S.J. Lee, H.J. Kim, J. Lee, Appl. Catal. B 129 (2013) 106-113.
- [195] S. Habibi, M. Jamshidi, Environ. Technol. (2019) 1-15.
- [196] H. Zhang, L. Zheng, X. Ouyang, Y. Ni, Ceram. Int. 44 (2018) 15754-15763.
- [197] Y. Duan, X. Chen, X. Zhang, W. Xiang, C. Wu, Solid State Sci. 86 (2018) 12-18.
- [198] W. Ren, Z. Ai, F. Jia, L. Zhang, X. Fan, Z. Zou, Appl. Catal. B 69 (2007) 138-144.
- [199] X. Lin, F. Rong, X. Ji, D. Fu, Microporous Mesoporous Mater. 142 (2011) 276-281.
- [200] F. Dong, H. Wang, Z. Wu, J. Phys. Chem. C 113 (2009) 16717-16723.
- [201] M. Hamadanian, A. Reisi-Vanani, A. Majedi, Mater. Chem. Phys. 116 (2009) 376-382.
- [202] J. Madarász, A. Brăileanu, M. Crișan, M. Răileanu, G. Pokol, J. Therm. Anal. Calorim. 97 (2009) 265-271.
- [203] J. Yu, S. Liu, Z. Xiu, W. Yu, G. Feng, J. Alloys Compd. 471 (2009) L23-L25.
- [204] E. Grabowska, A. Zaleska, J.W. Sobczak, M. Gazda, J. Hupka, Procedia Chem. 1 (2009) 1553-1559.
- [205] R.P. Cavalcante, R.F. Dantas, B. Bayarri, O. Gonzalez, J. Gimenez, S. Esplugas, A.M. Junior, Catal. Today 252 (2015) 27-34.
- [206] N.O. Gopal, H.-H. Lo, T.-F. Ke, C.-H. Lee, C.-C. Chou, J.-D. Wu, S.-C. Sheu, S.-C. Ke, J. Phys. Chem. C 116 (2012) 16191-16197.
- [207] Y. Wu, M. Xing, B. Tian, J. Zhang, F. Chen, Chem. Eng. J. 162 (2010) 710-717.
- [208] M.V. Dozzi, B. Ohtani, E. Sellli, Phys. Chem. Chem. Phys. 13 (2011) 18217-18227.
- [209] H. Xu, L. Zhang, J. Phys. Chem. C 114 (2010) 940-946.
- [210] Y. Ma, J.-W. Fu, X. Tao, X. Li, J.-F. Chen, Appl. Surf. Sci. 257 (2011) 5046-5051.
- [211] A. Abdelhaleem, W. Chu, J. Hazard. Mater. 338 (2017) 491-501.
- [212] H. Hou, F. Gao, M. Shang, L. Wang, J. Zheng, Z. Yang, J. Xu, W. Yang, J. Mater. Sci.: Mater. Electron. 28 (2017) 3796-3805.
- [213] D. Kusano, M. Emori, H. Sakama, RSC Adv. 7 (2017) 1887-1898.
- [214] N.S. Luong, V.D. Ngo, N.M. Tien, T.N. Dung, N.M. Nghia, N.T. Loc, V.T. Thu, T. Dai Lam, J. Electron. Mater. 46 (2017) 158-166.
- [215] M.A. Mohamed, W. Salleh, J. Jaafar, A. Ismail, N.A.M. Nor, Mater. Chem. Phys. 162 (2015) 113-123.
- [216] L. Huang, W. Fu, X. Fu, B. Zong, H. Liu, H. Bala, X. Wang, G. Sun, J. Cao, Z. Zhang, Mater. Lett. 209 (2017) 585-588.
- [217] S.A. Bakar, C. Ribeiro, Appl. Surf. Sci. 377 (2016) 121-133.
- [218] Y. Shao, C. Cao, S. Chen, M. He, J. Fang, J. Chen, X. Li, D. Li, Appl. Catal. B 179 (2015) 344-351.
- [219] C. Li, Z. Zhao, H.S. Lomboleni, H. Huang, Z. Peng, J. Mater. Res. 32 (2017) 737-747.
- [220] S.M.M. Ali, K. Sandhya, RSC Adv. 6 (2016) 60522-60529.
- [221] T. Suwannaruang, K. Wantala, Appl. Surf. Sci. 380 (2016) 257-267.
- [222] Y. Hirose, A. Itadani, T. Ohkubo, H. Hashimoto, J. Takada, S. Kittaka, Y. Kuroda, Dalton Trans. 46 (2017) 4435-4451.
- [223] C. Yan, K.-F. Chen, C.-H. Lai, S.-W. Lai, Q. Chang, Y.-P. Peng, J. Environ. Sci. 26 (2014) 1505-1512.
- [224] N.C. Martins, J. Ângelo, A.V. Girão, T. Trindade, L. Andrade, A. Mendes, Appl. Catal. B 193 (2016) 67-74.
- [225] H.H.H. Lin, A.Y.C. Lin, C.L. Hung, J. Chem. Technol. Biotechnol. 90 (2015) 1345-1354.
- [226] C. Du, J. Zhou, F. Li, W. Li, Y. Wang, Q. He, Appl. Phys. A 122 (2016) 714.
- [227] M.A. Mohamed, W.N.W. Salleh, J. Jaafar, M.S. Rosmi, Z.A.M. Hir, M.A. Mutalib, A.F. Ismail, M. Tanemura, Appl. Surf. Sci. 393 (2017) 46-59.
- [228] J. Lu, Y. Wang, J. Huang, J. Fei, L. Cao, C. Li, Dyes Pigm. 144 (2017) 203-211.
- [229] L. Yu, Y. Lin, J. Huang, S. Lin, D. Li, J. Am. Ceram. Soc. 100 (2017) 333-342.
- [230] D. He, Y. Li, J. Wu, Y. Yang, Q. An, Appl. Surf. Sci. 391 (2017) 318-325.
- [231] H.-P. Qi, Y.-Z. Liu, L. Chang, H.-L. Wang, J. Environ. Chem. Eng. 5 (2017) 6114-6121.
- [232] A. Lin, D. Qi, H. Ding, L. Wang, M. Xing, B. Shen, J. Zhang, Catal. Today 281 (2017) 636-641.
- [233] V. Etacheri, G. Michlits, M.K. Seery, S.J. Hinder, S.C. Pillai, ACS Appl. Mater. Interfaces 5 (2013) 1663-1672.
- [234] A. Giannakas, M. Antonopoulou, C. Daikopoulos, Y. Deligiannakis, I. Konstantinou, Appl. Catal. B 184 (2016) 44-54.
- [235] D. Quiñones, A. Rey, P.M. Álvarez, F. Beltrán, G.L. Puma, Appl. Catal. B 178 (2015) 74-81.
- [236] G. Liu, C. Sun, L. Cheng, Y. Jin, H. Lu, L. Wang, S.C. Smith, G.Q. Lu, H.-M. Cheng, J. Phys. Chem. C 113 (2009) 12317-12324.
- [237] G. Liu, J. Pan, L. Yin, J.T. Irvine, F. Li, J. Tan, P. Wormald, H.M. Cheng, Adv. Funct. Mater. 22 (2012) 3233-3238.
- [238] C. Carlucci, B. Scrimen, T. Sibillano, C. Giannini, E. Filippo, P. Perulli, A. Capodilupo, G. Corrente, G. Ciccarella, Inorganics 2 (2014) 264-277.
- [239] C. Han, J. Andersen, V. Likodimos, P. Falaras, J. Linkugel, D.D. Dionysiou, Catal. Today 224 (2014) 132-139.

Introduction

- [240] L. Szatmáry, S. Bakardjieva, J. Šubrt, P. Bezdička, J. Jirkovský, Z. Bastl, V. Brezová, M. Korenko, Catal. Today 161 (2011) 23-28.
- [241] Y.O. Shvadchina, M. Cherepivskaya, V. Vakulenko, A. Sova, I. Stolyarova, R. Prikhodko, J. Water Chem. Technol. 37 (2015) 283-288.
- [242] Y. Xia, Y. Jiang, F. Li, M. Xia, B. Xue, Y. Li, Appl. Surf. Sci. 289 (2014) 306-315.
- [243] S. Wang, S. Zhou, J. Hazard. Mater. 185 (2011) 77-85.
- [244] G.S. Shao, F.Y. Wang, T.Z. Ren, Y. Liu, Z.Y. Yuan, Appl. Catal. B 92 (2009) 61-67.
- [245] C. Jin, R.Y. Zheng, Y. Guo, J.L. Xie, Y.X. Zhu, Y.C. Xie, J. Mol. Catal. A Chem. 313 (2009) 44-48.
- [246] E.M. Samsudin, S.B.A. Hamid, J.C. Juan, W.J. Basirun, G. Centi, Appl. Surf. Sci. 370 (2016) 380-393.
- [247] E.M. Samsudin, S.B.A. Hamid, J.C. Juan, W.J. Basirun, A.E. Kandjani, S.K. Bhargava, Appl. Surf. Sci. 365 (2016) 57-68.
- [248] J.K. Zhou, L. Lv, J. Yu, H.L. Li, P.-Z. Guo, H. Sun, X. Zhao, J. Phys. Chem. C 112 (2008) 5316-5321.
- [249] G. Veréb, L. Manczinger, A. Oszkó, A. Sienkiewicz, L. Forró, K. Mogyorósi, A. Dombi, K. Hernádi, Appl. Catal. B 129 (2013) 194-201.
- [250] G. Liu, C. Sun, X. Yan, L. Cheng, Z. Chen, X. Wang, L. Wang, S.C. Smith, G.Q.M. Lu, H.-M. Cheng, J. Mater. Chem. 19 (2009) 2822-2829.
- [251] Q. Zhang, Y. Li, E.A. Ackerman, M. Gajdardziska-Josifovska, H. Li, Appl. Catal. A-Gen. 400 (2011) 195-202.
- [252] N. Lu, X. Quan, J. Li, S. Chen, H. Yu, G. Chen, J. Phys. Chem. C 111 (2007) 11836-11842.
- [253] I.-C. Kang, Q. Zhang, J. Kano, S. Yin, T. Sato, F. Saito, J. Photochem. Photobiol. A 189 (2007) 232-238.
- [254] X. Tang, D. Li, J. Phys. Chem. C 112 (2008) 5405-5409.
- [255] C. Yang, Z. Wang, T. Lin, H. Yin, X. Lü, D. Wan, T. Xu, C. Zheng, J. Lin, F. Huang, J. Am. Chem. Soc. 135 (2013) 17831-17838.
- [256] Y. Su, X. Zhang, S. Han, X. Chen, L. Lei, Inorg. Chem. 9 (2007) 2291-2298.
- [257] M.H. Kim, J.M. Baik, J. Zhang, C. Larson, Y. Li, G.D. Stucky, M. Moskovits, A.M. Wodtke, J. Phys. Chem. C 114 (2010) 10697-10702.
- [258] P. Carmichael, D. Hazafy, D.S. Bhachu, A. Mills, J.A. Darr, I.P. Parkin, Phys. Chem. Chem. Phys. 15 (2013) 16788-16794.
- [259] M. Quesada-González, N.D. Boscher, C.J. Carmalt, I.P. Parkin, ACS Appl. Mater. Interfaces 8 (2016) 25024-25029.
- [260] C. Sotelo-Vazquez, N. Noor, A. Kafizas, R. Quesada-Cabrera, D.O. Scanlon, A. Taylor, J.R. Durrant, I.P. Parkin, Chem. Mater. 27 (2015) 3234-3242.
- [261] Y. Suda, H. Kawasaki, T. Ueda, T. Ohshima, Thin solid films 453 (2004) 162-166.
- [262] T. Lindgren, J.M. Mwabora, E. Avendaño, J. Jonsson, A. Hoel, C.-G. Granqvist, S.-E. Lindquist, J. Phys. Chem. B 107 (2003) 5709-5716.
- [263] S.-Z. Chen, P.-Y. Zhang, D.-M. Zhuang, W.-P. Zhu, Catal. Commun. 5 (2004) 677-680.
- [264] Y. Suda, H. Kawasaki, T. Ueda, T. Ohshima, Thin solid films 475 (2005) 337-341.
- [265] I. Ruzybayev, S.I. Shah, Surf. Coat. Technol. 241 (2014) 148-153.
- [266] Y.-P. Peng, E. Yassitepe, Y.-T. Yeh, I. Ruzybayev, S.I. Shah, C. Huang, Appl. Catal. B 125 (2012) 465-472.
- [267] T. Umebayashi, T. Yamaki, S. Tanaka, K. Asai, Chem. Lett. 32 (2003) 330-331.
- [268] M. Sathish, B. Viswanathan, R. Viswanath, Appl. Catal. B 74 (2007) 307-312.
- [269] X. Chen, P.-A. Glans, X. Qiu, S. Dayal, W.D. Jennings, K.E. Smith, C. Burda, J. Guo, J. Electron Spectros. Relat. Phenomena 162 (2008) 67-73.
- [270] M. Shen, Z. Wu, H. Huang, Y. Du, Z. Zou, P. Yang, Mater. Lett. 60 (2006) 693-697.
- [271] X. Cui, H. Gu, J. Lu, J. Shen, Z. Zhang, J. Nanosci. Nanotechnol. 7 (2007) 3140-3145.
- [272] C. Yang, X. Zhang, J. Qin, X. Shen, R. Yu, M. Ma, R. Liu, J. Catal. 347 (2017) 36-44.
- [273] H. Rasoulnezhad, G. Kavei, K. Ahmadi, M.R. Rahimipour, Appl. Surf. Sci. 408 (2017) 1-10.
- [274] S. Liu, L. Yang, S. Xu, S. Luo, Q. Cai, Inorg. Chem. 11 (2009) 1748-1751.
- [275] C. Sarantopoulos, A.N. Gleizes, F. Maury, Thin solid films 518 (2009) 1299-1303.
- [276] K. Prabakar, T. Takahashi, T. Nezuka, K. Takahashi, T. Nakashima, Y. Kubota, A. Fujishima, Renew. Energy 33 (2008) 277-281.
- [277] Y. Wang, C. Feng, M. Zhang, J. Yang, Z. Zhang, Appl. Catal. B 104 (2011) 268-274.
- [278] S. Hu, F. Li, Z. Fan, J. Hazard. Mater. 196 (2011) 248-254.
- [279] L. Mi, P. Xu, P.-N. Wang, Appl. Surf. Sci. 255 (2008) 2574-2580.
- [280] A. Kachina, E. Puzenat, S. Ould-Chikh, C. Geantet, P. Delichere, P. Afanasiev, Chem. Mater. 24 (2012) 636-642.
- [281] Y.K. Kim, S. Park, K.-J. Kim, B. Kim, J. Phys. Chem. C 115 (2011) 18618-18624.
- [282] P.-S. Yap, T.-T. Lim, M. Lim, M. Srinivasan, Catal. Today 151 (2010) 8-13.
- [283] J. Yuan, M. Chen, J. Shi, W. Shangguan, Int. J. Hydrog. Energy 31 (2006) 1326-1331.
- [284] D. Mitoraj, H. Kisch, Chem. Eur. J. 16 (2010) 261-269.

Introduction

- [285] M. Maeda, T. Watanabe, *J. Electrochem. Soc.* 153 (2006) C186-C189.
- [286] O. Diwald, T.L. Thompson, T. Zubkov, E.G. Goralski, S.D. Walck, J.T. Yates, *J. Phys. Chem. B* 108 (2004) 6004-6008.
- [287] F.-D. Duminica, F. Maury, R. Hausbrand, *Surf. Coat. Technol.* 201 (2007) 9349-9353.
- [288] Y. Guo, X.-w. Zhang, W.-H. Weng, G.-r. Han, *Thin solid films* 515 (2007) 7117-7121.
- [289] C.W. Dunnill, Z.A. Aiken, J. Pratten, M. Wilson, D.J. Morgan, I.P. Parkin, *J. Photochem. Photobiol. A* 207 (2009) 244-253.
- [290] C.W. Dunnill, I.P. Parkin, *Chem. Vap. Depos.* 15 (2009) 171-174.
- [291] S. Peng, Y. Yang, G. Li, J. Jiang, K. Jin, T. Yao, K. Zhang, X. Cao, Y. Wang, G. Xu, *J. Alloys Compd.* 678 (2016) 355-359.
- [292] M. Baker, H. Fakhouri, R. Grilli, J. Pulpitel, W. Smith, F. Arefi-Khonsari, *Thin solid films* 552 (2014) 10-17.
- [293] B. Liu, L. Wen, X. Zhao, *Sol. Energy Mater. Sol.* 92 (2008) 1-10.
- [294] J.M. Mwabora, T. Lindgren, E. Avendaño, T.F. Jaramillo, J. Lu, S.-E. Lindquist, C.-G. Granqvist, *J. Phys. Chem. B* 108 (2004) 20193-20198.
- [295] M.-H. Chan, F.-H. Lu, *Thin solid films* 518 (2009) 1369-1372.
- [296] H. Fakhouri, J. Pulpitel, W. Smith, A. Zolfaghari, H.R. Mortaheb, F. Meshkini, R. Jafari, E. Sutter, F. Arefi-Khonsari, *Appl. Catal. B* 144 (2014) 12-21.
- [297] G. Abadias, F. Paumier, D. Eyidi, P. Guerin, T. Girardeau, *Surf. Interface Anal.* 42 (2010) 970-973.
- [298] Y.-P. Peng, Y.-T. Yeh, S.I. Shah, C. Huang, *Appl. Catal. B* 123 (2012) 414-423.
- [299] J. Cao, Y. Zhang, H. Tong, P. Li, T. Kako, J. Ye, *ChemComm.* 48 (2012) 8649-8651.
- [300] L. Zhao, Q. Jiang, J. Lian, *Appl. Surf. Sci.* 254 (2008) 4620-4625.
- [301] G. Sauthier, F. Ferrer, A. Figueras, E. György, *Thin solid films* 519 (2010) 1464-1469.
- [302] R. Hahn, A. Ghicov, J. Salonen, V.-P. Lehto, P. Schmuki, *Nanotechnology* 18 (2007) 105604.
- [303] B. Neumann, P. Bogdanoff, H. Tributsch, S. Sakthivel, H. Kisch, *J. Phys. Chem. B* 109 (2005) 16579-16586.
- [304] R. Hahn, F. Schmidt-Stein, J. Salonen, S. Thiemann, Y. Song, J. Kunze, V.P. Lehto, P. Schmuki, *Angew. Chem. Int. Ed.* 48 (2009) 7236-7239.
- [305] Y. Zhao, Y. Li, C.-W. Wang, J. Wang, X.-Q. Wang, Z.-W. Pan, C. Dong, F. Zhou, *Solid State Sci.* 15 (2013) 53-59.
- [306] X. Hu, T. Zhang, Z. Jin, J. Zhang, W. Xu, J. Yan, J. Zhang, L. Zhang, Y. Wu, *Mater. Lett.* 62 (2008) 4579-4581.
- [307] N. Kılınç, E. Şennik, M. Işık, A.Ş. Ahsen, O. Öztürk, Z.Z. Öztürk, *Ceram. Int.* 40 (2014) 109-115.
- [308] G. Socol, Y. Gnatyuk, N. Stefan, N. Smirnova, V. Djokić, C. Sutan, V. Malinovschi, A. Stanculescu, O. Korduban, I. Mihailescu, *Thin solid films* 518 (2010) 4648-4653.
- [309] I. Ruzybayev, E. Yassitepe, A. Ali, A. Bhatti, R.M. Mohamed, M. Islam, S.I. Shah, *Mater. Sci. Semicond. Process.* 39 (2015) 371-376.
- [310] Y. Xie, X. Zhao, H. Tao, Q. Zhao, B. Liu, Q. Yuan, *Chem. Phys. Lett.* 457 (2008) 148-153.
- [311] H. Irie, S. Washizuka, K. Hashimoto, *Thin solid films* 510 (2006) 21-25.
- [312] M.-S. Wong, S.-H. Wang, T.-K. Chen, C.-W. Weng, K.K. Rao, *Surf. Coat. Technol.* 202 (2007) 890-894.
- [313] J. Yuan, H. Li, S. Gao, D. Sang, L. Li, D. Lu, *Mater. Lett.* 64 (2010) 2012-2015.
- [314] J. Sung, M. Shin, P. Deshmukh, H.S. Hyun, Y. Sohn, W.G. Shin, *J. Alloys Compd.* 767 (2018) 924-931.
- [315] Y. Su, S. Han, X. Zhang, X. Chen, L. Lei, *Mater. Chem. Phys.* 110 (2008) 239-246.
- [316] S.-J. Shen, T.-S. Yang, M.-S. Wong, *Surf. Coat. Technol.* 303 (2016) 184-190.
- [317] M. Harb, P. Sautet, P. Raybaud, *J. Phys. Chem. C* 117 (2013) 8892-8902.
- [318] J. Ni, S. Fu, C. Wu, J. Maier, Y. Yu, L. Li, *Adv. Mater.* 28 (2016) 2259-2265.
- [319] V. Bessergenev, M.d.C. Mateus, D. Vasconcelos, J. Mariano, A. Botelho do Rego, R. Lange, E. Burkel, *Int. J. Photoenergy* 2012 (2012).
- [320] C.W. Dunnill, Z.A. Aiken, J. Pratten, M. Wilson, I.P. Parkin, *Chem. Vap. Depos.* 16 (2010) 50-54.
- [321] V. Bessergenev, R. Pereira, M. Mateus, I. Khmelinskii, D. Vasconcelos, R. Nicula, E. Burkel, A.B. Do Rego, A. Saprykin, *Thin solid films* 503 (2006) 29-39.
- [322] S. Yamamoto, A. Takeyama, M. Yoshikawa, *Nucl. Instrum. Methods Phys. Res., B* 242 (2006) 377-379.
- [323] X. Chen, X. Zhang, Y. Su, L. Lei, *Appl. Surf. Sci.* 254 (2008) 6693-6696.
- [324] A. Sobczyk-Guzenda, S. Owczarek, A. Wojciechowska, D. Batory, M. Fijalkowski, M. Gazicki-Lipman, *Thin solid films* 650 (2018) 78-87.
- [325] S.R. Kurtz, R.G. Gordon, *Thin solid films* 147 (1987) 167-176.
- [326] P. Roy, S. Berger, P. Schmuki, *Angew. Chem. Int. Ed.* 50 (2011) 2904-2939.
- [327] Y.C. Nah, I. Paramasivam, P. Schmuki, *ChemPhysChem*, 11 (2010) 2698-2713.
- [328] S. Hu, F. Li, Z. Fan, J. Gui, *J. Power Sources* 250 (2014) 30-39.
- [329] H. Liu, Z. Fan, C. Sun, S. Yu, S. Feng, W. Chen, D. Chen, C. Tang, F. Gao, L. Dong, *Appl. Catal. B* 244 (2019) 671-683.

Introduction

- [330] R. Trejo-Tzab, J. Alvarado-Gil, P. Quintana, P. Bartolo-Pérez, *Catal. Today* 193 (2012) 179-185.
- [331] P. Mazierski, M. Nischk, M. Gołkowska, W. Lisowski, M. Gazda, M.J. Winiarski, T. Klimczuk, A. Zaleska-Medynska, *Appl. Catal. B* 196 (2016) 77-88.
- [332] J. Georgieva, E. Valova, S. Artyanov, D. Tatchev, S. Sotiropoulos, I. Avramova, N. Dimitrova, A. Hubin, O. Steenhaut, *Appl. Surf. Sci.* 413 (2017) 284-291.
- [333] M. Favaro, S. Leonardi, C. Valero-Vidal, S. Nappini, M. Hanzlik, S. Agnoli, J. Kunze-Liebhäuser, G. Granozzi, *Adv. Mater. Interfaces* 2 (2015) 1400462.
- [334] L. Hu, K. Huo, R. Chen, B. Gao, J. Fu, P.K. Chu, *Anal. Chem.* 83 (2011) 8138-8144.
- [335] Y. Mizukoshi, N. Ohtsu, S. Semboshi, N. Masahashi, *Appl. Catal. B* 91 (2009) 152-156.
- [336] A. Ghicov, J.M. Macak, H. Tsuchiya, J. Kunze, V. Haeublein, L. Frey, P. Schmuki, *Nano Lett.* 6 (2006) 1080-1082.
- [337] X. Song, W. Li, D. He, H. Wu, Z. Ke, C. Jiang, G. Wang, X. Xiao, *Adv. Energy Mater.* 8 (2018) 1800165.
- [338] N. Masahashi, M. Oku, *Appl. Surf. Sci.* 254 (2008) 7056-7060.
- [339] T. Umebayashi, T. Yamaki, S. Yamamoto, A. Miyashita, S. Tanaka, T. Sumita, K. Asai, *J. Appl. Phys.* 93 (2003) 5156-5160.
- [340] C. Chen, H. Bai, C. Chang, *J. Phys. Chem. C* 111 (2007) 15228-15235.
- [341] X. Liu, Z. Liu, J. Zheng, X. Yan, D. Li, S. Chen, W. Chu, *J. Alloys Compd.* 509 (2011) 9970-9976.
- [342] D.J. Pulsipher, I.T. Martin, E.R. Fisher, *ACS Appl. Mater. Interfaces* 2 (2010) 1743-1753.
- [343] T. Sreethawong, S. Laehslee, S. Chavadej, *Catal. Commun.* 10 (2009) 538-543.
- [344] R. Sasikala, A. Shirole, V. Sudarsan, C. Sudakar, R. Naik, R. Rao, S. Bharadwaj, *Appl. Catal. A-Gen.* 377 (2010) 47-54.
- [345] H. Wu, Z. Zhang, *Int. J. Hydrog. Energy* 36 (2011) 13481-13487.
- [346] M.-C. Wu, J. Hiltunen, A.s. Sápi, A. Avila, W. Larsson, H.-C. Liao, M. Huuhtanen, G.z. Tóth, A. Shchukarev, N.m. Laufer, *Acs Nano* 5 (2011) 5025-5030.
- [347] Q. Xiang, J. Yu, W. Wang, M. Jaroniec, *ChemComm.* 47 (2011) 6906-6908.
- [348] V.J. Babu, M.K. Kumar, A.S. Nair, T.L. Kheng, S.I. Allakhverdiev, S. Ramakrishna, *Int. J. Hydrog. Energy* 37 (2012) 8897-8904.
- [349] F. Pei, Y. Liu, S. Xu, J. Lü, C. Wang, S. Cao, *Int. J. Hydrog. Energy* 38 (2013) 2670-2677.
- [350] C. Wang, Q.-Q. Hu, J.-Q. Huang, Z.-H. Deng, H.-L. Shi, L. Wu, Z.-G. Liu, Y.-G. Cao, *Int. J. Hydrog. Energy* 39 (2014) 1967-1971.
- [351] B. Naik, S.M. Kim, C.H. Jung, S.Y. Moon, S.H. Kim, J.Y. Park, *Adv. Mater. Interfaces* 1 (2014) 1300018.
- [352] S. Sun, P. Gao, Y. Yang, P. Yang, Y. Chen, Y. Wang, *ACS Appl. Mater. Interfaces* 8 (2016) 18126-18131.
- [353] K.K. Mandari, A.K.R. Police, J.Y. Do, M. Kang, C. Byon, *Int. J. Hydrog. Energy* 43 (2018) 2073-2082.
- [354] H.J. Yun, H. Lee, N.D. Kim, D.M. Lee, S. Yu, J. Yi, *ACS nano* 5 (2011) 4084-4090.
- [355] G. Jia, Y. Wang, X. Cui, W. Zheng, *ACS Sustain. Chem. Eng.* 6 (2018) 13480-13486.
- [356] C. Yang, J. Qin, Z. Xue, M. Ma, X. Zhang, R. Liu, *Nano Energy*, 41 (2017) 1-9.
- [357] S.-H. Liu, H.-R. Syu, *Int. J. Hydrog. Energy* 38 (2013) 13856-13865.
- [358] R.J. Ramalingam, A. Kannan, *Int. J. Hydrog. Energy* 38 (2013) 13572-13578.
- [359] W. Zhang, S. Wang, J. Li, X. Yang, *Catal. Commun.* 59 (2015) 189-194.
- [360] W. Yuan, L. Cheng, Y. An, S. Lv, H. Wu, X. Fan, Y. Zhang, X. Guo, J. Tang, *Adv. Sci.* 5 (2018) 1700870.
- [361] S. Martha, D. Das, N. Biswal, K. Parida, *J. Mater. Chem.* 22 (2012) 10695-10703.
- [362] J. Tang, H. Quan, J. Ye, *Chem. Mater.* 19 (2007) 116-122.
- [363] G.L. Chiarello, M.V. Dozzi, M. Scavini, J.-D. Grunwaldt, E. Sell, *Appl. Catal. B* 160 (2014) 144-151.
- [364] C. Burda, Y. Lou, X. Chen, A.C. Samia, J. Stout, J.L. Gole, *Nano Lett.* 3 (2003) 1049-1051.
- [365] A. Samokhvalov, *Renew. Sust. Energ. Rev.* 72 (2017) 981-1000.
- [366] C. Di Valentin, G. Pacchioni, A. Selloni, *Phys. Rev. B* 70 (2004) 085116.
- [367] F. Napoli, M. Chiesa, S. Livraghi, E. Giannello, S. Agnoli, G. Granozzi, G. Pacchioni, C. Di Valentin, *Chem. Phys. Lett.* 477 (2009) 135-138.
- [368] S.P. Albu, A. Ghicov, S. Aldabergenova, P. Drechsel, D. LeClere, G.E. Thompson, J.M. Macak, P. Schmuki, *Adv. Mater.* 20 (2008) 4135-4139.
- [369] Y. Ji, K.-C. Lin, H. Zheng, J.-j. Zhu, A.C.S. Samia, *Inorg. Chem.* 13 (2011) 1013-1015.
- [370] N. Wang, Z. Bai, Y. Qian, J. Yang, *Adv. Mater.* 28 (2016) 4126-4133.
- [371] A. Vittadini, A. Selloni, F. Rotzinger, M. Grätzel, *Phys. Rev. Lett.* 81 (1998) 2954.
- [372] H.G. Yang, G. Liu, S.Z. Qiao, C.H. Sun, Y.G. Jin, S.C. Smith, J. Zou, H.M. Cheng, G.Q. Lu, *J. Am. Chem. Soc.* 131 (2009) 4078-4083.
- [373] C. Li, C. Koenigsmann, W. Ding, B. Rudshteyn, K.R. Yang, K.P. Regan, S.J. Konezny, V.S. Batista, G.W. Brudvig, C.A. Schmuttenmaer, *J. Am. Chem. Soc.* 137 (2015) 1520-1529.
- [374] C. Jin, B. Liu, Z. Lei, J. Sun, *Nanoscale Res. Lett.* 10 (2015) 95.
- [375] X. Wang, Y. Li, X. Liu, S. Gao, B. Huang, Y. Dai, *Chinese J. Catal.* 36 (2015) 389-399.
- [376] M.-Y. Xing, W.-K. Li, Y.-M. Wu, J.-L. Zhang, X.-Q. Gong, *J. Phys. Chem. C* 115 (2011) 7858-7865.

Introduction

- [377] C. Sun, D.J. Searles, *J. Phys. Chem. C* 117 (2013) 26454-26459.
- [378] V. Jaiswal, S. Umrao, R.B. Rastogi, R. Kumar, A. Srivastava, *ACS Appl. Mater. Interfaces* 8 (2016) 11698-11710.
- [379] A. Czoska, S. Livraghi, M.C. Paganini, E. Giamello, C. Di Valentin, G. Pacchioni, *Phys. Chem. Chem. Phys.* 13 (2011) 136-143.
- [380] G. Liu, L.-C. Yin, J. Wang, P. Niu, C. Zhen, Y. Xie, H.-M. Cheng, *Energy Environ. Sci.* 5 (2012) 9603-9610.
- [381] S. Cravanzola, F. Cesano, F. Gaziano, D. Scarano, *Catalysts* 7 (2017) 214.
- [382] M. Zhu, C. Zhai, L. Qiu, C. Lu, A.S. Paton, Y. Du, M.C. Goh, *ACS Sustain. Chem. Eng.* 3 (2015) 3123-3129.
- [383] A. Czoska, S. Livraghi, M. Chiesa, E. Giamello, S. Agnoli, G. Granozzi, E. Finazzi, C.D. Valentin, G. Pacchioni, *J. Phys. Chem. C* 112 (2008) 8951-8956.
- [384] H. Xu, S. Ouyang, L. Liu, P. Reunchan, N. Umezawa, J. Ye, *J. Mater. Chem. A* 2 (2014) 12642-12661.
- [385] J. Tao, T. Luttrell, M. Batzill, *Nat. Chem.* 3 (2011) 296.
- [386] R. Zheng, L. Lin, J. Xie, Y. Zhu, Y. Xie, *J. Phys. Chem. C* 112 (2008) 15502-15509.
- [387] S.P. Madhusudanan, B. Gangaja, A.G. Shyla, A.S. Nair, S.V. Nair, D. Santhanagopalan, *ACS Sustain. Chem. Eng.* 5 (2017) 2393-2399.
- [388] D.-D. Qin, X.-H. Wang, Y. Li, J. Gu, X.-M. Ning, J. Chen, X.-Q. Lu, C.-L. Tao, *J. Phys. Chem. C* 120 (2016) 22195-22201.
- [389] R.D. Shannon, *Acta Crystallogr. A* 32 (1976) 751-767.
- [390] C. Yu, Q. Fan, Y. Xie, J. Chen, C.Y. Jimmy, *J. Hazard. Mater.* 237 (2012) 38-45.
- [391] S. Yang, S. Guo, D. Xu, H. Xue, H. Kou, J. Wang, G. Zhu, *J. Fluor. Chem.* 150 (2013) 78-84.
- [392] J. Song, H.B. Yang, X. Wang, S.Y. Khoo, C. Wong, X.-W. Liu, C.M. Li, *ACS Appl. Mater. Interfaces* 4 (2012) 3712-3717.
- [393] J.-L. Song, X. Wang, C. Wong, *Electrochim. Acta* 173 (2015) 834-838.
- [394] Q. Hou, Y. Zheng, J.-F. Chen, W. Zhou, J. Deng, X. Tao, *J. Mater. Chem.* 21 (2011) 3877-3883.
- [395] S. Yang, H. Xue, H. Wang, H. Kou, J. Wang, G. Zhu, *J. Phys. Chem. Solids* 73 (2012) 911-916.
- [396] D. Li, H. Haneda, S. Hishita, N. Ohashi, N.K. Labhsetwar, *J. Fluor. Chem.* 126 (2005) 69-77.
- [397] S. Sakthivel, H. Kisch, *Angew. Chem. Int. Ed.* 42 (2003) 4908-4911.
- [398] C. Di Valentin, G. Pacchioni, A. Selloni, *Chem. Mater.* 17 (2005) 6656-6665.
- [399] L. Zhao, X. Chen, X. Wang, Y. Zhang, W. Wei, Y. Sun, M. Antonietti, M.M. Titirici, *Adv. Mater.* 22 (2010) 3317-3321.
- [400] S. Lee, Y. Lee, D.H. Kim, J.H. Moon, *ACS Appl. Mater. Interfaces* 5 (2013) 12526-12532.
- [401] L. Ji, Y. Zhang, S. Miao, M. Gong, X. Liu, *Carbon* 125 (2017) 544-550.
- [402] S. Xu, X. Sun, Y. Zhao, Y. Gao, Y. Wang, Q. Yue, B. Gao, *Appl. Surf. Sci.* 448 (2018) 78-87.
- [403] C. Cheng, Y. Sun, *Appl. Surf. Sci.* 263 (2012) 273-276.
- [404] S. Liu, N. Zhang, Z.-R. Tang, Y.-J. Xu, *ACS Appl. Mater. Interfaces* 4 (2012) 6378-6385.
- [405] W. Jiang, M. Zhang, J. Wang, Y. Liu, Y. Zhu, *Appl. Catal. B* 160 (2014) 44-50.
- [406] S. Ullah, E.P. Ferreira-Neto, A.A. Pasa, C.C. Alcántara, J.J. Acuna, S.A. Bilmes, M.L.M. Ricci, R. Landers, T.Z. Fermino, U.P. Rodrigues-Filho, *Appl. Catal. B* 179 (2015) 333-343.
- [407] T.A. Gad-Allah, K. Fujimura, S. Kato, S. Satokawa, T. Kojima, *J. Hazard. Mater.* 154 (2008) 572-577.
- [408] Z. Zhang, Y. Zhou, Y. Zhang, X. Sheng, S. Zhou, S. Xiang, *Appl. Surf. Sci.* 286 (2013) 344-350.
- [409] M. Inagaki, Y. Hirose, T. Matsunaga, T. Tsumura, M. Toyoda, *Carbon*, 41 (2003) 2619-2624.
- [410] T. Tsumura, N. Kojitani, I. Izumi, N. Iwashita, M. Toyoda, M. Inagaki, *J. Mater. Chem.* 12 (2002) 1391-1396.
- [411] J. Zhang, Z.-h. Huang, X. Yong, F.-y. Kang, *New Carbon Mater.* 26 (2011) 63-70.
- [412] T. Xia, W. Zhang, Z. Wang, Y. Zhang, X. Song, J. Murowchick, V. Battaglia, G. Liu, X. Chen, *Nano Energy* 6 (2014) 109-118.
- [413] I. Sargin, G. Yanalak, G. Arslan, I.H. Patir, *Int. J. Hydrog. Energy* 44 (2019) 21781-21789.
- [414] P. Zhang, C. Shao, Z. Zhang, M. Zhang, J. Mu, Z. Guo, Y. Liu, *Nanoscale* 3 (2011) 2943-2949.
- [415] M. Inagaki, F. Kojin, B. Tryba, M. Toyoda, *Carbon* 43 (2005) 1652-1659.
- [416] F. Liu, N. Feng, L. Yang, Q. Wang, J. Xu, F. Deng, *J. Phys. Chem. C* 122 (2018) 10948-10955.
- [417] S. Chen, X. Li, W. Zhou, S. Zhang, Y. Fang, *Appl. Surf. Sci.* 466 (2019) 254-261.
- [418] X. Zhu, S. Shen, Z. Tang, J. Yang, *Compos. Interfaces* (2019).
- [419] Y. Guo, X. Kong, Z. Liang, Y. Xue, H. Cui, J. Tian, *J. Colloid Interface Sci.* (2020).
- [420] F. Jia, Z. Yao, Z. Jiang, C. Li, *Catal. Commun.* 12 (2011) 497-501.
- [421] Y. Surendranath, M. Dinca, D.G. Nocera, *J. Am. Chem. Soc.* 131 (2009) 2615-2620.
- [422] D.K. Bediako, C. Costentin, E.C. Jones, D.G. Nocera, J.-M. Savéant, *J. Am. Chem. Soc.* 135 (2013) 10492-10502.
- [423] C. Ding, J. Shi, D. Wang, Z. Wang, N. Wang, G. Liu, F. Xiong, C. Li, *Phys. Chem. Chem. Phys.* 15 (2013) 4589-4595.

Introduction

- [424] K. Kajii, T. Ohsaka, F. Kitamura, Inorg. Chem. 12 (2010) 970-972.
- [425] D. Strmcnik, D. Van Der Vliet, K.-C. Chang, V. Komanicky, K. Kodama, H. You, V. Stamenkovic, N. Markovic, The Journal of Physical Chem. Lett. 2 (2011) 2733-2736.
- [426] D. Strmcnik, K. Kodama, D. Van der Vliet, J. Greeley, V.R. Stamenkovic, N. Marković, Nat. Chem. 1 (2009) 466.
- [427] M.J. Kenney, M. Gong, Y. Li, J.Z. Wu, J. Feng, M. Lanza, H. Dai, Science 342 (2013) 836-840.
- [428] C. Ding, X. Zhou, J. Shi, P. Yan, Z. Wang, G. Liu, C. Li, J. Phys. Chem. B 119 (2015) 3560-3566.
- [429] G. Zhang, W. Zhang, D. Minakata, Y. Chen, J. Crittenden, P. Wang, Int. J. Hydrol. Energy 38 (2013) 11727-11736.
- [430] J. Nelson, The physics of solar cells, World Scientific Publishing Company, 2003.
- [431] K. O'Donnell, X. Chen, Appl. Phys. Lett. 58 (1991) 2924-2926.
- [432] L. Andrade, T. Lopes, A. Mendes, Energy Procedia 22 (2012) 23-34.
- [433] P. Dias, T. Lopes, L. Meda, L. Andrade, A. Mendes, Phys. Chem. Chem. Phys. 18 (2016) 5232-5243.
- [434] S.-C. Moon, H. Mametsuka, S. Tabata, E. Suzuki, Catal. Today 58 (2000) 125-132.
- [435] X. Chen, S. Shen, L. Guo, S.S. Mao, Chem. Rev. 110 (2010) 6503-6570.
- [436] C. Ding, J. Shi, Z. Wang, C. Li, ACS Catal. 7 (2016) 675-688.
- [437] K. Maeda, K. Domen, J. Phys. Chem. C 111 (2007) 7851-7861.
- [438] M. Zalas, M. Laniecki, Sol. Energy Mater. Sol. 89 (2005) 287-296.
- [439] B. Zielińska, E. Borowiak-Palen, R.J. Kalenczuk, Int. J. Hydrol. Energy 33 (2008) 1797-1802.
- [440] Z. Haider, Y.S. Kang, ACS Appl. Mater. Interfaces 6 (2014) 10342-10352.
- [441] N.R. Reddy, M.M. Kumari, K. Cheralathan, M. Shankar, Int. J. Hydrol. Energy 43 (2018) 4036-4043.
- [442] M. Tahir, Int. J. Hydrol. Energy 44 (2019) 3711-3725.
- [443] G.K. Naik, S.M. Majhi, K.-U. Jeong, I.-H. Lee, Y.T. Yu, J. Alloys Compd. 771 (2019) 505-512.
- [444] A. Galińska, J. Walendziewski, Energy Fuels 19 (2005) 1143-1147.
- [445] A.S. Hainer, J.S. Hodgins, V. Sandre, M. Vallieres, A.E. Lanterna, J.C. Scaiano, ACS Energy Lett. 3 (2018) 542-545.
- [446] Q. Zhang, D.D. Zheng, L.S. Xu, C.-T. Chang, Catal. Today 274 (2016) 8-14.
- [447] M. Yasuda, T. Matsumoto, T. Yamashita, Renew. Sust. Energ. Rev. 81 (2018) 1627-1635.
- [448] P. Chowdhury, G. Malekshoar, M.B. Ray, J. Zhu, A.K. Ray, Ind. Eng. Chem. Res. 52 (2013) 5023-5029.
- [449] E.P. Melián, O.G. Díaz, A.O. Méndez, C.R. López, M.N. Suárez, J.D. Rodríguez, J. Navío, D.F. Hevia, J.P. Peña, Int. J. Hydrol. Energy 38 (2013) 2144-2155.
- [450] W. Sun, S. Zhang, Z. Liu, C. Wang, Z. Mao, Int. J. Hydrol. Energy 33 (2008) 1112-1117.
- [451] C.R. López, E.P. Melián, J.O. Méndez, D.E. Santiago, J.D. Rodríguez, O.G. Díaz, J. Photochem. Photobiol. A 312 (2015) 45-54.
- [452] C. Zhou, Z. Ren, S. Tan, Z. Ma, X. Mao, D. Dai, H. Fan, X. Yang, J. LaRue, R. Cooper, Chem. Sci. 1 (2010) 575-580.
- [453] T. Kawai, T. Sakata, Journal of the Chemical Society, ChemComm. (1980) 694-695.
- [454] W.-C. Lin, W.-D. Yang, I.-L. Huang, T.-S. Wu, Z.-J. Chung, Energy Fuels 23 (2009) 2192-2196.
- [455] J. Hensel, G. Wang, Y. Li, J.Z. Zhang, Nano Lett. 10 (2010) 478-483.
- [456] J.S. Jang, S.M. Ji, S.W. Bae, H.C. Son, J.S. Lee, J. Photochem. Photobiol. A 188 (2007) 112-119.
- [457] J.S. Jang, U.A. Joshi, J.S. Lee, J. Phys. Chem. C 111 (2007) 13280-13287.
- [458] J. Zhang, Y. Wang, J. Zhang, Z. Lin, F. Huang, J. Yu, ACS Appl. Mater. Interfaces 5 (2013) 1031-1037.
- [459] L. Wang, W. Wang, Y. Chen, L. Yao, X. Zhao, H. Shi, M. Cao, Y. Liang, ACS Appl. Mater. Interfaces 10 (2018) 11652-11662.
- [460] C.Y. Toe, Z. Zheng, H. Wu, J. Scott, R. Amal, Y.H. Ng, J. Phys. Chem. C 122 (2018) 14072-14081.
- [461] J. Jia, Q. Zhang, Z. Li, X. Hu, E. Liu, J. Fan, J. Mater. Chem. A (2019).
- [462] Y. Sasaki, A. Iwase, H. Kato, A. Kudo, J. Catal. 259 (2008) 133-137.
- [463] S.W. Bae, S.M. Ji, S.J. Hong, J.W. Jang, J.S. Lee, Int. J. Hydrol. Energy 34 (2009) 3243-3249.
- [464] Y. Sano, A. Onoda, T. Hayashi, ChemComm. 47 (2011) 8229-8231.
- [465] E.A. Kozlova, T.P. Korobkina, A.V. Vorontsov, V.N. Parmon, Appl. Catal. A-Gen. 367 (2009) 130-137.
- [466] S.G. Lee, S. Lee, H.-I. Lee, Appl. Catal. A-Gen. 207 (2001) 173-181.
- [467] T. Inoue, T. Watanabe, A. Fujishima, K.i. Honda, K. Kohayakawa, J. Electrochem. Soc. 124 (1977) 719-722.
- [468] N. Keriche, A. Bouguelia, M. Trari, Int. J. Hydrol. Energy 31 (2006) 1196-1203.
- [469] S. Shen, L. Guo, X. Chen, F. Ren, S.S. Mao, Int. J. Hydrol. Energy 35 (2010) 7110-7115.
- [470] Q. Wang, J. Lian, Q. Ma, S. Zhang, J. He, J. Zhong, J. Li, H. Huang, B. Su, Catal. Today 281 (2017) 662-668.
- [471] S.R. Morrison, Electrochemistry at semiconductor and oxidized metal electrodes, United States: N. p., 1980. Web.
- [472] A.J. Bard, A.B. Bocarsly, F.R.F. Fan, E.G. Walton, M.S. Wrighton, J. Am. Chem. Soc. 102 (1980) 3671-

Introduction

3677.

[473] N.S. Lewis, Inorg. Chem. 44 (2005) 6900-6911.

[474] M. Grätzel, Nature 414 (2001) 338.

CHAPTER 2.

Objectives and Scientific Strategy

2.1 Objectives

Considerable research work has been devoted to enhance the efficiency of photocatalytic / photoelectrochemical water splitting for hydrogen production over photocatalysts based on metal oxides semiconductors. [1-3] TiO₂ is one of the most important and promising photocatalyst due to its excellent photocatalytic efficiency, long-term chemical stability, low cost and nontoxicity. [4-6] However, TiO₂ with a broad bandgap is only activated under ultraviolet (UV) light, which means only 3%-5% of the incoming solar energy on the earth's surface can be utilized by pure TiO₂. [7, 8] Therefore, considerable efforts have been made to extend its optical absorption into visible light region. [9-11] Both carbon doping and coating are independently employed to activate the visible-light response of TiO₂. [12-15] The synergy of carbon doping and coating in TiO₂ is still unclear and the comprehensive investigation of synergistic effect of carbon doping and coating is highly expected. Except TiO₂, the next generation photocatalysts with acceptable photocatalytic activity under solar light or visible light are still in exploring. Magnéli materials as a group of titanium suboxides (Ti_nO_{2n-1}) possess better electrical conductivity comparing to TiO₂ [16] and shows superior stability when using as electrocatalysts supports. [17, 18] The semiconductor-metal transition in Ti_nO_{2n-1} can specially facilitate the charge separation and the photocatalytic activity. The fabrication approaches of Ti_nO_{2n-1} employ high temperature above 1100 °C for sintering and complex organics such as PVA, polyethylene as the resources of reducing agent, which are costive, polluting and uncontrollable. [19, 20] The difficulty on controllable and green synthesis of Magnéli materials confines their further application in energy-related fields. Thus, the development of Magnéli materials on both synthesis and application in PEC water splitting is also in need. In the practical application of PEC water splitting, the electrolytic environments have crucial impact on the PEC performance of photoanodes based on metal oxides. [21-24] The electrolytic parameters such as electrolyte cations, [22] pH values, [25] sacrificial additives [26, 27] and temperature [24, 28] all affect PEC performance differently. The research work on the impact of electrolytic environments on PEC performance is very limited. Why and how these electrolytic parameters affect the PEC performance on a general photoanode based on metal oxides are far from being understandable. In addition to develop specific materials for PEC water splitting, modification of electrolytic environments might be an alternative approach for enhancing the PEC performance of metal oxides.

The main objective of this PhD thesis is thus to investigate the effect of doping, coating and electrolytic environment on the photocatalytic and photoelectrochemical activity of

metal oxide semiconducting materials to improve the photocatalytic and photoelectrochemical performance of metal oxide semiconducting materials. The simultaneous doping and coating of TiO₂ obtained with different carbon amounts and calcined at different temperatures and a series of Magnéli (Ti_nO_{2n-1}) materials with different oxygen deficiency have been prepared, characterized and tested in photocatalytic and photoelectrochemical production of H₂ by water splitting. To study the effect of electrolytic environment on the photoelectrochemical activity, a series of metal oxide semiconducting materials have been used in the H₂ production by water splitting.

2.1.1 Synergy of carbon doping and coating in TiO₂ for enhanced photocatalysis and photoelectrochemical performance of TiO₂

Since TiO₂ with metal or metal oxides dopants suffered from lower photocatalytic activity, poor photostability and expensive cost.^[29, 30] Among different doping components, carbon is one of the most effective, economical and stable choice because of its large electron-storage capacity, wide range of visible light absorption and good permeability into TiO₂.^[31, 32] Carbon doping in TiO₂ might result in new and unexpected features owing to induced localized electronic states in the band gap and enhanced the absorption of light but also.^[33, 34] Meanwhile, carbon coating is another effective method to enhance the photocatalytic activity of TiO₂.^[35, 36] Carbon coating can improve the thermal stability of TiO₂ by suppressing the phase transformation from anatase to rutile at high temperature leading to high crystallinity and consequently better photoactivity.^[14, 37] Moreover, carbon coating in the growth of TiO₂ can also prevent the grain aggregation of TiO₂ resulting in increased specific surface area which provides more active sites.^[38, 39] Carbon layer coated around TiO₂ can also improve the conductivity of TiO₂ boosting the mass transfer and the charge separation.^[40, 41] However, the dual effect of both carbon doping and coating has seldom been reported. Actually, the carbon doping might accompany carbon coating while carbon doping might occur in carbon coating. Even though carbon doping or coating has been widely applied to enhance the photocatalytic activity.^[42, 43] Little work has been done in the synergy of carbon doping and coating in TiO₂. Therefore, the first objective of present work is to investigate the synergy of carbon doping and coating which can provide an overall understanding of carbon doping and coating in TiO₂ and a better guide for the further application of carbon composed TiO₂ in photocatalysis.

2.1.2 Magnéli (Ti_nO_{2n-1}) materials for PEC water splitting

Titanium suboxides, which is known as magnéli materials (Ti_nO_{2n-1}) is often observed in non-metal doped TiO_2 as well as in carbon doped TiO_2 especially after calcination at high temperature (>1000 °C). [44, 45] The magnéli materials are made up of two-dimensional chains of TiO_6 but with an oxygen deficiency in every n titanium octahedral sites. [46] The magnéli materials with semiconductor-metal phase have high electrical conductivity at room temperature and been already applied in many areas, such as batteries, electrocatalysis and energy conversion. [47, 48] However, their application for PEC water splitting is seldom reported. Therefore, the second objective is to design a facile and environment-friendly method for the synthesis of functional Ti_nO_{2n-1} materials for PEC water splitting.

2.1.3 Impact of electrolytic environment on the PEC performance of metal oxides

For other metal oxides semiconductors (MOSSs) such as WO_3 , Fe_2O_3 , $BiVO_4$, $LaFeO_3$ with visible-light photocatalytic activity mainly suffer from the rapid recombination of photogenerated electron/hole pairs and the effect of “surface back-reaction” (SBR). [49-51] Adding sacrificial reagents (SRs) such as methanol, carboxylic acids and Na_2S as electron donors can effectively scavenge holes and prevent the recombination of electron/hole pairs. [52, 53] Moreover, the evolution of oxygen production as well as the reproducing of H_2O are also hindered. Thus, the efficiency for PEC water splitting is highly enhanced. Except the SRs, other electrolytic parameters such as electrolyte cations, pH values and temperature can also influence the PEC performance of photoanodes based on metal oxides. [54] Comparing to developing or modification the photoanode materials, adjusting electrolytic environments to enhance PEC performances over MOSSs photoanodes might be an alternative way. Thus, the third objective is to work on the impact of electrolytic environments on PEC performance over different MOSSs. We aim at providing a systematic understanding of how electrolytic environments affect the PEC behaviors of a general metal oxide.

2.1 Scientific strategy

2.2.1 Materials synthesis

2.2.1.1 Synthesis of the carbon coated and doped TiO_2

The hydrolysis treatment of $TiCl_4$ in liquid solution containing organics could result in

Objectives & scientific strategy

intermediate carbohydrates coated amorphous TiO₂. [55, 56] The fructose is specially chosen due to its non-toxicity, easy accessibility and zero emissions of pollutant. The aqueous hydrolysis of TiCl₄, as indicated in reactions 1 and 2, leads to the production of amorphous TiO₂. [57, 58] Due to the heat released from hydrolysis process of TiCl₄, the fructose will dehydrate into intermediate carbohydrates. The intermediate carbohydrates will be firstly coated on the surface of the amorphous TiO₂ as carbon source. The carbon coated and doped TiO₂ will be obtained after calcination under Ar.



2.2.1.2 Synthesis of carbon composed Ti_nO_{2n-1}

The hydrolysis of TiCl₄ in fructose can produce intermediate carbohydrates coated amorphous TiO₂. During the sintering process in Ar, the coated intermediate carbohydrates can provide reductive environment for the growth of titanium suboxide (Ti_nO_{2n-1}), Magnéli materials. For strictly control the growth of Ti_nO_{2n-1}, the reductive atmosphere must be protected. Sealing of crucibles for calcination is necessary. The carbon composed Ti_nO_{2n-1} materials can be obtained after the calcination under Ar. The concentration of fructose in precursors, sintering temperature and duration can all be adjusted to control the n value of Ti_nO_{2n-1} materials.

2.2.1.3 Metal-oxide-semiconductors (MOSS) ordered porous thin films as photoanodes

The template method is employed to fabricate various MOSSs using Ti electrode as susbtrates. The monolayer polystyrene sphere (PS) template are prepared on the glass slide by air/water interfacial self-assembly. Then monolayer PS template can be transferred on the Ti electrode through precursor of target MOS. After drying and calcination, the organic PS spheres can be removed and the ordered porous skeleton of a series of metal oxides with the uniform, porous and micro/nano sized structure will be obtained. The reproducibility and reliability of photoanodes based on each type of metal oxides on Ti electrodes can be assured by the uniformity of the original PS template and the same effective area (1cm²) of the substrate (Ti electrode).

2.2.2 Chemicals

Precursors for preparing metal oxides

Titanium tetrachloride ($\geq 99.9\%$)

TiCl₄

Sigma-Aldrich

Objectives & scientific strategy

Iron (III) nitrate nonahydrate ($\geq 99.9\%$)	$\text{Fe}(\text{NO}_3)_3 \cdot 9\text{H}_2\text{O}$	Sigma-Aldrich
Bismuth (III) nitrate pentahydrate ($\geq 99.9\%$)	$\text{Bi}(\text{NO}_3)_3 \cdot 9\text{H}_2\text{O}$	Sigma-Aldrich
Vanadium (IV) oxide sulfate hydrate ($\geq 99.9\%$)	$\text{VOSO}_4 \cdot x\text{H}_2\text{O}$	Sigma-Aldrich
Lanthanum (III) chloride heptahydrate ($\geq 99.9\%$)	$\text{LaCl}_3 \cdot 7\text{H}_2\text{O}$	Sigma-Aldrich
Zinc nitrate hexahydrate ($\geq 99.9\%$)	$\text{Zn}(\text{NO}_3)_2 \cdot 6\text{H}_2\text{O}$	Sigma-Aldrich
Chromic nitrate nonahydrate ($\geq 99.9\%$)	$\text{Cr}(\text{NO}_3)_3 \cdot 9\text{H}_2\text{O}$	Sigma-Aldrich

Applied Electrolytes

Lithium hydroxide ($\geq 98\%$)	LiOH	Sigma-Aldrich
Potassium hydroxide ($\geq 98\%$)	KOH	Sigma-Aldrich
Sodium hydroxide ($\geq 98\%$)	NaOH	Sigma-Aldrich
Potassium chloride ($\geq 98\%$)	KCl	Sigma-Aldrich
Sodium sulfide ($\geq 99.5\%$)	Na_2S	Sigma-Aldrich
Sodium sulfite ($\geq 99.5\%$)	Na_2SO_3	Sigma-Aldrich
Sodium iodide ($\geq 99.5\%$)	NaI	Sigma-Aldrich
Sodium iodate ($\geq 99.5\%$)	NaIO_3	Sigma-Aldrich
Sulfuric acid (95.0-98.0%)	H_2SO_4	Sigma-Aldrich

Organics

Fructose	$\text{C}_6\text{H}_{12}\text{O}_6$	Sigma-Aldrich
Methanol	CH_3OH	Sigma-Aldrich
Polystyrene sphere (PS) (2.5wt% in water)	$[\text{CH}_2\text{CH}(\text{C}_6\text{H}_5)]_n$	Alfa aesar

Others

Ammonia solution in water (25%)	NH_3	Fisher scientific
Hydrochloric acid (37%)	HCl	Fisher scientific

All solutions prepared in this thesis are using deionized water as solvent.

2.2.3 Characterization and instruments

2.2.3.1 Powder X-ray diffraction

Powder X-ray diffraction was performed on a PANalytical X'pert Pro with Cu K_α radiation ($\lambda = 1.54 \text{ \AA}$) on a Philips PW1820 diffractometer running at a voltage of 40 kV and current of 30 mA. It was employed to determine the crystalline structure of all the prepared metal oxides in

this thesis.

2.2.3.2 Nuclear magnetic resonance spectroscopy (NMR)

The ^{13}C solid-state MAS NMR experiments were carried out on a Bruker Avance 500 MHz (11.7 T) spectrometer using 4 mm zirconia rotors as sample holders with a rate of spinning = 10 kHz. The NMR spectra was used to know the information about the final chemical composition of polysaccharide coated on the surface of amorphous TiO_2 .

2.2.3.3 Scanning electron microscopy (SEM)

Scanning electron microscopy (SEM) was carried out on a field emission scanning electron microscopy (FESEM, FEI Sirion 200) with Au-sputtered specimen at 15 KeV. The morphologies of all the obtained products in this thesis were observed by SEM.

2.2.3.4 Transmission electron microscopy (TEM)

Transmission electron microscopy (TEM) was carried out on JEOL JEM-2100 microscope operated at 120 kV. Energy-dispersive X-ray spectroscopy (EDS) was attached to the JEM-2010F microscope. The samples for TEM observation were prepared by dispersing the particles in alcohol after ultrasonic treatment onto a copper grid with carbon film. The TEM was used for microstructural examinations and identification of resultant metal oxides in this thesis.

2.2.3.5 N_2 adsorption analysis

The isothermal nitrogen adsorption-desorption measurements were carried out on a Micromeritics Tristar 3000 with prior degassing under vacuum of 100 °C overnight. It was used for porous structure parameters, surface area, pore size distribution and pore volume of the obtained powder samples TiO_2 and $\text{Ti}_n\text{O}_{2n-1}$ in this thesis.

2.2.3.6 UV-Visible absorption spectroscopy

The UV-vis absorbance spectra were measured using a UV-vis spectrophotometer (Perkin Elmer Lambda 35 spectrometer fitted with a Labsphere for analysis in diffuse reflectance mode) in the range of 200 – 800 nm. First, it was used to measure the absorbance spectra of TiO_2 to calculate the band gap of TiO_2 . Second, it was employed for determination of concentration of the dye molecule (methylene blue) in photocatalytic degradation testing to evaluate the photocatalytic activity of carbon coated and doped TiO_2 and reference samples in this thesis.

2.2.3.7 Raman

Raman spectra were recorded on a confocal Raman spectrometer (Renishaw in Via Reflex) excited by the laser, at 532 nm in wavelength and 0.17 mW in power with 10 s of integral time and 1 μm of spot size on the sample in diameter. The Raman spectra was used to determine vibrational modes and structure of carbon coated and doped TiO₂ and other reference samples in this thesis.

2.2.3.8 X-ray photoelectron spectroscopy (XPS)

The X-ray photoelectron spectroscopy (XPS) analysis was carried out on a K-Alpha^{TM+} X-ray photoelectron spectrometer (XPS). The XPS analysis was used for the surface elemental analysis of as-prepared metal oxides in this thesis.

2.2.4 Evaluation of photocatalytic activity

2.2.4.1 Photocatalytic test of the degradation of dye pollutant

A series photocatalytic testing was carried out under a full spectrum light irradiation (300–800 nm) using 6 neon lamps of 18 W. The luminous power of each lamp was 1250 lm. The photocatalytic degradation of dye pollutant was firstly tested to primarily evaluate the photocatalytic activity of the obtained carbon doped and coated TiO₂.

2.2.4.2 Photocatalytic H₂ production performance

The photocatalytic H₂ evolution experiments were tested on a commercial reaction system (Labsolar-6A, Beijing Perfectlight Science & Technology Co., LTD) equipped with a Microsolar 300 Xenon lamp. The temperature was maintained at 20 °C using a water-cooling system. The generated H₂ was analyzed by an FULI-GC-9790II gas chromatograph (GC) (Zhejiang Fuli Analytical Instrument Co., Ltd.) equipped with a thermal conductivity detector (TCD). After photocatalytic H₂ evolution experiments, the photocatalytic performances of pristine TiO₂, carbon doped TiO₂, carbon coated TiO₂ and carbon doped and coated TiO₂ for H₂ production from water splitting were compared.

2.2.4.3 Photoelectrochemical measurements

The photoelectrochemical measurements were carried out in a measurement system (SCS10, Zolix) connected with an electrochemical workstation (CHI 660E). The photocurrents of

Objectives & scientific strategy

photoanodes based on the as-prepared metal oxides were measured in a standard quartz-made three-electrode cell with Saturated Calomel Electrode (SCE) and platinum foil as reference electrode and counter electrode, respectively. The applied potential and photocurrent of the photoanodes were controlled and collected by a potentiostat (CHI 660E), respectively.

References

- [1] S.K. Saraswat, D.D. Rodene, R.B. Gupta, *Renew. Sust. Energ. Rev.* 89 (2018) 228-248.
- [2] T. Hisatomi, J. Kubota, K. Domen, *Chem. Soc. Rev.* 43 (2014) 7520-7535.
- [3] C.-H. Liao, C.-W. Huang, J. Wu, *Catalysts* 2 (2012) 490-516.
- [4] J. Hu, S. Zhang, Y. Cao, H. Wang, H. Yu, F. Peng, *ACS Sustain. Chem. Eng.* 6 (2018) 10823-10832.
- [5] V. Kumaravel, S. Mathew, J. Bartlett, S.C. Pillai, *Appl. Catal. B* 244 (2019) 1021-1064.
- [6] J. Guayaquil-Sosa, B. Serrano-Rosales, P. Valadés-Pelayo, H. De Lasa, *Appl. Catal. B* 211 (2017) 337-348.
- [7] E.M. Samsudin, S.B. Abd Hamid, *Appl. Surf. Sci.* 391 (2017) 326-336.
- [8] H. Choi, S. Khan, J. Choi, D.T. Dinh, S.Y. Lee, U. Paik, S.-H. Cho, S. Kim, *Appl. Catal. B* 210 (2017) 513-521.
- [9] M. Nolan, A. Iwaszuk, A.K. Lucid, J.J. Carey, M. Fronzi, *Adv. Mater.* 28 (2016) 5425-5446.
- [10] S.N.A. Sulaiman, M.Z. Noh, N.N. Adnan, N. Bidin, S.N. Ab Razak, *J Phys: Conf Ser.*, 2018, pp. 012006.
- [11] K.K. Mandari, A.K.R. Police, J.Y. Do, M. Kang, C. Byon, *Int. J. Hydrog. Energy* 43 (2018) 2073-2082.
- [12] A.V. Raghu, K.K. Karuppannan, B. Pullithadathil, *Adv. Mater. Interfaces* 6 (2019) 1801714.
- [13] H. Wang, Z. Wu, Y. Liu, *J. Phys. Chem. C* 113 (2009) 13317-13324.
- [14] M. Inagaki, Y. Hirose, T. Matsunaga, T. Tsumura, M. Toyoda, *Carbon* 41 (2003) 2619-2624.
- [15] T.A. Gad-Allah, K. Fujimura, S. Kato, S. Satokawa, T. Kojima, *J. Hazard. Mater.* 154 (2008) 572-577.
- [16] R. Shi, M. Li, Y. Zhang, Y. Lei, Y. Zhu, R. Jiang, X. He, Z. Lei, Z. Liu, H. Zhu, *Electrochim. Acta* (2020) 136120.
- [17] R.A.M. Esfahani, S.K. Vankova, A.H.M. Videla, S. Specchia, *Appl. Catal. B* 201 (2017) 419-429.
- [18] C. Alegre, E. Modica, C.L. Vecchio, S. Siracusano, A. Arico, V. Baglio, *Int. J. Hydrog. Energy* 41 (2016) 19579-19586.
- [19] B. Xu, H.Y. Sohn, Y. Mohassab, Y. Lan, *RSC Adv.* 6 (2016) 79706-79722.
- [20] M. Liu, D. Zhao, W. Zhai, J. Yang, B. Yang, H.Y. Sohn, B. Xu, *J. Alloys Compd.* 816 (2020) 152516.
- [21] C. Ding, J. Shi, Z. Wang, C. Li, *ACS Catal.* 7 (2017) 675-688.
- [22] C. Ding, X. Zhou, J. Shi, P. Yan, Z. Wang, G. Liu, C. Li, *J. Phys. Chem. B* 119 (2015) 3560-3566.
- [23] S. Guo, X. Zhao, W. Zhang, W. Wang, *Mater. Sci. Eng. B* 227 (2018) 129-135.
- [24] P. Dias, T. Lopes, L. Meda, L. Andrade, A. Mendes, *Phys. Chem. Chem. Phys.* 18 (2016) 5232-5243.
- [25] C.-F. Liu, Y.-J. Lu, C.-C. Hu, *ACS omega* 3 (2018) 3429-3439.
- [26] R. Ahmed, Y. Xu, G. Zangari, *Electrochim. Acta* 259 (2018) 1095-1103.
- [27] Y.-G. Lin, Y.-K. Hsu, Y.-C. Chen, L.-C. Chen, S.-Y. Chen, K.-H. Chen, *Nanoscale* 4 (2012) 6515-6519.
- [28] P. Dias, T. Lopes, L. Andrade, A. Mendes, *J. Power Sources* 272 (2014) 567-580.
- [29] P.S. Basavarajappa, S.B. Patil, N. Ganganagappa, K.R. Reddy, A.V. Raghu, C.V. Reddy, *Int. J. Hydrog. Energy* 45 (2020) 7764-7778.
- [30] S.B. Patil, P.S. Basavarajappa, N. Ganganagappa, M. Jyothi, A. Raghu, K.R. Reddy, *Int. J. Hydrog. Energy* 44 (2019) 13022-13039.
- [31] C. Yang, X. Zhang, J. Qin, X. Shen, R. Yu, M. Ma, R. Liu, *J. Catal.* 347 (2017) 36-44.
- [32] G. Jia, Y. Wang, X. Cui, W. Zheng, *ACS Sustain. Chem. Eng.* 6 (2018) 13480-13486.

Objectives & scientific strategy

- [33] H. Wang, J.P. Lewis, *J. Condens. Matter Phys.* 17 (2005) L209.
- [34] S. Goldstein, D. Behar, *J. Phys. Chem. C* 112 (2008) 15134-15139.
- [35] Z. Liang, X. Bai, P. Hao, Y. Guo, Y. Xue, J. Tian, H. Cui, *Appl. Catal. B* 243 (2019) 711-720.
- [36] B. Li, Z. Zhao, F. Gao, X. Wang, J. Qiu, *Appl. Catal. B* 147 (2014) 958-964.
- [37] T. Tsumura, N. Kojitani, I. Izumi, N. Iwashita, M. Toyoda, M. Inagaki, *J. Mater. Chem.* 12 (2002) 1391-1396.
- [38] F. Liu, N. Feng, L. Yang, Q. Wang, J. Xu, F. Deng, *J. Phys. Chem. C* 122 (2018) 10948-10955.
- [39] M. Inagaki, M. Nonaka, F. Kojin, T. Tsumura, M. Toyoda, *Environ. Technol.* 27 (2006) 521-528.
- [40] T. Xia, W. Zhang, Z. Wang, Y. Zhang, X. Song, J. Murowchick, V. Battaglia, G. Liu, X. Chen, *Nano Energy* 6 (2014) 109-118.
- [41] L.W. Zhang, H.B. Fu, Y.F. Zhu, *Adv. Funct. Mater.* 18 (2008) 2180-2189.
- [42] R. Leary, A. Westwood, *Carbon* 49 (2011) 741-772.
- [43] K. Palanivelu, J.-S. Im, Y.-S. Lee, *Carbon Lett.* 8 (2007) 214-224.
- [44] D. Regonini, V. Adamaki, C. Bowen, S. Pennock, J. Taylor, A. Dent, *Solid State Ion.* 229 (2012) 38-44.
- [45] X. Mao, F. Yuan, A. Zhou, W. Jing, *Chin. J. Chem. Eng.* 26 (2018) 1978-1984.
- [46] F. Walsh, R. Wills, *Electrochim. Acta* 55 (2010) 6342-6351.
- [47] U. Zubair, J. Amici, C. Francia, D. McNulty, S. Bodoardo, C. O'Dwyer, *Chemsuschem.* (2018) 1-11.
- [48] S.-Y. Park, S.-I. Mho, E. Chi, Y. Kwon, H. Park, *Thin solid films* 258 (1995) 5-9.
- [49] J. Low, J. Yu, M. Jaroniec, S. Wageh, A.A. Al-Ghamdi, *Adv. Mater.* 29 (2017) 1601694.
- [50] W. Zhou, H. Fu, *Inorg. Chem. Front.* 5 (2018) 1240-1254.
- [51] H. Wang, L. Zhang, Z. Chen, J. Hu, S. Li, Z. Wang, J. Liu, X. Wang, *Chem. Soc. Rev.* 43 (2014) 5234-5244.
- [52] M. Wang, S. Shen, L. Li, Z. Tang, J. Yang, *J. Mater. Sci.* 52 (2017) 5155-5164.
- [53] P. Nazari, O. Nouri, S.R. Setayesh, *J. Chem. Sci.* 132 (2020) 1-10.
- [54] C. Ding, J. Shi, D. Wang, Z. Wang, N. Wang, G. Liu, F. Xiong, C. Li, *Phys. Chem. Chem. Phys.* 15 (2013) 4589-4595.
- [55] F. Fringuelli, F. Pizzo, L. Vaccaro, *J. Org. Chem.* 66 (2001) 4719-4722.
- [56] J.A. Gallego-Urrea, J.P. Holmberg, M. Hassellöv, *Environ. Sci. Nano* 1 (2014) 181-189.
- [57] H.K. Park, D.K. Kim, C.H. Kim, *J. Am. Ceram. Soc.* 80 (1997) 743-749.
- [58] T.-H. Wang, A.M. Navarrete-López, S. Li, D.A. Dixon, J.L. Gole, *J. Phys. Chem. A* 114 (2010) 7561-7570.

CHAPTER 3.

Synergistic effects of carbon doping and coating of TiO₂ with exceptional photocurrent enhancement for high performance H₂ production from water splitting

Abstract

The “one pot” simultaneous carbon coating and doping of TiO₂ materials by the hydrolysis of TiCl₄ in fructose is reported. The synergistic effect of carbon doping and coating of TiO₂ to significantly boost textural, optical and electronic properties and photocurrent of TiO₂ for high performance visible light H₂ production from water splitting has been comprehensively investigated. Carbon doping can significantly increase the thermal stability, thus inhibiting the phase transformation of the Titania material from anatase to rutile while carbon coating can suppress the grain aggregation of TiO₂. The synergy of carbon doping and coating can not only ensure an enhanced narrowing effect of the electronic band gap of TiO₂ thus extending the absorption of photocatalysts to the visible regions, but also promote dramatically the separation of electron-hole pairs. Owing to these synergistic effects, the carbon coated and doped TiO₂ shows much superior photocatalytic activity for both degradation of organics and photocatalytic/photoelectrochemical (PEC) water splitting under simulated sunlight illumination. The photocatalytic activity of obtained materials can reach 5, 4 and 2 times higher than that of pristine TiO₂, carbon doped TiO₂ and carbon coated TiO₂, respectively in the degradation of organic pollutants. The carbon coated and doped TiO₂ materials exhibited more than 37 times and hundreds of times photocurrent enhancement under simulated sunlight and visible light, respectively compared to that of pristine TiO₂. The present work providing new comprehensive understanding on carbon coating and doping effect could be very helpful for the development of advanced TiO₂ materials for a large series of applications.

This chapter has been published in J. Energy Chem. DOI: 10.1016/j.jecchem.2020.08.002

3.1 Introduction

A large series of research has been devoted to extend light absorption zone and to prevent the electron-hole recombination by doping or coating of TiO₂ [1–11]. Carbon is often chosen as a prospective altering element to improve the visible-light photocatalytic performance of TiO₂ in the forms of either doping or coating [3–11] due to its availability, high light absorptivity, low electron transfer resistance and large electron-storage capacity [12–14]. For example, the carbon-doped TiO₂ nanotube was found to be five times more active than bare TiO₂ in the liquid photocatalytic degradation of symmetrical dimethylhydrazine under visible light [15]. The improved photoelectrochemical properties of carbon-doped TiO₂ were also reported by Yang et al. that C-doped TiO₂ materials exhibited a photocurrent value being 10 times higher than undoped Titania [16]. Carbon doping can strongly affect the electronic structure of TiO₂ by substituting lattice oxygen sites and introducing localized occupied states in the bandgap which results in narrowing the bandgap of TiO₂ and enhancing photogeneration of electron/hole pairs [11, 17–19]. On the other hand, the coating of TiO₂ photocatalysts with carbon materials such as graphene/graphite as a kind of surface decoration can lead to efficient photoexcited electrons transfer at the interface between TiO₂ and the liquid media [20, 21]. Because of the high electric conductivity of coated carbon, the rapid and stable separation of electron/hole pairs can be achieved [22]. It was found that carbon-coated mesoporous TiO₂ microspheres [23] achieved photocatalytic performance 4-times higher under visible light than uncoated TiO₂. Moreover, the efficient and stable photocatalytic water splitting under solar light was obtained on TiO₂ hierarchical nanotubes with carbon coating [24]. It is clear that carbon doping or coating can be highly effective to enhance the photocatalytic performance of TiO₂. However, the synergistic effect of carbon doping and coating in TiO₂ has seldom been investigated. Such study might help the development of advanced photocatalytic and photoelectrochemical materials by simply using carbon coating and doping.

Herein we report the “one-pot” simultaneous doping and coating of TiO₂ materials during the hydrolysis of TiCl₄ in an aqueous fructose solution. The fructose polymerization is hydrothermally induced during the TiCl₄ hydrolysis process. The amount of coated and doped carbon can be tuned. The carbon doping reduces the bandgap of TiO₂ and thus increases the efficiency of visible light utilization. The high electrical conductivity of coated carbon fastens the transfer and separation of photoinduced electron-hole pairs. The aggregation of TiO₂ particles is inhibited due to the surface protection of coated carbon resulting in increased specific surface area and providing more surface-active sites for photocatalytic reactions. Due

to the synergistic effects, the carbon coated and doped TiO₂ system exhibits much higher photoactivity than solely doped TiO₂ or coated TiO₂ under simulated sunlight. Most importantly, the carbon coated and doped TiO₂ photocatalysts achieve hundreds of times photocurrent enhancement under visible light and reach the highest and stable hydrogen production rate of 1.3 μmol g⁻¹ h⁻¹ without the presence of any co-catalysts under simulated sunlight. It is envisioned that this work provides a new perspective for the industrial application of carbon coated and doped TiO₂ for photocatalytic waste water treatment and H₂ production.

3.2 Experimental

3.2.1 Materials Synthesis

Ammonia (25%), TiCl₄ (99. 99% pure), and fructose were purchased from Aldrich, TiO₂ powder (P25) from Degussa, Germany. All the solutions used were freshly prepared with deionized water. Fig. S3.1 shows the schematic illustration of the synthesis procedure at room temperature. 2 mL TiCl₄ was slowly added under stirring at 350 rpm into an ammonia base solution (12.5% volume of ammonia) containing fructose with varying concentrations of 0, 0.1, 0.5 and 1 g/L. A precipitate was instantly formed and was washed with distilled water and collected by centrifugation for several times at 8000 rpm, until the final pH value of the precipitates was close to 7. The resulting materials were subsequently dried in air for 24 h and were denoted as F_x, (in the name of Fructose, x = 0, 0.1, 0.5 and 1 according to the concentration of fructose e. g. F₀, F_{0.1}, F_{0.5} and F₁, respectively). Dried samples were then annealed at various temperatures at a ramp rate of 2 °C /min for 3 h under argon. The final products were simply denoted as TiO₂-x/T (T: calcination temperature). For example, F₀, F_{0.1}, F_{0.5} and F₁ calcined at 500 °C are denoted as TiO₂-0/500, TiO₂-0.1/500, TiO₂-0.5/500 and TiO₂-1/500, respectively. For comparison, the carbon coated TiO₂ (2 wt% carbon) was prepared as follows. 1 g anatase TiO₂ obtained by annealing precipitate F₀ under air at 450 °C for 3 h was added into 10mL fructose solution (5 g/L), the mixture was then dried at 80 °C followed by annealing at 650 °C under Ar for 3 h. The sample is denoted as TiO₂-CC (CC: coated carbon). The sample TiO₂-0.5/700 was calcined at 550 °C under air for 3 h to remove all the carbon coating while keeping doped carbon in TiO₂, which is denoted as TiO₂-DC (DC: doped carbon).

3.2.2 Materials characterization

The ¹³C solid-state MAS NMR experiments were realized on a Bruker Avance 500 MHz (7 T) spectrometer using 4 mm zirconia rotors as sample holders with a rate of spinning = 10 kHz.

Thermal gravimetric analysis and differential thermal gravimetric analysis (TGA/DTG) were carried out with a DSC-TGA (SDTQ600, TA Instruments) under the air atmosphere from room temperature to 800 °C and 1000 °C at a heating rate of 10 °C/min. The total carbon amount in each sample was determined (Fig. S3.2). Powder X-ray diffraction was performed on a PANalytical X'pert Pro with Cu $K\alpha$ radiation ($\lambda = 1.54 \text{ \AA}$). The morphology of the products was observed on a field emission scanning electron microscopy (FESEM, FEI Sirion 200). Microstructural examinations were conducted on JEOL JEM-2100 transmission electron microscopy (TEM) operated at 120 kV. The isothermal nitrogen adsorption-desorption measurements were carried out on a Micromeritics Tristar 3000 with prior degassing under vacuum of 100 °C overnight. Raman spectra were recorded on a confocal Raman spectrometer (Renishaw in Via Reflex) excited by the laser, at 532 nm in wavelength and 0.17 mW in power with 10 s of integral time and 1 μm of spot size on the sample in diameter. The X-ray photoelectron spectroscopy (XPS) analysis was performed on a K-Alpha^{TM+} X-ray photoelectron spectrometer (XPS). The UV-vis absorbance spectra were obtained using a UV-vis spectrophotometer (Perkin Elmer Lambda 35 UV-visible spectrometer fitted with a Labsphere for analysis in diffuse reflectance mode) in the range of 200–800 nm.

3.2.3 Photocatalytic test of the degradation of dye pollutant

Photocatalytic testing was carried out under a full spectrum light irradiation (300–800 nm) using 6 neon lamps of 18 W. The emission spectrum of the neon light lamp is shown in Fig. S3.3. The luminous power of each lamp was 1250 lm thus a total power of 7500 lm inside the photocatalytic reactor. The reaction temperature was maintained at room temperature. Methylene blue (MB) is used as the representative dye pollutant molecule. In each experiment, 50 mg photocatalyst was mixed with 50 mL of methylene blue solution with an initial concentration of 10 ppm in a quartz tube which is inserted into the photocatalytic reactor. The suspension was kept under stirring at 200 rpm. To reach an adsorption-desorption equilibrium and exclude the effects of adsorption, the whole system was placed in a dark environment for 120 min prior illumination. During irradiation, 0.2 mL of the suspension was withdrawn for analysis every 30 min. The liquid was separated from the solid catalyst by centrifugation. The concentration of methylene blue solution was then determined by the UV-vis spectrophotometry. The residual catalyst was recycled after washing with distilled water and drying for the following runs.

3.2.4 Electrochemical and Photoelectrochemical measurement

Mott-Schottky curves were measured at different frequencies ranging from 0.5 to 2.5 kHz using AUTOLAB electrochemical station in 0.1 M Na₂SO₄ (pH = 6) under the dark environment. A platinum foil and saturated Ag/AgCl were used as counter and reference electrodes, respectively. Ag/AgCl potential is converted into the Reversible Hydrogen Electrode (RHE) potential according to the Nernst equation, as follows [20, 25]:

$$E_{\text{RHE}} = E_{\text{Ag/AgCl}} + 0.1976 + 0.059 \times pH = E_{\text{Ag/AgCl}} + 0.5516 \text{ V at } 25^\circ\text{C} \quad (1)$$

The photoelectrochemical measurement was carried out using the solar cell quantum efficiency measurement system (SCS10, Zolix) which is connected with a conventional electrochemical workstation (CHI 660E). Typically, 15.0 mg of each photocatalyst was mixed with deionized water (100 µL) and 20 µL of a Nafion ® 117 solution (5% in a mixture of lower aliphatic alcohols and water). The mixture was placed under sonication for 5 min followed by grinding for 20 min in order to obtain a homogeneous suspension. The 0.6 g indium tin oxide (ITO) glass (1 cm²) was used as substrate. The suspension was dropped onto the surface of two ITO glasses equally. After naturally drying overnight, the final weight of each ITO glass loaded with a sample was around 0.607 g. The photocurrent was measured in a standard quartz-made three-electrode cell with as-prepared ITO glass as working electrode. The PEC water splitting experiments were carried out in 0.1 M Na₂SO₄ (Aldrich, 25 °C, pH = 6) electrolyte with Saturated Calomel Electrode (SCE) and platinum foil as reference electrode and counter electrode, respectively. The potential and photocurrent of the photoelectrode were controlled by a potentiostat (CHI 660E) and the SCE potential is converted into the RHE potential according to the Nernst equation, as follows [20, 25]:

$$E_{\text{RHE}} = E_{\text{SCE}} + 0.2438 + 0.0592 \times pH = E_{\text{SCE}} + 0.6 \text{ V at } 25^\circ\text{C} \quad (2)$$

The samples were illuminated by a sunlight simulator, consisting of a controllable 500 W Xenon lamp (Model: Gloria-X500A, Titan Electro-Octics Co., Ltd.) and an AM 1.5 filter (100 mW/cm², thermopile detector from Zolix was used for the measurements). The photocurrent action spectra were obtained under illumination through a monochromator (Omini-λ300, Zolix).

3.2.5 Photocatalytic H₂ production performance

The photocatalytic H₂ evolution experiments were conducted on a commercial reaction system (Labsolar-6A, Beijing Perfectlight Science & Technology Co., LTD) using a Microsolar 300 Xenon lamp with a UV light intensity of 52 mW/cm² and visible light intensity of 392 mW/cm². Typically, 100 mg of each photocatalyst was added in 100 mL of an aqueous solution containing

50% volume ratio of ethanol as the sacrificial agents. The mixture was sealed in a quartz vessel and stirred during photoreactions. The solution temperature was controlled at 20 °C by using a water-cooling system. After degassing, the vessel was under irradiation of the Microsolar 300 Xenon lamp. The generated H₂ was analyzed periodically by an FULI-GC-9790II gas chromatograph (GC) (Zhejiang Fuli Analytical Instrument Co., Ltd.) equipped with a thermal conductivity detector (TCD).

3.3 Results and discussions

Fig. 3.1 presents the preparation and formation of simultaneously carbon coated and doped TiO₂. The aqueous hydrolysis of TiCl₄, as indicated in reactions 3 and 4, leads to the production of amorphous TiO₂ [26, 27]. The polymerization of fructose (C₆H₁₂O₆), induced by the heat released by the hydrolysis of TiCl₄, leading to the formation of polysaccharide ((C₆H₁₀O₅)_n). The polysaccharide was coated on the surface of the amorphous TiO₂ at the early stage.

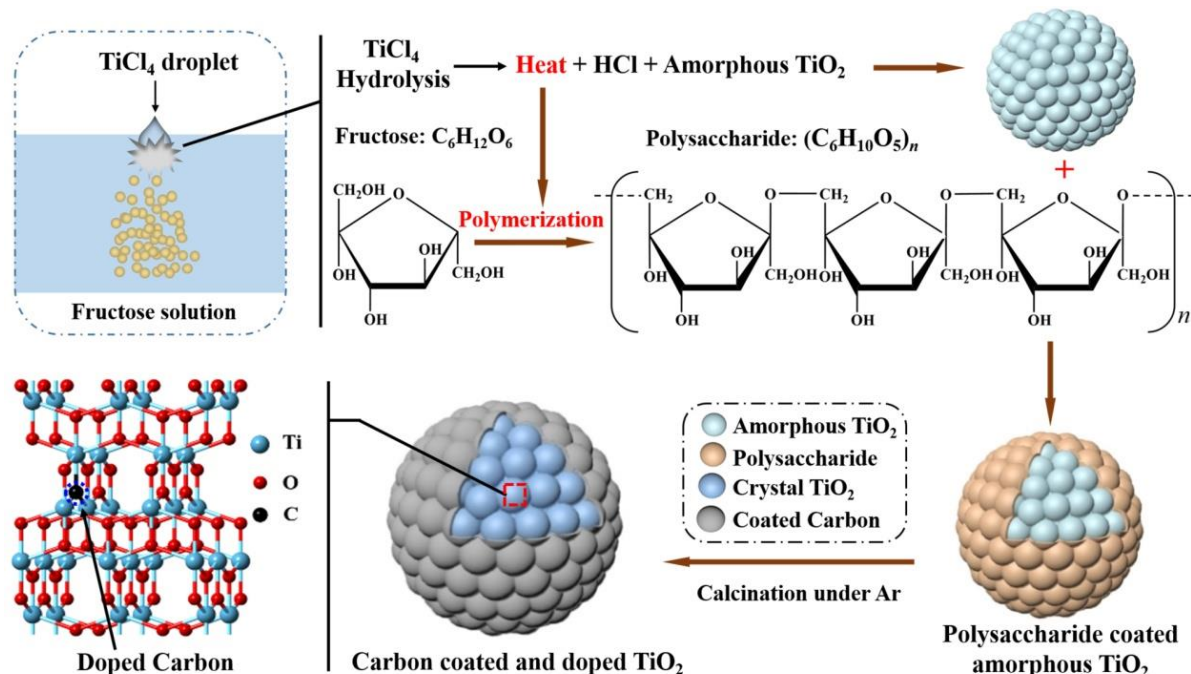


Fig. 3.1. Schematic illustration of the preparation procedure of carbon-doped and -coated TiO₂ samples.

On account of polysaccharide derived from fructose polymerization induced by the heat released from the hydrolysis of TiCl₄, the color of samples changed to brownish yellow (Fig.

S3.1 F_{0.1}–F₁). To determine the final chemical structure of polysaccharide in TiO₂ before calcination, the ¹³C solid state NMR measurement was carried out. Fig. S3.4 shows a comparison of ¹³C NMR spectra and photography of (a) sample F_{0.5} without calcination and (b) fructose. All the peaks of fructose are mainly located in the area of 50–100 ppm. The peaks of F_{0.5} sample observed at 0–50 ppm can be attributed to mobile CH_n groups [28]. Several small peaks observed at 100–175 ppm are correlated with sp² hybridized carbon. The peak at around 180 ppm is assigned to carboxyl group like COOH [29, 30]. The most prominent peaks are observed at 50–100 ppm due to the existence of the high concentration OCH_n, which is similar to that of fructose [31]. The polymerized fructose, homopolysaccharide dominated among these carbohydrate molecules in amorphous TiO₂. The doped carbon atoms and coated carbon layer were originated from the polysaccharide and synchronously crystallized with TiO₂ along with the calcination process. The carbon content can be adjusted by changing the concentration of fructose. By using 0, 0.1, 0.5 and 1 g/L fructose, TiO₂-0/T, TiO₂-0.1/T, TiO₂-0.5/T and TiO₂-1/T containing 0 wt% C, 0.28 wt% C, 2.0 wt% C and 4.0 wt% C, respectively according to the thermogravimetry analysis as shown in Fig. S3.3.

3.3.1 Crystalline structure and textural properties

Figs. 3.2 and S3.5 show the evolution of crystalline phase of TiO₂-0/T (Figs. 3.2(a) and S3.5(a)), TiO₂-0.1/T (Figs. 3.2(b) and S3.5(b)), TiO₂-0.5/T (Figs. 3.2(c) and S3.5(c)) and TiO₂-1/T (Figs. 3.2(d) and S3.5(d)) from anatase into rutile after annealing under argon at different temperatures, respectively. It can be seen that the as-prepared carbon coated and doped TiO₂ materials exhibit increased phase transformation temperatures from anatase to rutile phase at 650, 675, 700 and 725 °C with increasing carbon content from 0 wt%, 0.28 wt%, 2.0 wt% to 4.0 wt%, respectively, indicating that carbon doping and coating can enhance the thermal stability of the anatase phase of Titania.

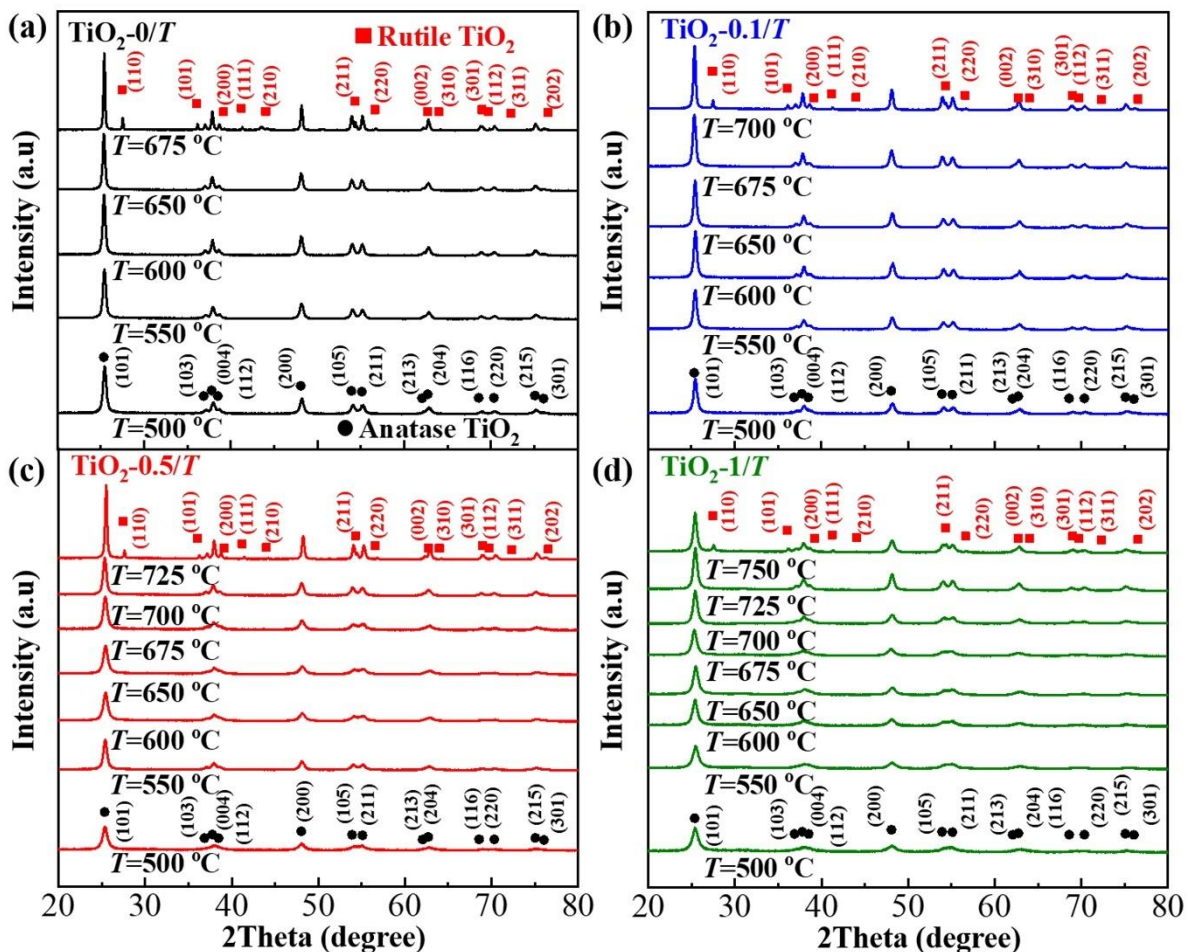


Fig. 3.2. X-ray diffraction patterns of (a) TiO₂-0/T, (b) TiO₂-0.1/T, (c) TiO₂-0.5/T and (d) TiO₂-1/T calcined at different temperatures.

The crystallite sizes of pure anatase TiO₂ can be calculated by the Scherrer equation using the full-width at half maximum (FWHM) values derived from fitted XRD peaks as shown in Fig. S3.6. Fig. S3.7(a and b) presents the FWHM values of the peak at around 25.4° corresponding to the crystal planes of (101) of anatase TiO₂ (JCPDS: 00-001-0562) and calculated crystallite sizes of TiO₂-0/T, TiO₂-0.1/T, TiO₂-0.5/T and TiO₂-1/T samples as a function of increasing calcination temperatures, respectively. For a defined calcination temperature, as the carbon content in TiO₂ increases, the FWHM value increases and the crystallite size decreases. This phenomenon is mainly ascribed to the fact that the grain aggregation of TiO₂ is inhibited under the protection of coated carbon layers. The crystallite sizes of samples TiO₂-0/650, TiO₂-0.1/675, TiO₂-0.5/700 and TiO₂-1/725 (calcined at phase transition temperatures) are found to be 26.6, 21.0, 18.0 and 16.0 nm. Meanwhile, the crystallite sizes of as-prepared TiO₂-CC and TiO₂-DC are calculated to be 18.5 and 20.3 nm using the same method (Fig. S3.8).

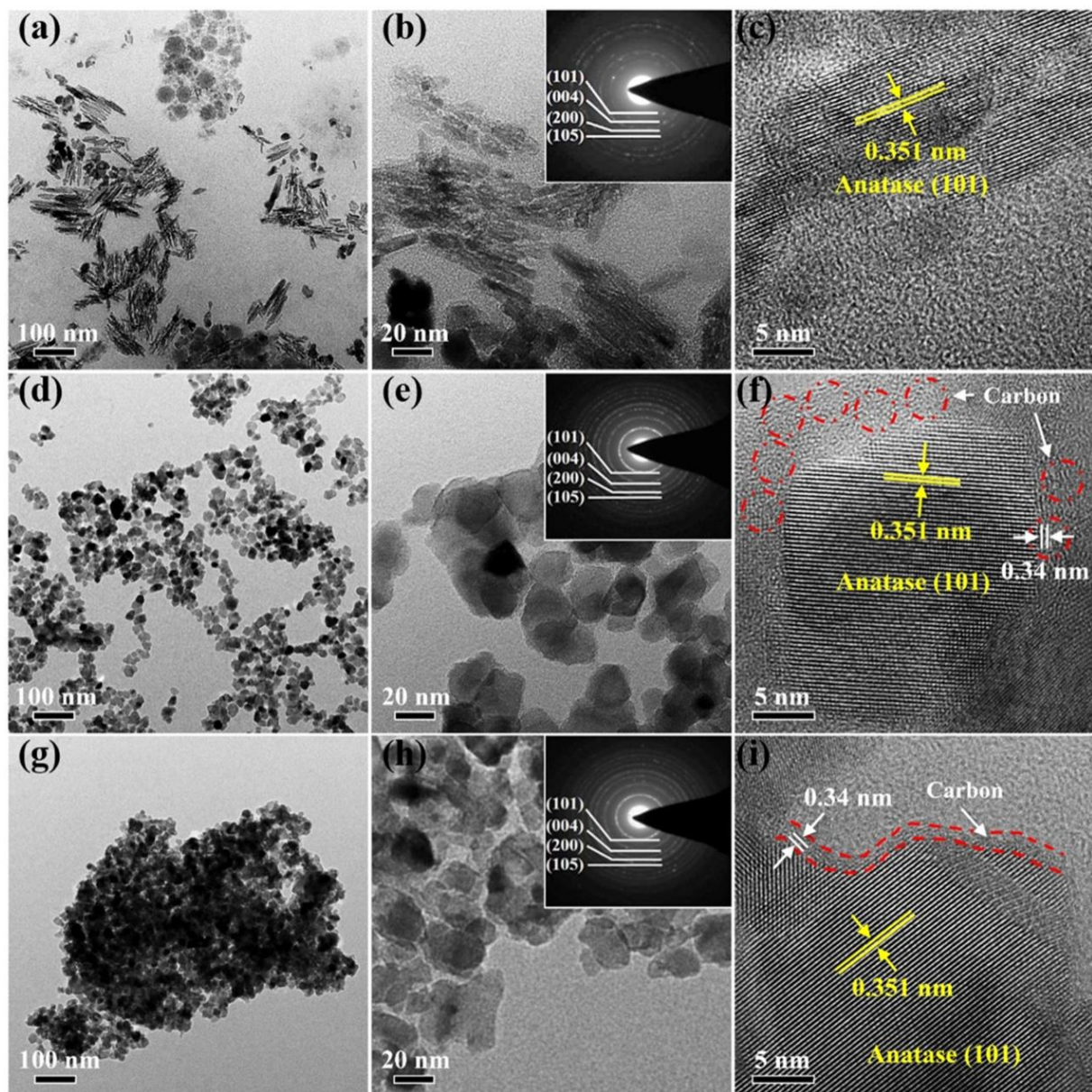


Fig. 3.3. The TEM images, SAED observation (inset) and HRTEM images of $\text{TiO}_2\text{-}0/650$ (a–c), $\text{TiO}_2\text{-}0.5/700$ (d–f) and $\text{TiO}_2\text{-}1/725$ (g–i), respectively.

The morphologies and microstructures of the selected samples were investigated by Scanning Electron Microscope (SEM) (Fig. S3.9) and Transmission Electron Microscopy (TEM) (Figs. 3.3 and S3.10). Low magnification TEM images of Selected Area Electron Diffraction (SAED) patterns and High-Resolution TEM (HR-TEM) characterization of the $\text{TiO}_2\text{-}0/650$, $\text{TiO}_2\text{-}0.5/700$ and $\text{TiO}_2\text{-}1/725$ samples are shown in Fig. 3.3 and those of $\text{TiO}_2\text{-}0.1/675$ in Fig. S3.10. Without carbon coating and doping, SEM images of $\text{TiO}_2\text{-}0.1/675$ sample shows TiO_2 particles with different sizes from several to around 50 nm while with carbon coating and doping, the TiO_2 particles of $\text{TiO}_2\text{-}0.5/700$ (Fig. S3.9(b)) and $\text{TiO}_2\text{-}1/725$ (Fig. S3.9(c)) samples are very homogeneously sized. Without carbon doping and coating, the as-prepared $\text{TiO}_2\text{-}0/650$ exhibits

multiple morphologies including zero-dimensional nanoparticles and one-dimensional nano-needles as seen in Fig. 3.3(a and b), being in good agreement with SEM observation (Fig. S3.9(a)). While the TEM images of $\text{TiO}_2\text{-}0.5/700$ containing 2.0 wt% carbon show very uniform nanoparticles with a particles size distribution centered at 20 nm (Fig. 3.3(d and e)), being in good accordance with SEM observation (Fig. S3.9(b)). With higher carbon content of 4.0 wt% for $\text{TiO}_2\text{-}1/725$ sample, the nanoparticles aggregate together as shown in Fig. 3.3(g and h). The HRTEM images in Fig. 3.3(c, f, and i) indicate single crystallinity of TiO_2 with neighboring lattice fringe distance of 0.35 nm, which corresponds to the distance of the (101) anatase plane. The result also demonstrates that the composition of these three samples are pure anatase TiO_2 , being in good agreement with the XRD results. HR-TEM images (Figs. 3.3(f and i) and S3.10(c)) show several layers of graphitic carbon with a distance between successive planes of 0.34 nm and amorphous carbon coated around TiO_2 particles in $\text{TiO}_2\text{-}0.5/700$ and $\text{TiO}_2\text{-}1/725$ as indicated by red lines and circles.

Nitrogen adsorption-desorption isotherms of as-prepared samples, $\text{TiO}_2\text{-}0/T$, $\text{TiO}_2\text{-}0.1/T$, $\text{TiO}_2\text{-}0.5/T$ and $\text{TiO}_2\text{-}1/T$ ($T = 500, 650, 675, 700$ and 725°C) are illustrated in Figs. S3.11 and S3.12. Type IV adsorption isotherms with H_2 type hysteresis loop that are characteristics of mesoporous materials can be observed for all the materials^[32]. The mesopores mainly originate from the aggregation of TiO_2 nanoparticles. The homogeneous pore size distribution curves (insets in Figs. S3.11 and S3.12) calculated via the Barrett-Joyner-Halenda (BJH) method implies that the materials have uniform pore channels in the mesoporous region.

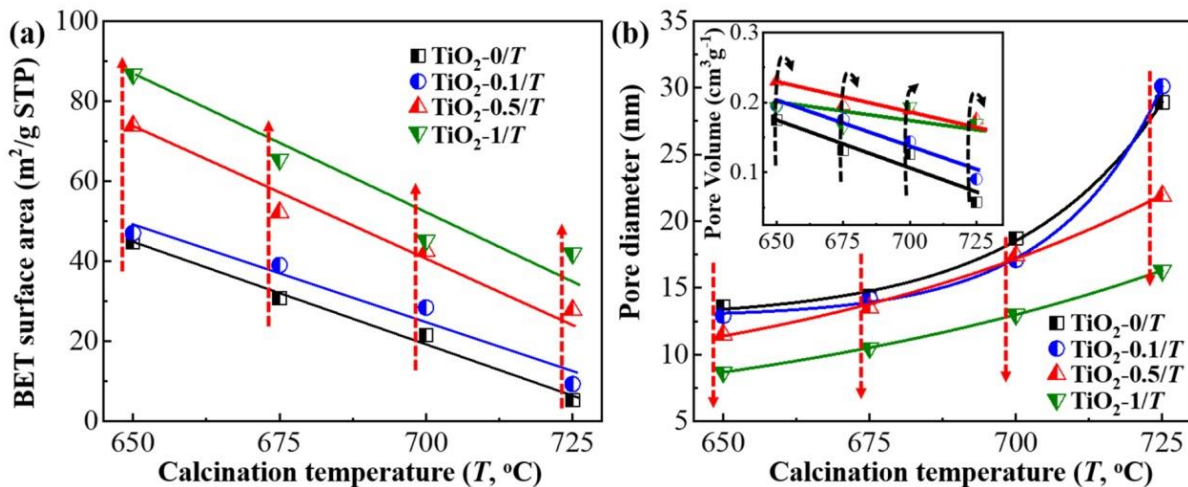


Fig. 3.4. (a) BET specific surface area, (b) average pore diameter and (inset) pore volume change with calcination temperature.

The Brunauer-Emmett-Teller (BET) specific surface areas, pore diameters and pore volumes

of TiO₂ samples are summarized in Fig. 3.4 and Table S3.1. At the same calcination temperature, the BET surface area of carbon coated and doped TiO₂ samples increases with increasing carbon content (Fig. 3.4(a)). In addition, the samples without carbon, generally TiO₂-0/T, give a relative broad pore size distribution due to the larger crystallite sizes of different morphologies. The pore size distribution curves become narrower with carbon doping and coating (Fig. 3.4(b) and Table S3.1). It is above-mentioned that with increasing carbon content in the sample, the crystallite size decreases. It is expected that with increasing carbon content, the aggregation of smaller crystallites should give a smaller pore size. Meanwhile, the pore volume of samples also increases as the carbon content increases. However, when the content of carbon in TiO₂ increased up to 4.0 wt% in the sample, the residual and individual carbon particles start to obstruct the mesopores leading to a decrease of the pore volume as shown in Fig. 3.4(b) (inset) and Table S3.1. The highest surface area of 116 m²/g is found for the sample TiO₂-0.5/500 with a diameter of 8.0 nm and pore volume of 0.23 cm³/g. The surface area and pore volume of this sample decreases to about 30 m²/g and 0.20 cm³/g while pore diameter increases to 20 nm with increasing calcination temperature to 725 °C. All the samples with a defined carbon content have the same tendency with the increasing calcination temperature. Increasing calcination temperature will decrease the surface area and pore volume and enlarge the pore diameter (Fig. 3.4(a and b)). The porous structure of carbon coated and doped TiO₂ facilitates the diffusion of reactants and light penetration and improves light trapping as well as light scattering, leading to a more effective utilization of light.

Raman spectroscopic measurements have been carried out to understand the structure of carbon coated and doped TiO₂. Anatase TiO₂ has five Raman-active modes, which are A_{1g} (515 cm⁻¹), B_{1g} (395 and 515 cm⁻¹) and E_g (144, 195 and 639 cm⁻¹) as shown in Fig. S3.13(a) [33, 34]. All the samples including carbon coated TiO₂ (TiO₂-CC) and carbon doped TiO₂ (TiO₂-DC) only present characteristic peaks of anatase phase, which is consistent with the XRD results. The nature of carbon in different types of TiO₂ samples, carbon coated and doped TiO₂ (TiO₂-0.1/675, TiO₂-0.5/700 and TiO₂-1/725), carbon coated TiO₂ (TiO₂-CC) and carbon doped TiO₂ (TiO₂-CC) was also studied by Raman spectroscopy. The results are shown in Fig. S3.13(b) and the amplified spectrum (150 times magnification) of TiO₂-DC is illustrated in the Fig. S3.13(c). For all carbon modified samples including carbon doped TiO₂, two peaks at 1366 and 1605 cm⁻¹ were observed in the Fig. S3.13(b and c), which specifically correspond to the distinctive G-band and D-band of carbon materials, respectively [35, 36]. The D-band at 1366 cm⁻¹ originates from defective carbon from the doped carbon atoms bonding with Ti or O atoms and defective carbon atoms from the broken graphitic hexagonal structure [36, 37] while the G-

band at 1605 cm^{-1} is assigned to the tangential vibrations of the hexagonal lattice of sp^2 carbon atoms from the graphitic carbon and amorphous carbon which come from coated carbon [35, 38]. High intensity of G-band thus indicates the presence of high amount of coated carbon. The intensity ratio of D-band to G-band ($I_{\text{D}}/I_{\text{G}}$) is normally used to evaluate the degree of disordering of sp^2 carbon in TiO_2 which can determine the carbon nature of coating or doping type in TiO_2 [39–41]. Thus, all the intensities and intensity ratios of D-band and G-band of are collected and summarized in Table S3.2. The higher ratio ($I_{\text{D}}/I_{\text{G}}$) reveals a higher number of defects in carbon structure. The carbon atoms substitutionally or interstitially doped in the lattice of TiO_2 for example in the forms of C–Ti or C–O bonds must result in defective carbon atoms. Thus, the doped carbon contributes to the intensity of D band. However, the defective carbon from broken graphitic hexagonal structure of carbon can also give rise the intensity of D-band. The intensity ratios ($I_{\text{D}}/I_{\text{G}}$) of $\text{TiO}_2\text{-0.1/675}$, $\text{TiO}_2\text{-0.5/700}$ and $\text{TiO}_2\text{-1/725}$ are much higher than that of $\text{TiO}_2\text{-CC}$ indicating coexistence of different type of carbon, coated and doped carbon in TiO_2 . The intensity ratio ($I_{\text{D}}/I_{\text{G}}$) reaches a maximum value of 0.95 for the sample of $\text{TiO}_2\text{-0.5/700}$ with carbon content of 2 wt%, indicating large amount of both coated and doped carbon in TiO_2 . Neither G-band nor D-band are observed in pure TiO_2 sample, indicating clearly neither coated carbon nor doped carbon this this sample. For the carbon doped TiO_2 sample, it is known that the amount of doped carbon is very low. The intensity of both G-band and D-band of this sample is very low compared to carbon coated TiO_2 and carbon coated and doped TiO_2 samples, indicating the presence of negligible amount of coated carbon and doped carbon due to the removal of all the coated carbon and even some doped carbon by calcination $\text{TiO}_2\text{-0.5/700}$ in air. This part of results reveals that carbon doped TiO_2 and pure TiO_2 samples do not contain coated carbon and no doped carbon in pure TiO_2 . We will discuss in following paragraphs the presence of doped carbon in $\text{TiO}_2\text{-DC}$ and no carbon doping in $\text{TiO}_2\text{-CC}$.

3.3.2 Surface elemental analysis

X-ray photoelectron spectroscopic (XPS) analysis was performed to confirm the presence of doped carbon species in as-prepared samples. The carbon coated TiO_2 ($\text{TiO}_2\text{-CC}$) and the carbon doped sample ($\text{TiO}_2\text{-DC}$) were prepared as reference. The carbon doped sample was prepared by annealing the $\text{TiO}_2\text{-0.5/700}$ sample in air in order to remove carbon coating.

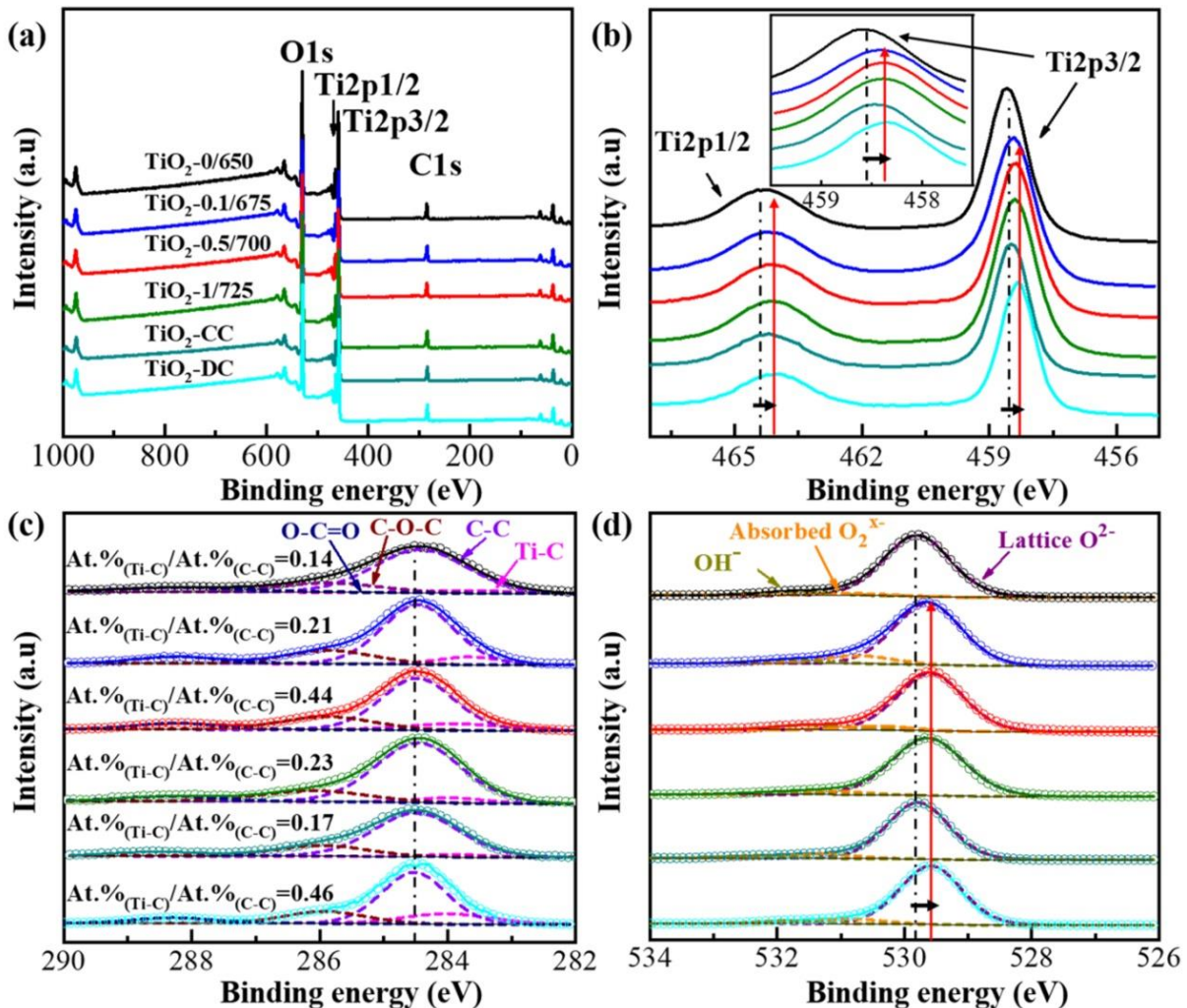


Fig. 3.5. (a) Wide range XPS spectra and High-resolution XPS spectra of (b) Ti 2p, (c) O 1s and (d) C 1s region of $\text{TiO}_2\text{-}0/650$, $\text{TiO}_2\text{-}0.1/675$, $\text{TiO}_2\text{-}0.5/700$, $\text{TiO}_2\text{-}1/725$, $\text{TiO}_2\text{-CC}$ and $\text{TiO}_2\text{-DC}$.

Fig. 3.5(a) exhibits the wide range XPS survey spectra of as-prepared samples, $\text{TiO}_2\text{-}0/650$, $\text{TiO}_2\text{-}0.1/675$, $\text{TiO}_2\text{-}0.5/700$, $\text{TiO}_2\text{-}1/725$, $\text{TiO}_2\text{-CC}$ and $\text{TiO}_2\text{-DC}$. Fig. 3.5(b-d) show the high-resolution XPS spectra of Ti2p, O1s and C1s species, respectively. In Fig. 3.5(b), samples present two main peaks at around 464.3 eV and 458.6 eV that are attributed to the Ti ($2p_{1/2}$) and Ti ($2p_{3/2}$), respectively^[42, 43]. The Ti signals of $\text{TiO}_2\text{-}0.1/675$, $\text{TiO}_2\text{-}0.5/700$, $\text{TiO}_2\text{-}1/725$ and $\text{TiO}_2\text{-DC}$ are shifted towards lower energy compared to that of $\text{TiO}_2\text{-}0/650$ and $\text{TiO}_2\text{-CC}$, indicating directly the presence of Ti–C bond in $\text{TiO}_2\text{-DC}$ and both carbon coated and doped TiO_2 samples^[44, 45]. Each C1s spectra can be fitted by three or four peaks at 283.5, 284.5, 286.0 and 288.3 eV as shown in Fig. 3.5(c). The peaks at 284.5, 286.0 and 288.3 eV are attributed to C–C, C–O–C and O–C=O, respectively^[46, 47]. As carbon contamination which is used as a reference for XPS spectra also has C–C, C–O–C and O–C=O components, the presence of

C–C peak in pure TiO₂ and carbon doped TiO₂ (TiO₂-DC) samples does not mean the presence of coated carbon in these two samples. As the peak at 283.5 eV is specially assigned to the Ti–C bond from the doped carbon in TiO₂. The content ratios of doped carbon can be compared by the atomic ratios of carbon from Ti–C and C–C among these samples [48, 49]. The atomic ratios of O=C=O, O–C–O, C–C and Ti–C are collected and summarized in Table S3.3. The order for the atmoic ratios of at%_(Ti-C) / at%_(C-C) in different samples is: TiO₂-0/650 < TiO₂-CC < TiO₂-0.1/675 < TiO₂-1/725 < TiO₂-0.5/700 < TiO₂-DC, which is consistent with the order for the ratios of I_D/I_G in Raman result if not consider the pristine sample TiO₂-0/650, implying the order for the content of doped carbon in these samples. Furthermore, all the O1s spectra can be fitted by three peaks at 529.8 eV, 530.8 eV and 531.6 eV, as shown in Fig. 3.5(d), these three peaks are ascribed to lattice oxygen, absorbed O^{v-} species and hydroxyls species OH⁻ respectively [22, 50]. Clearly, the peaks position of lattice oxygen from TiO₂-0.1/675, TiO₂-0.5/700, TiO₂-1/725 and TiO₂-DC are shifted towards lower energy. This shift can be attributed to the decrease of the oxidation state [51, 52], indicating the presence of C–O–Ti bond. Thus, the successful carbon doping is confirmed in carbon coated and doped TiO₂ samples such as, TiO₂-0.1/675, TiO₂-0.5/700 and TiO₂-1/725 and also in carbon doped TiO₂ (TiO₂-DC). The XPS analysis provides the detailed information about the existence of doped carbon in TiO₂. Combining XPS result with synthesis methods used, TEM and Raman results, it can be concluded that the “one pot” simultaneous coating and doping of TiO₂ was successful and that the carbon doped TiO₂ contains only doped carbon and the carbon coated TiO₂ sample contains only the coated carbon while carbon coated and doped TiO₂ contain indeed both coated and doped carbon.

3.3.3 Optical properties

The optical absorption property of semiconductors is correlated with the electronic structure, being the key factor in determining photocatalytic performance [53, 54]. The colour of as-prepared anatase TiO₂ calcined at phase transition temperature (TiO₂-0/650, TiO₂-0.1/675, TiO₂-0.5/700 and TiO₂-1/725) changes from light grey to black as the carbon content increases from 0.0 wt% to 4.0 wt% as seen in ordinary photographs in Fig. S3.1. In order to understand the photocatalytic characteristics of these samples, the typical optical properties of the above-mentioned samples were measured by UV-vis spectroscopy. It can be seen from Fig. S3.14 that, the pristine TiO₂ (TiO₂-0/650) shows a sharp rising of absorption at 396 nm (3.13 eV) which is typical absorption edge of TiO₂. Comparing to pristine TiO₂, the carbon coated and doped

samples ($\text{TiO}_2\text{-}0.1/675$, $\text{TiO}_2\text{-}0.5/700$ and $\text{TiO}_2\text{-}1/725$) show an increased absorption in the visible-light region with increasing amount of carbon loading. The absorption of $\text{TiO}_2\text{-CC}$ is between that of $\text{TiO}_2\text{-}0.5/700$ and $\text{TiO}_2\text{-}1/725$. Due to the broad background of absorption in the visible light region, band gap energy of these samples could not be observed. After removing coated carbon in TiO_2 by calcination $\text{TiO}_2\text{-}0.5/700$ under air, absorption of the carbon doped sample $\text{TiO}_2\text{-DC}$ in visible-light region decreases dramatically. But $\text{TiO}_2\text{-DC}$ still gives higher absorption in both UV and slight visible-light region than pristine TiO_2 . The absorption edge of $\text{TiO}_2\text{-DC}$ is found to be 412 nm (3.00 eV). The slight red-shift of 16 nm may be caused by the modification of doped carbon in TiO_2 . Carbon doping can alter the electronic structure of TiO_2 by introducing localized states in the bandgap and also reconstruct the surface structure of TiO_2 which facilitates the charge transfer^[55-57]. Carbon coating widen the absorption region of TiO_2/C system ranging from UV to visible or even near-infrared (NIR) region. Increasing carbon content can extend the absorption range of carbon modified TiO_2 owing to on one hand the high absorption in the whole wavelength range from 200–2500 nm of carbon and also to the doped carbon, on the other hand. Carbon coating and doping improves thus efficiency of light utilization of TiO_2 and the followed photocatalytic activity.

3.3.4 Photocatalytic & Photoelectrochemical activity

3.3.4.1 Photocatalytic activity

To access the synergistic effect of carbon coating and doping on the photocatalytic activity of as-prepared samples, the degradation of Methylene blue (MB) under the full spectrum light irradiation is firstly investigated (Figs. S3.15–S3.21). The simultaneous carbon coated and doped samples obtained by calcination at phase transition temperature ($\text{TiO}_2\text{-}0/650$, $\text{TiO}_2\text{-}0.1/675$, $\text{TiO}_2\text{-}0.5/700$ and $\text{TiO}_2\text{-}1/725$) exhibited the best activity in their corresponding series: $\text{TiO}_2\text{-}0/T$, $\text{TiO}_2\text{-}0.1/T$, $\text{TiO}_2\text{-}0.5/T$ and $\text{TiO}_2\text{-}1/T$, respectively as shown in Fig. S3.19.

Their photocatalytic degradation performance as well as other samples $\text{TiO}_2\text{-CC}$ and $\text{TiO}_2\text{-DC}$ are summarized in Fig. S3.22. The blank experiment of MB degradation without the presence of any photocatalyst shows a very low degradation rate (black line in Fig. S3.22(a)) less than 10% after 240 min. This value was taken into consideration while calculating the efficiency of all the tested samples. The $\text{TiO}_2\text{-}0/650$ sample exhibited very poor photocatalytic activity, with only 26% of methylene blue degradation during 60 min. The samples $\text{TiO}_2\text{-}0.1/675$, $\text{TiO}_2\text{-}0.5/700$ and $\text{TiO}_2\text{-}1/725$ degraded 67%, 85% and 70% of MB during 60min. The carbon coated TiO_2 ($\text{TiO}_2\text{-CC}$) shows more adsorption under dark environment and much less activity on

photocatalytic degradation comparing to both doped and coated TiO₂, such as TiO₂-0.5/700. The doped TiO₂ (TiO₂-DC) obtained by removing all the coated carbon by calcination of TiO₂-0.5/700 under air atmosphere, shows a significant decrease in the photocatalytic activity to the same scale with that of pristine TiO₂ while the photocatalytic activity of carbon doped and coated TiO₂ is much superior to that of pristine TiO₂. Furthermore, the TiO₂-0.5/700 sample showed a photo-degradation activity 5, 4 and 2 times higher than that of pristine TiO₂ (TiO₂-0/650), carbon doped TiO₂ (TiO₂-DC) and carbon coated TiO₂ (TiO₂-CC), respectively. The corresponding kinetics (*k*) of MB degradation with different samples are illustrated in Fig. S3.22(b). The order for the photocatalytic degradation rates of MB is as follow: TiO₂-0.5/700 > TiO₂-0.1/675 > TiO₂-1/725 > TiO₂-CC > TiO₂-DC > TiO₂-0/650.

Clearly, simultaneous carbon doping and coating are indispensable for enhancing the photocatalytic activity of TiO₂. The crystallization degree and specific surface area of anatase TiO₂ increase with carbon doping and coating benefiting the photocatalytic activity. Simultaneously doped and coated carbon can enhance the red-shift of the absorption edge of TiO₂ to visible light region. Thus, the photogeneration of electron / hole pairs is highly promoted under full spectrum light irradiation compared to independently carbon doping or carbon coating. Due to the synergistic effect of carbon doping and coating, the “one pot” synthesised carbon doped and coated TiO₂ exhibited highly enhanced photocatalytic activity under visible light. It is worth noting that, with more content of carbon in TiO₂, for example, 4.0 wt% in the sample TiO₂-1/725, TiO₂ receives less photoenergy after light penetration through the thicker carbon layer, meanwhile the diffusion rate of reactive molecules might also be reduced. The photogeneration of electron / hole pairs and the followed photocatalytic reactions are obstructed by high carbon content. The sample TiO₂-0.5/700 calcined at transition temperature containing 2.0 wt% carbon exhibits the highest kinetic constant as well as the best photocatalytic activity. Besides, the photocatalytic stability of the photocatalyst TiO₂-0.5/700 is estimated by recycling tests as exhibited in Fig. S3.22(c). In the third run, no obvious decrease is observed. The excellent durability of carbon doped and coated TiO₂ photocatalyst is therefore ensured.

3.3.4.2 Photocatalytic H₂ production

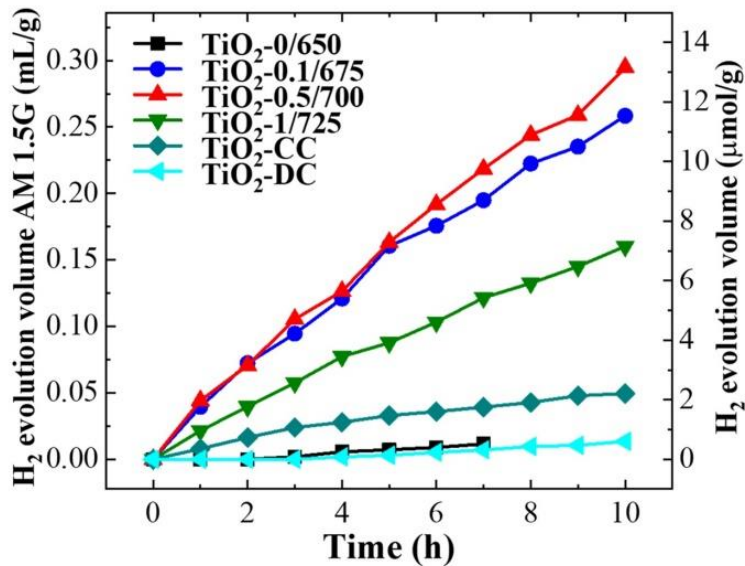


Fig. 3.6. Photocatalytic H₂ evolution over different TiO₂ samples.

The photocatalytic H₂ evolution activities over various photocatalysts were evaluated under simulated solar light irradiation and the corresponding results are presented in Fig. 3.6. The pristine TiO₂ exhibits a rather low H₂ production rate of 0.077 $\mu\text{mol h}^{-1} \text{g}^{-1}$, due to the large band gap, weak light absorption and massive recombined charge carriers under solar light [19]. The coated carbon in TiO₂ effectively enhances the charge transfer and separation, leading to an enhancement in H₂ production compared to pristine TiO₂. Carbon coated TiO₂ (TiO₂-CC) thus also gives an enhancement in H₂ production rate (0.22 $\mu\text{mol h}^{-1} \text{g}^{-1}$) compared to pristine TiO₂. However, most of these absorbed photons cannot be utilized without the help of doped carbon. The doped carbon in TiO₂ crystal lattice can introduce new states above the valence band of TiO₂ [57–60]. Electrons are then emitted from the carbon doping level to the conduction band of TiO₂ under visible light irradiation. Thus, the carbon doped and coated TiO₂, TiO₂-0.5/700 exhibits an outstanding photocatalytic H₂ production of 1.3 $\mu\text{mol h}^{-1} \text{g}^{-1}$, being 17, 6 and 18 times higher than that of pristine TiO₂, carbon coated TiO₂ (TiO₂-CC) and carbon coated TiO₂ (TiO₂-DC). It can be concluded that the synergistic effects of carbon doping and coating lead to a largely enhanced photocatalytic H₂ production. It is clearly seen that the highly enhanced H₂ production owing to simultaneous carbon coating and doping is not a simple imposition of the effect produced by separate doping and coating, a synergistic effect of carbon coating and doping occurs.

3.3.4.3 Photoelectrochemical (PEC) water splitting

To better understand the synergistic effect of carbon coating and doping on the photocatalytic activity, systematic photoelectrochemical measurements were carried out on photoelectrodes fabricated with TiO₂-0/650, TiO₂-0.5/700, TiO₂-CC and TiO₂-DC. As shown in Fig. 3.7(a), the TiO₂-0.5/700 photoelectrode exhibits a much higher photocurrent density throughout the whole potential window under AM 1.5 illumination, suggesting highly efficient charges separation. At 1.23 V vs. RHE, the photocurrent of TiO₂-0.5/700 reached a high value of 28 $\mu\text{A cm}^{-2}$ which is 37, 8 and 11 times higher than that of pristine TiO₂ (0.75 $\mu\text{A cm}^{-2}$), carbon coated TiO₂ (TiO₂-CC: 3.4 $\mu\text{A cm}^{-2}$) and carbon doped TiO₂ (TiO₂-DC: 2.4 $\mu\text{A cm}^{-2}$), respectively (Fig. 3.7(a)). The in-situ and simultaneous carbon doping and coating in TiO₂ specially enhance the photogeneration and separation of electron-hole pairs and thereby resulted in higher photocurrent response [61–63]. The Fig. 3.7(b) illustrates variation of the photocurrent density obtained from TiO₂-0.5/700 within 120h. The carbon coated and doped TiO₂ can be very stable after 13h testing, and shows around 23% decrease of photocurrent density after 120 h testing. This result shows that our carbon coated and doped sample with a good stability for water splitting for such long period.

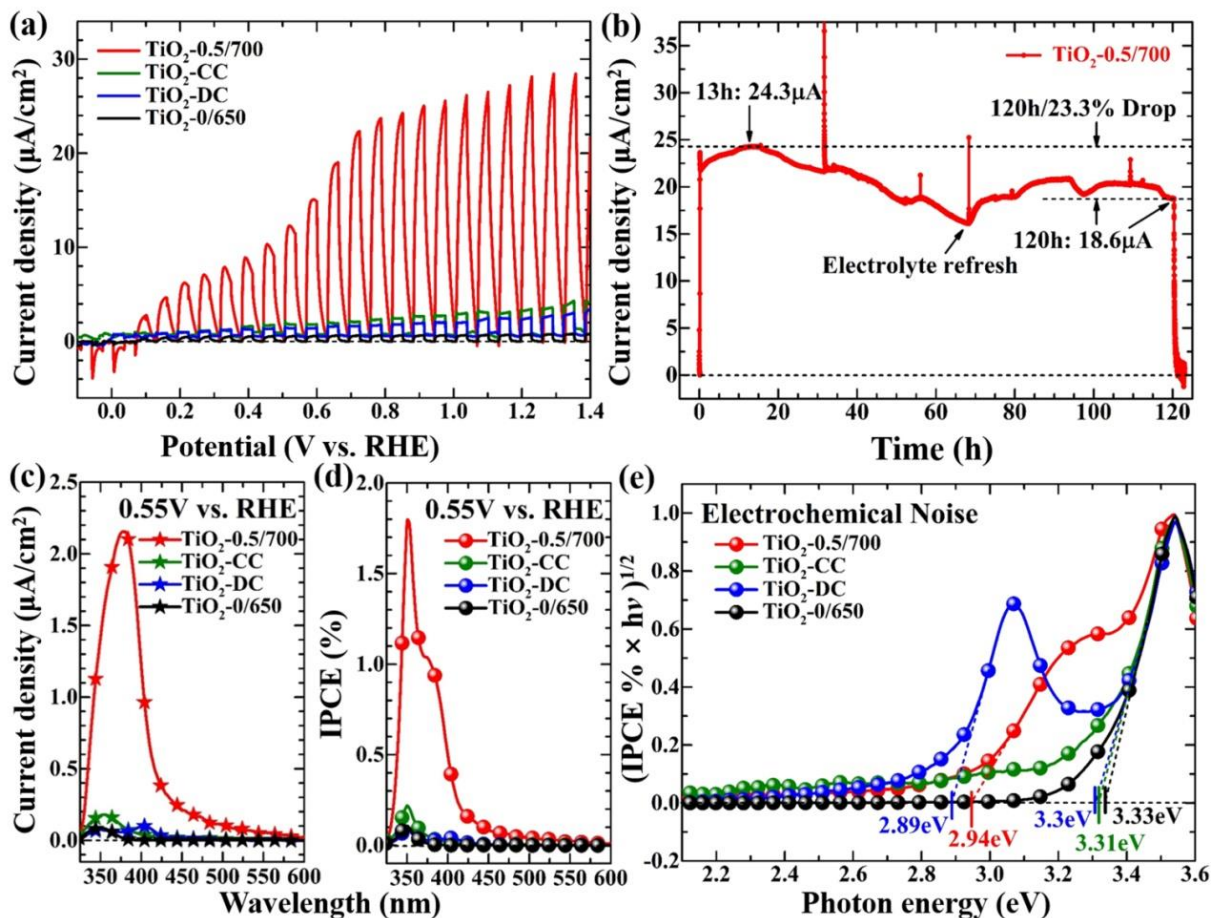


Fig. 3.7. (a) Linear sweep voltammogram (LSV) curves of different photoelectrodes fabricated with $\text{TiO}_2\text{-0/650}$, $\text{TiO}_2\text{-0.5/700}$, $\text{TiO}_2\text{-CC}$ and $\text{TiO}_2\text{-DC}$; (b) photocurrent density-time plot of $\text{TiO}_2\text{-0.5/700}$ at applied voltage of 1.2 V (vs. RHE); (c) photocurrents density versus the monochromatic light; (d) derived IPCE (%) spectra; (e) band gap determination extracted from IPCE spectra by a function of $(\text{IPCE}\% \times h\nu)^{1/2}$ vs. $h\nu$.

The photocurrents of different photoanodes were measured under monochromatic light irradiation as shown in Fig. 3.7(c). Significantly higher photocurrent response is observed in both UV and visible region for $\text{TiO}_2\text{-0.5/700}$. The maximum photocurrent of $\text{TiO}_2\text{-0.5/700}$ ($2.2 \mu\text{A cm}^{-2}$) at 360 nm is around 244 and 12 times higher than that of pristine TiO_2 ($\text{TiO}_2\text{-0/650}$) and $\text{TiO}_2\text{-CC}$ (0.008 and $0.18 \mu\text{A cm}^{-2}$ at 350 nm, respectively). The photocurrent of $\text{TiO}_2\text{-CC}$ is 20 times higher than that of pristine TiO_2 at 350 nm. The pristine TiO_2 and $\text{TiO}_2\text{-CC}$ show no apparent photocurrent under visible light. Obviously, the independent carbon coating can only promote the photocurrent under UV light. At the wavelength of 400 nm, the photocurrent of $\text{TiO}_2\text{-0.5/700}$ ($1.3 \mu\text{A cm}^{-2}$) is 100 times higher than that of $\text{TiO}_2\text{-DC}$ ($0.13 \mu\text{A cm}^{-2}$). Without carbon coating, the improvement of PEC performance of TiO_2 is quite limited by carbon doping. All of these results give the insight that, the simultaneous carbon doping and

coating highly enhance the photoactivity of the TiO₂ under both UV and visible light region. The incident monochromatic photon to current conversion efficiency (IPCE) can be given as a function of wavelength (λ) as shown in Eq. (5).

$$\text{IPCE}(\lambda) = \frac{\text{electrons/cm}^2/\text{s}}{\text{photons/cm}^2/\text{s}} = \frac{|i_{\text{ph}}(\text{mA/cm}^2)| \times 1239.8(\text{V} \times \text{nm})}{P_{\text{mono}}(\text{mW/cm}^2) \times \lambda(\text{nm})}, \quad (5)$$

where 1239.8 V × nm is the product of h (Planck's constant) and P_{mono} is the calibrated illumination power intensity of the monochromatic light with wavelength of λ . The IPCE (%) of the carbon coated and doped TiO₂, TiO₂-0.5/700 is 1.8 at 350 nm and 0.5 at 400 nm as shown in Fig. 3.7(d).

In addition, the band gaps of samples can be evaluated from the IPCE spectra by a Tauc plotting (IPCE% $\times h\nu$)^{1/2} versus photon energy ($h\nu$)^[64, 65] as shown in Fig. 3.7(e). The extracted band gaps of TiO₂-0/650, TiO₂-0.5/700 and TiO₂-CC were found to be 3.33, 2.94 and 3.31 eV. The carbon doped sample, TiO₂-DC shows two optical thresholds in the tauc plot corresponding to two band gap energies, one is 3.30 eV from the intrinsic TiO₂, and another is 2.89 eV from the carbon doped level above the valence band of TiO₂.

The Mott-Schottky measurement was employed to evaluate the flat band potential V_{fb} of TiO₂ electrodes as shown in Figs. S3.23 and S3.24. The V_{fb} of TiO₂-0/650, TiO₂-0.5/700, TiO₂-CC and TiO₂-DC were observed at -0.056, -0.064, -0.063 and -0.041 V, respectively. The flat potential (in the units of volts, V) can be referred to the position of conduction band (in the units of electron volts, eV)^[66, 67]. The order of carrier densities obtained at 2 kHz is: TiO₂-0.5/700 (3.37×10^{27}) > TiO₂-CC (2.75×10^{27}) > TiO₂-DC (2.55×10^{27}) > TiO₂-0/650 (2.38×10^{27}). Based on above results, we proposed the band structures of as-prepared samples, TiO₂-0/650, TiO₂-0.5/700, TiO₂-CC and TiO₂-DC corresponding to pristine TiO₂, carbon coated and doped TiO₂, carbon coated TiO₂ and carbon doped TiO₂, respectively, as seen in Fig. 3.8.

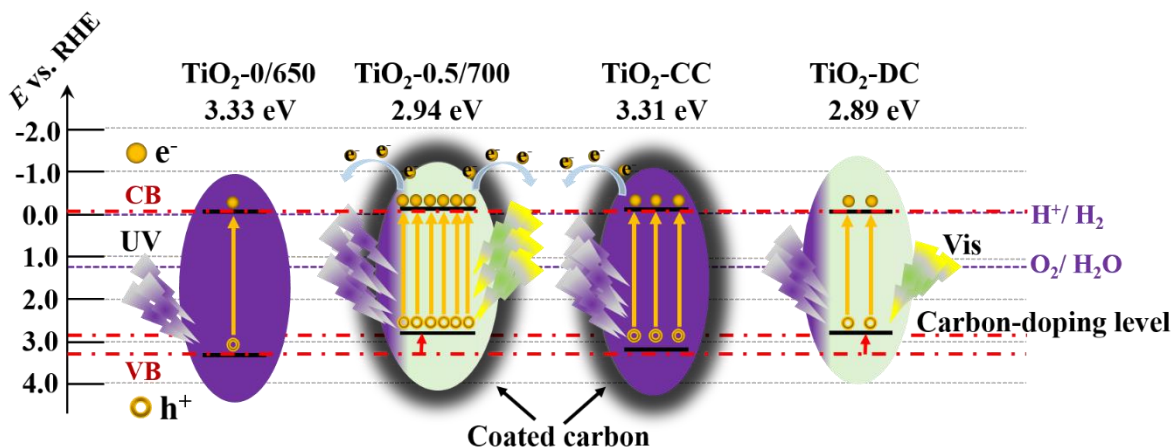


Fig. 3.8. Proposed band structure of as-prepared samples and redox potentials of water splitting.

The positions of valence band of TiO₂-0.5/700 and TiO₂-DC shifted more negatively due to doping level created by carbon doping. The band alignment by coated carbon in TiO₂ is very limited. The coated carbon only enhances the UV-light absorption without the help of doped carbon. The carbon doping can narrow the band gap of TiO₂ extending the absorption edge to visible light region. The introduced new state from doped carbon in TiO₂ crystal lattice may locate above the valence band of TiO₂ resulting in the lowered excitation energy. Electrons are generated from the carbon doping level to the conduction band of TiO₂ under visible light irradiation [58–61]. The defect states induced by carbon doping may act as acceptors trapping photoexcited electrons facilitating electrons transfer under visible light [68, 69]. However, with only carbon doping, the light absorption in both UV and visible light is defined. The rapid recombination of photogenerated electron/hole pairs cannot be prevented by only carbon doping resulting in low carrier density in carbon doped TiO₂. With the help of coated carbon, the light absorption can be enhanced under both UV and visible light region. These large amount of absorbed carriers can be transferred to the surface of TiO₂ instantaneously due to the good conductance of carbon layer around TiO₂. The charges separation and mass transport can be significantly improved by coated carbon. Thus, the amount of charge carriers is highly increased under the help of both carbon doping and coating.

Moreover, the carbon doped and coated TiO₂ has larger specific surface area which improves the utilization of solar light, provides more active sites and captures more intermediate products for photocatalytic reactions. During the photocatalytic water splitting process, these H₂O molecules and protons on electrodes will be reduced and oxidized by electrons and holes into oxygen and hydrogen respectively. It is clear to see that such carbon-induced synergic effect allows a wide range absorption of solar energy and efficient electron-hole pair's separation and

consequently highly enhanced photocatalytic activity for the application of TiO₂ photocatalysts.

3.4 Conclusions

We have presented “one pot” simultaneous carbon coating and doping of TiO₂ by simply hydrolysis TiCl₄ in fructose solution. By controlling the concentration of fructose, the content of carbon can be adjusted. The doped carbon in TiO₂ exhibits the suppression effect of phase transformation from anatase to rutile phase by increasing the starting phase transformation temperature while the coated carbon layer keeps the small crystallite size of TiO₂. The carbon doped and coated TiO₂ exhibited 5 times photocatalytic degradation rate, 23 times H₂ production rate and more than 37 times photocurrent response as that of pristine TiO₂ under simulated sunlight. The high photocatalytic and photoelectrochemical performance could be attributed to synergistic effect of both carbon doping and coating in TiO₂, which could not only improve the light absorption both in UV and visible light region, but also efficiently promote the mobility and separation of photogenerated charge carriers. The comprehensive understanding on the synergistic effect of carbon coating and doping can serve an important contribution to researchers in the fields of Photocatalytic / Photoelectrochemical and energy-related sciences.

References

- [1] M. Zalfani, B. Van der Schueren, Z.Y. Hu, J.C. Rooke, R. Bourguiga, M. Wu, Y. Li, G.V. Tendeloo, B.L. Su, *J. Mater. Chem. A* 3 (2015) 21244–21256.
- [2] Y. Yang, L.C. Yin, Y. Gong, P. Niu, J.Q. Wang, L. Gu, X. Chen, G. Liu, L. Wang, H.M. Cheng, *Adv. Mater.* 30 (2018) 1704479.
- [3] W. Ren, Z. Ai, F. Jia, L. Zhang, X. Fan, Z. Zou, *Appl. Catal. B* 69 (2007) 138–144.
- [4] A. Parker, M. Marszewski, M. Jaroniec, *ACS Appl. Mater. Interfaces* 5 (2013) 1948–1954.
- [5] R. Leary, A. Westwood, *Carbon* 49 (2011) 741–772.
- [6] J. Lu, Y. Wang, J. Huang, J. Fei, L. Cao, C. Li, *Dyes. Pigm.* 144 (2017) 203–211.
- [7] Y. Zhang, J. Chen, L. Hua, S. Li, X. Zhang, W. Sheng, S. Cao, J. Hazard. Mater. 340 (2017) 309–318.
- [8] V.R. Posa, V. Annavaram, J.R. Koduru, P. Bobbala, A.R. Somala, *J. Exp. Nanosci.* 11 (2016) 722–736.
- [9] X. Zhang, Y. Zhao, *Mater. Res. Express* 6 (2019) 036109.
- [10] Y. Park, W. Kim, H. Park, T. Tachikawa, T. Majima, W. Choi, *Appl. Catal. B* 91 (2009) 355–361.
- [11] Z. Noorimotlagh, I. Kazeminezhad, N. Jaafarzadeh, M. Ahmadi, Z. Ramezani, S.S. Martinez, *J. Hazard. Mater.* 350 (2018) 108–120.
- [12] J. Tang, Y. Yuan, T. Liu, S. Zhou, *J. Power Sources* 274 (2015) 170–176.
- [13] J. Chen, K. Li, Y. Luo, X. Guo, D. Li, M. Deng, S. Huang, Q. Meng, *Carbon* 47 (2009) 2704–2708.
- [14] T. Sun, B.D. Levin, J.J. Guzman, A. Enders, D.A. Muller, L.T. Angenent, J. Lehmann, *Nat.*

- Commun. 8 (2017) 14873.
- [15] L. Ji, Y. Zhang, S. Miao, M. Gong, X. Liu, Carbon 125 (2017) 544–550.
- [16] C. Yang, X. Zhang, J. Qin, X. Shen, R. Yu, M. Ma, R. Liu, J. Catal. 347 (2017) 36–44.
- [17] X. Wang, S. Meng, X. Zhang, H. Wang, W. Zhong, Q. Du, Chem. Phys. Lett. 444 (2007) 292–296.
- [18] L. Zhao, X. Chen, X. Wang, Y. Zhang, W. Wei, Y. Sun, M. Antonietti, M.-M. Titirici, Adv. Mater. 22 (2010) 3317–3321.
- [19] C.D. Valentin, G. Pacchioni, A. Selloni, Chem. Mater. 17 (2005) 6656–6665.
- [20] X. Cheng, H. Liu, Q. Chen, J. Li, P. Wang, Carbon 66 (2014) 450–458.
- [21] C. Chen, M. Long, H. Zeng, W. Cai, B. Zhou, J. Zhang, Y. Wu, D. Ding, D. Wu, J. Mol. Catal. A Chem. 314 (2009) 35–41.
- [22] Y. Wang, G. Duan, Y. Zhu, H. Zhang, Z. Xu, Z. Dai, W. Cai, Sensor. Actuat. B Chem. 228 (2016) 74–84.
- [23] B. Li, Z. Zhao, F. Gao, X. Wang, J. Qiu, Appl. Catal. B 147 (2014) 958–964.
- [24] Z. Liang, X. Bai, P. Hao, Y. Guo, Y. Xue, J. Tian, H. Cui, Appl. Catal. B 243 (2019) 711–720.
- [25] G.K. Mor, O.K. Varghese, M. Paulose, K. Shankar, C.A. Grimes, Sol. Energ. Mat. Sol. C 90 (2006) 2011–2075.
- [26] W. Zheng, X. Liu, Z. Yan, L. Zhu, ACS Nano 3 (2008) 115–122.
- [27] T.H. Wang, A.M. Navarrete-López, S. Li, D.A. Dixon, J.L. Gole, J. Phys. Chem. A 114 (2010) 7561–7570.
- [28] C. Falco, N. Baccile, M.M. Titirici, Green Chem. 13 (2011) 3273–3281.
- [29] J. Poerschmann, B. Weiner, R. Koehler, F.D. Kopinke, ACS Sustain. Chem. Eng. 5 (2017) 6420–6248.
- [30] W.R. Gunther, Y. Wang, Y. Ji, V.K. Michaelis, S.T. Hunt, R.G. Griffin, Y.R. Leshkov, Nat. Commun. 3 (2012) 1109.
- [31] J.M. Anderson, R.L. Johnson, K. Schmidt-Rohr, B.H. Shanks, Carbon 74 (2014) 333–345.
- [32] K. Sing, Pure. Appl. Chem. 54 (1982) 2201–2218.
- [33] F.I. Toshiaki Ohsaka, Y. Fujiki, J. Raman. Spectrosc. 7 (1978) 321–324.
- [34] L.W. Zhang, H.B. Fu, Y.F. Zhu, Adv. Funct. Mater. 18 (2008) 2180–2189.
- [35] S. Brown, A. Jorio, A.P. Corio, M. Dresselhaus, G. Dresselhaus, R. Saito, K. Kneipp, Phys. Rev. B 63 (2001) 155414.
- [36] M.J. Matthews, M.A. Pimenta, G. Dresselhaus, M.S. Dresselhaus, and M. Endo, Phys. Rev. B 59 (1999) R6585.
- [37] Y. Wang, D.C. Alsmeyer, R.L. McCreery, Chem. Mater. 2 (1990) 557–563.
- [38] J. Kaufman, S. Metin, D. Saperstein, Phys. Rev. B 39 (1989) 13053.
- [39] C.G. Salzmann, S.A. Llewellyn, G. Tobias, M.A. Ward, Y. Huh, M.L. Green, Adv. Mater. 19 (2007) 883–887.
- [40] M. Pimenta, G. Dresselhaus, M.S. Dresselhaus, L. Cancado, A. Jorio, R. Saito, Phys. Chem. Chem. Phys. 9 (2007) 1276–1290.
- [41] W.K. Jo, N.C.S. Selvam, Appl. Catal. A-Gen. 525 (2016) 9–22.
- [42] B. Erdem, R.A. Hunsicker, G.W. Simmons, E.D. Sudol, V.L. Dimonie, M.S. ElAasser, Langmuir 17 (2001) 2664–2669.
- [43] W. Göpel, J.A. Anderson, D. Frankel, M. Jaehnig, K. Phillips, J.A. Schäfer, G. Rocker, Surf. Sci. 139 (1984) 333–346.
- [44] W. Tu, Y. Zhou, Q. Liu, S. Yan, S. Bao, X. Wang, M. Xiao, Z. Zou, Adv. Funct. Mater. 23 (2013) 1743–1749.
- [45] B. Qiu, Y. Zhou, Y. Ma, X. Yang, W. Sheng, M. Xing, J. Zhang, Sci. Rep. 5 (2015) 8591.
- [46] J. Yang, H. Bai, X. Tan, J. Lian, Appl. Surf. Sci. 253 (2006) 1988–1994.
- [47] A. Jitianu, T. Cacciaguerra, R. Benoit, S. Delpeux, F. Beguin, S. Bonnamy, Carbon 42

- (2004) 1147–1151.
- [48] Q. Huang, S. Tian, D. Zeng, X. Wang, W. Song, Y. Li, W. Xiao, C. Xie, *ACS Catal.* 3 (2013) 1477–1485.
- [49] A. Voevodin, M. Capano, S. Laube, M. Donley, J. Zabinski, *Thin Solid Films* 298 (1997) 107–115.
- [50] G.P. López, D.G. Castner, B.D. Ratner, *Surf. Interface. Anal.* 17 (1991) 267–272.
- [51] M. Atashbar, H. Sun, B. Gong, W. Włodarski, R. Lamb, *Thin Solid Films* 326 (1998) 238–244.
- [52] B.M. Reddy, B. Chowdhury, P.G. Smirniotis, *Appl. Catal. A-Gen.* 211 (2001) 19–30.
- [53] J. Tang, Z. Zou, J. Ye, *Angew. Chem.* 116 (2004) 4563–4566.
- [54] J. Liu, H. Zhao, M. Wu, B. Van der Schueren, Y. Li, O. Deparis, J. Ye, G.A. Ozin, T. Hasan, B.L. Su, *Adv. Mater.* 29 (2017) 1605349.
- [55] X. Wu, S. Yin, Q. Dong, C. Guo, H. Li, T. Kimura, T. Sato, *Appl. Catal. B* 142 (2013) 450–457.
- [56] J. Shao, W. Sheng, M. Wang, S. Li, J. Chen, Y. Zhang, S. Cao, *Appl. Catal. B* 209 (2017) 311–319.
- [57] R. Asahi, T. Morikawa, T. Ohwaki, K. Aoki, Y. Taga, *Science* 293 (2001) 269–271.
- [58] L. Zhang, M.S. Tse, O.K. Tan, Y.X. Wang, M. Han, *J. Mater. Chem. A* 1 (2013) 4497–4507.
- [59] S.A. Ansari, M.-M. Khan, M.O. Ansari, M.H. Cho, *New J. Chem.* 40 (2016) 3000–3009.
- [60] S. Livraghi, M.C. Paganini, E. Giannello, A. Selloni, C.D. Valentin, G. Pacchioni, *J. Am. Chem. Soc.* 128 (2006) 15666–15671.
- [61] L. Zheng, S. Han, H. Liu, P. Yu, X. Fang, *Small* 12 (2016) 1527–1536.
- [62] J.H. Park, S. Kim, A.J. Bard, *Nano Lett.* 6 (2006) 24–28.
- [63] G. Wu, T. Nishikawa, B. Ohtani, A. Chen, *Chem. Mater.* 19 (2007) 4530–4537.
- [64] D. Wood, J. Tauc, *Phys. Rev. B* 5 (1972) 3144.
- [65] Z. Chen, H.N. Dinh, E. Miller, *Photoelectrochemical water splitting*, First ed., Springer, 2013, pp. 6–15.
- [66] A. Hankin, J. Alexander, G. Kelsall, *Phys. Chem. Chem. Phys.* 16 (2014) 16176–16186.
- [67] S. Huang, W. Luo, Z. Zou, *J. Phys. D* 46 (2013) 235108.
- [68] C.D. Valentin, G. Pacchioni, *Catal. Today* 206 (2013) 12–18.
- [69] Y. Xiao, X. Yu, Y. Gao, J. Liu, Z. Li, *Catal. Commun.* 102 (2017) 1–4.

Supplementary information

The ordinary photographs of TiO₂ products before annealing (F_x) and after annealing (TiO₂-x/T) are shown in Fig. S3.1, respectively. It can be seen that, before annealing, the as prepared F₀ product has a white colour. In samples with fructose additive (F_{0.1} to F₁), their colour turns into brownish yellow. With the increased concentration of fructose, the colour of the as-prepared TiO₂ products after calcination changed from grey to dark.

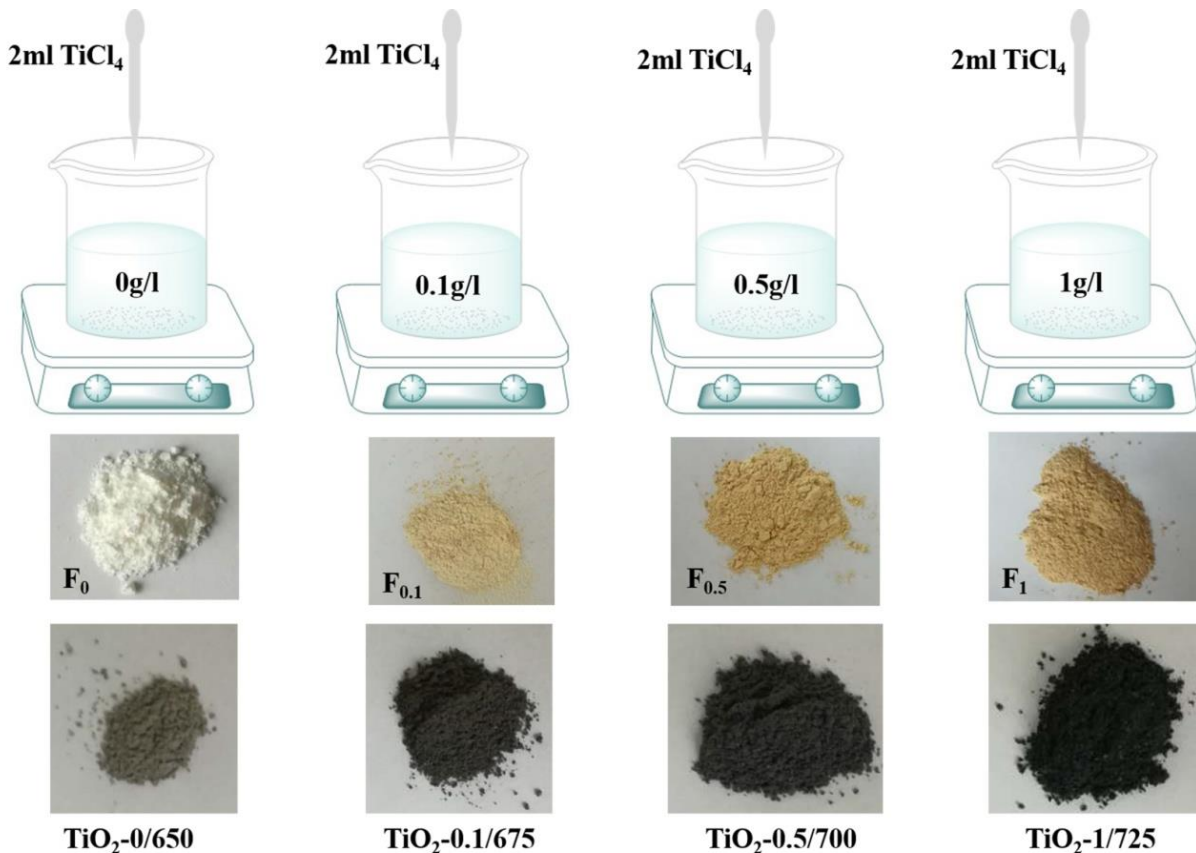


Fig. S3.1. The schematic diagram of synthetic procedure for preparation TiO₂ and carbon doped and coated TiO₂.

Thermogravimetric analysis (TGA) performed to estimate the carbon content in TiO₂. Fig. S3.2 presents the TGA-DSC result of as-prepared samples. For pure TiO₂, as shown in Fig. S3.2(a), the first rapid weight loss from 15 °C to 200 °C mainly originates from desorption of water molecules. The later slow weight loss corresponds to the gradual decomposition of chemisorbed hydroxyl species. For carbon coated and doped TiO₂, except the weight loss of water and hydroxyl species, the oxidation of carbon is attributable for the weight loss commencing at approximately 330 °C, 285 °C and 255 °C of TiO₂-0.1/T, TiO₂-0.5/T, TiO₂-1/T ($T = 500, 600$ and 700 °C) respectively. The corresponding derivative curves of weight loss displays remarkable peaks of weight loss resulting from carbon oxidation and reaching its maximum rate at around 420 °C. The average mass ratios of carbon in TiO₂-0/T, TiO₂-0.1/T, TiO₂-0.5/T and TiO₂-1/T are respectively 0 wt%, 0.28 wt%, 2.0 wt% and 4.0 wt%. Apparently, the carbon content increased with increasing concentration of fructose in precursor.

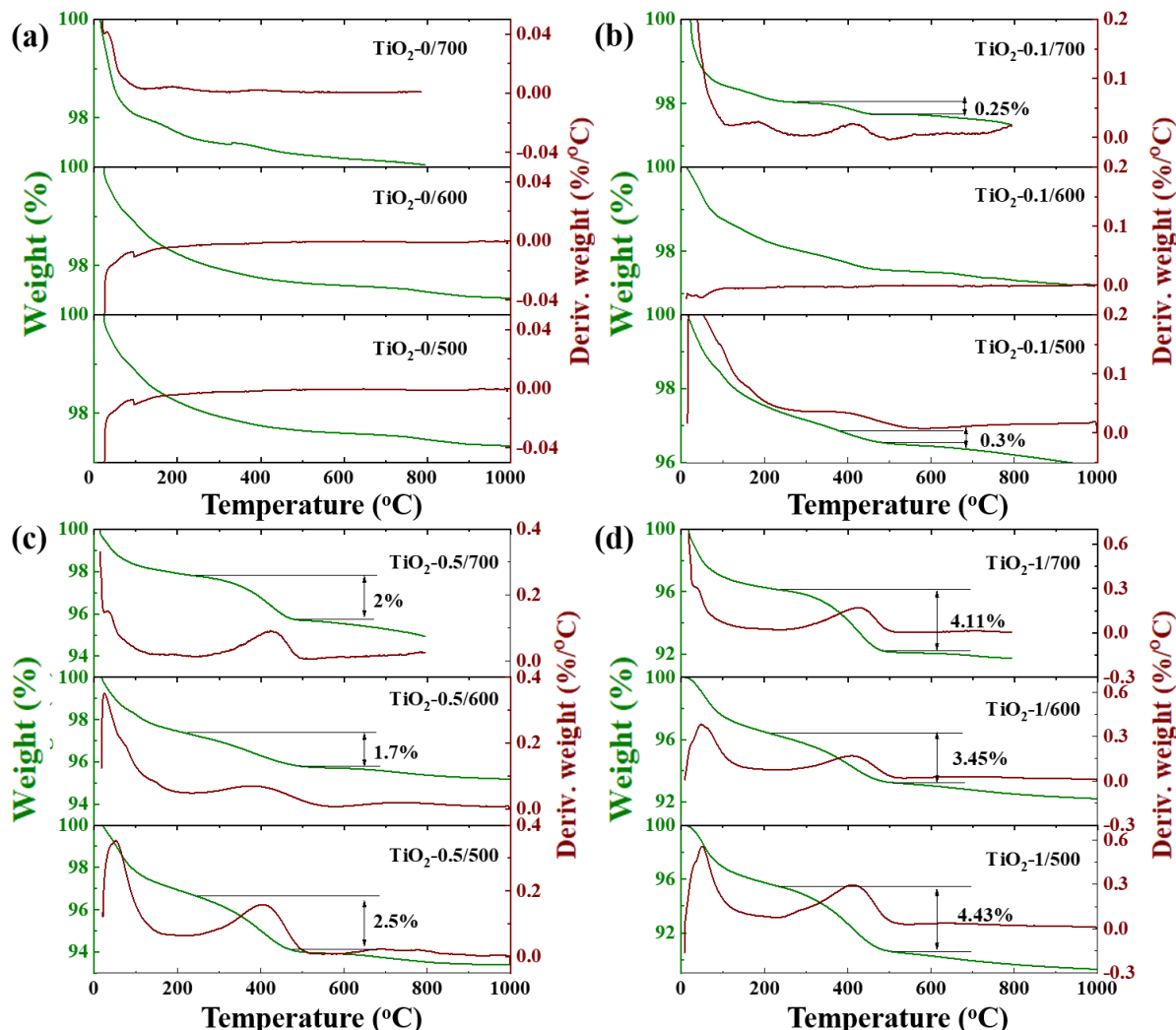


Fig. S3.2. The TGA-DSC curves of (a) TiO₂-0/T, (b) TiO₂-0.1/T, (c) TiO₂-0.5/T and (d) TiO₂-

$1/T$ ($T = 500, 600$ and $700\text{ }^{\circ}\text{C}$).

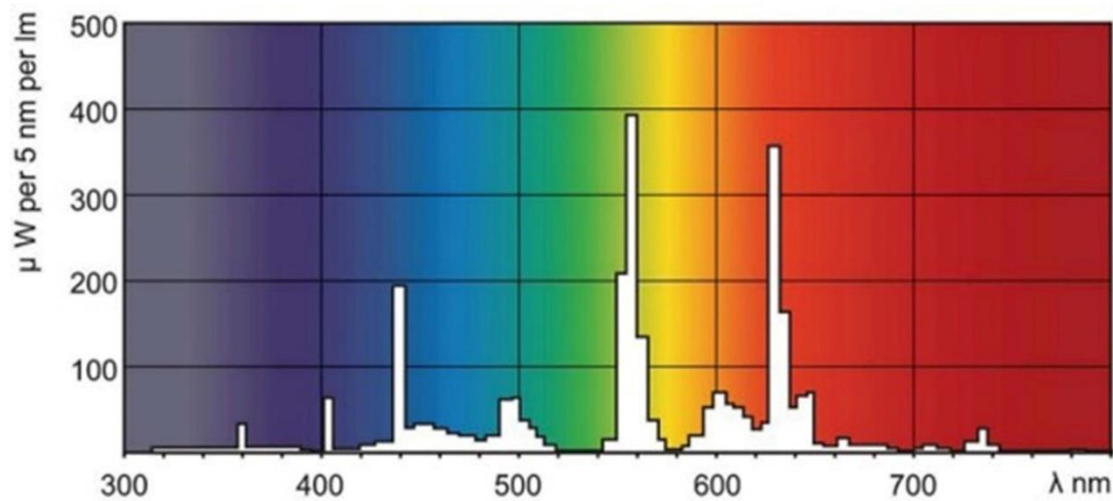


Fig. S3.3. Emission spectrum of the 18 W neon light lamp for the photocatalytic degradation of Methylene blue.

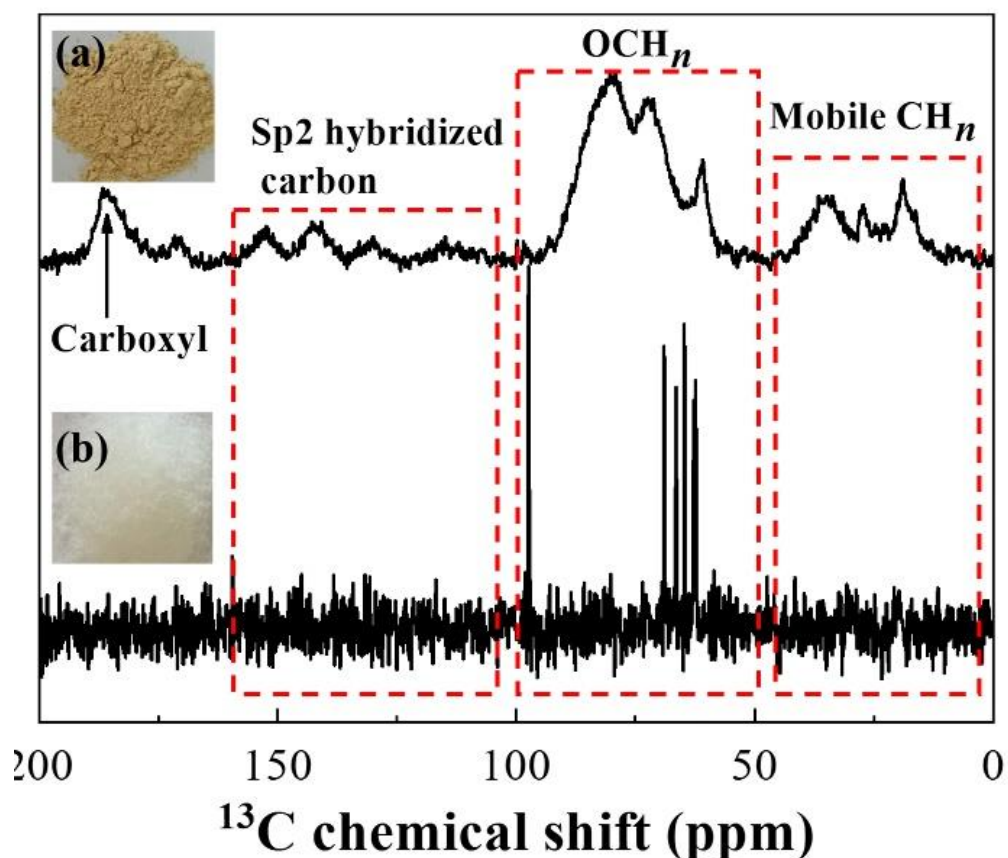


Fig. S3.4. Solid state ^{13}C NMR spectra and photography of (a) F_{0.5} and (b) Fructose.

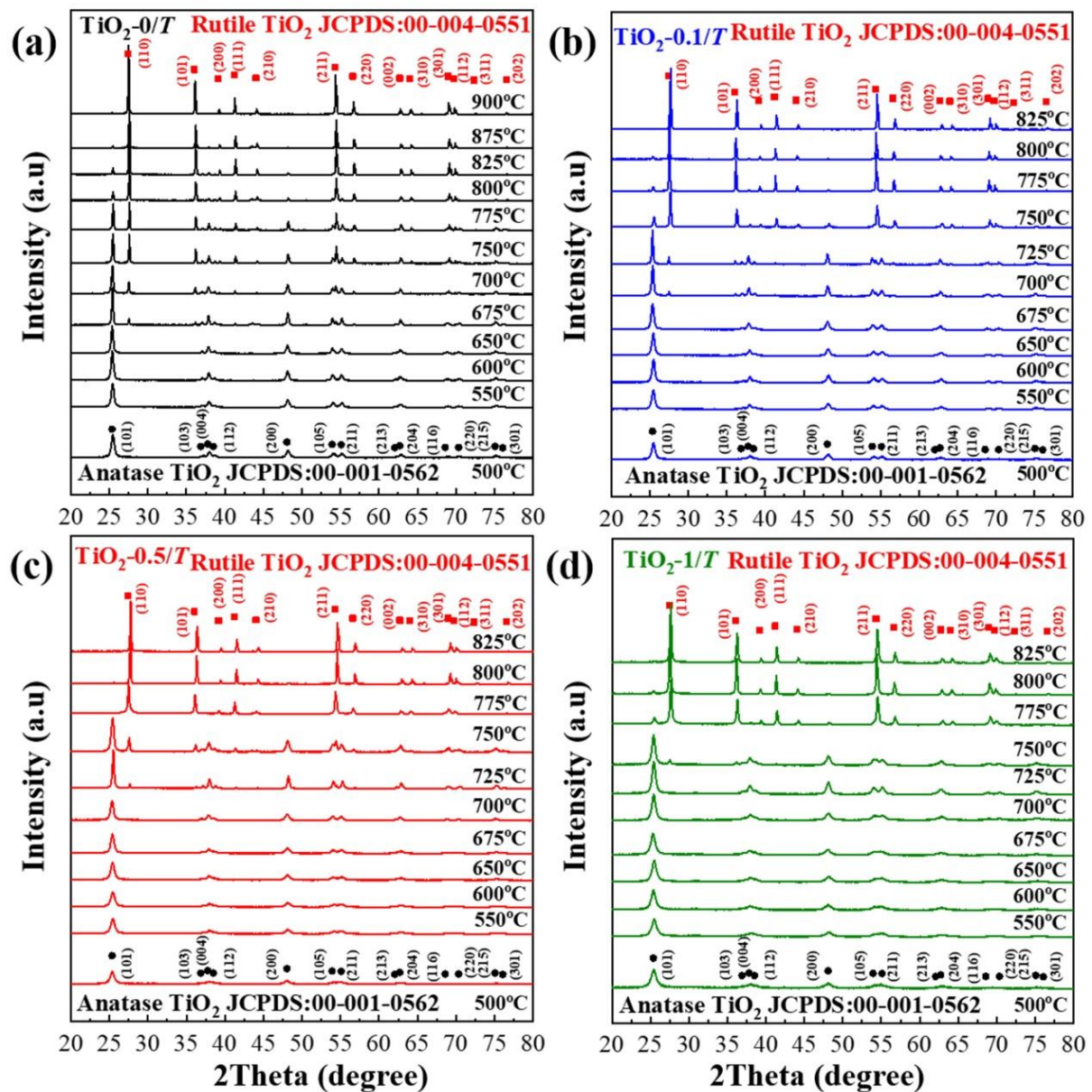


Fig. S3.5. X-ray diffraction patterns of (a) $\text{TiO}_2\text{-}0/T$, (b) $\text{TiO}_2\text{-}0.1/T$, (c) $\text{TiO}_2\text{-}0.5/T$ and (d) $\text{TiO}_2\text{-}1/T$ calcined at different temperature.

The original XRD peaks of (101) anatase planes of TiO_2 are all fitted by the software of X'Pert HighScore and the corresponding FWHM values are recorded as shown in Fig. S3.6. According to Scherrer equation:

$$\text{Crystallite size} = \frac{b\lambda}{D\cos\theta}$$

Where b is the shape factor with a typical value of about 0.9, λ is the X-ray wavelength, and $\lambda = 1.54060 \text{ \AA}$ (in the case of Cu K α 1). D is value of FWHM, θ is the Bragg angle. The crystallite size can thus be calculated.

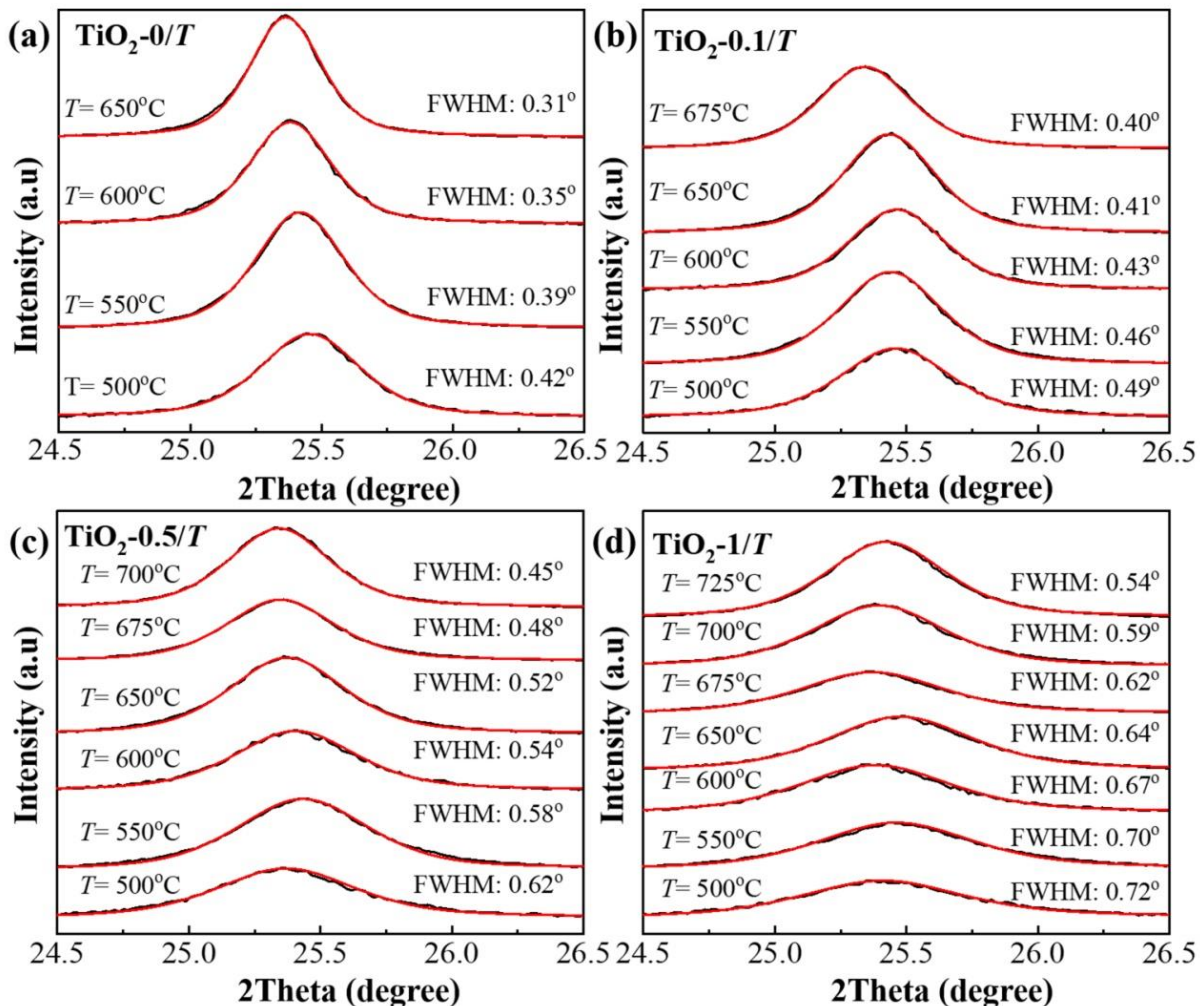


Fig. S3.6. (a) The enlarged XRD of (101) anatase planes (black line) and the corresponding fitted one (red) of all the as-prepared TiO_2 samples with pure anatase phase.

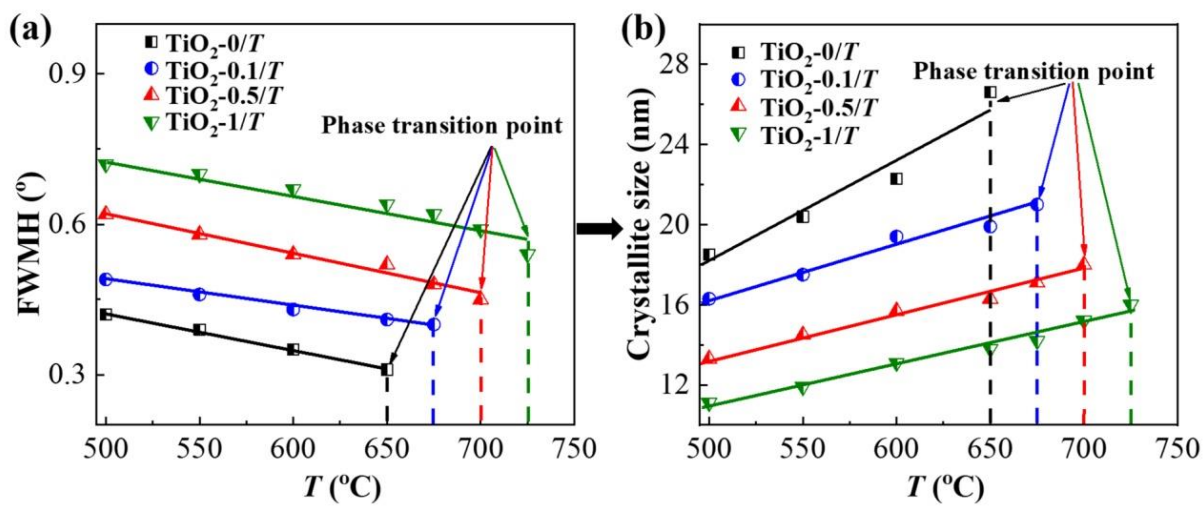


Fig. S3.7. (a) The FWHM values of (101) anatase planes and (b) calculated crystallite sizes of all the as-prepared TiO_2 samples with pure anatase phase.

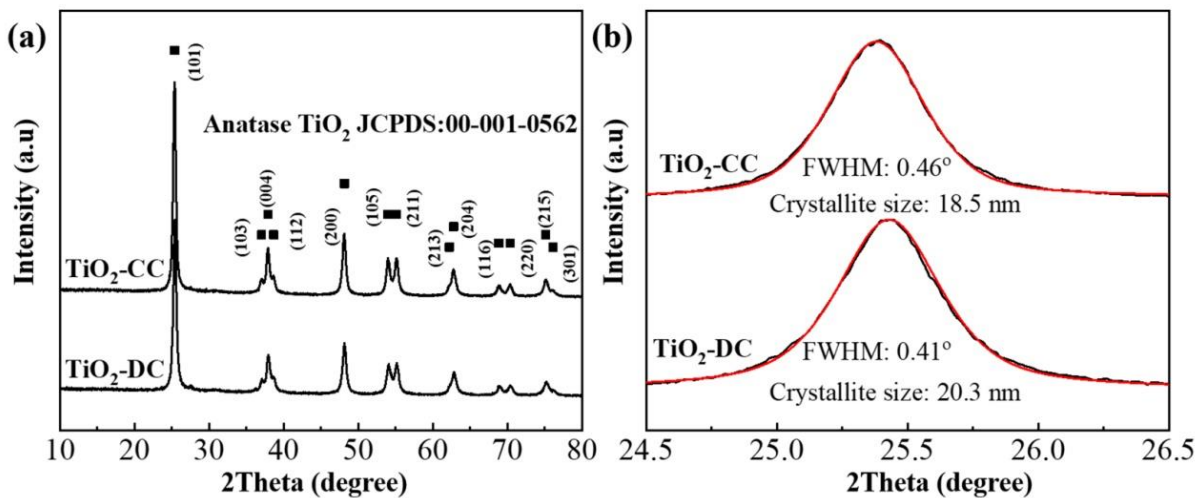


Fig. S3.8. (a) X-ray diffraction patterns of $\text{TiO}_2\text{-CC}$ and $\text{TiO}_2\text{-DC}$ samples; (b) The enlarged part of (101) anatase planes (black line) and the corresponding fitting one (red).

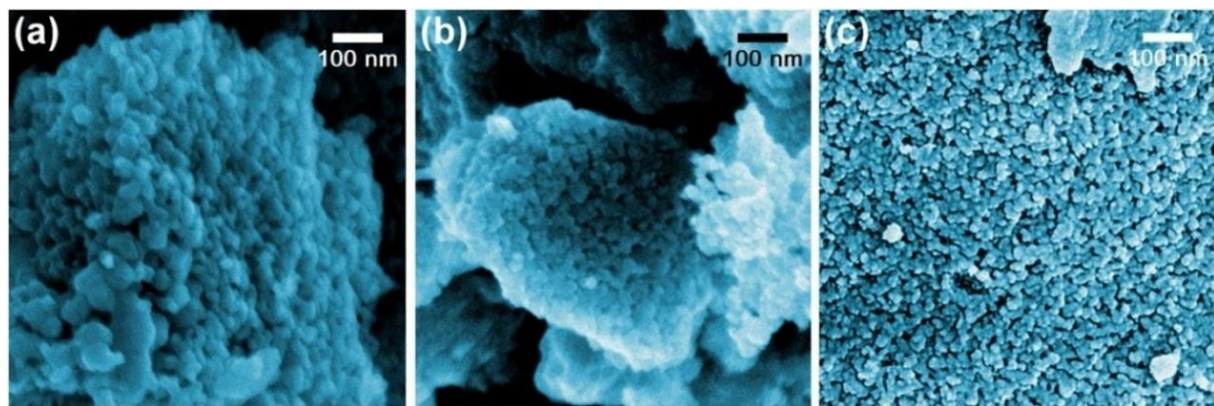


Fig. S3.9. SEM observation images of (a) $\text{TiO}_2\text{-}0/650$, (b) $\text{TiO}_2\text{-}0.5/700$ and (c) $\text{TiO}_2\text{-}1/725$, respectively.

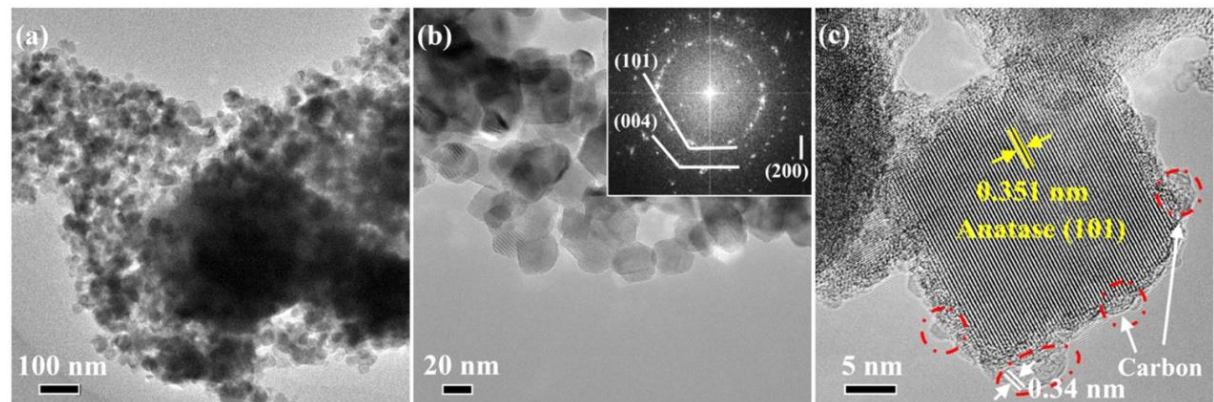


Fig. S3.10. (a) The TEM image, (b) SAED observation (inset) and (c) HRTEM image of $\text{TiO}_2\text{-}0.1/675$.

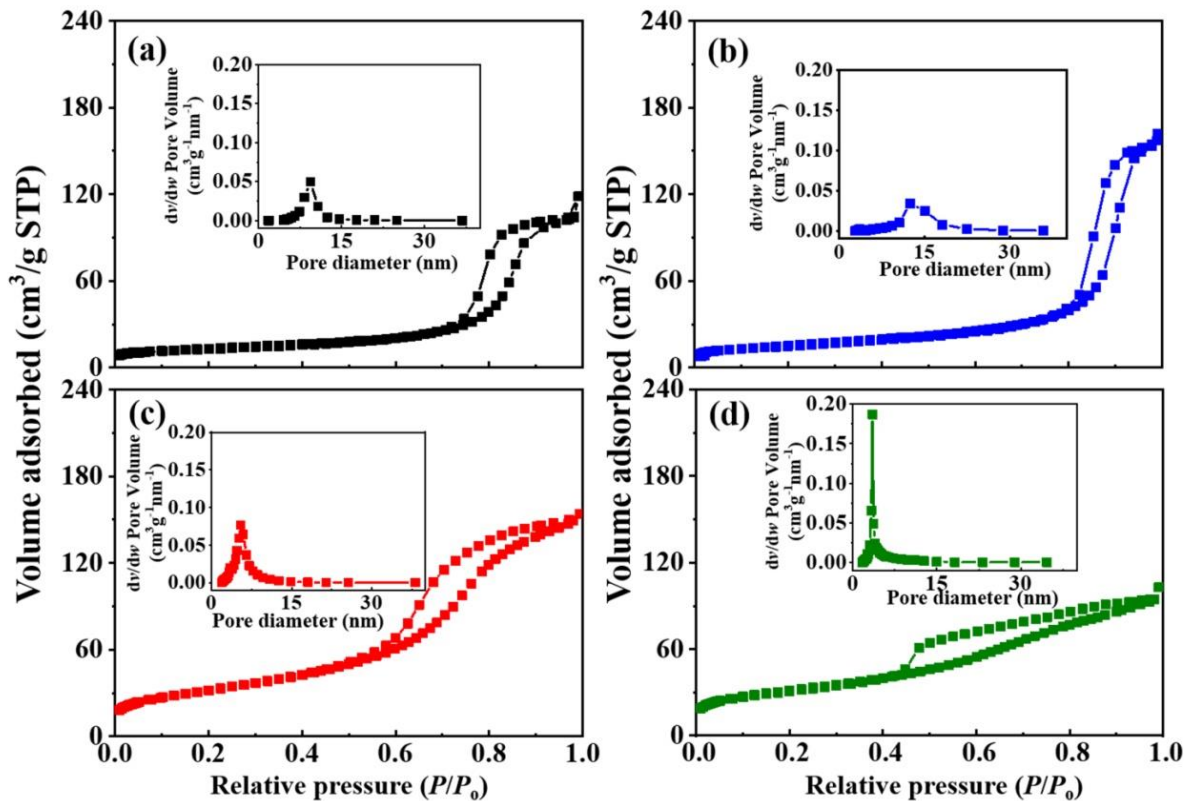


Fig. S3.11. Nitrogen adsorption-desorption isotherms and pore size distribution curve (inset) of (a) TiO₂-0/500, (b) TiO₂-0.1/500, (c) TiO₂-0.5/500 and (d) TiO₂-1/500.

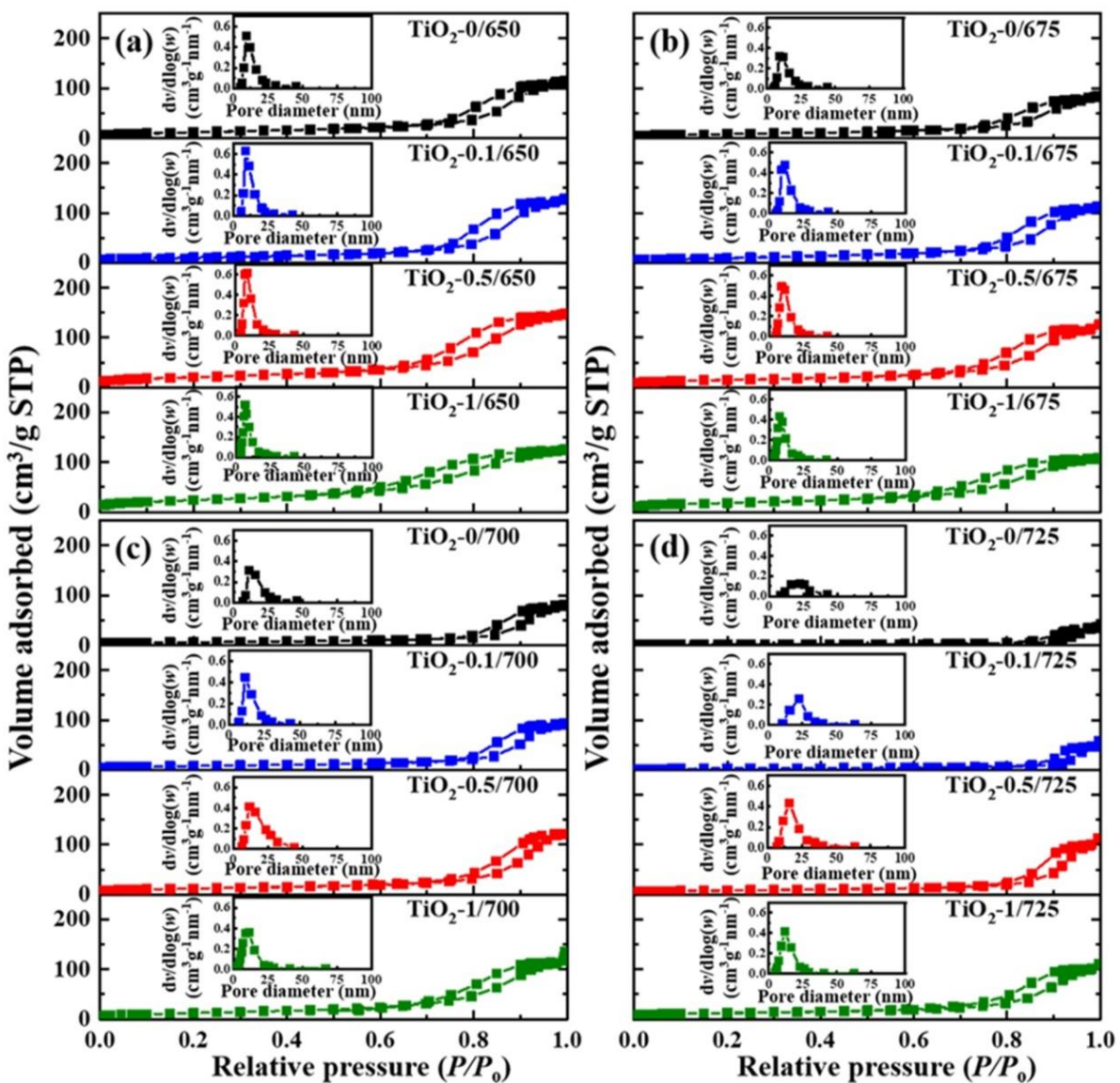


Fig. S3.12. Nitrogen adsorption-desorption isotherms and pore size distribution curves (inset) of TiO_2-0/T , $\text{TiO}_2-0.1/T$, $\text{TiO}_2-0.5/T$ and TiO_2-1/T samples at (a) $T = 650^\circ\text{C}$, (b) $T = 675^\circ\text{C}$, (c) $T = 700^\circ\text{C}$ and (d) $T = 725^\circ\text{C}$, respectively.

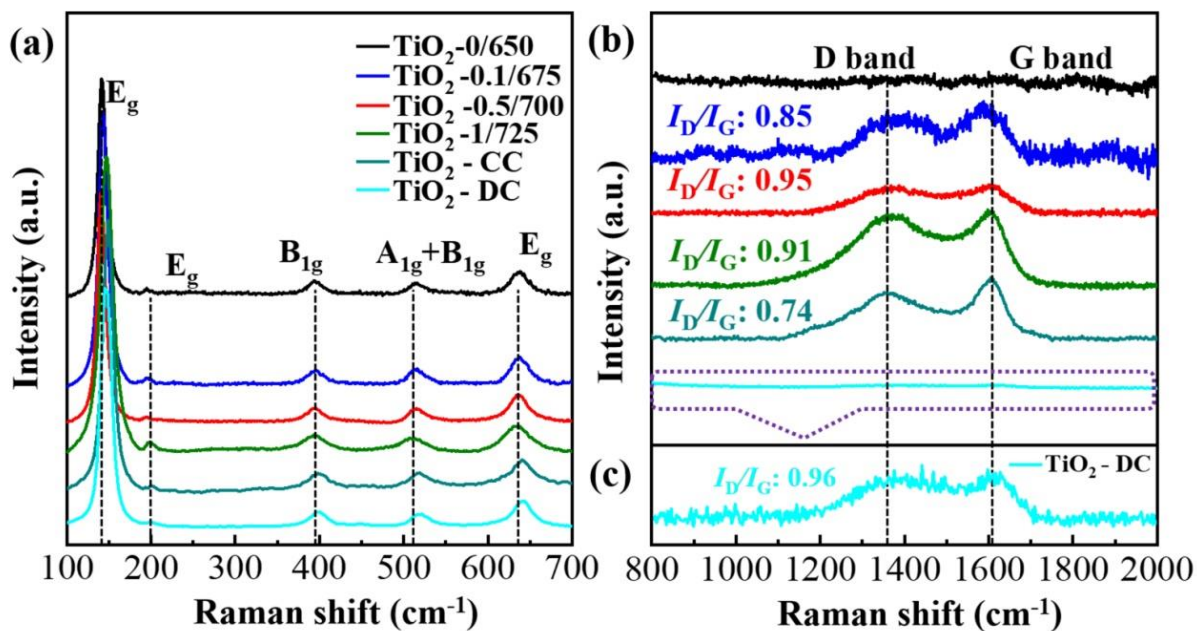


Fig. S3.13. Raman spectra of different TiO_2 samples in the zone of (a) 100–700 cm^{-1} , (b) 800–2000 cm^{-1} and (c) amplified spectrum of $\text{TiO}_2\text{-DC}$.

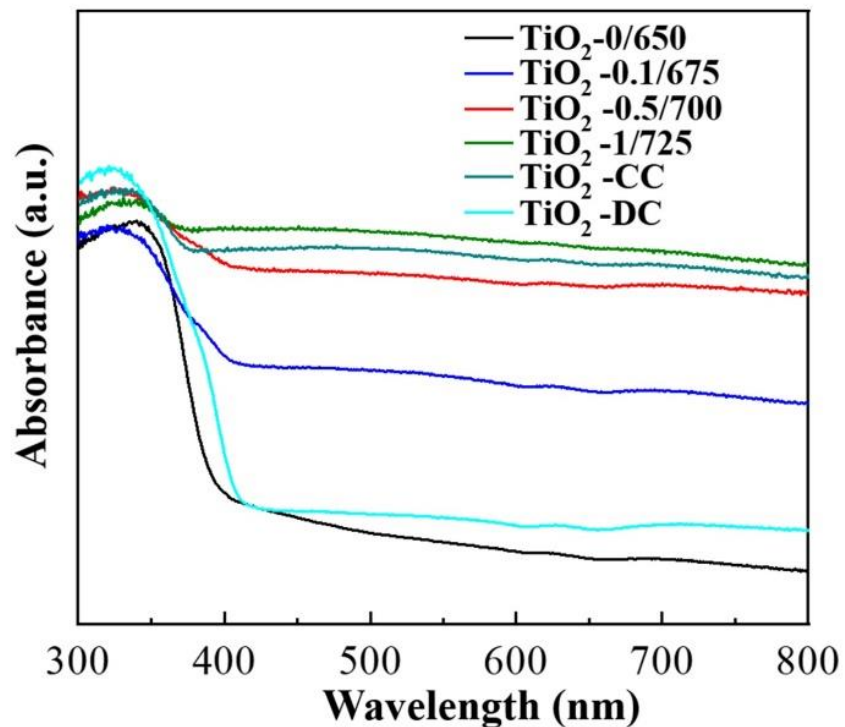


Fig. S3.14. UV-Visible absorption spectra of various TiO_2 samples.

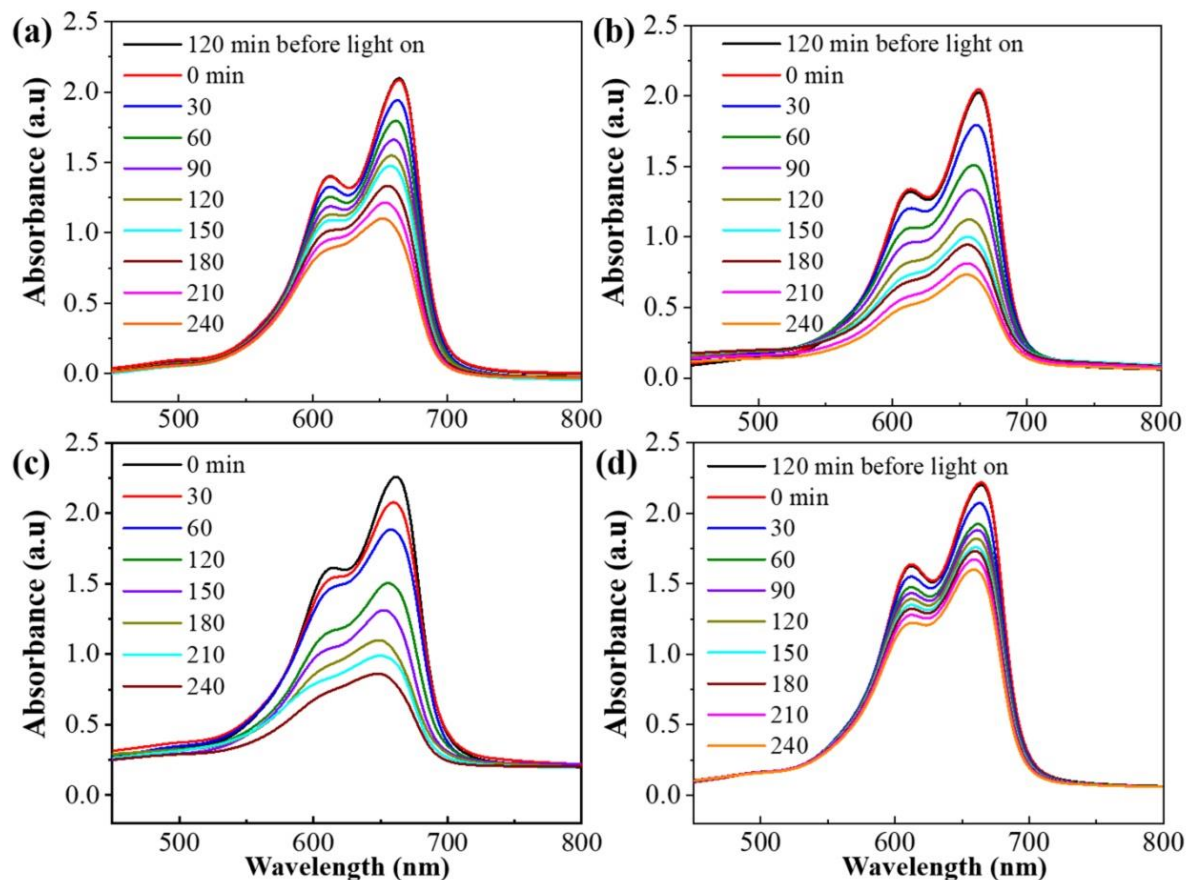


Fig. S3.15. The evolution of the absorption spectra of the Methylene blue (MB) solution over
 (a) TiO₂-0/500, (b) TiO₂-0/650, (c) TiO₂-0/750 and (d) TiO₂-0/900.

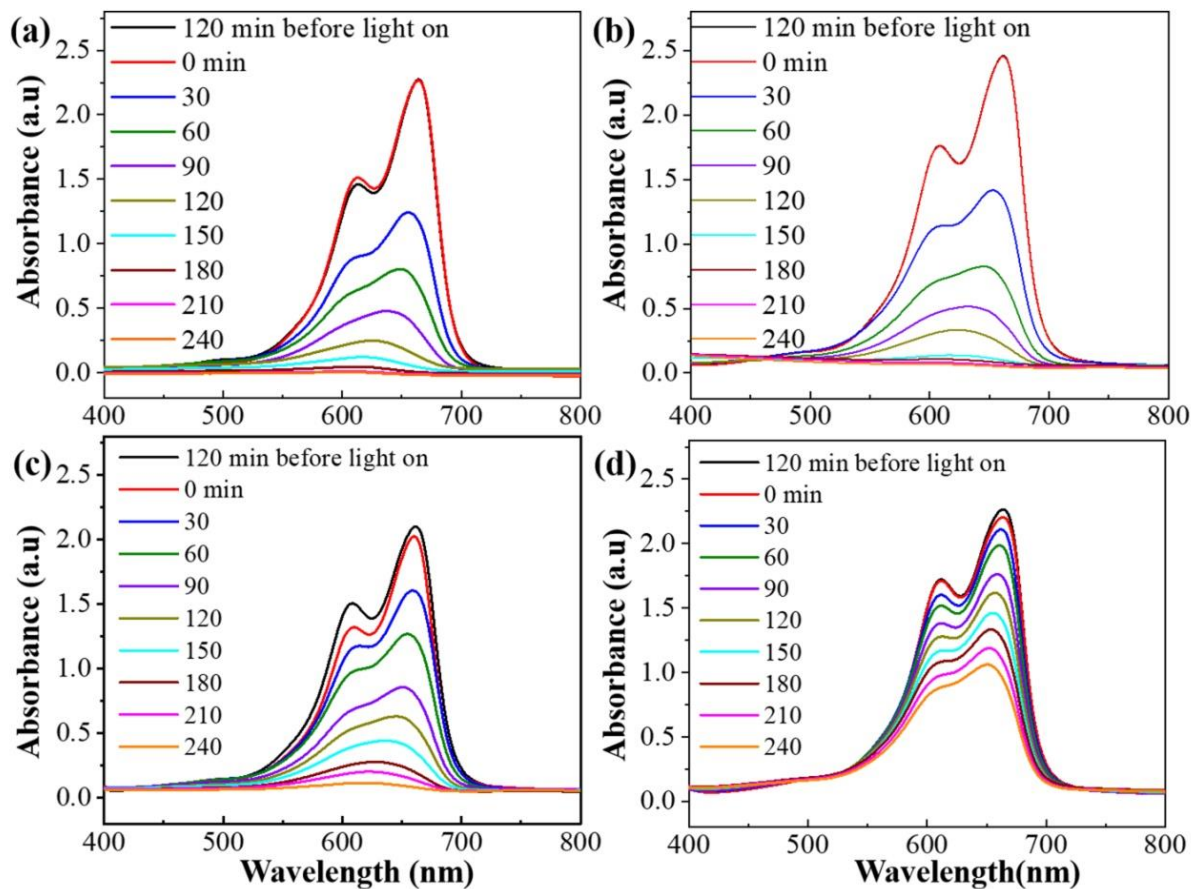


Fig. S3.16. The evolution of the absorption spectra of the MB solution over (a) $\text{TiO}_2\text{-}0/500$, (b) $\text{TiO}_2\text{-}0.1/675$, (c) $\text{TiO}_2\text{-}0.1/700$ and (d) $\text{TiO}_2\text{-}0.1/825$.

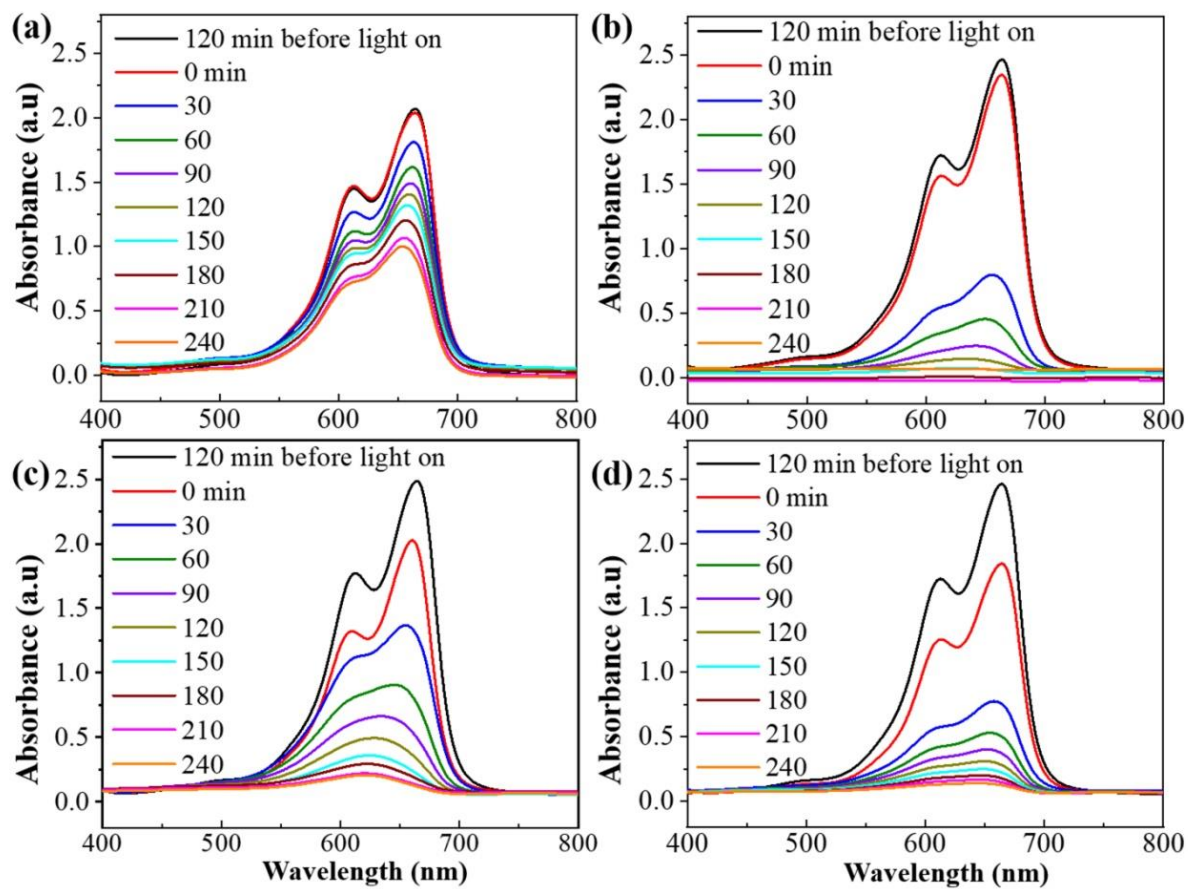


Fig. S3.17. The evolution of the absorption spectra of the MB solution over (a) $\text{TiO}_2\text{-}0.5/500$, (b) $\text{TiO}_2\text{-}0.5/700$, (c) $\text{TiO}_2\text{-}0.5/725$ and (d) $\text{TiO}_2\text{-}0.5/825$.

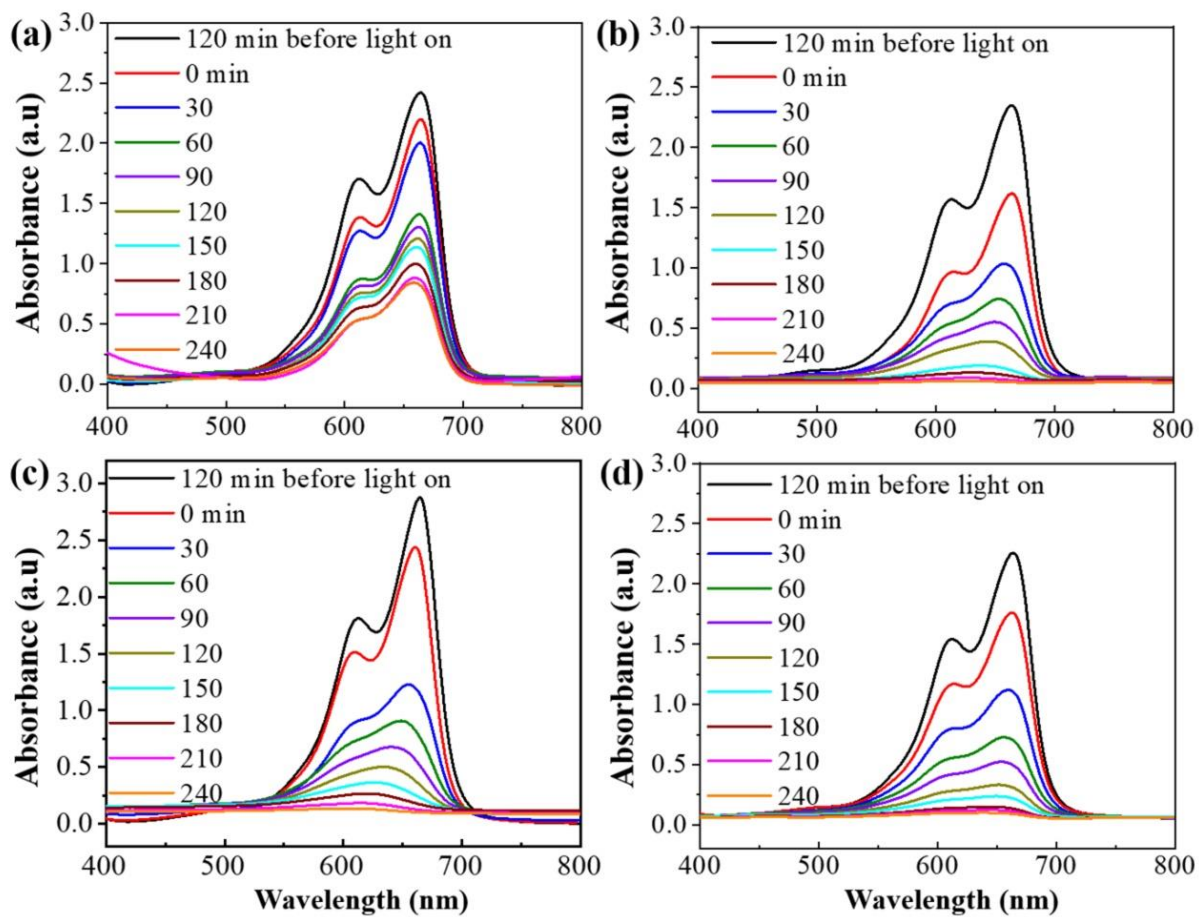


Fig. S3.18. The temporal evolution of the absorption spectra of the MB solution over (a) $\text{TiO}_2\text{-1/500}$, (b) $\text{TiO}_2\text{-1/725}$, (c) $\text{TiO}_2\text{-1/750}$ and (d) $\text{TiO}_2\text{-1/825}$.

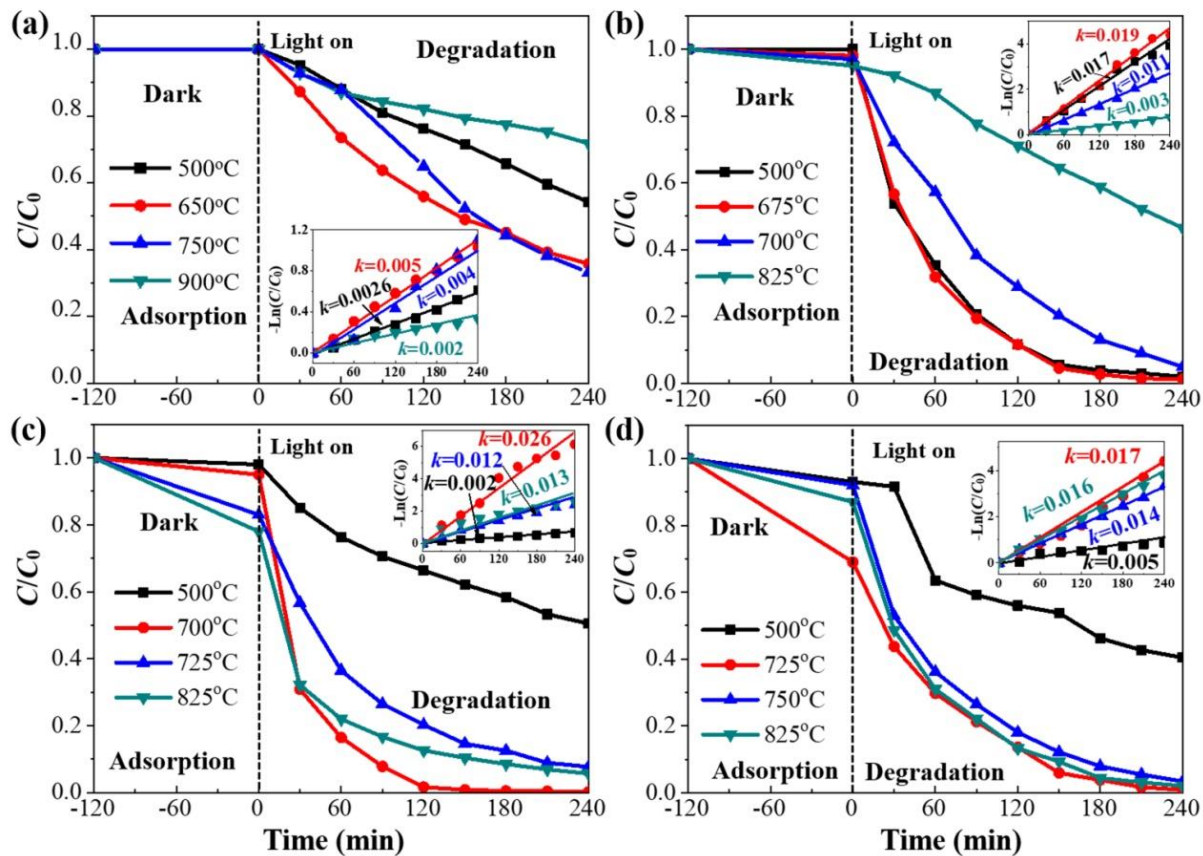


Fig. S3.19. The variation of MB concentrations (C/C_0) over different type of TiO_2 calcined at different temperature: (a) $\text{TiO}_2\text{-}0/T$, (b) $\text{TiO}_2\text{-}0.1/T$, (c) $\text{TiO}_2\text{-}0.5/T$ and (d) $\text{TiO}_2\text{-}1/T$.

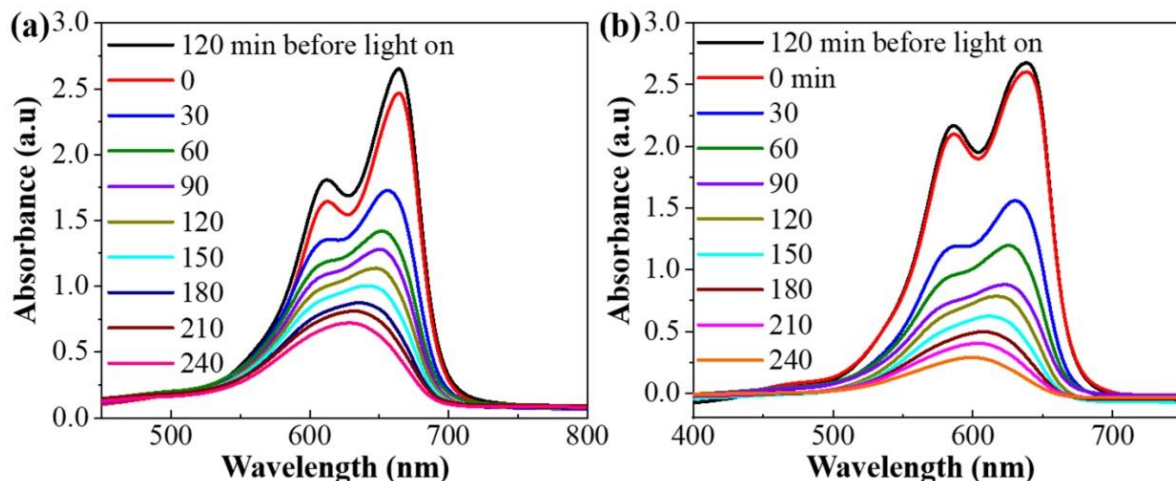


Fig. S3.20. The evolution of the absorption spectra of the MB solution over (a) $\text{TiO}_2\text{-DC}$ and (b) $\text{TiO}_2\text{-CC}$.

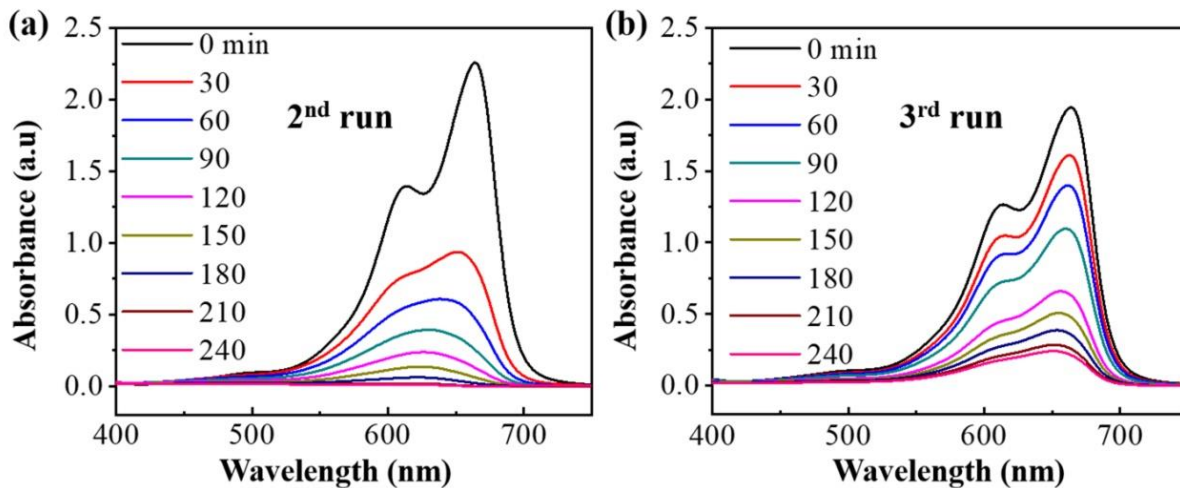


Fig. S3.21. The evolution of the absorption spectra of the MB solution over $\text{TiO}_2\text{-}0.5/700$ for (a) second time run and (b) third time run.

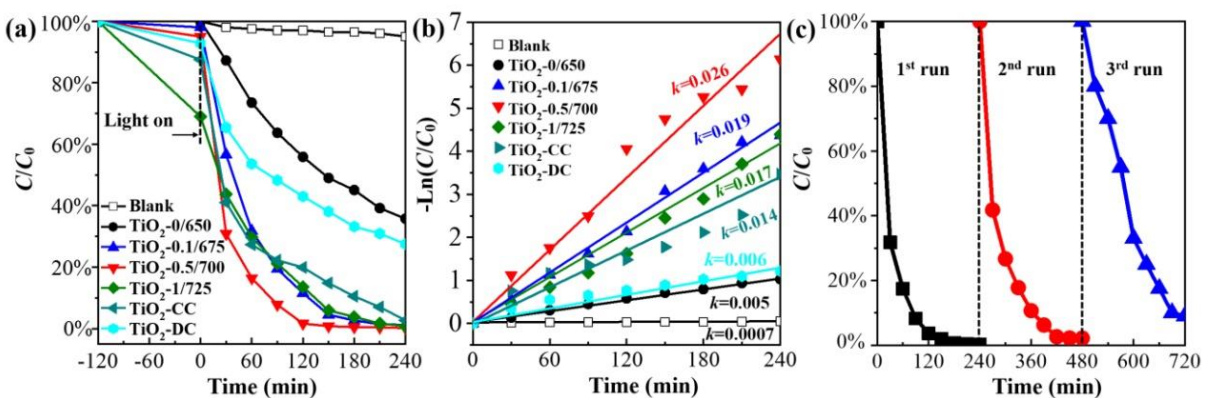


Fig. S3.22. (a) Photocatalytic degradation of Methylene blue under solar light irradiation over different photocatalysts, (b) corresponding kinetic curves and recycling tests of the $\text{TiO}_2\text{-}0.5/700$ photocatalyst for the degradation of MB.

The capacity C of semiconductor follows the Mott-Schottky relationship:

$$\frac{1}{C^2} = \frac{2}{\varepsilon \varepsilon_0 e N_d} (V - V_{fb} - \frac{kT}{e})$$

Where C is the charge space capacity, N_d is the carrier density, ε is the relative electric permittivity, ε_0 is the vacuum electric permittivity, e is the elementary charge, k is the Boltzman constant, T is the absolute temperature, V_{fb} is the flat band potential and V is the applied voltage. By linear fitting as shown in Fig. S3.23, the V_{fb} and N can be deduced. The V_{fb} approximately equals to intercept. N_d approximately equals to $(\frac{\varepsilon \varepsilon_0 e}{2}) * 1/\text{slope}$. Thus, the V_{fb} of $\text{TiO}_2\text{-0/650}$, $\text{TiO}_2\text{-0.5/700}$, $\text{TiO}_2\text{-CC}$ and $\text{TiO}_2\text{-DC}$ were observed at -0.45, -1.25, -0.85 and -0.98V, respectively. The calculated carrier densities of $\text{TiO}_2\text{-0.5/700}$, $\text{TiO}_2\text{-CC}$, $\text{TiO}_2\text{-DC}$ and $\text{TiO}_2\text{-0/650}$ obtained at 2 kHz are 3.37×10^{27} , 2.75×10^{27} , 2.55×10^{27} and 2.38×10^{27} as shown in Fig. S3.24.

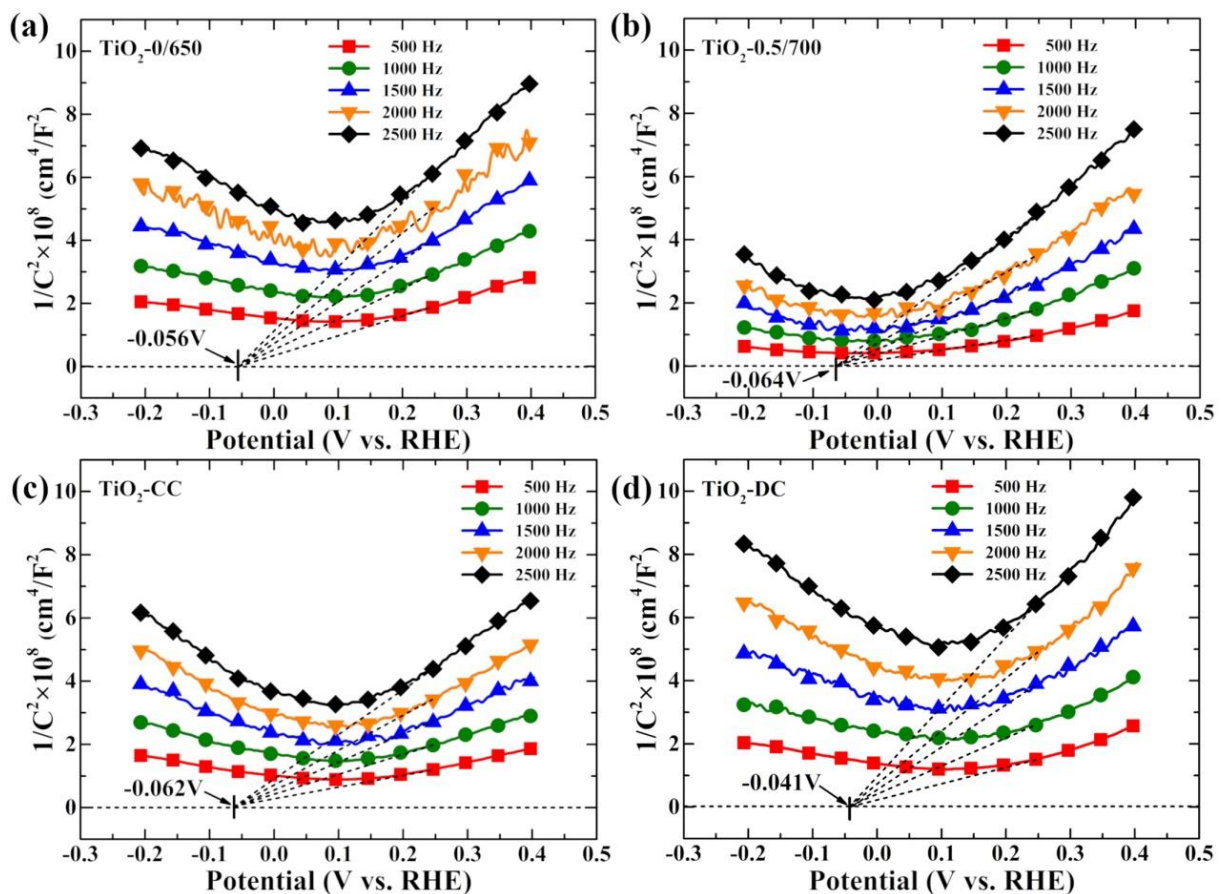


Fig. S3.23. Mott-Schottky plots of various photoelectrodes (a) $\text{TiO}_2\text{-0/650}$, (b) $\text{TiO}_2\text{-0.5/700}$, (c) $\text{TiO}_2\text{-CC}$ and (d) $\text{TiO}_2\text{-DC}$ collected at different frequencies in the dark environments.

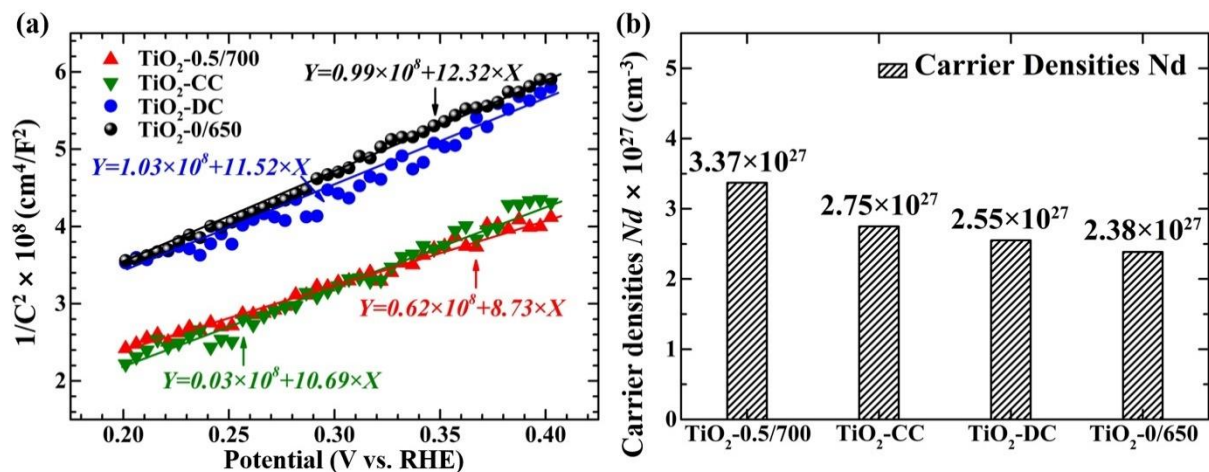


Fig. S3.24. (a) Mott-Schottky plots collected at 2 kHz at a linear potential region between 0.2 to 0.4V vs. RHE and (b) Calculated carrier densities of $\text{TiO}_2\text{-}0/650$, $\text{TiO}_2\text{-}0.5/700$, $\text{TiO}_2\text{-CC}$ and $\text{TiO}_2\text{-DC}$.

Table S3.1. Textural properties of pure TiO₂ and carbon doped TiO₂

Sample	ABET (m ² /g)	V _{BJH} (cm ³ /g)	Pore diameter(nm)
TiO₂-0/500	46	0.24	17.8
TiO₂-0.1/500	59	0.27	18.5
TiO₂-0.5/500	116	0.23	8
TiO₂-1/500	109	0.14	5.3

Table S3.2. Intensity of D-band and G-band

Sample	I _D	I _G	I _D /I _G
TiO₂-0/650	0	0	-
TiO₂-0.1/675	1158	1362	0.85
TiO₂-0.5/700	1000	1052	0.95
TiO₂-1/725	2680	2945	0.91
TiO₂-CC	1670	2257	0.74
TiO₂-DC	72	74	0.96

Table S3.3. The atomic ratios of different carbon components in C1s spectra

Sample	At.% _(O-C=O)	At.% _(O-C-O)	At.% _(C-C)	At.% _(Ti-C)	At.% _{(C-C)/At.%_(Ti-C)}
TiO₂-0/650	11.75	4.29	73.80	10.17	0.14
TiO₂-0.1/675	7.88	15.09	63.66	13.37	0.21
TiO₂-0.5/700	7.1	12.25	56.2	24.45	0.44
TiO₂-1/725	4.5	11.68	68.38	15.45	0.23
TiO₂-CC	5.96	11.09	71.08	11.88	0.17
TiO₂-DC	7.42	6.23	59.00	27.35	0.46

CHAPTER 4.

**A novel synthesis of carbon composed two-dimensional Ti_nO_{2n-1}
for PEC water splitting**

Abstract

Carbon composed Ti_nO_{2n-1} ($3 \leq n \leq 9$) were prepared by a simple sintering of polysaccharide coated amorphous TiO_2 derived from hydrolysis of $TiCl_4$ in fructose solution under Ar. The concentration of fructose in precursor solution, calcination duration and calcination temperature can effectively adjust the n value of Ti_nO_{2n-1} . The formation mechanism of carbon composed Ti_nO_{2n-1} supposed to be the reduction of TiO_2 by the reductive gases, H_2 and CO produced from the decomposition of polysaccharides under hypoxic atmosphere. Ti_nO_{2n-1} including Magnéli materials ($4 \leq n \leq 9$) possess unique crystallite structure with one oxygen deficiency in every layer of TiO_6 octahedrons. The oxygen deficiency in Ti_nO_{2n-1} results in semiconductor-metal transition which can act as inherent semiconductor-metal junction improving the charge separation and the followed photocatalytic activity. When the semiconductor-metal transition is enhanced with lower n value, the photon harvesting and the excitation of electron/hole pairs are suppressed resulting in weakened PEC performance. Thus, Magnéli phase with higher n value such as Ti_6O_{11} and Ti_9O_{17} show superior PEC performance comparing to pristine TiO_2 and non-Magnéli phase Ti_3O_5 . This work not only expands the controllable synthesis approach of Magnéli materials, but also provides an overall investigation of PEC properties of Magnéli materials, which is very helpful for the practical application of Magnéli materials for energy conversion and energy storage.

4.1 Introduction

The titanium suboxides (TSO) are materials with a generic formula Ti_nO_{2n-1} . When the n value ranges from four to ten, Ti_nO_{2n-1} materials are called Magnéli materials (in honor of Arne Magnéli, who was the first to study these compounds). [1] The titanium suboxides ($3 \leq n \leq 9$) with the trade also are named as Ebonex® show an unusual chemical inertness in corrosive and aggressive media leading to high chemical stability. [2-4] The Ti_nO_{2n-1} ($3 \leq n \leq 9$) materials have unique crystal structures derived from TiO_2 , which are made up of two-dimensional chains of TiO_6 but with an oxygen deficiency in every n titanium octahedral sites. [2] These oxygen deficiencies, combined with large unit cells increase the concentration of $3d^1 Ti^{3+}$ and enhance the electrical conduction. This kind of semiconductor-metal phase transition is antihunt without any further calcination and along with substantial adjustment in optical, electrical and magnetic properties. For example, Ti_5O_9 , Ti_4O_7 and Ti_3O_5 all exhibit high electrical conductivity at room temperature. Especially the most conductive phase, Ti_4O_7 has a conductivity of 1500s/cm, which is comparable with that of graphite (2000-3000 s/cm //basal plane). In addition, the discovery of superconductive properties in both Ti_4O_7 and Ti_3O_5 prepared in the form of thin films were reported recently. [5] The Magnéli-phase Ti_4O_7 can replace carbon electrocatalyst support and the RuO_2 composed Ti_4O_7 as oxygen electrodes in Li – O₂ batteries exhibited enhanced performance with a low overpotential of 0.9 V. [6] Another type of Magnéli phase Ti_8O_{15} loading with Pd shows good electrocatalytic activity and stability. [7] The current density of the Pd/ Ti_8O_{15} catalyst (2791 mA mg⁻¹) is four times than that of Pd/C catalyst (682 mA mg⁻¹). Until now, the TSO materials have been already applied in many areas, such as batteries, fuel cells, electrocatalysis and energy conversion. [8-12] However, the Ti_nO_{2n-1} materials as anode materials for potential application in photoelectrochemical (PEC) water splitting has seldom been studied.

On the other hand, TSO can be synthesized either by thermal reduction of TiO_2 at high temperatures (>1273 K) using a reducing agent such as hydrogen gas or by heating TiO_2 with metallic Ti under an inert atmosphere. [13, 14] Lately, the formation of some Magnéli phases was observed in the process of carbon coating TiO_2 . [15-18] The heat treatment of the powder mixture of TiO_2 and carbon precursor became more practical to obtain Ti_nO_{2n-1} with different n values. [19, 20] These manufacturing approaches still employ high temperature above 1100 °C for sintering and complex organics such as PVA, polyethylene as the resources of reducing agent. [19, 20] Therefore, it is highly expected to design a facile and environment-friendly method for the synthesis of functional Ti_nO_{2n-1} materials for PEC water splitting.

Herein, we present a novel, controllable and one-pot synthesis process of Ti_nO_{2n-1} at a relatively low temperature. Carbon composed Ti_nO_{2n-1} materials including Magnéli phases with different n values are obtained by the hydrolysis of $TiCl_4$ in fructose solution followed by calcination under Ar. The n value can be adjusted by the concentration of fructose and the calcination temperature and duration. The formation mechanism of the Ti_nO_{2n-1} materials is specially discussed after systematic characterization such as XRD, BET, TGA, TEM and XPS as well as NMR. The PEC performances of the as-prepared Ti_nO_{2n-1} series were further evaluated in this thesis.

4.2 Materials and methods

4.2.1 Preparation of Ti_nO_{2n-1} materials

Ammonia (25%), $TiCl_4$ (99.99% pure), fructose were purchased from Aldrich. 10 ml $TiCl_4$ was dropped into a Fructose solution (0, 1, 5, 10 and 20 g/L) with 25 mL ammonia and 175 mL distilled water. The precipitates were collected and washed by centrifugation 5 times, and then were subsequently dried for 24 hours. These precipitate denoted as F_x ($x=0, 1, 5, 10, 20$) were then sealed in crucibles with 1 g fructose on the topside of the caps. The 1 g fructose is added to consume residual oxygen in the oven. The resulting products were obtained after calcination at 950 °C with a ramping rate of 5 °C/min for different duration (y hours) under argon atmosphere. The obtained products are denoted as F_x-yh .

4.2.2 Materials characterization

The ^{13}C solid-state MAS NMR experiments were carried on a Bruker Avance 300 MHz (7T) spectrometer using 4 mm zirconia rotors as sample holders, spinning at MAS rate vMAS = 10 kHz. Powder X-ray diffraction was performed on a PANalytical X'pert Pro with Cu Ka radiation ($\lambda = 1.54 \text{ \AA}$). The isothermal nitrogen adsorption measurements were carried out on a Micromeritics Tristar 3000 with prior degassing. The morphology of the products was observed on field emission scanning electron microscopy (FESEM, FEI Sirion 200). Microstructural examinations were conducted on JEOL JEM-2100 transmission electron microscopy (TEM) operated at 120 kV. Thermal gravimetric analysis and differential thermal gravimetric analysis (TGA/DTG) were carried out with a DSC-TGA (SDTQ600, TA Instruments) under air atmosphere from room temperature to 1200 °C at a heating rate of 10 °C/min. The X-ray photoelectron spectroscopy (XPS) analyses were performed on a K-AlphaTM + X-ray photoelectron spectrometer (XPS).

4.2.3 Photoelectrochemical measurement

The photoelectrochemical measurement was carried out using the solar cell quantum efficiency measurement system (SCS10, Zolix) which is connected with a conventional electrochemical workstation (CHI 660E). Typically, 15.0 mg of each photocatalyst was mixed with deionized water (100 μ L) and 20 μ L of a Nafion ® 117 solution (5% in a mixture of lower aliphatic alcohols and water). The mixture was placed under sonication for 5 min followed by grinding for 20 min in order to obtain a homogeneous suspension. The indium tin oxide (ITO) glass (1 cm^2) was used as substrate. The suspension was dropped onto the surface of two ITO glasses equally. After naturally drying overnight, the weight of the sample on each ITO glass was obtained by the subtraction of the weight of ITO glass from the final weight of ITO glass with loaded sample. The photocurrent was measured in a standard quartz-made three-electrode cell with ITO glass as working electrode. The PEC water splitting experiments were carried out in 0.1 M Na₂SO₄ (Aldrich, 25 °C, pH = 6) electrolyte with Saturated Calomel Electrode (SCE) and platinum foil as reference electrode and counter electrode, respectively. The potential and photocurrent of the photoelectrode were controlled by a potentiostat (CHI660E) and the SCE potential is converted into the Reversible Hydrogen Electrode (RHE) potential according to the Nernst equation, as follows:

$$E_{\text{RHE}} = E_{\text{SCE}} + 0.244 + 0.0592 \times \text{pH} = E_{\text{SCE}} + 0.6 \text{ V at } 25 \text{ }^\circ\text{C} \quad (1)$$

The samples were illuminated by an artificial sunlight simulator, consisting of a controllable 500W Xenon lamp (Model: Gloria-X500A, Titan Electro-Octics Co., Ltd.) and an AM 1.5 filter (100 mW/cm², thermopile detector from Zolix was used for the measurements). The photocurrent were measured under illumination through a monochromator (Omini-λ300, Zolix).

4.3 Result and discussion

4.3.1 Synthesis of carbon composed Ti_nO_{2n-1} materials

The preparation scheme is illustrated in Fig. 4.1. When the TiCl₄ was dropped into the fructose solution, the fructose (C₆H₁₂O₆) polymerized into polysaccharide ((C₆H₁₀O₅)_n) assisted by the heat released from the hydrolysis of TiCl₄. The polysaccharide was primarily coated on the surface of the amorphous TiO₂. The coated polysaccharide produced the reductive environment for the growth of titanium suboxide (Ti_nO_{2n-1}), Magnéli materials. In addition, the growth of Ti_nO_{2n-1} is highly anaerobic. To consume the residual oxygen in the oven for calcination and

protect reductive atmosphere, 1 g extra fructose was put on the top of sealed crucibles. The carbon composed $\text{Ti}_n\text{O}_{2n-1}$ materials were obtained after the calcination under Ar.

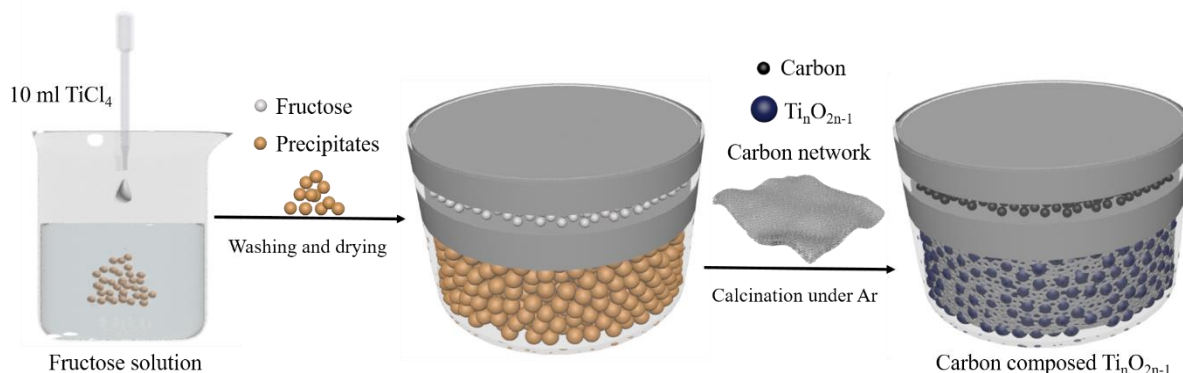


Fig. 4.1. Schematic illustration of the preparation procedure of carbon composed $\text{Ti}_n\text{O}_{2n-1}$.

To better understand the polymerization process of fructose, solid-state ^{13}C NMR spectra were recorded and depicted in Fig. 4.2. A few peaks observed at 0-50 ppm are attributed to mobile CH_3 or CH_2 groups. The most prominent peaks observed between 60 and 100 ppm belong to cyclic forms of fructose.^[21] The intensity of the fructose peaks at 60-100 ppm gradually increases as the concentration of fructose increases indicating the increased extent of polymerization. Besides the polymerization of fructose, the fructose underwent hydrothermal carbonization during the hydrolysis of TiCl_4 . Thus, the further dehydration of fructose forming other carbonaceous materials is unavoidable. The peaks observed between 100-180 ppm are assigned to some intermediates such as hydroxymethylfurfural (HMF) and furfura ($\text{C}_6\text{H}_6\text{O}_2$ or $\text{C}_6\text{H}_6\text{O}_3$).^[22-24] Similarly, as the fructose concentration increases, the intensities of peaks at 100-180 ppm also increases. These carbonaceous materials coated on the surface of the amorphous TiO_2 were decomposed into reductive carbon monoxide, carbon or even H_2 during the sintering process. The TiO_2 is reduced into suboxides ($\text{Ti}_n\text{O}_{2n-1}$) in the sealed environment.

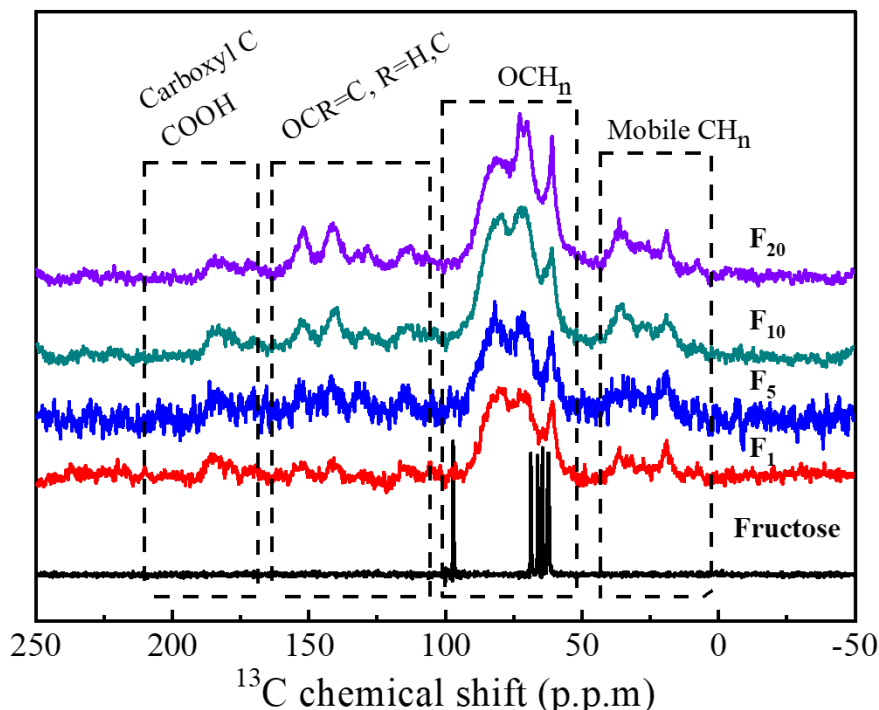


Fig. 4.2. Solid-state ^{13}C NMR spectra of fructose and the obtained F_1 , F_5 , F_{10} , F_{20} .

Thermogravimetric analysis (TGA) was performed to estimate the carbon content in different $\text{Ti}_n\text{O}_{2n-1}$. Fig. 4.3 presents the TGA-DSC result of as-prepared samples, F_1 -8h, F_5 -8h, F_{10} -8h and F_{20} -8h at 950 °C. During the TGA-DSC procedure under air atmosphere, carbonaceous materials were oxidized into CO_2 causing the weight loss while the $\text{Ti}_n\text{O}_{2n-1}$ was oxidized into TiO_2 leading to slight weight increase. The final weight loss is obtained by subtraction of carbon loss and weight gaining from oxygen. The composed $\text{Ti}_n\text{O}_{2n-1}$ is expressed as $\text{Ti}_n\text{O}_{2n-1}\text{C}_x$. The total weight loss is $(12x-16)/(48n+(2n-1)\times 16)$. Thus, the carbon content is calculated to be 0.8, 4.1, 7.0 and 11.1 wt% for F_1 -8h, F_5 -8h, F_{10} -8h and F_{20} -8h, respectively.

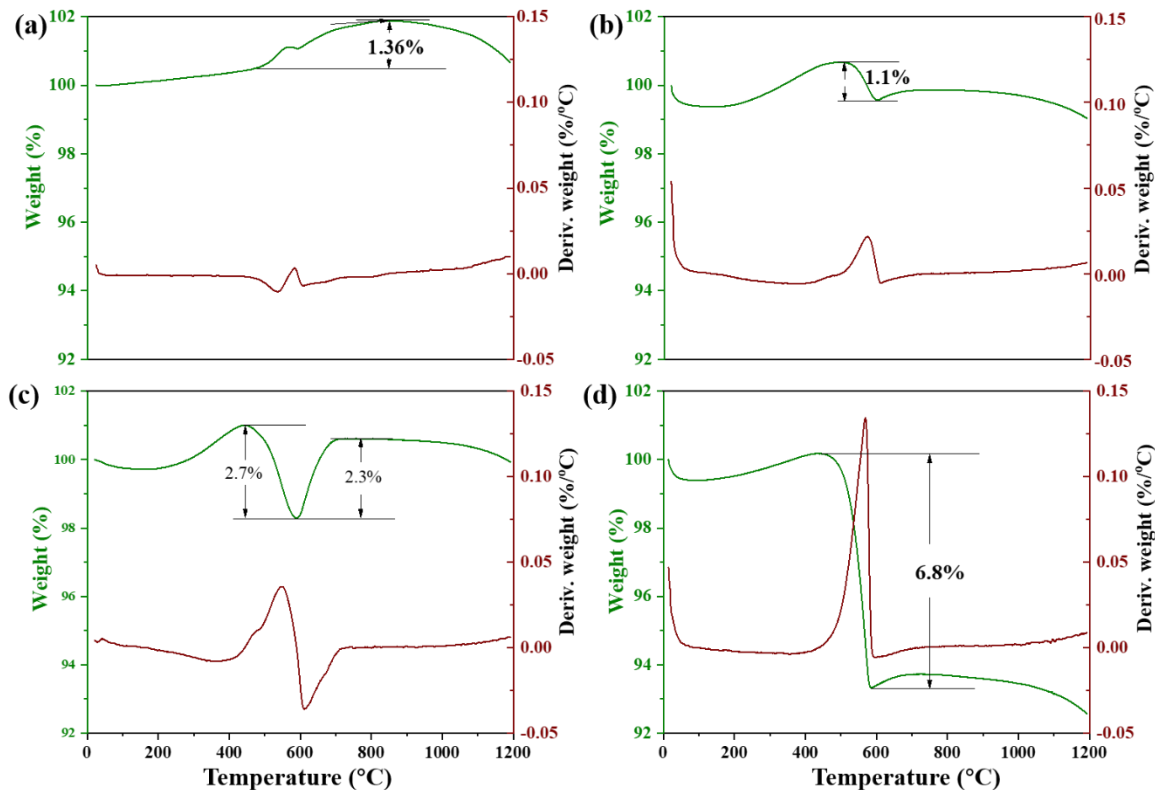


Fig. 4.3. The TGA-DSC curves of (a) F₁-8h, (b) F₅-8h, (c) F₁₀-8h and (d) F₂₀-8h at 950 °C.

The detailed nitrogen adsorption-desorption isotherms are illustrated in Fig. 4.4. The homogeneous pore size distribution curves (insets in Fig. 4.4) calculated via the Barrett-Joyner-Halenda (BJH) method. Except the F₀-8h, F₁-8h, F₅-8h, F₁₀-8h and F₂₀-8h are mesoporous showing typical type IV adsorption isotherms with H₂ type hysteresis loop. The Brunauer-Emmett-Teller (BET) specific surface areas, pore volumes and pore diameters are summarized in table 1. The Brunauer-Emmett-Teller (BET) specific surface area increases from zero to 116 m²/g as the concentration of fructose in precursors increased from zero to 20 g/L. The as-prepared Ti_nO_{2n-1} materials ($3 \leq n \leq 9$) F₁-8h, F₅-8h, F₁₀-8h and F₂₀-8h are mesoporous with pore diameters of 29.5, 16.1, 11.1, 8.45 nm, respectively indicating that increasing fructose precursor decreases the pore diameter and increases the surface area and pore volume.

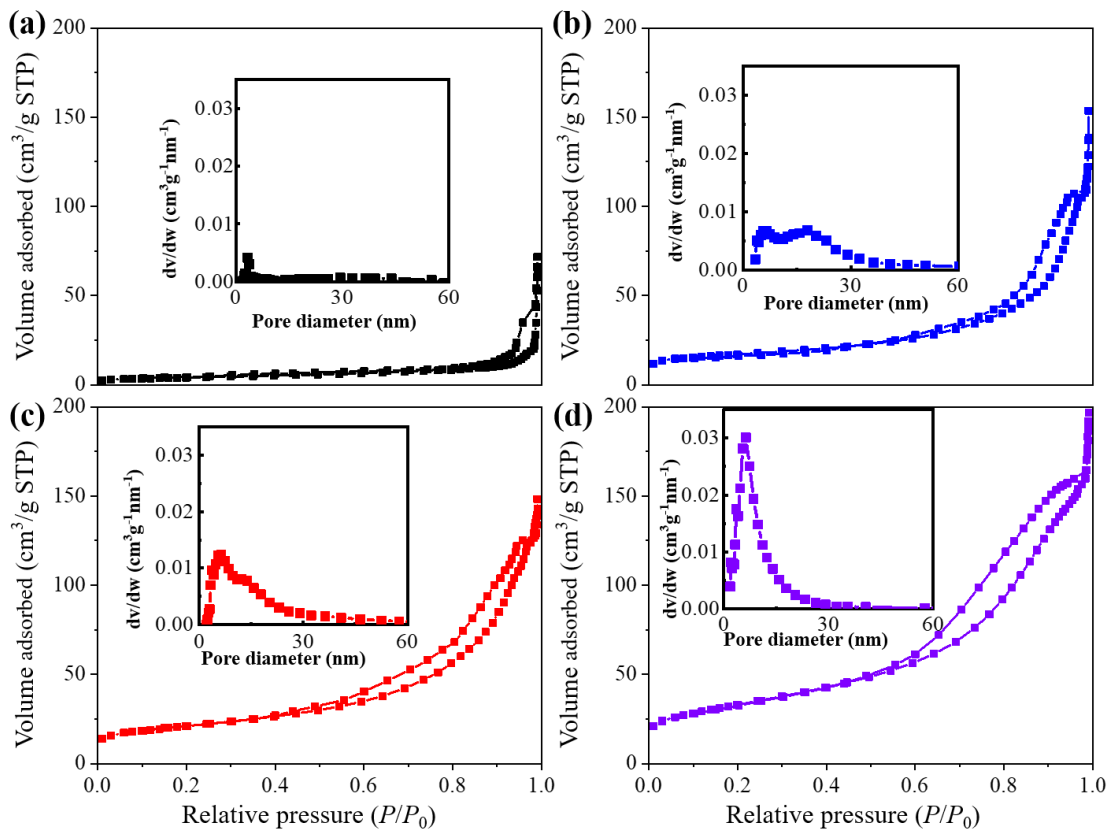


Fig. 4.4. Nitrogen adsorption-desorption isotherms and pore size distribution curves (inset) of (a) F₁-8h, (b) F₅-8h, (c) F₁₀-8h and (d) F₂₀-8h calcined at 950 °C.

Table 1. BET specific surface area, pore volume and average pore diameter of F₀-8h, F₁-8h, F₅-8h, F₁₀-8h and F₂₀-8h at 950 °C

Sample	S _{BET} (m ² /g)	V _{BJH} (cm ³ /g)	Pore diameter (nm)
F ₀ -8h	0	0	0
F ₁ -8h	13.9	0.102	29.5
F ₅ -8h	56.3	0.216	16.1
F ₁₀ -8h	71.8	0.217	11.1
F ₂₀ -8h	116	0.300	8.45

4.3.2 The influence factors on the growth of Magnéli materials

Fig. 4.5 illustrates the XRD patterns of amorphous samples (F₀, F₁, F₅, F₁₀, and F₂₀) calcined under different conditions in Ar atmosphere. Typically, the sample F₀ which contains no fructose in precursor directly became rutile TiO₂ after annealing at high temperature (950 °C) as shown in Fig. 4.5a. When the fructose was utilized as the resource of reducing agent,

different Ti_nO_{2n-1} are obtained. The n value of Ti_nO_{2n-1} can be adjusted by increasing the concentration of fructose. For example, F_{1-8h} mainly contains Magnéli phase Ti_9O_{17} while F_{5-8h} consists of three Magnéli phases, Ti_7O_{13} (15%), Ti_6O_{11} (5%), and Ti_4O_7 (80%). The n value of Ti_nO_{2n-1} decreased to three until the concentration of fructose increased to 10 g/L and the non-Magnéli phase Ti_3O_5 dominates in F_{10-8h} . The sample F_{20-8h} mainly containing Ti_4O_7 is obtained with the fructose concentration of 20 g/L. The formation of Ti_nO_{2n-1} was derived from the reduction of TiO_2 by the reductive polysaccharide. By increasing the concentration of fructose, the amount of polysaccharide increased resulting in increased production of crystal carbon. As shown in Fig. 4.5b, the increasing trends of BET surface area and the carbon content with the concentration of fructose are very similar. This phenomenon is because of the crystal growth of Ti_nO_{2n-1} was inhibited by the composed carbon coated at the surface of Ti_nO_{2n-1} crystals. Moreover, the aggregation of carbon nanoparticles can also result in mesopores as well as increased BET surface area. In addition to the concentration of fructose, the calcination time and temperature can also affect the n value of Ti_nO_{2n-1} . As illustrated in Fig. 4.5c, various Ti_nO_{2n-1} from Ti_9O_{17} to Ti_2O_3 are observed in the samples of F_{10} calcined at 950 °C for different duration ranging from 3 h to 10 h. The sample F_{10-3h} and F_{10-5h} consists only Ti_9O_{17} indicating that for F_{10} , longer than 5 h calcinations is needed to obtain Magnéli phase with lower n value than 9.

The sample F_{10-7h} consists 85% Ti_4O_7 and 15% Ti_3O_5 while F_{10-8h} consists only Ti_3O_5 . Ti_2O_3 is further observed in the sample F_{10-10h} , when calcined F_{10} for 10 h. By prolonging the calcination time, the extent of reduction of TiO_2 can be enhanced, thus the n values decreased. Besides, high calcination temperature can accelerate the phase transfer from TiO_2 to Ti_nO_{2n-1} with lower n value. As shown in Fig. 4.5d, Ti_2O_3 is identified when the annealing temperature increased up to 1100 °C for 8h. The phases ($Ti_7O_{13}/ Ti_6O_{11}/ Ti_4O_7$) with lower n value than that of Ti_3O_5 , which calcined at 950 °C are observed at lower temperature (800 °C).

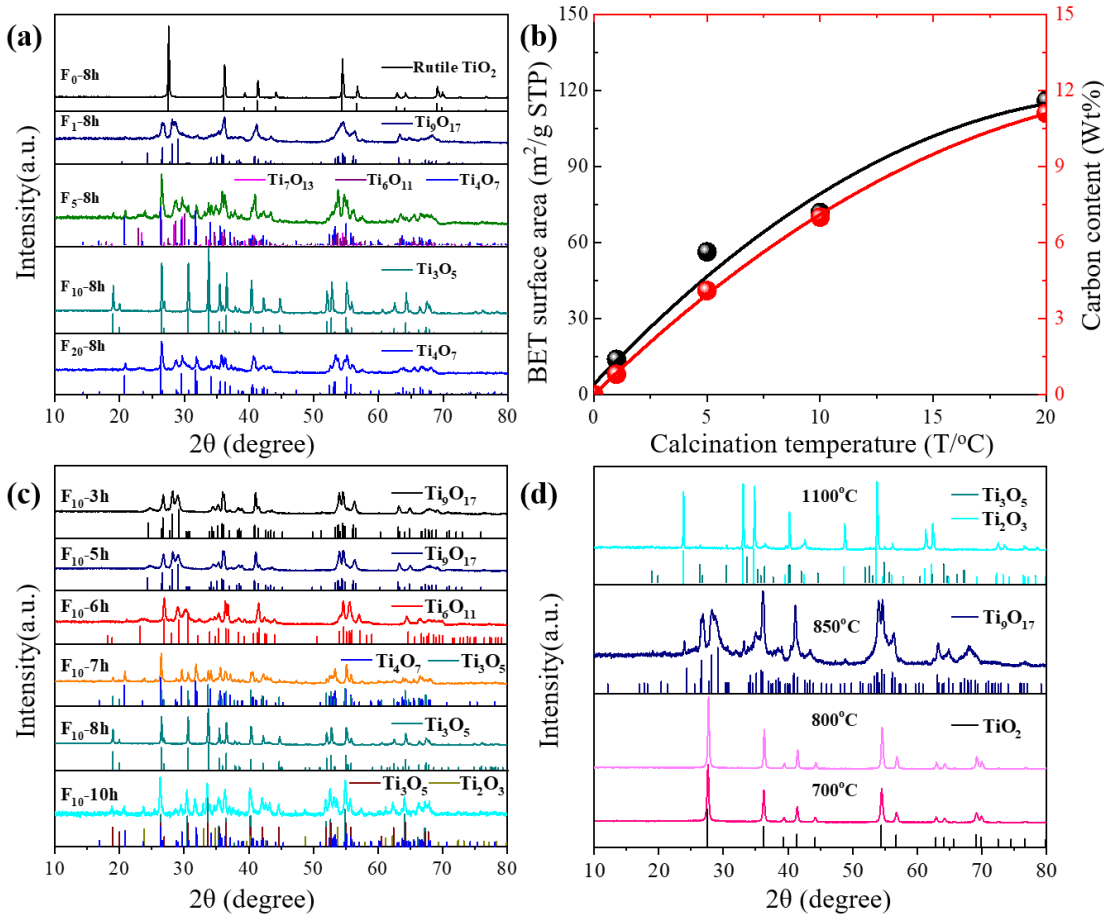


Fig. 4.5. X-ray diffraction patterns of (a) F₀, F₁, F₅, F₁₀ and F₂₀-8h at 950 °C; (b) BET specific surface area (black line) and the carbon content (red line) with the concentration of fructose; (c) XRD patterns of F₁₀ calcined at 950 °C and (d) XRD patterns of F₁₀ calcined at other temperatures, respectively.

4.3.3 Crystal structures of two-dimensional Ti_nO_{2n-1} (3 ≤ n ≤ 9) materials

The crystal structures of these obtained materials are simulated by crystal maker software according to the XRD results. The crystal structures of Ti_nO_{2n-1} series (3 ≤ n ≤ 9) are different from rutile TiO₂ as illustrated in Fig. 4.6. The rutile TiO₂ is tetragonal (P42/mnm) while the as-prepared Ti_nO_{2n-1} materials are monoclinic (I2/c) and anorthic (A-1/I-1). In rutile TiO₂, every Ti cation is shared by six anions, every O anion is shared by three Ti cations. However, in Ti_nO_{2n-1} (3 ≤ n ≤ 9), every Ti cation is still shared by six oxygen anions, some O anions indicated by dotted circles in Fig. 4.7 and 4.8 are shared by four Ti cations. As shown in Fig. 4.7, the as-prepared Ti_nO_{2n-1} (3 ≤ n ≤ 9) materials have two-dimensional chains of octahedral TiO₂, with every layer missing one oxygen atom to accommodate the loss in stoichiometry. Specifically, there are three TiO₆ octahedrons in every layer in the structure of Ti₃O₅. In every TiO₆

octahedron, four oxygen atoms circled by black dotted line are shared by four Ti cations and rest two oxygen atoms are shared by normal three Ti cations as illustrated in Fig. 4.7c. Similarly, there are four TiO_6 octahedrons in every layer in the structure of Ti_3O_5 . In edge TiO_6 octahedron on both sides of the layer, four oxygen atoms are shared by four Ti cations and rest two oxygen atoms are shared by normal three Ti cations. In every TiO_6 octahedron next to the edge one, two oxygen atoms are shared by four Ti cations and rest four oxygen atoms are shared by normal three Ti cations. Stoichiometrically, there is one oxygen deficiency in every layer of TiO_6 octahedrons in the structure of both Ti_3O_5 and Ti_4O_7 . When the n value of $\text{Ti}_n\text{O}_{2n-1}$ materials is more than three, $\text{Ti}_n\text{O}_{2n-1}$ materials belong to Magnéli phases, thus the Ti_4O_7 is the intermediate phase of Magnéli materials. Other obtained Magnéli phases (Ti_6O_{11} / Ti_7O_{13} / Ti_9O_{17}) also exhibit the same edge-sharing situations with that in every layer of Ti_4O_7 as depicted in Fig. 4.8. Therefore, the formula $\text{Ti}_n\text{O}_{2n-1}$ of Magnéli phases can be expressed as $\text{Ti}_4\text{O}_7(\text{TiO}_2)_{n-4}$. The $\text{Ti}_n\text{O}_{2n-1}$ phases possess semiconductor-metal transition due to the oxygen deficiency which increase with lower n value. [25, 26] The oxygen deficiency induced semiconductor-metal transition might act as an inherent semiconductor-metal junction facilitating the separation of electron/hole pairs and photocatalytic activity. However, as the n decreases, the ratio of metallic state to semiconducting state increases. Due to the raised transition to metallic state in $\text{Ti}_n\text{O}_{2n-1}$ with lower n value, the photon absorption and photogeneration process of electrons from valence band to conducting band of semiconductor state might be depressed resulting in suppressed photoactivity.

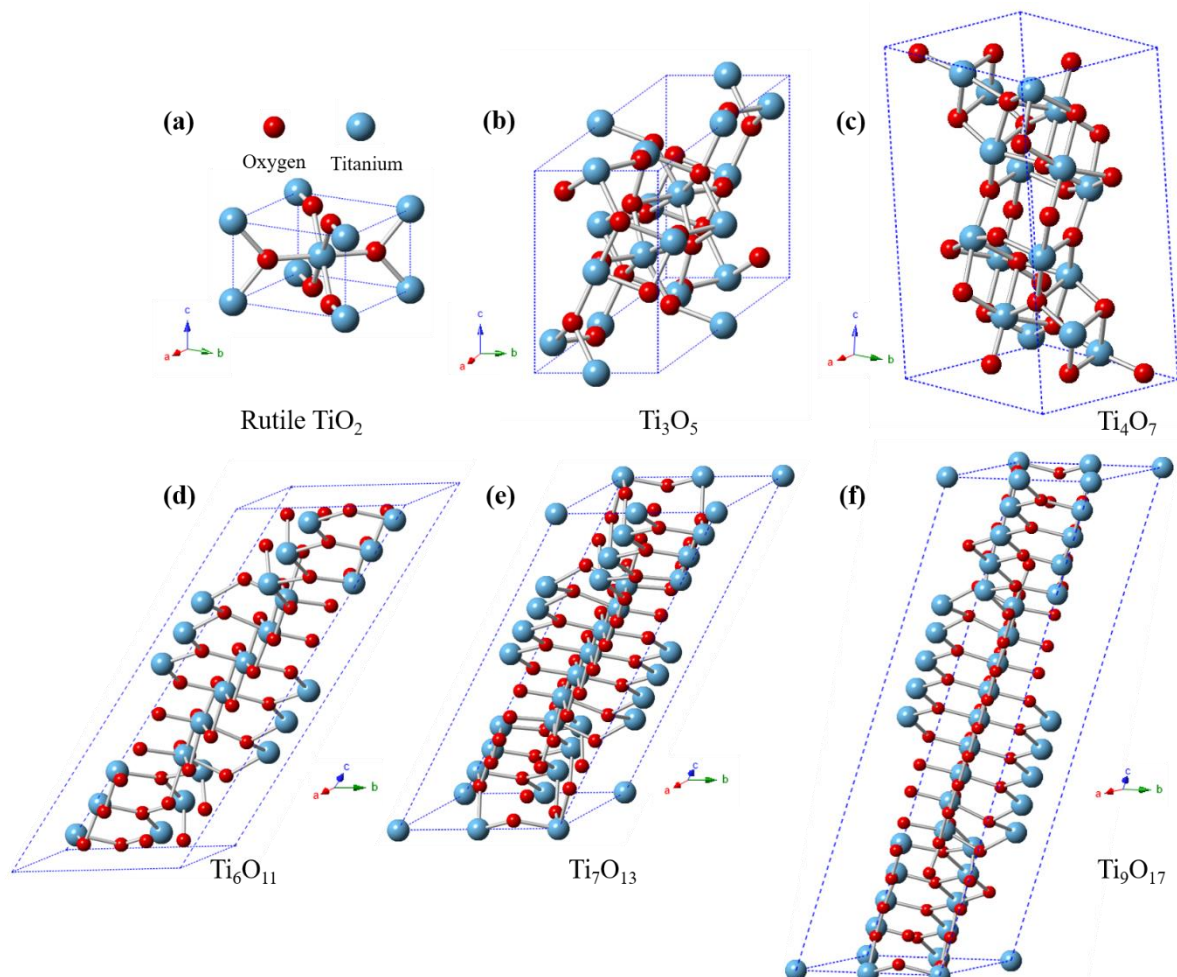


Fig. 4.6. Unit cells of (a) rutile TiO_2 (Tetragonal, P42/mnm); (b) $\gamma\text{-Ti}_3\text{O}_5$ (Monoclinic, I2/c); (c) Ti_4O_7 (Anorthic, A-1); (d) Ti_6O_{11} (Anorthic, I-1); (e) Ti_7O_{13} (Anorthic, I-1); (f) Ti_9O_{17} (Anorthic, I-1).

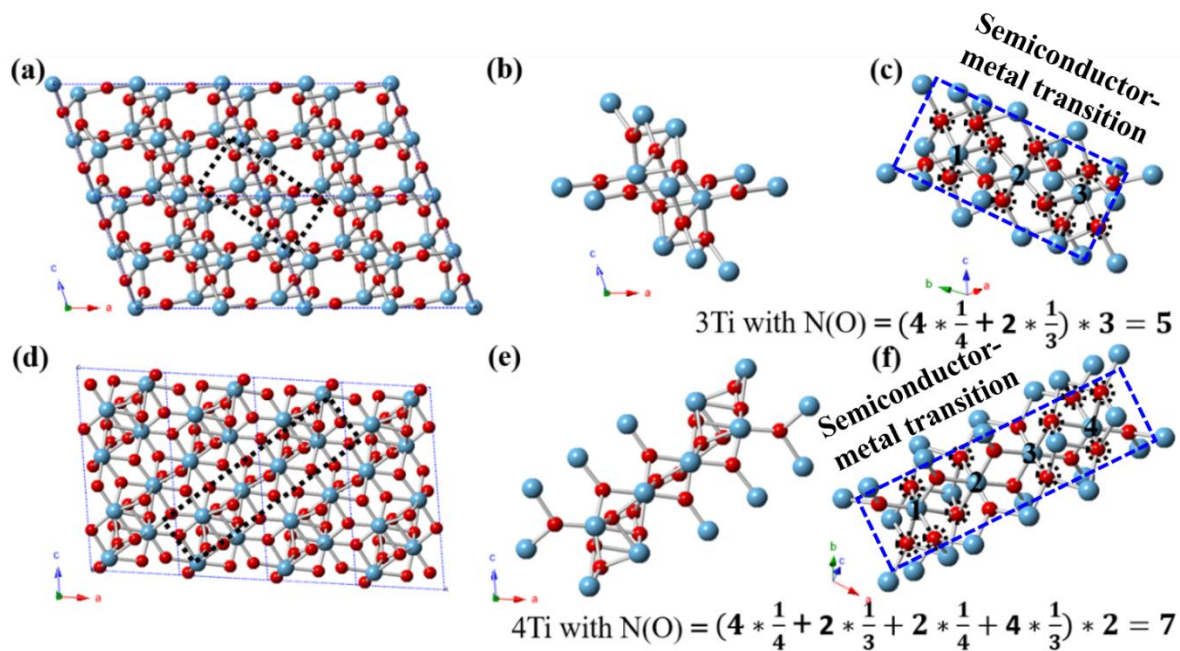


Fig. 4.7. (a) 3×3×3 Supercell of Ti_3O_5 along b axis; (b) (c) one layer of three TiO_6 octahedrons; (d) 3×3×3 Supercell of Ti_4O_7 along b axis; (e) (f) one layer of four TiO_6 octahedrons.

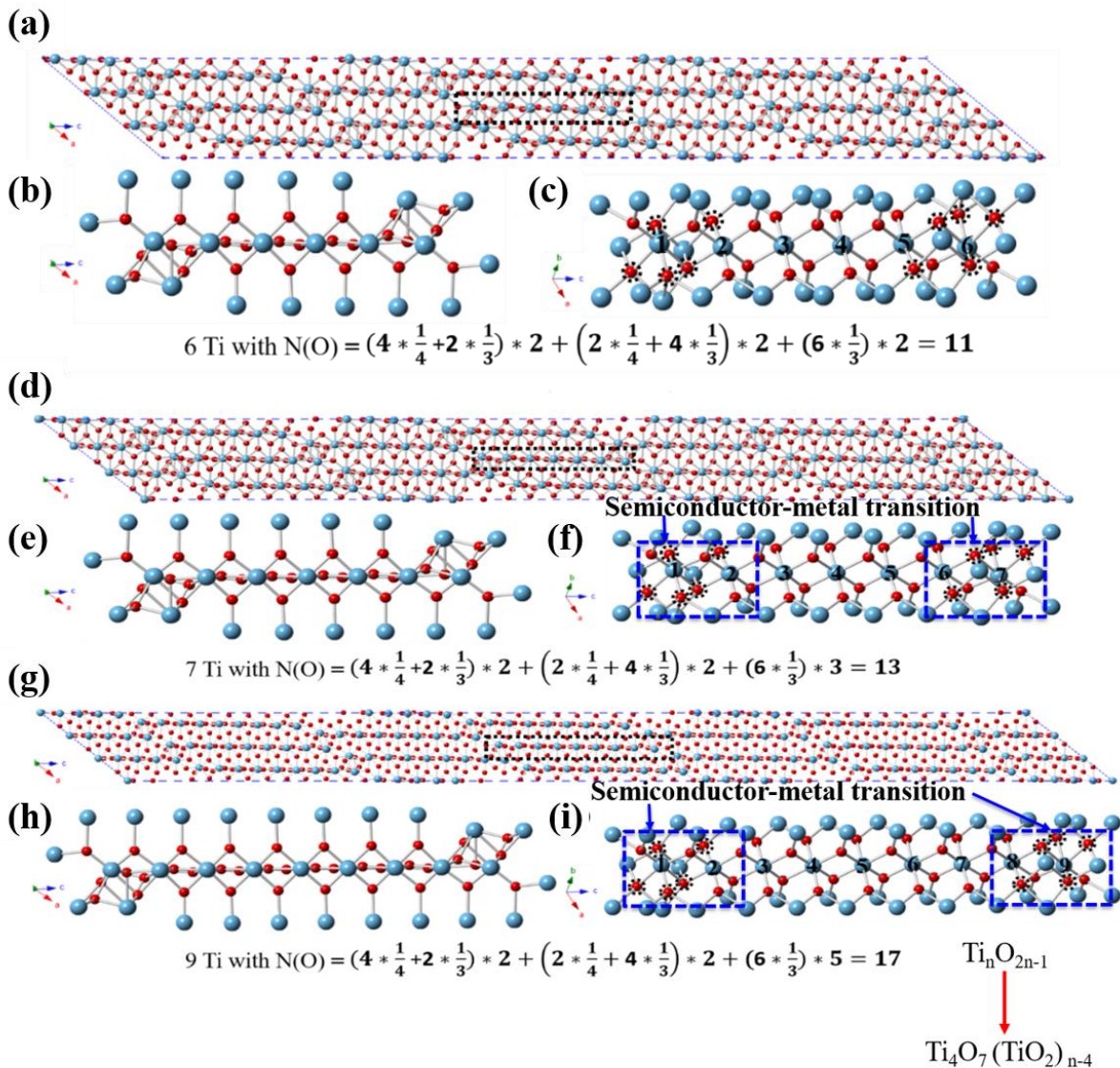


Fig. 4.8. (a) $3 \times 3 \times 3$ Supercell of Ti_6O_{11} along b axis; (b) (c) one layer of six TiO_6 octahedrons; (d) $3 \times 3 \times 3$ Supercell of Ti_7O_{13} along b axis; (e) (f) one layer of seven TiO_6 octahedrons; (g) $3 \times 3 \times 3$ Supercell of Ti_9O_{17} along b axis; (h) (i) one layer of nine TiO_6 octahedrons.

4.3.4 Morphologies and surface elemental analysis

Fig. 4.9 and Fig. S4.1 present SEM obervation of as-prepared samples, F_0 -8h, F_1 -8h, F_5 -8h, F_{10} -8h and F_{20} -8h calcined at 950 °C. Due to the high temperature sintering, F_0 -8h, F_1 -8h and F_5 -8h mainly consisted with large particles of size over 100 nm as shown in Fig. 4.9a, d, and g, respectively. The particles with size of hundreds nanometers in sample F_0 -8h pack closely as shown in Fig. 4.9b and c. With carbon compositing, the particles in F_1 -8h and F_5 -8h are surrounded by the carbon network as shown in Fig. 4.9f and i (typical area noted with red arrows), respectively. The large pore size of the carbon network in F_5 -8h can reach to 45.1 nm,

while the typical pore size is around 27.8 nm as shown in Fig. 4.9f. The carbon network in F₅-8h become denser and less observable from the SEM images (Fig. 4.9h and i). Few pores with large size of 38.2 nm and typical size of 24.3 nm. Normally, the surrounding carbon network might be helpful for light penetration and scattering for photocatalytic reactions. However, when increasing carbon content, for example, from 0.8 wt% in F₁-8h to 4.1 wt% in F₅-8h, the dense carbon might inhibit the light penetration to the surface of photocatalyst and increase the diffusion length for mass transport in photocatalytic reactions. The sample F₁₀-8h and F₂₀-8h also show morphology of big particles packing closely from the observation of SEM (Fig. S4.1), However, the BET results indicates that F₁₀-8h and F₂₀-8h have larger surface areas than that of F₁-8h, F₅-8h.

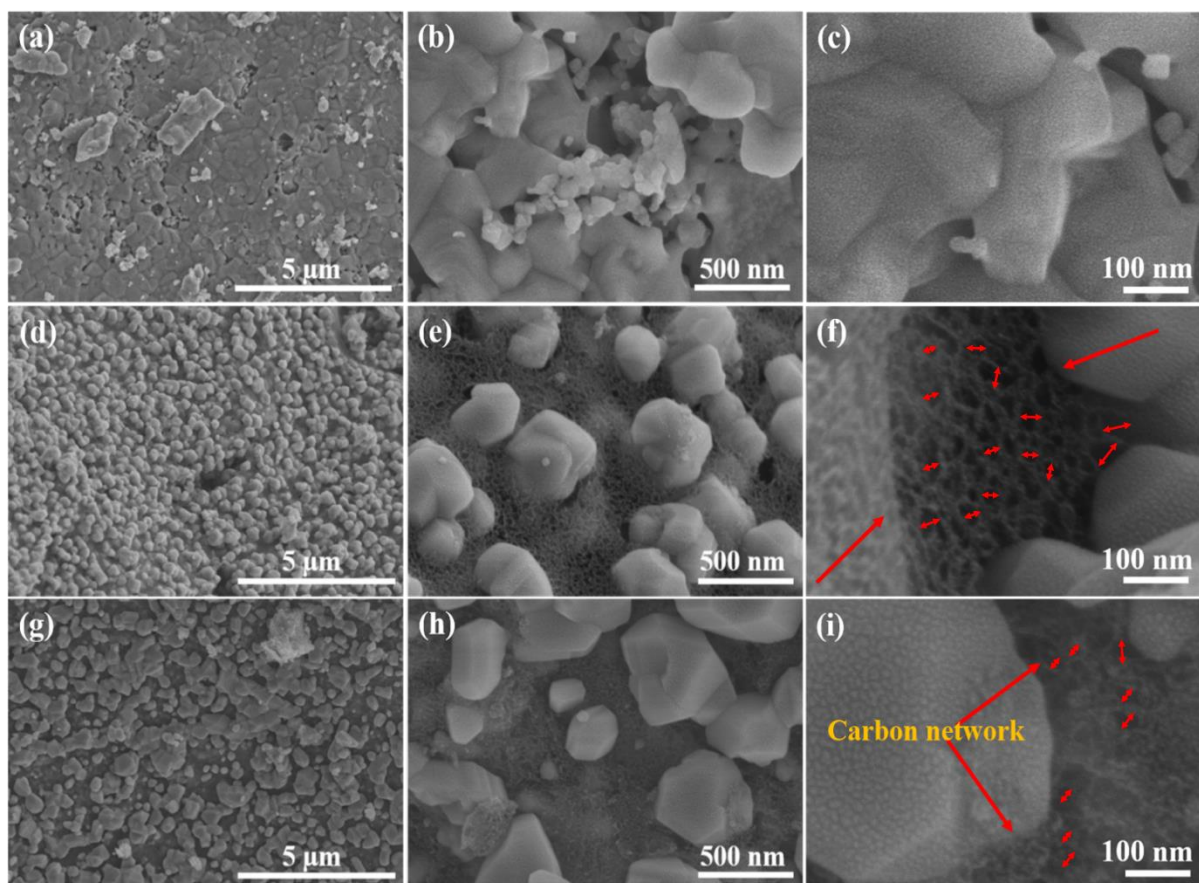


Fig. 4.9. SEM observation images of (a) (b) (c) F₀-8h, (d) (e) (f) F₁-8h, (g) (h) (i) F₅-8h calcined at 950 °C.

For further observing the microstructure of F₁₀-8h, the TEM was performed. F₁₀-8h mainly contains Ti₃O₅ with homogeneous nanoparticles size around 20 nm. The small particles of F₁₀-8h aggregated together forming big bulk as observed in SEM (Fig. S4.1). The HR-TEM image (Fig. 4.10d, e and f) show good crystallinity of Ti₃O₅ which is in good agreement with the XRD

result. The crystal and shapeless carbon was composed with Ti_3O_5 as shown in Fig. 4.10d, e and f (typical area noted in red arrows). The STEM image (Fig. 4.10g) and the corresponding EDX mapping of element Ti, O and C as shown in Fig. 4.10h, i and j, respectively show that the carbon disperses homogeneously around Ti_3O_5 nanoparticles. Other samples derived from F_{10} after calcination for 6h and 7h, F_{10-6h} and F_{10-7h} which mainly consist Ti_6O_{11} and Ti_4O_7 , respectively also show similar morphologies as shown in Fig. S4.2. The crystal $\text{Ti}_n\text{O}_{2n-1}$ closely surrounded with large amount carbon (7 wt%), as mentioned above, light penetration to the surface of $\text{Ti}_n\text{O}_{2n-1}$ photocatalyst might be prevented and the diffusion length for charge transport in photocatalytic reactions might be prolonged which might suppress the photocatalytic activity.

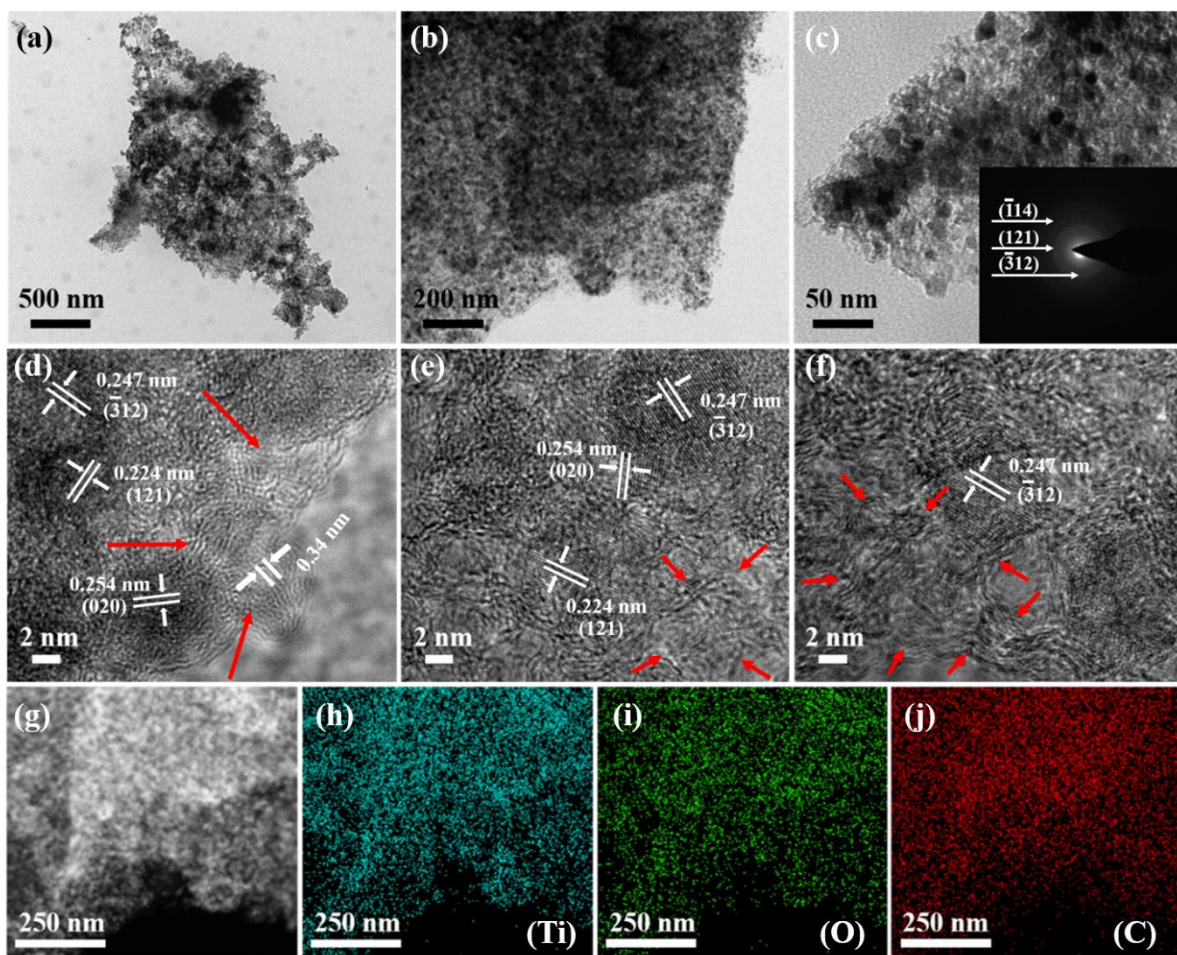


Fig. 4.10. (a, b, c) The TEM images, SAED observation (inset) and (c, d, e) HR-TEM images of F_{10-8h} ; (f) HADDF-STEM image and the corresponding EDX elemental mapping of (g) titanium, (h) oxygen and (i) carbon.

X-ray photoelectron spectroscopy (XPS) was performed to investigate the surface composition

and elemental oxidation states of as-prepared samples F₀-8h, F₁-8h, F₅-8h, F₁₀-8h and F₂₀-8h calcined at 950 °C as shown in Fig. 4.11. In Fig. 4.11a, the wide range XPS survey spectra indicate that the samples only consist of Ti, O and C. In Fig. 4.11b, F₀-8h presents two main peaks at around 463.6 eV and 457.8 eV that are attributed to the Ti 2p_{1/2} and Ti 2p_{3/2}, respectively. The peaks of Ti 2p_{1/2} and Ti 2p_{3/2} of F₁-8h, F₅-8h, F₁₀-8h and F₂₀-8h are all shifted to 464.2 and 458.6 eV due to the existence of Ti³⁺. [27-29] The detailed C1s spectra can be fitted by four peaks at 283 eV, 284.8 eV, 286 eV and 288 eV which are attributed to C-C, C-O-C, O-C=O and Ti-C bond, respectively. Specially, the C1s spectra of samples F₅-8h, F₁₀-8h and F₂₀-8h have a broad tail towards higher binding energy showing a shake-up feature due to the high concentration of Sp2 carbon as shown in Fig. 4.11c (insets). The intensity of this feature increases with higher carbon content, which is consistent with the result of TGA. Due to increased amount of surrounding carbon on the surface of Ti_nO_{2n-1} particles, the signals of Ti2P decreased gradually as shown in Fig. 4.11b. Certain amount of carbon in Ti_nO_{2n-1} might facilitate the light absorption and boost the charge transfer for photocatalytic reactions as mentioned in Chapter 3, while the large amount of carbon surrounding might prevent the light penetration like the penetration of X-ray in XPS measurements resulting in decreased photocatalytic activity. With respect to the spectra of O1s shown in Fig. 4.11d, four peaks of 529.7, 531.1, 532.1 and 532.6 have been fitted, which can be assigned to Ti-O-Ti (lattice oxygen), adsorbed O^{x-} and OH⁻/H₂O, respectively.

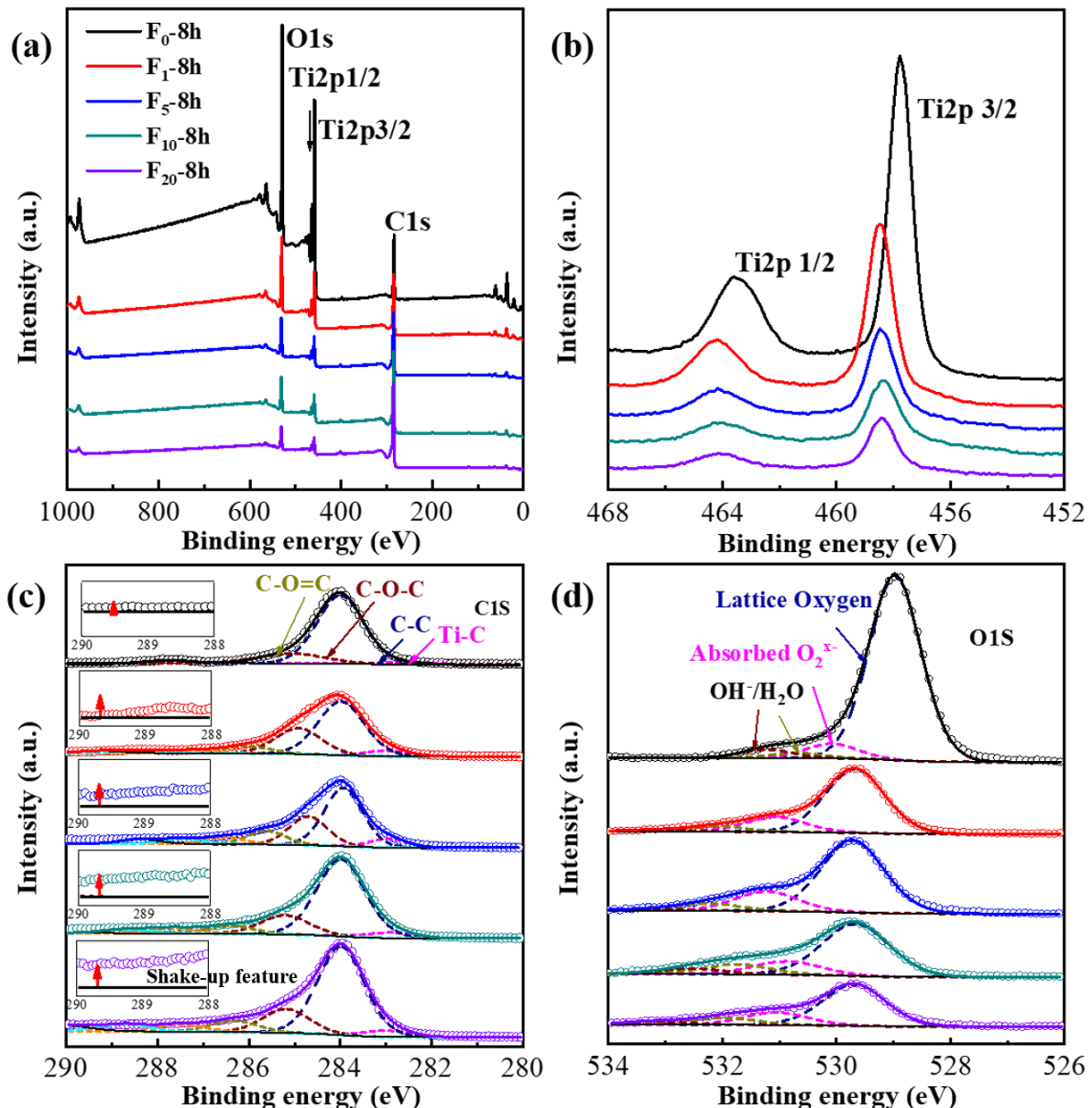


Fig. 4.11. (a) Wild range XPS spectrum and High-resolution XPS spectra of (b)Ti 2p, (c) C 1s and (d) O 1s regions of F_0 -8h, F_1 -8h, F_5 -8h, F_{10} -8h and F_{20} -8h.

4.3.5 Photoelectrochemical activity

The PEC performance of as-prepared samples were evaluated as shown in Fig. 4.12. The samples, F_5 -8h, F_{10} -7h and F_{20} -8h mainly contain Ti_4O_7 phase ($\geq 80\%$) with increased content of carbon as shown in Fig. 4.12a. Apparently, the photocurrent decreases as the carbon content increases. The extra carbon in Ti_4O_7/C system may block the light penetration and mass transport for photocatalytic reactions.

Various $\text{Ti}_n\text{O}_{2n-1}$ can be derived from F_{10} by changing the calcination durations. The F_{10-5h} , F_{10-6h} , F_{10-7h} and F_{10-8h} mainly contain Ti_9O_{17} , Ti_6O_{11} , Ti_4O_7 and Ti_3O_5 , respectively. The activity order is $\text{Ti}_6\text{O}_{11} > \text{Ti}_9\text{O}_{17} > \text{Ti}_4\text{O}_7 > \text{Ti}_3\text{O}_5$ as shown in Fig. 4.12b. The main trend is that Magnéli materials with higher value show better photocatalytic activity. The photoanode based on Ti_4O_7 (from F_{10-7h}) shows its potential in electrolysis of water under dark environment as shown in Fig. 4.12c. Under chopped light, $\text{Ti}_n\text{O}_{2n-1}$ materials exhibited certain amount of photocurrent and good photostability (Fig. 4.12d). The photocurrent density of $\text{Ti}_n\text{O}_{2n-1}$ for example F_{10-6h} which mainly consists Magnéli Ti_6O_{11} ($125 \mu\text{A cm}^{-2}$) is much higher than that of pristine TiO_2 ($0.7 \mu\text{A cm}^{-2}$) and at the same scale of that of carbon doped and coated TiO_2 ($27 \mu\text{A cm}^{-2}$) at $1.2 \text{ V}_{\text{RHE}}$ as mentioned in chapter 3. The existence of large amount of oxygen deficiencies in Magnéli $\text{Ti}_n\text{O}_{2n-1}$ results in semiconductor-metal properties and possible semiconductor-metal junction. [30] The inherent semiconductor-metal junction might be very helpful for efficient charge transfer and separation and the followed photocatalytic activity. [30] However, the enhanced semiconductor-metal transition in $\text{Ti}_n\text{O}_{2n-1}$ with lower n value would reduce the photon harvesting and the followed generation of electron/hole pairs. Thus, the intermediate Magnéli Ti_4O_7 and non-Magnéli Ti_3O_5 from the samples F_{10-7h} and F_{10-8h} , respectively show much lower photocurrent densities ($29 \mu\text{A cm}^{-2}$ and $20 \mu\text{A cm}^{-2}$, respectively). Nonetheless, the as-prepared Magnéli $\text{Ti}_n\text{O}_{2n-1}$ materials were composed with carbon, it is difficult to exclude the influence of carbon on the PEC performance. Since carbon is closely combined with $\text{Ti}_n\text{O}_{2n-1}$ particles, it is also difficult to remove carbon without changing the Magnéli phase. In addition, Magnéli materials obtained by reduction from organics usually consisted with mixed phases. [18, 20] For example, the sample F_{5-8h} contains 80% Ti_4O_7 , 15% Ti_7O_{13} and 5% Ti_6O_{11} and the sample F_{10-7h} consists with 85% Ti_4O_7 and 15% Ti_3O_5 . The photocatalytic behavior of mixed Magnéli phases must be different with the pure ones. Therefore, it is hard to obtain Magnéli $\text{Ti}_n\text{O}_{2n-1}$ and determine the PEC behavior of pure Magnéli materials.

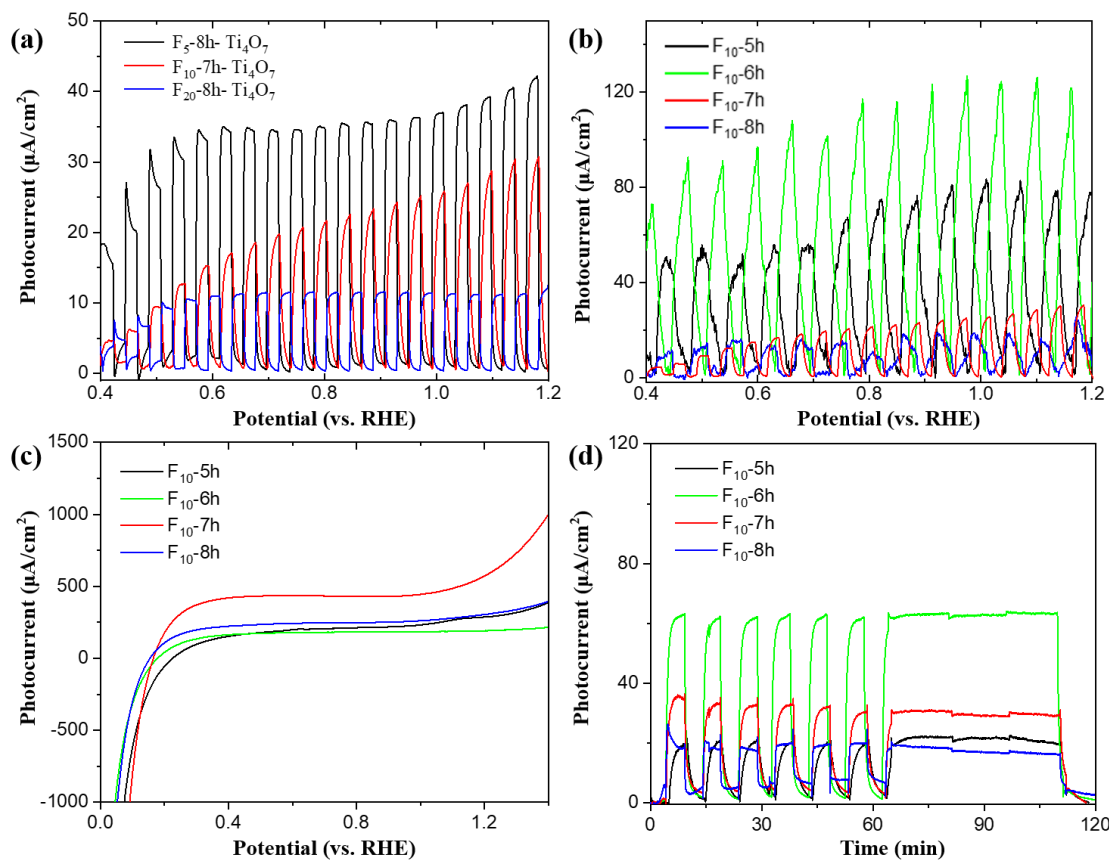


Fig. 4.12. (a) (b) Linear sweep voltammogram (LSV) curves of different photoelectrodes under chopped simulated sunlight (AM1.5, 100 mw/cm²), (c) LSV curves of different photoelectrodes under dark environment and (d) Photocurrent-time plots at applied voltage of 0.6 V (vs. RHE).

4.4 Conclusion

In summary, the controllable synthesis of various Ti_nO_{2n-1} including Magnéli materials is achieved by the facile hydrolysis of TiCl₄ droplet in fructose solution. The decomposition of polysaccharides at the strictly hypoxic environment at high temperature provides the reductive atmosphere for the growth of Ti_nO_{2n-1}. The synthesis approach allows for different variation such as fructose concentration in precursor, calcination temperature and duration to adjust the n value of Magnéli phases. The crystallite structures of Ti_nO_{2n-1} were specifically analyzed according to XRD results providing a comprehensive understanding of their unique crystallite structures with one oxygen deficiency in every layer of TiO₆ octahedrons. The oxygen deficiencies in Ti_nO_{2n-1} might be vital to form the semiconductor-metal junction which improves the charge transfer and separation, while the enhanced semiconductor-metal transition in Ti_nO_{2n-1} with lower n value might result in suppressed carrier harvesting and

depressed PEC performance. Thus, the photoelectrodes based on carbon composed Magnéli materials with higher n value show better PEC water splitting comparing to pristine TiO₂ and non-Magnéli Ti₃O₅. As a new type of photocatalysts, the Magnéli materials in this thesis show good potential for PEC water splitting. The investigation on synthesis and PEC properties of Magnéli materials can serve as a pathfinder for the future application of Magnéli materials in energy-related fields.

References

- [1] S. Andersson, B. Collén, U. Kuylensierna, A. Magnéli, *Acta chem. scand.*, 11 (1957) 1641-1652.
- [2] F. Walsh, R. Wills, *Electrochim. Acta* 55 (2010) 6342-6351.
- [3] F. Cardarelli, *Materials handbook*, Springer 2000.
- [4] K. Ellis, A. Hill, J. Hill, A. Loyns, T. Partington, *J. Power Sources* 136 (2004) 366-371.
- [5] S.-i. Ohkoshi, Y. Tsunobuchi, T. Matsuda, K. Hashimoto, A. Namai, F. Hakoe, H. Tokoro, *Nat. Chem.* 2 (2010) 539.
- [6] S. Lee, G.-H. Lee, J.-C. Kim, D.-W. Kim, *ACS Catal.* 8 (2018) 2601-2610.
- [7] P.K. Shen, C. He, S. Chang, X. Huang, Z. Tian, *J. Mater. Chem. A* 3 (2015) 14416-14423.
- [8] P. Hayfield, *Development of a New Material: Monolithic Ti₄O₇ Ebonex Ceramic*, Royal Society of Chemistry 2007.
- [9] J. Smith, F. Walsh, R. Clarke, *J. Appl. Electrochem.* 28 (1998) 1021-1033.
- [10] A. Loyns, A. Hill, K. Ellis, T. Partington, J. Hill, *J. Power Sources* 144 (2005) 329-337.
- [11] S.-Y. Park, S.-I. Mho, E. Chi, Y. Kwon, H. Park, *Thin solid films* 258 (1995) 5-9.
- [12] Z. Zhang, J. Liu, J. Gu, L. Su, L. Cheng, *Energy Environ. Sci.* 7 (2014) 2535-2558.
- [13] C. Tang, D. Zhou, Q. Zhang, *Mater. Lett.* 79 (2012) 42-44.
- [14] C. Acha, M. Monteverde, M. Nunez-Regueiro, A. Kuhn, M.A. Franco, *Eur. Phys. J. B* 34 (2003) 421-428.
- [15] T. Tsumura, Y. Hattori, K. Kaneko, Y. Hirose, M. Inagaki, M. Toyoda, *Desalination* 169 (2004) 269-275.
- [16] T. Tsumura, N. Kojitani, I. Izumi, N. Iwashita, M. Toyoda, M. Inagaki, *J. Mater. Chem.* 12 (2002) 1391-1396.
- [17] M. Toyoda, T. Yano, T. Tomoki, Y. Amao, M. Inagaki, *J. Adv. Oxid. Technol.* 9 (2006) 49-52.
- [18] M. Toyoda, T. Yano, B. Tryba, S. Mozia, T. Tsumura, M. Inagaki, *Appl. Catal. B* 88 (2009) 160-164.
- [19] Q. Shi, G. Chai, W. Huang, Y. Shi, B. Huang, D. Wei, J. Qi, F. Su, W. Xu, T. Lu, *J. Mater. Chem. C* 4 (2016) 10279-10285.
- [20] V. Adamaki, F. Clemens, P. Ragulis, S. Pennock, J. Taylor, C. Bowen, *J. Mater. Chem. A* 2 (2014) 8328-8333.
- [21] H.C. Jarrell, T.F. Conway, P. Moyna, I.C. Smith, *Carbohydr. Res.* 76 (1979) 45-57.
- [22] D. Jung, M. Zimmermann, A. Kruse, *ACS Sustain. Chem. Eng.* 6 (2018) 13877-13887.
- [23] M. Zhang, H. Yang, Y. Liu, X. Sun, D. Zhang, D. Xue, *Nanoscale Res. Lett.* 7 (2012) 38.
- [24] J. Poerschmann, B. Weiner, R. Koehler, F.-D. Kopinke, *ACS Sustain. Chem. Eng.* 5 (2017) 6420-6428.
- [25] L. Liborio, N. Harrison, *Phys. Rev. B* 77 (2008) 104104.
- [26] L.K. Keys, L.N. Mulay, *Phys. Rev.* 154 (1967) 453-456.
- [27] S.G. Ullattil, P. Periyat, *J. Mater. Chem. A* 4 (2016) 5854-5858.
- [28] M. Xing, W. Fang, M. Nasir, Y. Ma, J. Zhang, M. Anpo, *J. Catal.* 297 (2013) 236-243.
- [29] T. Le Mercier, J.M. Mariot, P. Parent, M.F. Fontaine, C.F. Hague, M. Quarton, *Appl. Surf. Sci.* 86 (1995) 382-386.
- [30] M. Domaschke, X. Zhou, L. Wergen, S. Romeis, M.E. Miehlich, K. Meyer, W. Peukert, P. Schmuki, *ACS Catal.* 9 (2019) 3627-3632.

Supplementary information

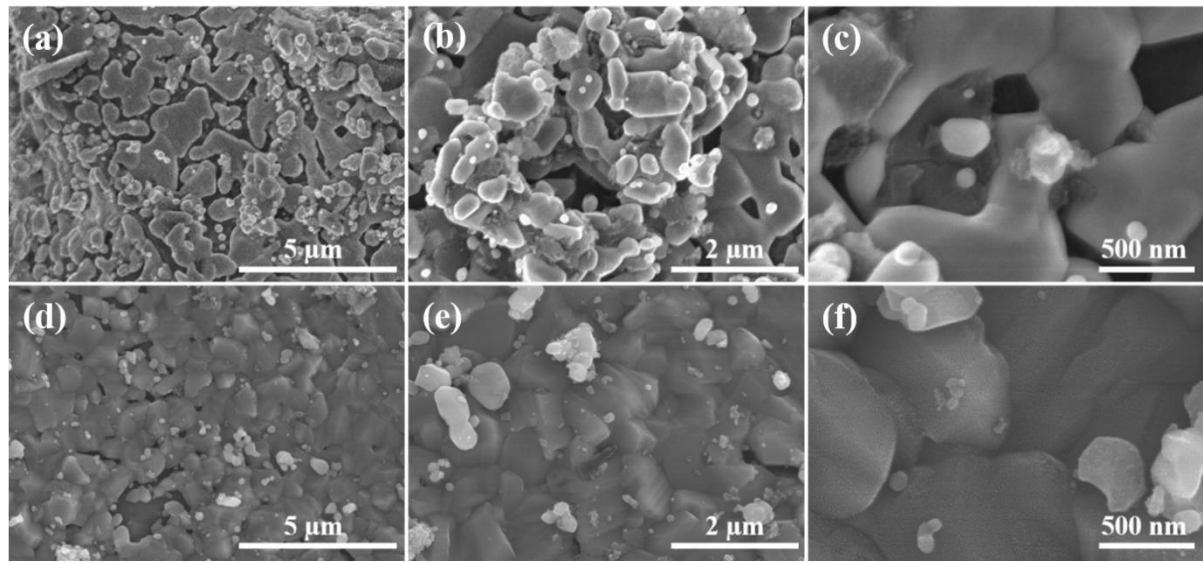


Fig. S4.1. SEM observation images of (a) (b) (c) F₁₀-8h and (d) (e) (f) F₂₀-8h calcined at 950 °C.

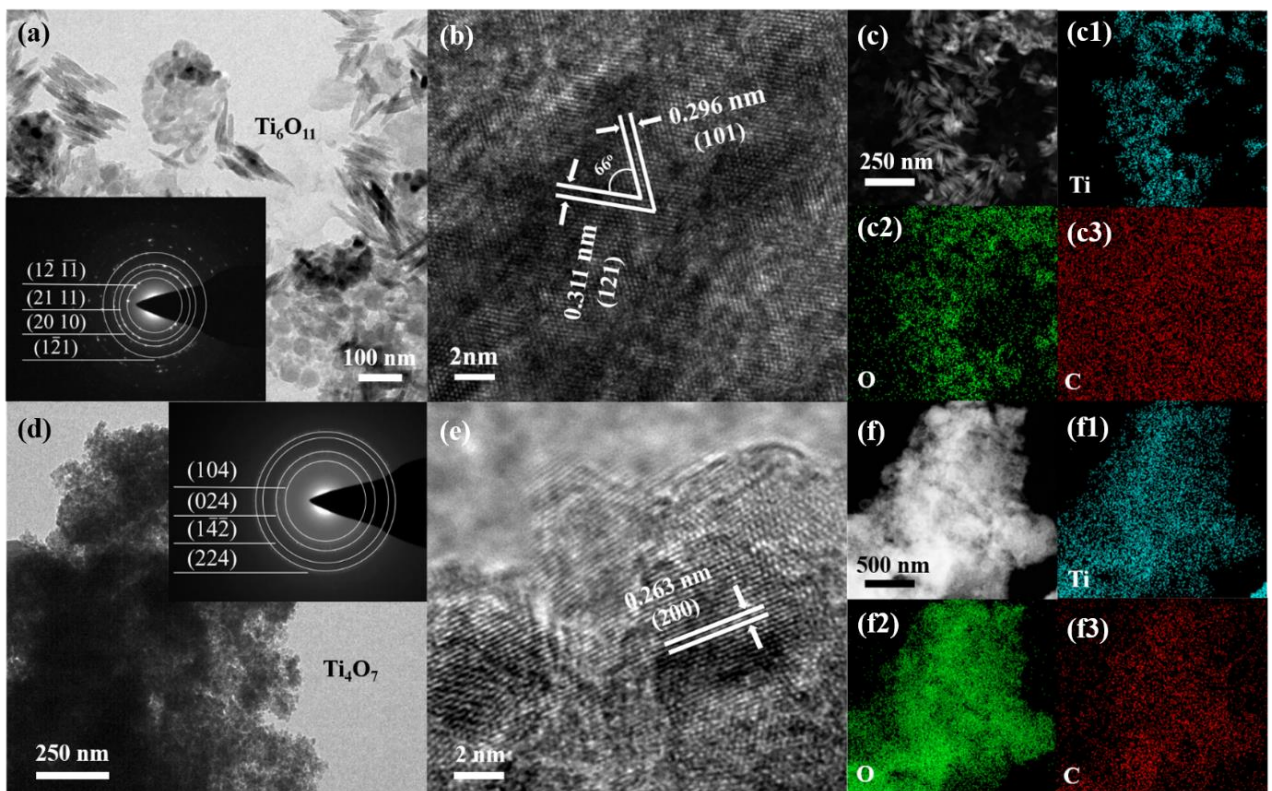


Fig. S4.2. (a) The TEM images and SAED observation (inset), (b) HR-TEM images, (c) HADDF-STEM image and the corresponding EDX elemental mapping of (c1) titanium, (c2) oxygen and (c3) carbon. (d) The TEM images and SAED observation (inset), (e) HR-TEM images, (f) HADDF-STEM image and the corresponding EDX elemental mapping of (f1)

titanium, (f2) oxygen and (f3) carbon.

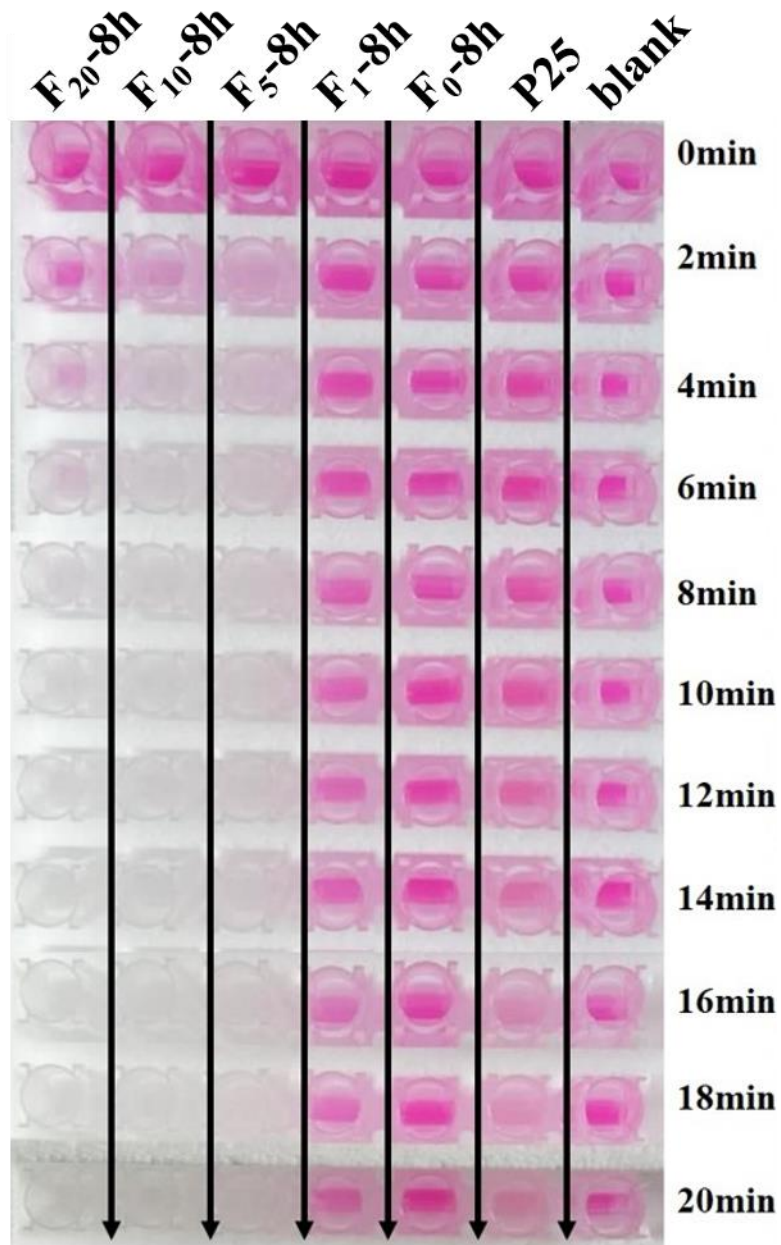


Fig. S4.3. The picture of all liquid samples taken from RhB (10 mh/L) solution within the as-prepared materials (F₀-8h, F₁-8h, F₅-8h, F₁₀-8h and F₂₀-8h,) and P25 as adsorbent

CHAPTER 5.

**Impact of electrolytic environments on solar light PEC water
splitting over different metal oxide semiconductors**

Abstract

The PEC performance in specific electrolytic environments over various photoanodes based on metal oxides semiconductor (MOSSs) synthesized by the template-based transferring method were investigated with different electrolyte cations, pH values, temperature and sacrificial reagents. The electrolyte cations have limited influence on the PEC performance of various MOSSs photoanodes. The pH values mainly affect the onset potentials of photoanodes for H₂ production. The electrolyte temperature strongly influences the photocurrent density of binary MOSSs such as BiVO₄, ZnFe₂O₄ and LaFeO₃ while shows no obvious impact on the mono MOSSs such as WO₃, TiO₂ and Fe₂O₃. For example, the photocurrent of LaFeO₃ operated at 60 °C (650 μA) is 16.3 times as that at 20 °C (40 μA) at 3 V_{RHE}. By using sacrificial electrolytes such as Na₂S and Na₂SO₃, the photocurrent of various MOSSs photoanodes was notably increased. For instance, the photocurrents of Fe₂O₃ in Na₂S (2250 μA) and Na₂SO₃ (730 μA) are 110 times and 35 times higher than that in NaOH (20 μA). The electrolytic environment especially the temperature and sacrificial additives can significantly affect the PEC performance of MOSSs photoanodes. Comparing to developing new functional photoanodes materials, modification of electrolytic environments might be an alternative and worthwhile route for enhancing the efficiency of PEC water splitting using MOSSs photoanodes.

5.1 Introduction

Considerable efforts have been devoted to the conversion of solar energy into H₂ production, however, the process of photoelectrochemical (PEC) H₂ production from pure water is still with low efficiency.^[1-3] The main problems reside in the fast and undesired recombination of photo-generated electron/hole pairs and the so-called “surface back-reaction” (SBR) effect on the semiconductor surface.^[4, 5] In order to overcome these problems and improve the efficiency of PEC water splitting for H₂ production, accommodating the electrolytic environment by adding different electron donors as sacrificial reagents, ionic species and pH mediators is simple and efficient way.^[6-9] The sacrificial electron donors in PEC electrolytes can effectively scavenge holes, prevent the recombination of photo-induced electron/hole pairs and make the photocatalysts electron-rich. Thus, sacrificial reagents (SRs) are widely utilized in the PEC water splitting systems to manage the reaction through the desired H₂ evolution and improve quantum efficiency. The often-used SRs includes alcohols,^[10, 11] amines,^[12-14] carboxylic acids^[15, 16] and inorganic Na₂S/Na₂SO₃,^[17-19] NaI/NaIO₃,^[20, 21] etc. It is clear that the SRs can profoundly influence the H₂ production efficiency and different photocatalysts can behave differently with different SRs. Selecting appropriate SRs for a defined photocatalysts is thus essential for highly efficient PEC water splitting. On the other hand, as the photogenerated carriers and adsorbed reactants accumulate on the interface of electrode-electrolyte, where the photocatalytic reactions take place, both electrolyte cations and anions can strongly influence the interface property, charge transfer and the final performance of PEC water splitting.^[22-25] Other than developing new photocatalysts, the high PEC efficiency could also be achieved by tuning electrolytic conditions. However, the knowledge and comparative studies on the specific influences of both SRs and electrolytes on the PEC performance of different photocatalysts are still very limited and it remains unclear how electrolytic species such as SRs and electrolyte cations/anions affect the behavior of different photocatalysts. In addition, other electrolytic parameters like pH values and electrolyte temperature can also eventually affect PEC performance.

Herein, we have investigated the performances of various photocatalysts on PEC water splitting under different electrolytic environments. We aim at providing the improved understanding of optimizing the electrolytic environments to enhance the efficiency of PEC water splitting over a general photoanode. In this work, different type of metal oxide semiconductors (MOSSs) are chosen as photoanodes to study the effect of electrolytic environments on their PEC performance. TiO₂ is the first and still the most investigated photocatalysts^[26-28] and used as

reference material while the hematite ($\alpha\text{-Fe}_2\text{O}_3$) has emerged as another promising photoanode material in the PEC system due to its abundance, non-toxicity and narrow band gap of 2.3 eV [29-31]. Besides, other types of MOFs such as spinel ZnFe_2O_4 (ZnCr_2O_4) [32-34], perovskite LaFeO_3 [35-37] and BiVO_4 [38-41] have also been attracted great attention for solar light PEC water splitting with visible-light response ($E_g < 3$ eV). The ordered porous thin films of different MOFs with metrics of high surface area, superior stability and reproducibility are often applied as photoanodes for PEC water splitting. [26, 42-44] Meanwhile, the template-based transferring method is generally used for synthesis of ordered porous thin films of various MOFs with multiple advantages of low cost, homogeneity and substrate compatibility. [45-47] Thus, different MOFs with the ordered porous structure were successfully fabricated based on template-based transferring method. The PEC performance in particular electrolytic environments over different photocatalysts based on ordered porous MOFs thin film photoelectrodes were studied. It is found that the electrolyte cations (Li^+ , Na^+ , K^+) differently affect the PEC behavior of these MOFs photoanodes, while the influence of cations on the PEC performance is very limited. The maximum increase of photocurrent using cation species can reach around 33%. The pH values mainly affect the onset potential (vs. RHE) of H_2 production. The electrolyte temperature of PEC cell shows no apparent influence on the photocurrent density over mono-metal oxides like TiO_2 , Fe_2O_3 and WO_3 , while the photocurrent density of binary metal oxides, BiVO_4 , ZnFe_2O_4 and LaFeO_3 increases as the electrolyte temperature increases. For example, the photocurrent of LaFeO_3 at 60 °C (650 μA) is 16.3 times as that at 20 °C (40 μA) obtained at 3 V_{RHE}. By using sacrificial electrolytes, the photocatalytic activity was notably enhanced for PEC water splitting over various photoanodes. For example, the photocurrents of Fe_2O_3 in Na_2S (2250 μA) and Na_2SO_3 (730 μA) are 110 times and 35 times higher than that in NaOH (20 μA). Clearly, the PEC performances of photoanodes based on these MOFs are effectively enhanced by adjusting electrolytic environment especially by using sacrificial electrolytes. The research on how electrolytic environments affect the PEC properties provides a new route for the designing and optimizing the efficiency of PEC water splitting, in addition to developing new functional photoanodes materials.

5.2 Materials and Methods

Preparation of Highly Ordered Monolayer Porous Film Photoelectrodes of Metal oxides: The suspension of well-dispersed polystyrene sphere (PS) with 1000 nm in diameter (2.5 wt% in water) was purchased from Alfa Aesar Corporation. The monolayer PS template was

prepared on the pre-cleaned glass slide by air/water interfacial assembly.^[48] The monolayer PS template with size under 500 nm is not visible and not easy to operate in practical experiments. Thus, the PS of 1000 nm is selected for the synthesis of the monolayer template. The monolayer templates exhibit closely packed PS with high uniformity as shown in Fig. S5.1. All precursors used for target MOFs are summarized in table S5.1. Fig. 5.1 presents the schematic illustration of the facile and general template-based transferring and precursor solution dipping strategy for synthesis of all kinds of MOS ordered micro/nano-structured porous thin films. The glass slide with monolayer PS template (Fig. 5.1a) was slowly dipped into the prepared precursor solution (Fig. 5.1b). The monolayer PS template slipped off from the glass substrate and floated on surface of the precursor solution (Fig. 5.1c). Subsequently, the floating template was moved on a target substrate, Si (for characterization) and Ti electrode (for PEC tests) (Fig. 5.1d). The template was completely filled by the precursor solution due to the capillarity effect. The monolayer PS template filled up with precursor on the substrate was withdrawn from the precursor solution and dried at 110 °C for 1 h (Fig. 5.1e). Then, the dried sample was calcined at 500 °C in air to remove the PS spheres. The uniformly ordered porous thin films of a series of metal oxides were obtained (Fig. 5.1f). Due to the uniformity of the PS template, each type of metal oxides on Ti slides with same effective area (1cm²) contains same loading amount assuring the reproducibility and reliability.

PEC measurements: The PEC performances of as-prepared photoelectrodes with a series of semiconducting metal oxide materials were evaluated in a standard quartz-made three-electrode cell with saturated calomel electrode (SCE) and platinum foil as reference electrode and counter electrode, respectively. The as-prepared metal oxide porous thin films on Ti slide are working as photoanodes. The effect of electrolyte environments such as different electrolytes, different sacrificial reagents, different pH values and different electrolyte temperatures on the PEC water splitting experiments was investigated. The potential of the photoanode was controlled by a potentiostat (CHI660E) and the SCE potential is converted into the Reversible Hydrogen Electrode (RHE) potential according to the Nernst equation, as follows:^[49]

$$E_{\text{RHE}} = E_{\text{SCE}} + 0.244 + 0.059 \times \text{pH} \quad \text{at } 25 \text{ }^{\circ}\text{C} \quad (1)$$

The photoanodes were illuminated by an artificial sunlight simulator equipped with a controllable 500 W Xenon lamp and an AM 1.5 filter (10 mW/cm²). All electrolytes used in this paper are summarized in table S5.2.

5.3 Result and discussion

5.3.1 Characterization of photoelectrodes

The monolayer polystyrene (PS) template was prepared by gas-liquid-solid interface self-assembly method.^[50, 51] Fig. S5.1 shows a photograph (inset) of the as-assembled PS with size of 1000 nm. The colourful appearance indicates its order and uniform arrangements.^[52, 53] As observed in SEM images, PS spheres are hexagonally close-packed together by self-assembly, forming a 2D colloidal crystal with long range order. The transfer process from the glass slide to a target substrate is illustrated in Fig. 5.1 (a-e). The practical transferring process for TiO₂ and BiVO₄ through target precursors is presented in Fig. S5.2. After organic PS templates were removed by calcination under air at 500 °C for 2 hours, the ordered nanoporous thin films of different MOFs were obtained as shown in Fig. 5.1f using Fe₂O₃ as example on Si substrate.

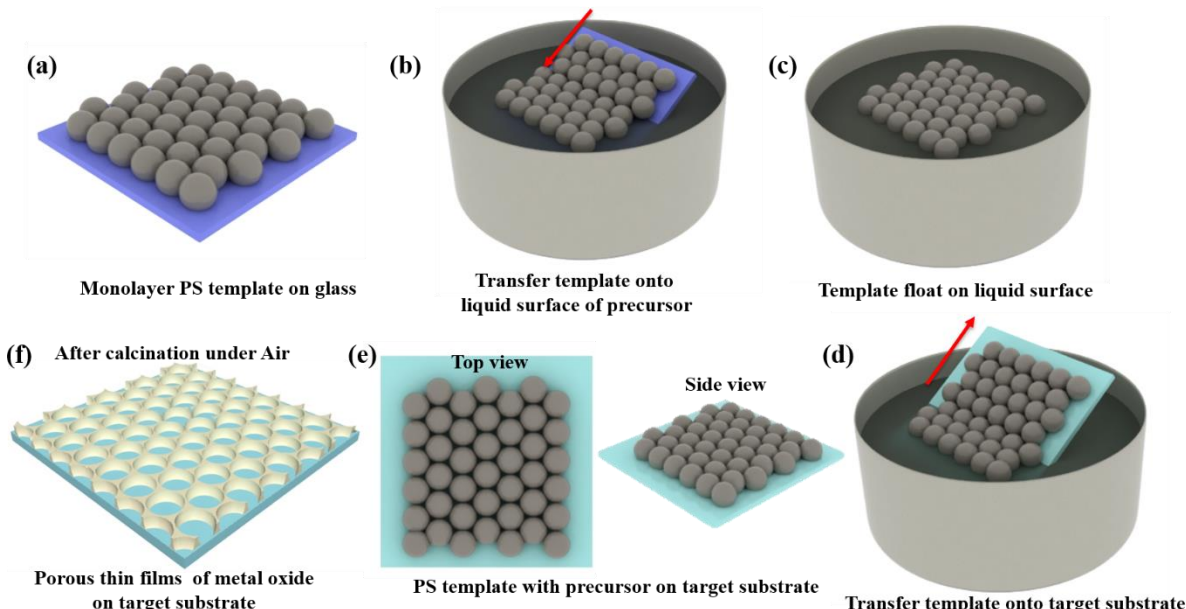


Fig. 5.1. Schematic illustration of the fabrication procedure of ordered porous thin films of metal oxides: (a) Monolayer self-assembled PS template on a glass slide; (b) The PS template is dipped into prepared precursor solution; (c) The template floating on the surface of the solution; (d) Floating template is harvested on a target substrate; (e) Substrate covered with the monolayer PS template filled up precursor solution; (f) The ordered porous thin film on target substrate after calcination.

The photoanodes for PEC measurements based on materials of different MOFs such as TiO₂, Fe₂O₃, WO₃, ZnFe₂O₄, ZnCr₂O₄, BiVO₄ and LaFeO₃ are well-prepared using above-mentioned

method. The XRD results confirm that all these samples have good crystallinity as shown in Fig. 5.2a. The typical morphology of ordered porous Fe_2O_3 thin film was firstly observed as representative example by FE-SEM (Fig. 5.2b), showing honeycomb-like hexagonal arrangement with limited cracks.

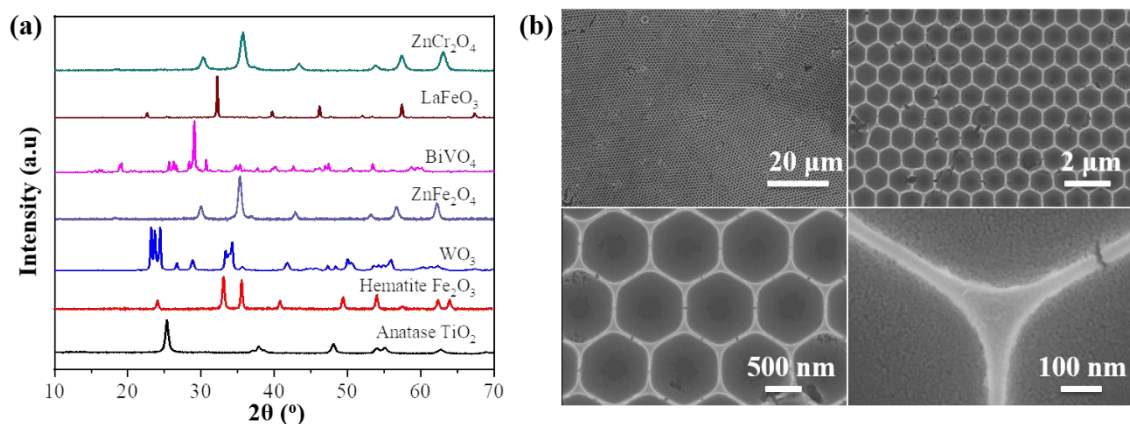


Fig. 5.2. (a) XRD patterns of as-prepared MOSSs films; (b) FE-SEM images of monolayer Fe_2O_3 ordered nanoporous thin film on Ti electrodes.

The optical band gap of TiO_2 [54, 55], WO_3 [56, 57], BiVO_4 [58, 59], Fe_2O_3 [60, 61], LaFeO_3 [62, 63] and ZnFe_2O_4 (ZnCr_2O_4) [64-66] are around 3.2, 2.8, 2.4, 2.3, 2 and 1.9 eV, respectively. The band gap and band potentials of MOSSs are summarized in Fig. 5.3. [67-69] The photoelectrodes with semiconducting metal oxides of a range of electronic bandgap varying from 3.2 to 1.9 eV are thus prepared.

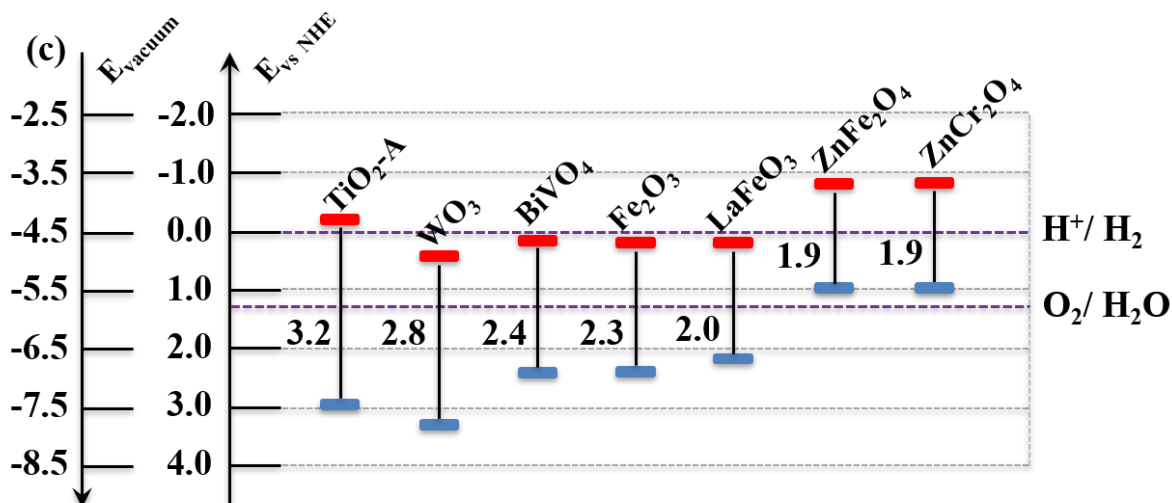


Fig. 5.3. Band structure of as-prepared MOSSs and redox potentials of water splitting.

5.3.2 Effect of different electrolyte environments on PEC water splitting performance

5.3.2.1 Effect of cations

The PEC performance of as-prepared MOSSs photoanodes was first evaluated using strong alkaline electrolytes (LiOH, NaOH, and KOH). Fig. S5.4 shows linear voltammetric curves of different MOSSs photoanodes obtained under chopped on/off light. The trends of curves are very similar in these electrolytes with different cations (Li^+ , Na^+ , K^+) for each type of photoanodes. The maximum photocurrents achieved in different electrolytes by different photoanodes are integrated in Fig. 5.4. TiO_2 and LaFeO_3 present higher photocurrent in NaOH than that in KOH and LiOH while Fe_2O_3 , BiVO_4 and ZnCr_2O_4 behave better in KOH and for ZnFe_2O_4 , the higher photocurrent is observed in LiOH. It has been proved that cations affect the dissociation of O-H bond which is vital to water oxidation by interacting with OH species adsorbed on the electrode. It has also been suggested that the strength of the interaction between alkali-metal cation and OH^- and the extent of O-H bond weakening increased in a sequence of $\text{Li}^+ > \text{Na}^+ > \text{K}^+$ by density functional theory (DFT). [23] However, most MOSSs photoanodes in our work show the lowest photocurrent in LiOH. This might be attributed to the strong adsorption strength of Li^+ terminal oxygen ions on the surface of MOSSs which blocks the active O_2 evolution sites and hinders the conversion efficiency of water splitting. [70] In addition, the perturbation effect of cations on water structure with a trend of $\text{K}^+ > \text{Li}^+ > \text{Na}^+$ is favorable for the mass transfer near the electrode surface and useful for water splitting reactions. Thus, most MOSSs show a better activity in KOH. Nevertheless, the activity difference varies a little in these three electrolytes over various photoanodes. The maximum increase of photocurrent achieved by LaFeO_3 from the lowest 32 μA in KOH to highest 43 μA in NaOH is around 33%. The enhancement of PEC performance contributed by adjusting cation species is very narrow. This part of work showed that the electrolyte cations (Li^+ , Na^+ , K^+) can differently affect the PEC behavior of these MOSSs photoanodes while their effect on the PEC performance is very limited.

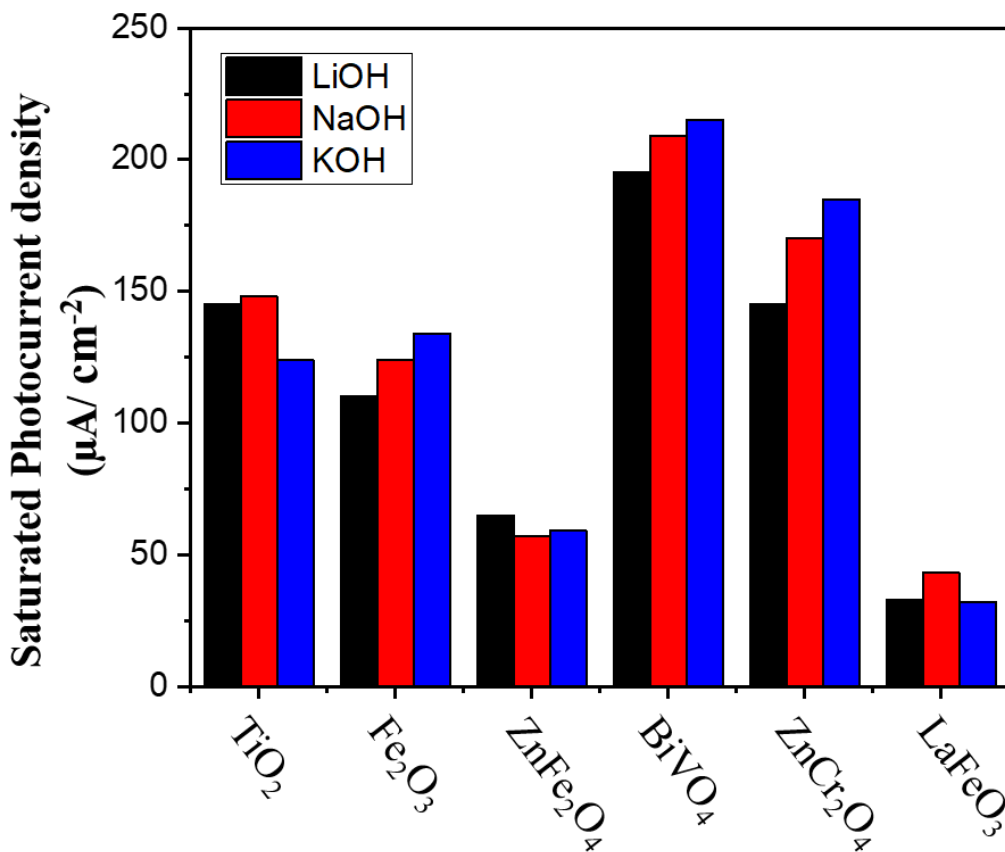


Fig. 5.4. The collected statistics of saturated photocurrents of MOSSs in different electrolytes.

5.3.2.2 Effect of pH values

The photoelectrochemical reactions of water splitting are significantly influenced by the pH value of the electrolytes which regulates the amount of H^+ or OH^- ions. The PEC performances of TiO_2 , Fe_2O_3 and ZnFe_2O_4 are systematically investigated in electrolytes with different pH values as shown in Fig. S5.5. In this part, KOH is applied to adjust the pH from 7 to 14 while HCl is used to adjust pH from 7 to 0. The concentration of the total cations or anions is adjusted by adding KCl to 1 mol/L. The SCE potential is converted into RHE potential according to Nernst equation [49]. As shown in Fig. 5.5a, the photocurrent of TiO_2 decreased as the pH value increased from 0 to 10 and then slightly increased as the pH increased to 14. As Fe_2O_3 and ZnFe_2O_4 are soluble in strong acid solution, the lowest pH value is set to 4. The Fe_2O_3 is more sensitive to pH value, the photocurrent at 1.5 V (vs. RHE) decreased dramatically from 78 μA at pH = 4 to 38 μA at pH = 10 and quickly increased up to 100 μA at pH = 14. ZnFe_2O_4 is

blunter with pH value but shows a similar activity trend with pH value as that of TiO_2 . The base electrolyte with high pH value provides more OH^- ions to react with photogenerated holes forming hydroxyl radicals and promoting the separation of electron/hole pairs. The abundant H^+ ions in acid environment can directly react with electrons to produce H_2 . Thus, MOSSs show better PEC performance in both acid and base electrolyte than that in neutral one.

Meanwhile, the onset potentials for PEC water splitting are shifted negatively as the pH value decreases. As shown in Fig. 5.5b, the onset potential of TiO_2 decreased from 0.0 V_{RHE} at pH = 14 down to -0.50 V_{RHE} at pH = 2. Due to the oxidation behaviour of HCl at pH = 0, the onset potential of TiO_2 photoelectrode is shifted positively to -0.32 V_{RHE}. The onset potentials of Fe_2O_3 and ZnFe_2O_4 are shifted from 0.41 V_{RHE} and 0.12 V_{RHE} at pH = 14 to 0.0 V_{RHE} and -0.2 V_{RHE} at pH = 4, respectively. In a photoelectrochemical system, the external energy has to be subtracted from the energy gain for calculating the solar-to-hydrogen conversion efficiency. Thus, the low onset potential is important to enhance the efficiency of PEC water splitting. By adjusting the pH value, the PEC performance of MOSSs can be improved. Unfortunately, even the low pH value results in low onset potential, most metal oxides are soluble in acid electrolyte except some metal oxides with high valency such as TiO_2 , SnO_2 and WO_3 et al. It is worth noting that for Fe_2O_3 and ZnFe_2O_4 , the best pH value of their utilization in PEC H_2 production should be 4.

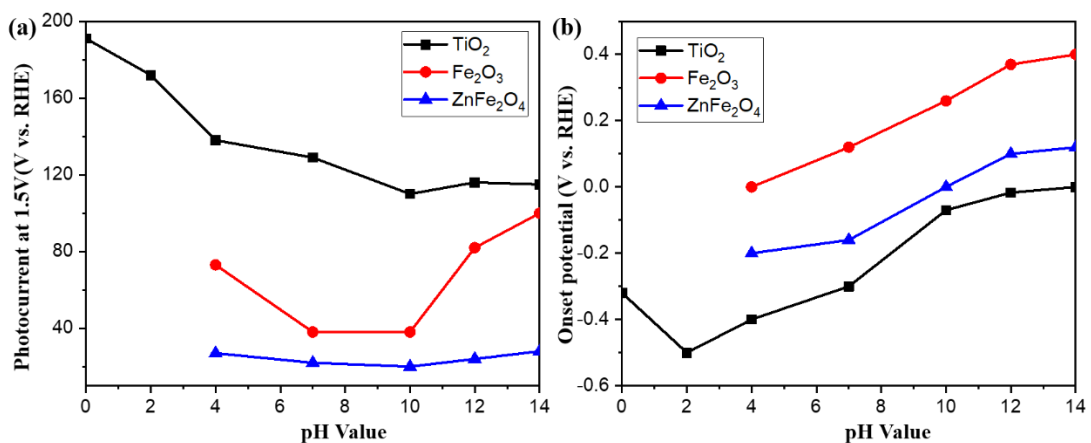


Fig. 5.5. The collected statistics of (a) photocurrent at 1.5 V (V vs. RHE) and (b) onset potential (V vs. RHE) of MOSSs in electrolytes with different pH values.

5.3.2.3 Effect of temperature

The PEC cells, as other solar cells are very sensitive to temperature. The temperature of electrolytic environment affects ionic mobility, diffusion and conductivity of electrolytes and both electrical and optical properties of photoelectrodes.^[71-73] High temperature might result in improved mass transport, photocatalytic activity and better PEC performance. Little work has been carried out concerning the effect of temperature on PEC performance for water splitting over different photoanode materials. In the present work, a PEC cell using as-prepared 6 MOFs photoanodes was operated from 20 to 60 °C with steps of ca. 10 °C. From the original LSV curves as shown in Fig. S5.6, we can see that the LSV curves of TiO₂ (Fig. S5.6a) and WO₃ (Fig. S5.6b) are very stable as the electrolyte temperature increases. The LSV curves of Fe₂O₃ (Fig. S5.6c), ZnFe₂O₄ (Fig. S5.6d), BiVO₄ (Fig. S5.6e) and LaFeO₃ (Fig. S5.6f) become steeper showing stronger catalytic current density as the temperature rises from 20 to 60 °C. However, the photocurrents of three mono-metal oxides, TiO₂, WO₃ and Fe₂O₃ at different temperatures remain relatively steady as the electrolyte temperature arises as depicted in Fig. S5.7a, b and c, respectively. The plots of photocurrents of TiO₂, WO₃ and Fe₂O₃ as electrolyte temperature from 20 to 60 °C are shown in Fig. S5.7d. The average increase percentages of photocurrents per 10 °C of TiO₂, WO₃ and Fe₂O₃ at 2 V_{RHE} is around 6%, 8% and 1%, respectively. Apparently, the PEC performances of TiO₂, WO₃ and Fe₂O₃ are not sensitive to electrolyte temperature. However, increasing the electrolyte temperature results in remarkably improvement of PEC performance using photoanodes based on binary-oxides such as ZnFe₂O₄, BiVO₄ and LaFeO₃ as shown in Fig. 5.6a, b and c, respectively. The photocurrents of BiVO₄, ZnFe₂O₄ and LaFeO₃ at 60 °C (505, 581 and 650 μA) are 2.5, 8.3 and 16.3 times as that at 20 °C (203, 70 and 40 μA) at 3 V_{RHE}, respectively as shown in Fig. 5.6d. Binary-metal oxides (BMOs) contain two different metal ions, one is active and the other one can be less electrochemically active.^[74, 75] At low temperature, the BMOs might be less active than one of the pure ones. For example, Fe₂O₃ performs better PEC activity than ZnFe₂O₄ and LaFeO₃ (40 and 31 μA at 2 V_{RHE}) with higher photocurrent at lower potential (175 μA at 2 V_{RHE}) at room temperature (20 °C). By thermal excitation at higher temperature, BMOs can exert the synergistic effect of pure ones which can ameliorate both catalytic and photocatalytic activity. Thus, the photocurrent of ZnFe₂O₄ and LaFeO₃ at 2 V_{RHE} (205 and 303 μA, respectively) reach to the same level as that of Fe₂O₃ photoanode (224 μA at 2 V_{RHE}) at 60 °C. However, the photocurrent of Fe₂O₃ already became saturated at 2 V_{RHE}, while the photocurrent of ZnFe₂O₄ and LaFeO₃ are still increasing as the applied potential increasing. At 3 V_{RHE}, the photocurrents

of ZnFe_2O_4 and LaFeO_3 (581 and 650 μA , respectively) are two times higher than the maximum photocurrent obtained by Fe_2O_3 photoanode (224 μA at 2 V_{RHE}).

Moreover, the phenomenon of thermal-assisted PEC performances over these photoanodes is closely related to photothermal catalysis which has become a sub-discipline of heterogeneous catalysis. [73, 76, 77] Without light illumination, three binary photoanodes, ZnFe_2O_4 , BiVO_4 and LaFeO_3 still show enhanced current density as shown in Fig. S5.6d, e and f, respectively, which can be ascribed to the thermochemical activity. The photothermal catalysis combines both thermochemical and photochemical processes which synergistically enhanced the photocurrent as well as the efficiency of water splitting. [73, 77] The fundamental mechanism is still unclear and more investigations are expected to be carried out.

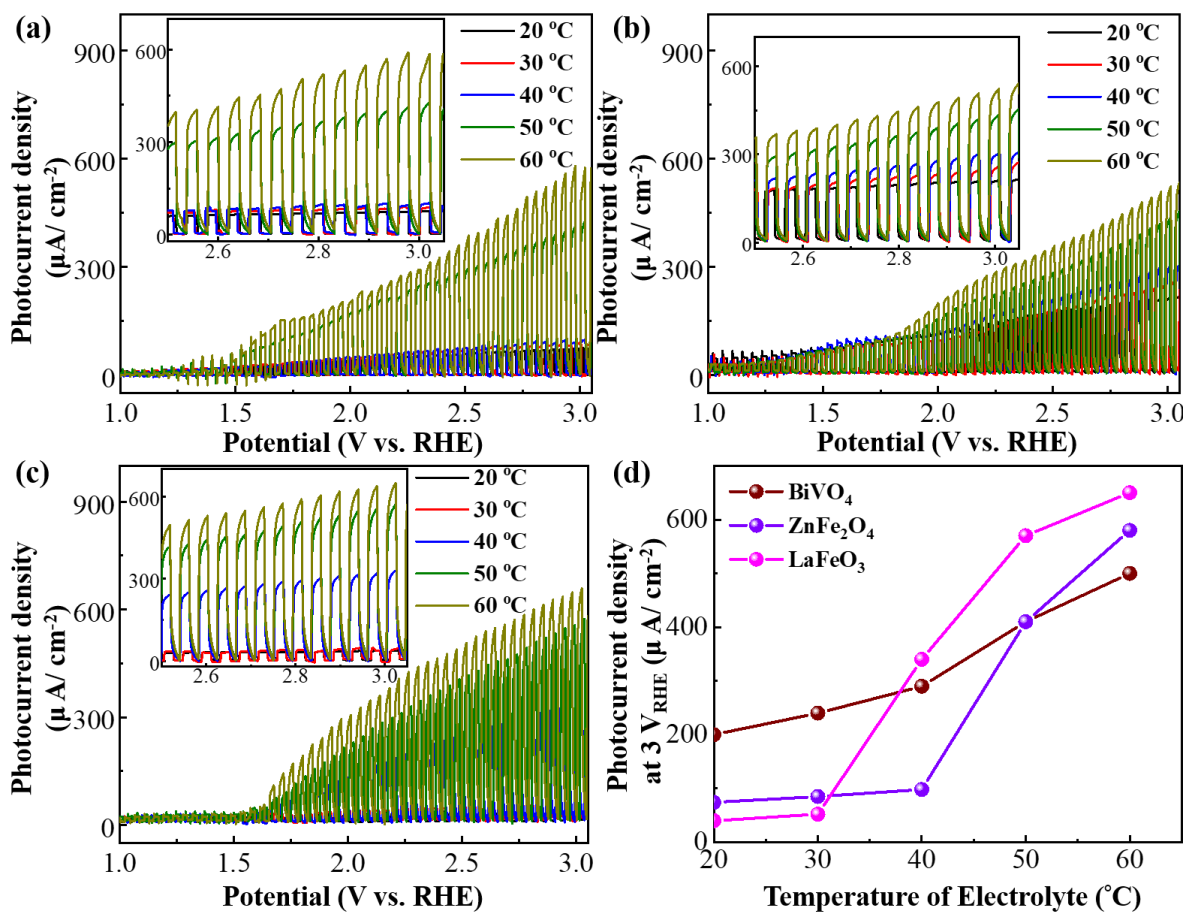


Fig. 5.6. Linear sweep voltammogram (LSV) curves under chopped light of different photoanodes based on (a) ZnFe_2O_4 , (b) BiVO_4 and (c) LaFeO_3 monolayer porous thin films (inset: magnified view) and (d) their collected photocurrent at 3 V_{RHE} at different electrolyte temperature.

5.3.2.4 Effect of Methanol, Na₂S, Na₂SO₃, NaI and NaIO₃ as Sacrificial Reagents

For most MOFs even with narrow bandgap lower than 2.5 eV such as Fe₂O₃ and LaFeO₃, the main problems of low solar-to-hydrogen (STH) conversion efficiency for photocatalytic water splitting are the rapid recombination of photogenerated electron/hole pairs and the “surface back-reaction” (SBR) effect. Addition of sacrificial reagents (SRs) as the electron donor or hole scavenger into electrolytes is a good solution to depress the recombination charge carriers and improve the photo-efficiency of H₂ production. Without the production of oxygen, the SBR effect is highly suppressed. Methanol is the mostly used SRs among various compounds due to its decreased oxidation potential and good permittivity. The PEC performances of six as-prepared MOFs were evaluated in electrolyte of 1 mol/L KOH with mixed methanol and water as solvent. As shown in Fig. S5.8, the photocurrents of all MOFs are enhanced by adding methanol especially at low potential (V_{SCE}). For example, the photocurrents of TiO₂, Fe₂O₃, ZnFe₂O₄, BiVO₄, ZnCr₂O₄ and LaFeO₃ are increased from 100, 15, 17, 46, 51 and 16 μA in pure aqueous solution to 150, 71, 26, 145, 94 and 43 μA, respectively in mixed methanol and water with a volume ratio of 1:4 at 0.2 V_{SCE}. The PEC performances of these MOFs are all enhanced by adding methanol into electrolytes. The volume ratio of 1:4 of methanol and water is the most acceptable one in most published literatures. There is a slight increase on photocurrent with higher volume ratio (1:2) of methanol to water. The H₂ production rate in methanol / water (1:4) is almost saturated. However, methanol as electron donors are continuously consumed in the photocatalytic reactions, the subsequent addition of methanol is thus absolutely required to sustain H₂ production.

Suitable SRs are normally necessary to improve the STH efficiency for photocatalytic H₂ production. The parameters of oxidation potentials and permittivity should also be considered in choosing optimal SRs for different photocatalysts. The standard thermodynamic values of various SRs comparing to that of water are summarized in table S5.3 as a reference for choosing SRs on the terms of splitting energy (eV). For example, diethyl ether (l) and hydrogen peroxide (l) with low splitting energy (0.61 and 0.62 eV, respectively) can be promising SRs for consuming holes enhancing H₂ production efficiency.

The Na₂S and Na₂SO₃ are frequently employed electrolytes and effective sacrificial reagents for PEC water splitting.^[78-81] Hara et al. first time found the phenomenon of H₂ production in pure Na₂S solution in 1999.^[82] Both Na₂S and Na₂SO₃ are able to produce H₂S, which can be oxidized much easier than H₂O over semiconductor photocatalysts. S²⁻, SO₃²⁻ and H₂S can work as electron donors helping effectively to prevent the recombination of electron/hole pairs. Ions

Chapter 5

like disulfide ions (S_2^{2-}) or sulfite ($S_2O_4^{2-}$) would form after the photoreactions. In present work, the PEC performances of different MOFs photoanodes were evaluated using Na_2S and Na_2SO_3 as electrolyte as shown in Fig. S5.9. Other sacrificial electrolytes NaI and $NaIO_3$ are also employed as shown in Fig. S5.10 and S11 as reference electrolytes. TiO_2 shows stably low photocurrents in different electrolytes as shown in Fig. 5.7a due to its large band gap. For other MOFs with narrow band gap (< 2.5 eV), the main problem of low photocatalytic activity is attributed to the rapid recombination of photogenerated electron/hole pairs. Upon the help of sacrificial electrolytes, the photocatalytic activity might be notably enhanced for PEC water splitting. The Fe_2O_3 , $BiVO_4$ and $ZnFe_2O_4$ photoanodes achieved outstanding photocurrents in Na_2S and Na_2SO_3 electrolytes as shown in Fig. 5.7b, c and d, respectively. The photocurrents in Na_2S (2250 μA) and Na_2SO_3 (730 μA) at 1V_{RHE} are 110 times and 35 times higher than that in $NaOH$ (20 μA) over Fe_2O_3 photocatalyst. The photocurrents of $BiVO_4$ in Na_2S (300 μA) and Na_2SO_3 (100 μA) are around 10 times and 3 times that in $NaOH$ (33 μA), respectively. For $ZnFe_2O_4$, the photocurrents in Na_2S (96 μA) and Na_2SO_3 (74 μA) are 12 times and 9 times as that in $NaOH$ (8 μA). $LaFeO_3$ also shows more or less 5 times photocurrents than in Na_2S (36 μA) and Na_2SO_3 (30 μA) as that in $NaOH$ (6 μA) as shown in Fig. 5.7e. The photocurrents of $ZnCr_2O_4$ also increase in Na_2S and Na_2SO_3 comparing to that in $NaOH$ as shown in Fig. 5.8f.

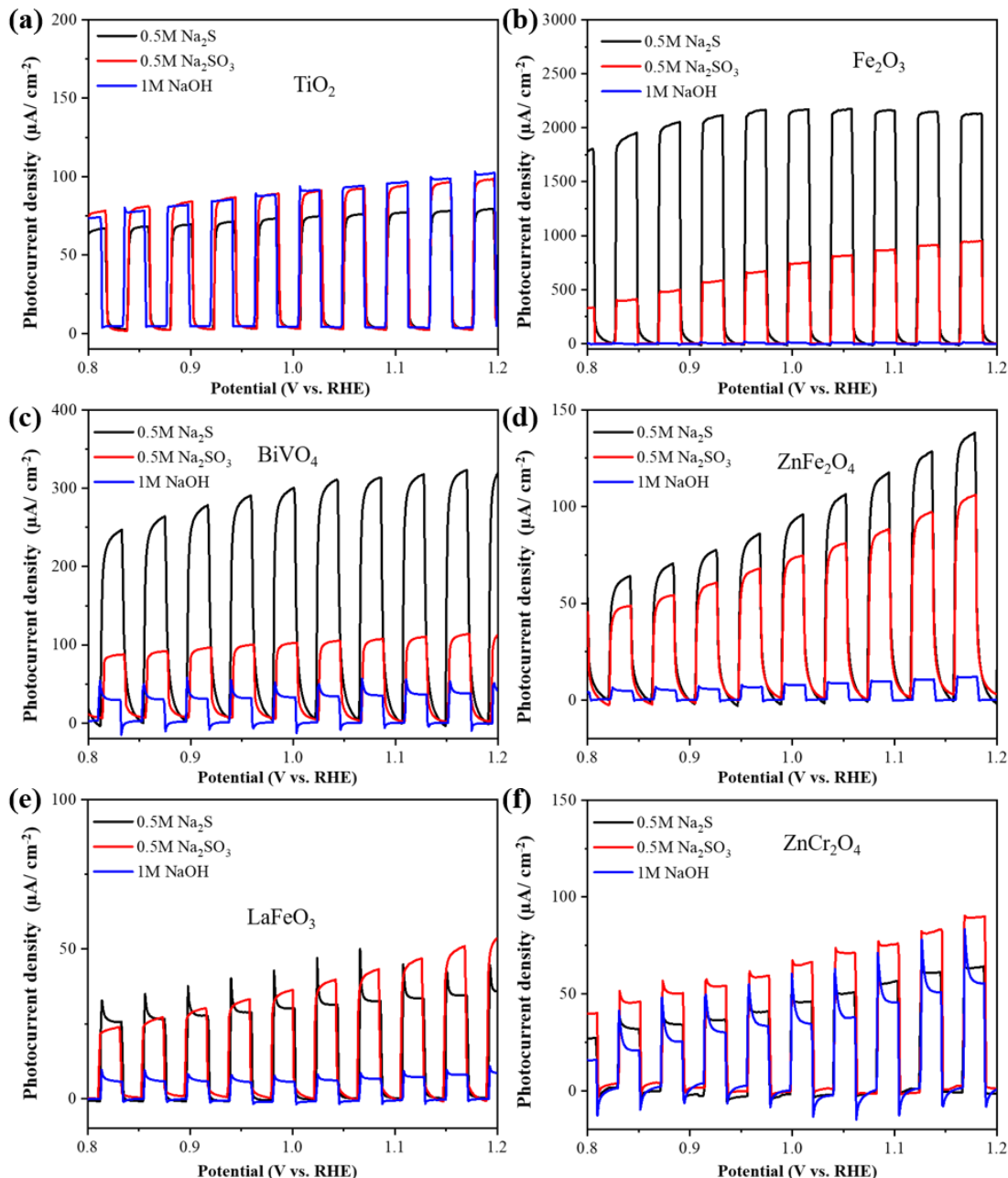


Fig. 5.7. Linear sweep voltammogram (LSV) curves of photocurrent density after subtracting current density under dark environments of (a) TiO_2 , (b) Fe_2O_3 , (c) BiVO_4 , (d) ZnFe_2O_4 , (e) LaFeO_3 and (f) ZnCr_2O_4 photoanodes using Na_2S , Na_2SO_3 and NaOH electrolytes.

For better comparison, the photocurrents density of various MOs in 5 kinds of eletrolytes at 1 V_{RHE} are collected in Fig. 5.8. Except TiO_2 , other MOs photoanodes all shows enhanced photocurrent in Na_2S and Na_2SO_3 comparing to that in NaOH. Apparently, the sacrificial electrolytes, especially Na_2S and Na_2SO_3 as electron donors have significantly improved the PEC performance of various MOs photoanodes. Some MOs are very sensitive to Na_2S and

Na_2SO_3 electrolytes. For example, the photocurrent of monolayer Fe_2O_3 thin film can be enhanced to mA level in Na_2S . The surface sulfide modification which leads to high electrical conductivity should be taken into consideration. The slight phase changing or reduction and small amount of sulfur doping could also occur. [83]

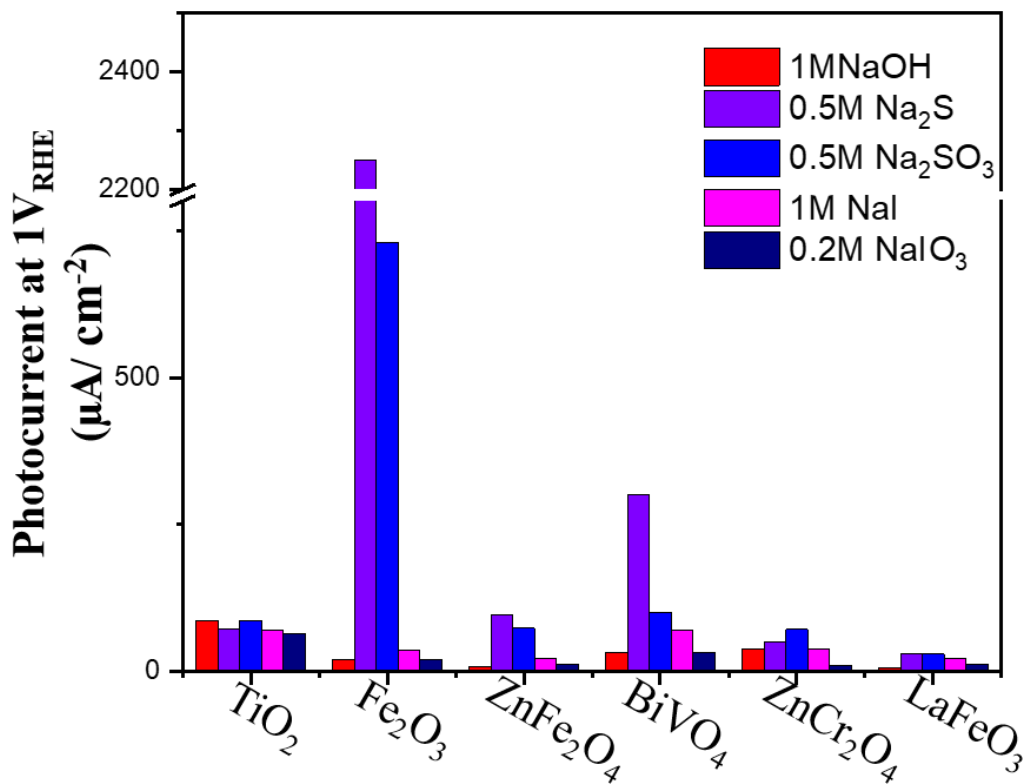


Fig. 5.8. The collected statistics of photocurrents density at 1V_{RHE} of MOSSs in different electrolytes.

5.4 Conclusion

The PEC performances of various metal-oxide-semiconductors as photocatalysts were comprehensively investigated under different electrolytic environments with different cations, pH values and temperature. It is found that the alkali cations have little influence on the PEC performance in alkali electrolyte solutions. Both strong acid and base electrolytes can boost high photocurrents. Even the low pH value leads to low onset potential (vs. RHE) of H_2 production, most MOSSs are soluble in acid electrolytes and prefer electrolyte with high pH values. Mono-metal oxides like TiO_2 , Fe_2O_3 and WO_3 show no apparent response to electrolyte temperature changed from 20 to 60 °C. However, the photocurrent of binary metal oxides (BMOs), BiVO_4 , ZnFe_2O_4 and LaFeO_3 can be highly enhanced by increasing the operating temperature. The photocurrent LaFeO_3 at 60 °C at 3 V_{RHE} (650 μA) is 16.3 times as that at 20

°C (40 μ A). The thermal-assisted PEC performances over BMOs could be assigned to the thermal-excited synergy of two metal components and their photothermal activity which highly enhance the photocurrents of these BMOs photoanodes. To the best of our knowledge, the photothermal catalytic activity of LaFeO₃ and ZnFe₂O₄ for PEC water splitting is first time observed. Meanwhile, by using sacrificial reagents as electrolytes, the photocatalytic activity can be highly enhanced. The photocurrents of Fe₂O₃ in Na₂S (2250 μ A) and Na₂SO₃ (730 μ A) are 110 times and 35 times higher than that in NaOH (20 μ A) at 1V_{RHE}. The sacrificial electrolytes, especially Na₂S and Na₂SO₃ as electron donors have vastly improved the PEC performance over various MOFs photoanodes. Comparing to developing functional photoanodes materials for improving PEC activity, the research on adjusting electrolytic environment to promote PEC performance might be another interesting and worthwhile way. The study on how electrolytic environments affect the PEC properties is still on the early stage and more efforts should be devoted.

References

- [1] L.J. Minggu, W.R.W. Daud, M.B. Kassim, Int. J. Hydrog. Energy 35 (2010) 5233-5244.
- [2] S.M. Ji, H. Jun, J.S. Jang, H.C. Son, P.H. Borse, J.S. Lee, J. Photochem. Photobiol. A 189 (2007) 141-144.
- [3] T. Bak, J. Nowotny, M. Rekas, C. Sorrell, Int. J. Hydrog. Energy 27 (2002) 991-1022.
- [4] X. Zhang, T. Peng, S. Song, J. Mater. Chem. A 4 (2016) 2365-2402.
- [5] X. Chen, C. Li, M. Grätzel, R. Kostecki, S.S. Mao, Chem. Soc. Rev. 41 (2012) 7909-7937.
- [6] Y. Li, D. Gao, S. Peng, G. Lu, S. Li, Int. J. Hydrog. Energy 36 (2011) 4291-4297.
- [7] V. Kumaravel, M.D. Imam, A. Badreldin, R.K. Chava, J.Y. Do, M. Kang, A. Abdel-Wahab, Catalysts 9 (2019) 276.
- [8] M. Tabata, K. Maeda, M. Higashi, D. Lu, T. Takata, R. Abe, K. Domen, Langmuir 26 (2010) 9161-9165.
- [9] N. Fajrina, M. Tahir, Int. J. Hydrog. Energy 44 (2019) 540-577.
- [10] W.-T. Chen, A. Chan, Z.H. Al-Azri, A.G. Dosado, M.A. Nadeem, D. Sun-Waterhouse, H. Idriss, G.I. Waterhouse, J. Catal. 329 (2015) 499-513.
- [11] K.-Y.A. Lin, C.-H. Lin, S.-Y. Chen, H. Yang, Chem. Eng. J. 303 (2016) 596-603.
- [12] M. Wen, K. Mori, T. Kamegawa, H. Yamashita, ChemComm. 50 (2014) 11645-11648.
- [13] Y. Pellegrin, F. Odobel, C R Chim. 20 (2017) 283-295.
- [14] M. Yasuda, T. Tomo, S. Hirata, T. Shiragami, T. Matsumoto, Catalysts 4 (2014) 162-173.
- [15] A. Galińska, J. Walendziewski, Energy Fuels 19 (2005) 1143-1147.
- [16] C. Saboureau, M. Troupel, J. Perichon, J. Appl. Electrochem. 20 (1990) 97-101.
- [17] Z. Yu, Z. Chen, Y. Chen, Q. Peng, R. Lin, Y. Wang, R. Shen, X. Cao, Z. Zhuang, Y. Li, Nano Res. 11 (2018) 3730-3738.
- [18] H. Zhao, L. Guo, C. Xing, H. Liu, X. Li, J. Mater. Chem. A (2020).
- [19] D. Pradhan, M. Chandra, ChemSusChem. (2020).
- [20] T. Hisatomi, J. Kubota, K. Domen, Chem. Soc. Rev. 43 (2014) 7520-7535.
- [21] H.S. Park, H.C. Lee, K.C. Leonard, G. Liu, A.J. Bard, ChemPhysChem. 14 (2013) 2277-2287.
- [22] C. Ding, J. Shi, D. Wang, Z. Wang, N. Wang, G. Liu, F. Xiong, C. Li, Phys. Chem. Chem. Phys. 15 (2013) 4589-4595.
- [23] C. Ding, X. Zhou, J. Shi, P. Yan, Z. Wang, G. Liu, C. Li, J. Phys. Chem. B 119 (2015) 3560-3566.
- [24] C. Ding, J. Shi, Z. Wang, C. Li, ACS Catal. 7 (2017) 675-688.
- [25] J. Suntivich, E.E. Perry, H.A. Gasteiger, Y. Shao-Horn, Electrocatalysis 4 (2013) 49-55.
- [26] R. Abe, K. Sayama, H. Arakawa, Chem. Phys. Lett. 371 (2003) 360-364.
- [27] Z. Li, L. Shi, D. Franklin, S. Koul, A. Kushima, Y. Yang, Nano Energy 51 (2018) 400-407.
- [28] R. Boppella, S.T. Kochuveedu, H. Kim, M.J. Jeong, F. Marques Mota, J.H. Park, D.H. Kim, ACS Appl. Mater. Interfaces 9 (2017) 7075-7083.
- [29] D. Chen, Z. Liu, M. Zhou, P. Wu, J. Wei, J. Alloys Compd. 742 (2018) 918-927.
- [30] R. Chong, Y. Du, Z. Chang, Y. Jia, S. Liu, Y. Liu, Y. Zhou, D. Li, Appl. Catal. B 250 (2019) 224-233.
- [31] F. Francisco, P. Dias, D. Ivanou, F. Santos, J. Azevedo, A. Mendes, ChemNanoMat. 5 (2019) 911-920.
- [32] S. Cao, X. Yan, Z. Kang, Q. Liang, X. Liao, Y. Zhang, Nano Energy 24 (2016) 25-31.
- [33] A.A. Tahir, K.U. Wijayantha, J. Photochem. Photobiol. A 216 (2010) 119-125.
- [34] J.H. Kim, J.H. Kim, J.W. Jang, J.Y. Kim, S.H. Choi, G. Magesh, J. Lee, J.S. Lee, Adv. Energy Mater. 5 (2015) 1401933.
- [35] Q. Peng, B. Shan, Y. Wen, R. Chen, Int. J. Hydrog. Energy 40 (2015) 15423-15431.
- [36] Y. Gao, G. Yang, Y. Dai, X. Li, J. Gao, N. Li, P. Qiu, L. Ge, ACS Appl. Mater. Interfaces 12 (2020) 17364-17375.
- [37] K.A. Stoerzinger, L. Wang, Y. Ye, M. Bowden, E.J. Crumlin, Y. Du, S.A. Chambers, J. Mater. Chem. A 6 (2018) 22170-22178.
- [38] S. Wang, P. Chen, Y. Bai, J.H. Yun, G. Liu, L. Wang, Adv. Mater. 30 (2018) 1800486.
- [39] S. Wang, T. He, J.H. Yun, Y. Hu, M. Xiao, A. Du, L. Wang, Adv. Funct. Mater. 28 (2018) 1802685.
- [40] S. Wang, P. Chen, J.H. Yun, Y. Hu, L. Wang, Angew. Chem. 129 (2017) 8620-8624.
- [41] M. Tayebi, B.-K. Lee, Renew. Sust. Energ. Rev. 111 (2019) 332-343.
- [42] C.-X. Lei, H. Zhou, C. Wang, Z.-D. Feng, Electrochim. Acta 87 (2013) 245-249.
- [43] Q. Pan, H. Zhang, Y. Yang, C. Cheng, Small 15 (2019) 1900924.
- [44] S. Waitz, C. Suchomski, T. Brezesinski, R. Marschall, ChemPhotoChem, 2 (2018) 1022-1026.
- [45] Z. Dai, C.-S. Lee, B.-Y. Kim, C.-H. Kwak, J.-W. Yoon, H.-M. Jeong, J.-H. Lee, ACS Appl. Mater. Interfaces 6 (2014) 16217-16226.
- [46] Z. Dai, T. Liang, J.-H. Lee, Nanoscale Adv. 1 (2019) 1626-1639.
- [47] Y. Wang, G. Duan, Y. Zhu, H. Zhang, Z. Xu, Z. Dai, W. Cai, Sens. Actuator B-Chem. 228 (2016) 74-84.
- [48] J. Zheng, Z. Dai, F. Mei, X. Xiao, L. Liao, W. Wu, X. Zhao, J. Ying, F. Ren, C. Jiang, J. Phys. Chem. C 118

Chapter 5

- (2014) 20521-20528.
- [49] Z. Xing, J. Zhang, J. Cui, J. Yin, T. Zhao, J. Kuang, Z. Xiu, N. Wan, W. Zhou, *Appl. Catal. B* 225 (2018) 452-467.
- [50] Z. Dai, Y. Li, G. Duan, L. Jia, W. Cai, *ACS nano* 6 (2012) 6706-6716.
- [51] M. Kondo, K. Shinozaki, L. Bergstroem, N. Mizutani, *Langmuir* 11 (1995) 394-397.
- [52] P. Mansky, E. Thomas, *J. Mater. Sci.* 30 (1995) 1987-1992.
- [53] X. Xia, J. Tu, J. Zhang, J. Xiang, X. Wang, X. Zhao, *ACS Appl. Mater. Interfaces* 2 (2010) 186-192.
- [54] J.-J. Wu, C.-C. Yu, *J. Phys. Chem. B* 108 (2004) 3377-3379.
- [55] C. Dette, M.A. Pérez-Osorio, C.S. Kley, P. Punke, C.E. Patrick, P. Jacobson, F. Giustino, S.J. Jung, K. Kern, *Nano Lett.* 14 (2014) 6533-6538.
- [56] A. Rougier, F. Portemer, A. Quédé, M. El Marssi, *Appl. Surf. Sci.* 153 (1999) 1-9.
- [57] J. Tang, D. Wang, Z.G. Zou, J.H. Ye, Modification of photophysical properties of WO₃ by doping different metals, *Materials Science Forum*, Trans Tech Publications Ltd., Zurich-Uetikon, Switzerland, 2003, pp. 163-166.
- [58] K. Sayama, A. Nomura, Z. Zou, R. Abe, Y. Abe, H. Arakawa, *ChemComm.* (2003) 2908-2909.
- [59] M. Xie, Z. Zhang, W. Han, X. Cheng, X. Li, E. Xie, *J. Mater. Chem. A* 5 (2017) 10338-10346.
- [60] A. Tanskanen, M. Karppinen, *Phys. Status Solidi-R* 12 (2018) 1800390.
- [61] Y.R. Smith, K.J.A. Raj, V.R. Subramanian, B. Viswanathan, *Colloids Surf. A Physicochem. Eng. Asp.* 367 (2010) 140-147.
- [62] S. Singh, S.S. Shastri, S.K. Pandey, *AIP Conf. Proc.* 2018, pp. 110018.
- [63] M.B. Bellakki, B.J. Kelly, V. Manivannan, *J. Alloys Compd.* 489 (2010) 64-71.
- [64] T. Nunome, H. Irie, N. Sakamoto, O. Sakurai, K. Shinozaki, H. Suzuki, N. Wakiya, *J. Ceram. Soc.* 121 (2013) 26-30.
- [65] J. Yang, X. Li, X. Deng, Z. Huang, Y. Zhang, *J. Ceram. Soc.* 120 (2012) 579-583.
- [66] H. Tajizadegan, A. Heidary, O. Torabi, M.H. Golabgir, A. Jamshidi, *Int. J. Appl. Ceram. Technol.* 13 (2016) 289-294.
- [67] W. Wu, C. Jiang, V.A. Roy, *Nanoscale* 7 (2015) 38-58.
- [68] J. Highfield, *Molecules*, 20 (2015) 6739-6793.
- [69] Z. Zhao, Z. Wang, J. Bao, Nanomaterials for hydrogen generation from solar water splitting, *Nanomaterials for Sustainable Energy*, Springer 2016, pp. 445-470.
- [70] J.C. Hill, K.-S. Choi, *J. Phys. Chem. C* 116 (2012) 7612-7620.
- [71] E.R. Corson, E.B. Creel, Y. Kim, J.J. Urban, R. Kostecki, B.D. McCloskey, *Rev. Sci. Instrum.* 89 (2018) 055112.
- [72] M. Grätzel, Photoelectrochemical cells, *World Scientific* 2011, pp. 26-32.
- [73] M. Zhao, T. Chen, B. He, X. Hu, J. Huang, P. Yi, Y. Wang, Y. Chen, Z. Li, X. Liu, *J. Mater. Chem. A* (2020).
- [74] Y. Zhang, L. Li, H. Su, W. Huang, X. Dong, *J. Mater. Chem. A* 3 (2015) 43-59.
- [75] M. Reddy, G. Subba Rao, B. Chowdari, *Chem. Rev.* 113 (2013) 5364-5457.
- [76] L. Zhu, M. Gao, C.K.N. Peh, G.W. Ho, *Mater. Horiz.* 5 (2018) 323-343.
- [77] M. Ghoussooub, M. Xia, P.N. Duchesne, D. Segal, G. Ozin, *Energy Environ. Sci.* 12 (2019) 1122-1142.
- [78] T. Wang, Y. Chai, D. Ma, W. Chen, W. Zheng, S. Huang, *Nano Res.* 10 (2017) 2699-2711.
- [79] T. Lemes, S. Khan, E.L. da Silva, L. de Costa, S. Teixeira, C. Aguzzoli, C. Malfatti, *Renew. Energy Power Qual. J.* 1 (2018) 778-781.
- [80] Z. Wang, T.D. Nguyen, L.P. Yeo, C.K. Tan, L. Gan, A.I.Y. Tok, *Small* (2020) 1905826.
- [81] P. Zhang, X.W. Lou, *Adv. Mater.* 31 (2019) 1900281.
- [82] K. Hara, K. Sayama, H. Arakawa, *J. Photochem. Photobiol. A* 128 (1999) 27-31.
- [83] Q. Wang, Y. Wang, *ACS Appl. Mater. Interfaces* 8 (2016) 10334-10342.

Supplementary information

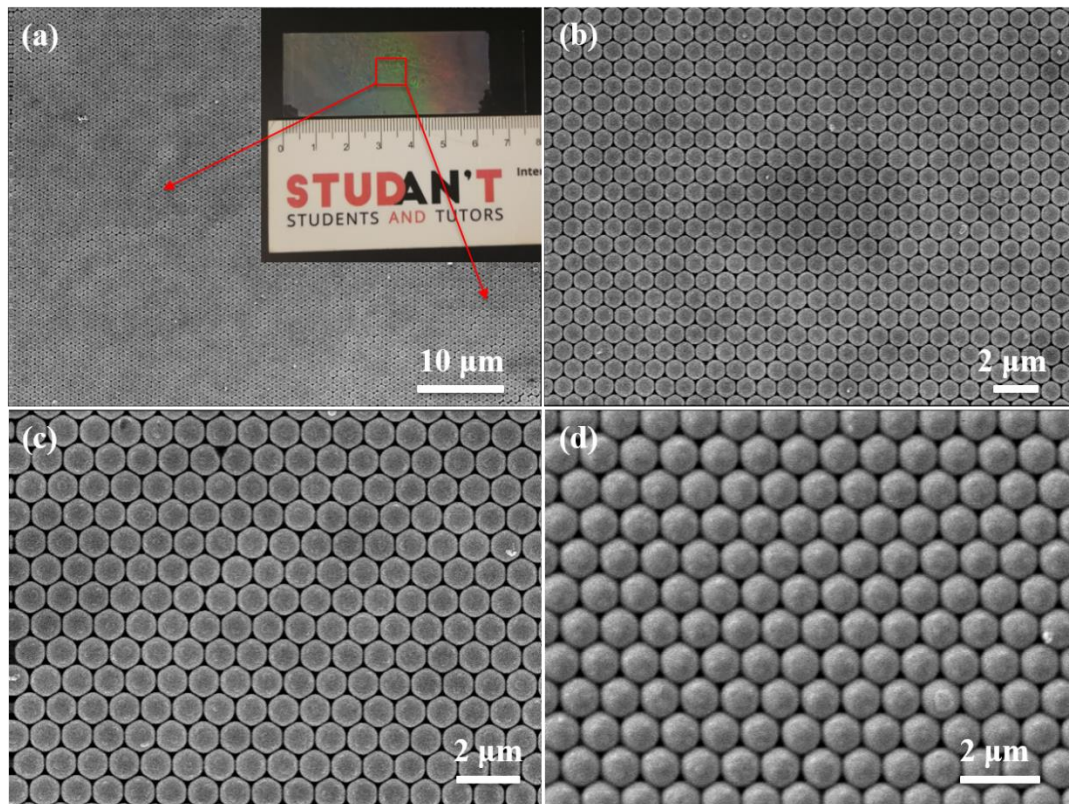


Fig. S5.1. Photograph (inset) and FE-SEM images of the monolayer PS template on a glass slide and via the gas-liquid-solid interface self-assembly method.

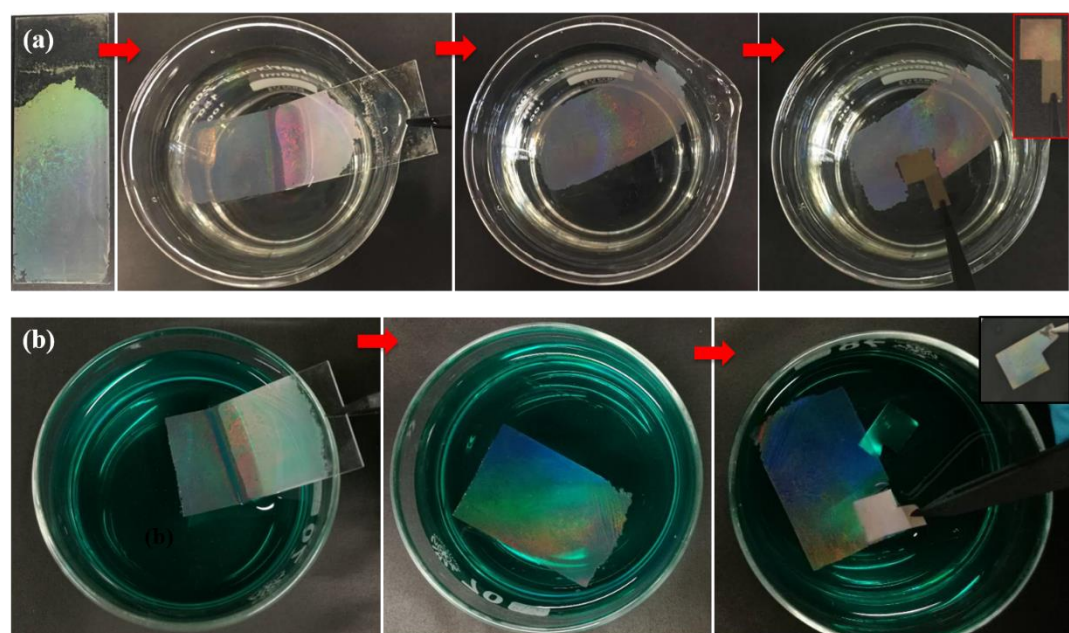


Fig. S5.2. The photographs of practical transferring process for (a) TiO₂ and (b) BiVO₄ through target precursors.

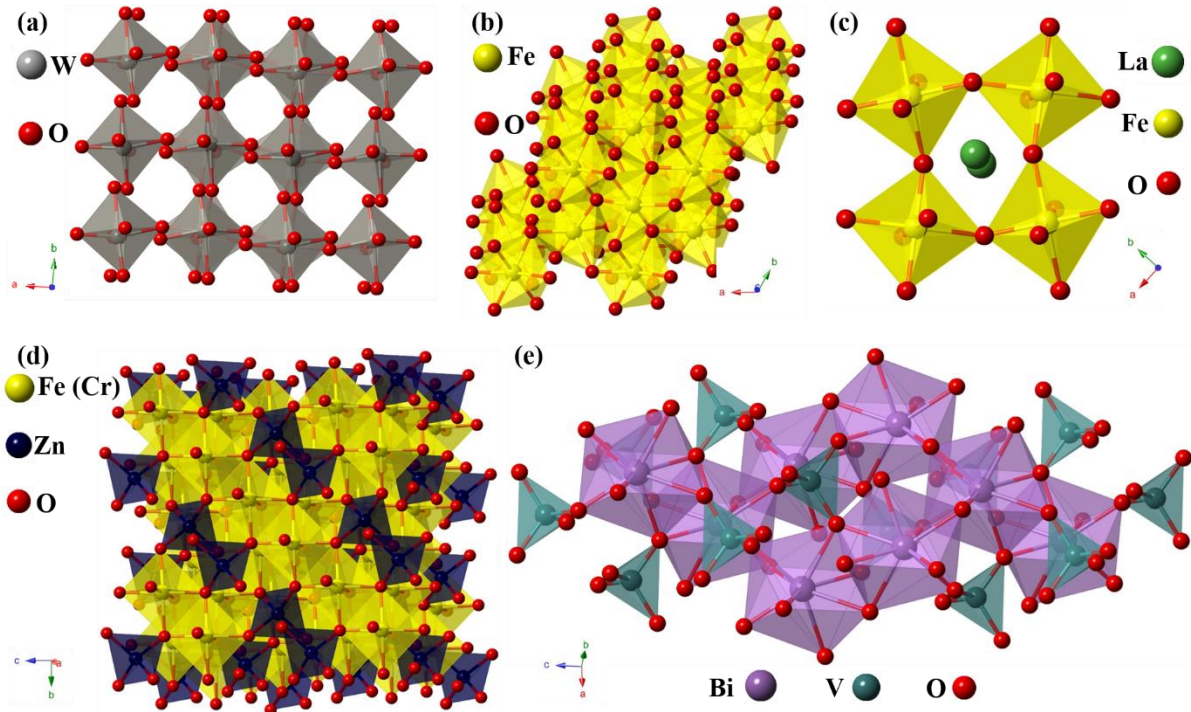


Fig. S5.3. 2×2×2 Supercell of (a) Monoclinic WO₃, (b) Rhombohedral Fe₂O₃, (c) Orthorhombic LaFeO₃, (d) Cubic ZnFe₂O₄ (ZnCr₂O₄) and (e) Monoclinic BiVO₄.

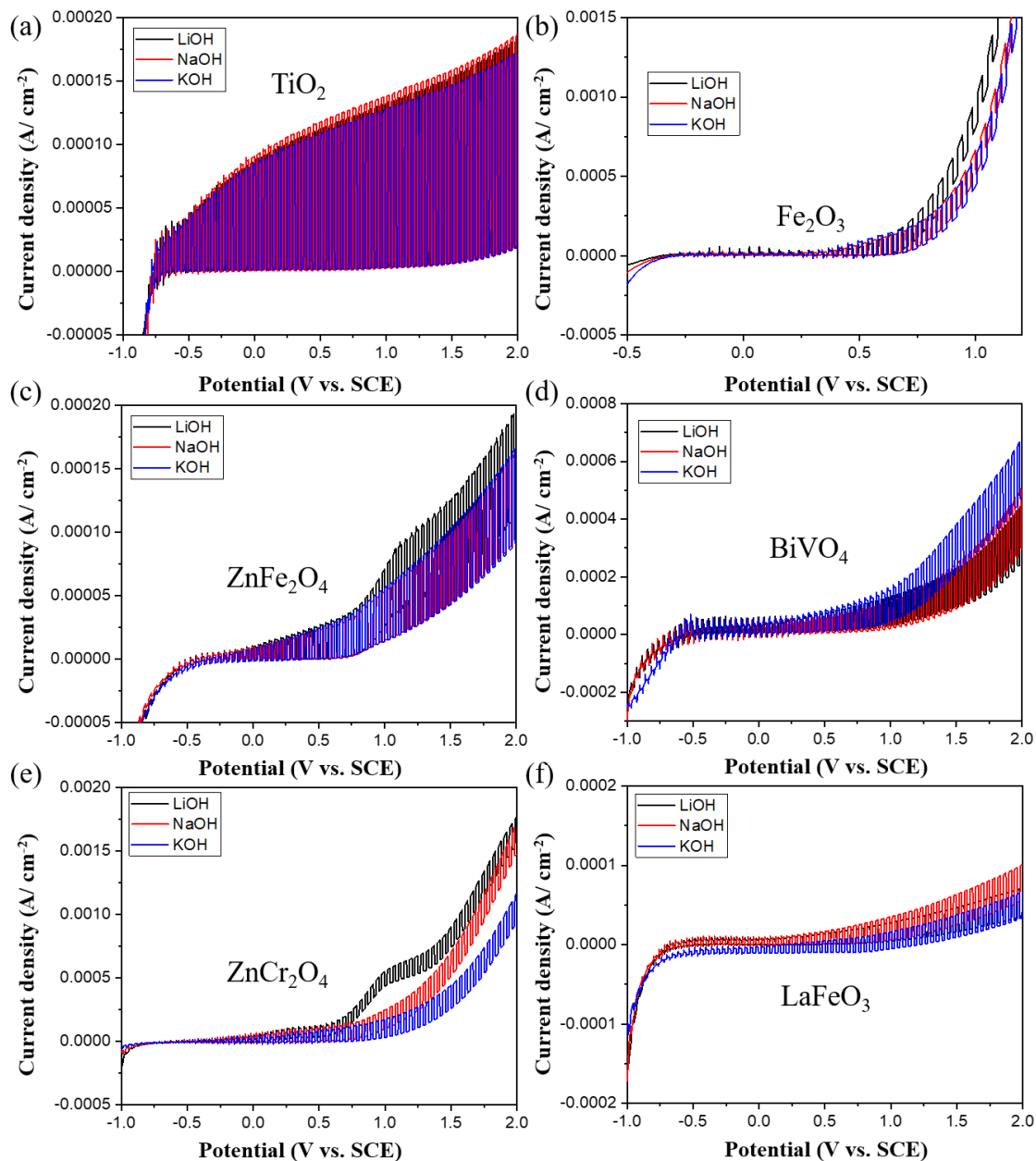


Fig. S5.4. Linear sweep voltammogram (LSV) curves of different photoanodes based on (a) TiO_2 , (b) Fe_2O_3 , (c) ZnFe_2O_4 , (d) BiVO_4 , (e) ZnCr_2O_4 and (f) LaFeO_3 monolayer porous thin films using strong alkaline electrolytes ($\text{pH} = 14$) with different cations (Li^+ , Na^+ , K^+).

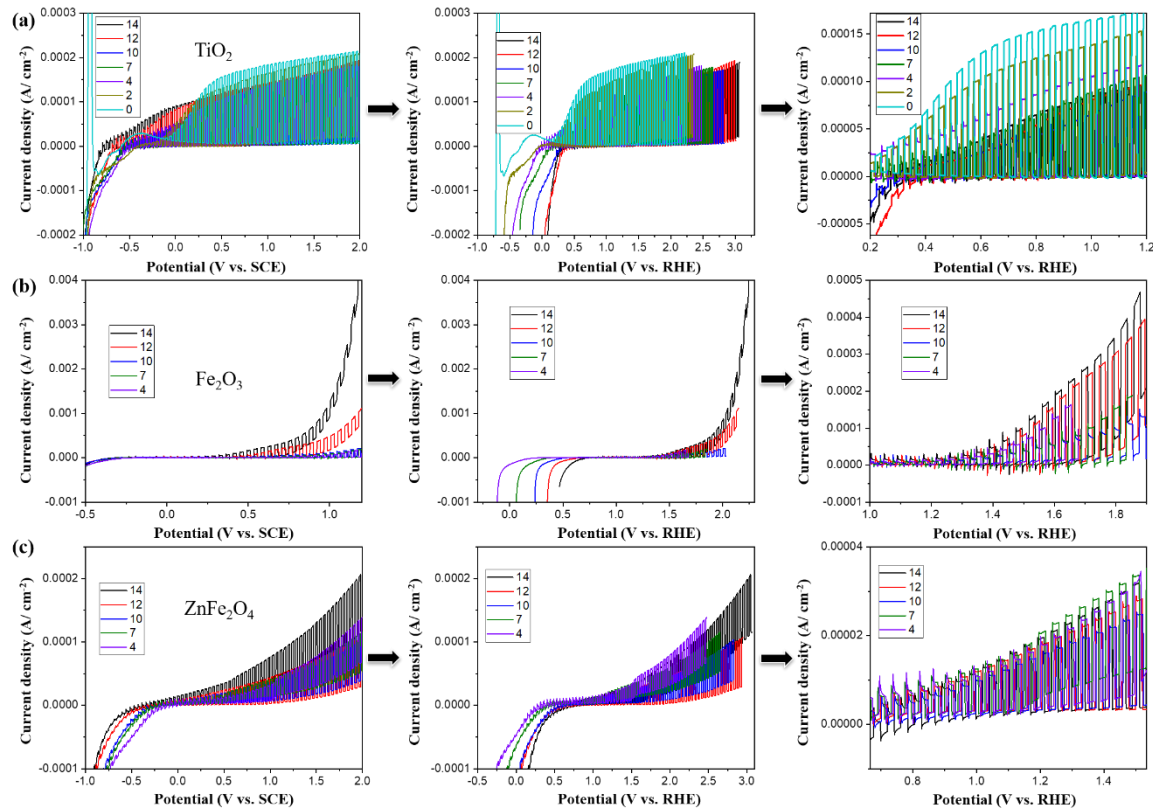


Fig. S5.5. Linear sweep voltammogram (LSV) curves of different photoanodes based on (a) TiO_2 , (b) Fe_2O_3 and (c) ZnFe_2O_4 monolayer porous thin films using electrolyte with different pH values.

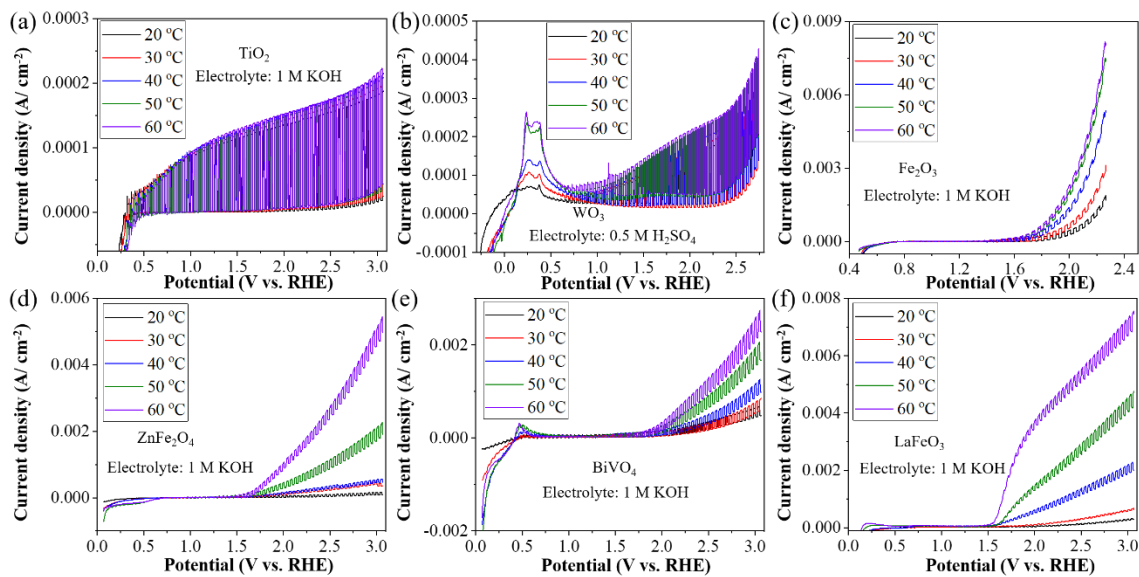


Fig. S5.6. Linear sweep voltammogram (LSV) curves under chopped light of different photoanodes based on (a) TiO_2 , (b) Fe_2O_3 , (c) WO_3 (d) ZnFe_2O_4 , (e) BiVO_4 and (f) LaFeO_3 monolayer porous thin films operated at different temperature.

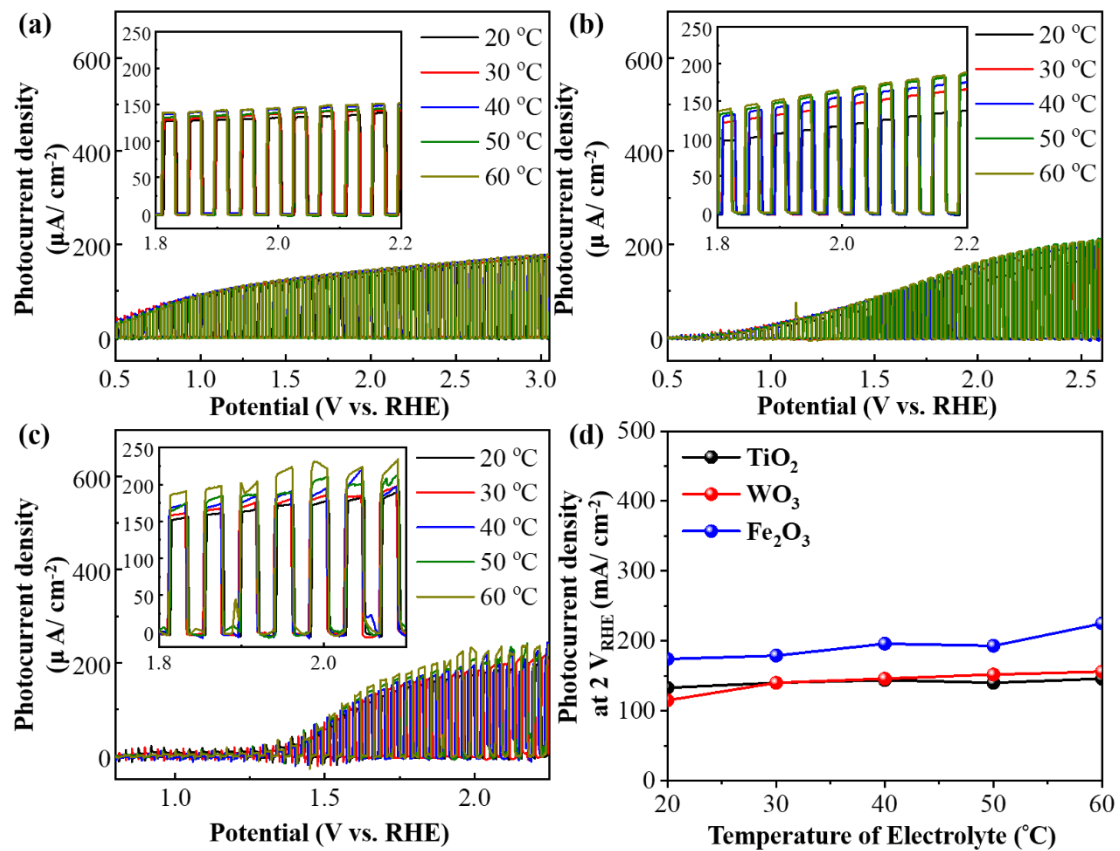


Fig. S5.7. Linear sweep voltammogram (LSV) curves under chopped light of different photoanodes based on (a) TiO_2 , (b) WO_3 and (c) Fe_2O_3 monolayer porous thin films (inset: magnified view) and (d) their collected photocurrent at 2 V_{RHE} operated at different temperature.

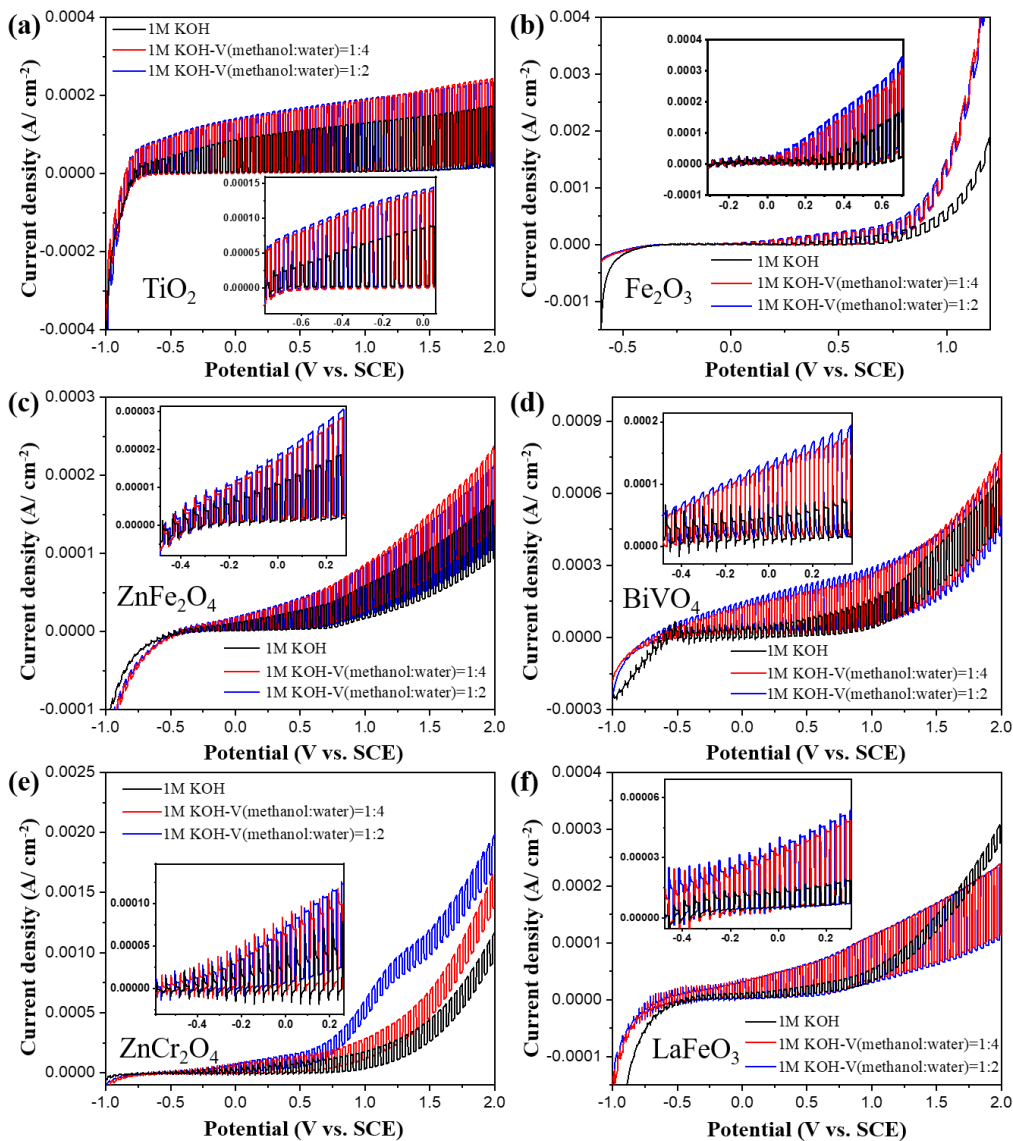


Fig. S5.8. Linear sweep voltammogram (LSV) curves of different photoanodes based on (a) TiO_2 , (b) Fe_2O_3 , (c) ZnFe_2O_4 , (d) ZnCr_2O_4 and (e) LaFeO_3 monolayer porous thin films using methanol as SRs.

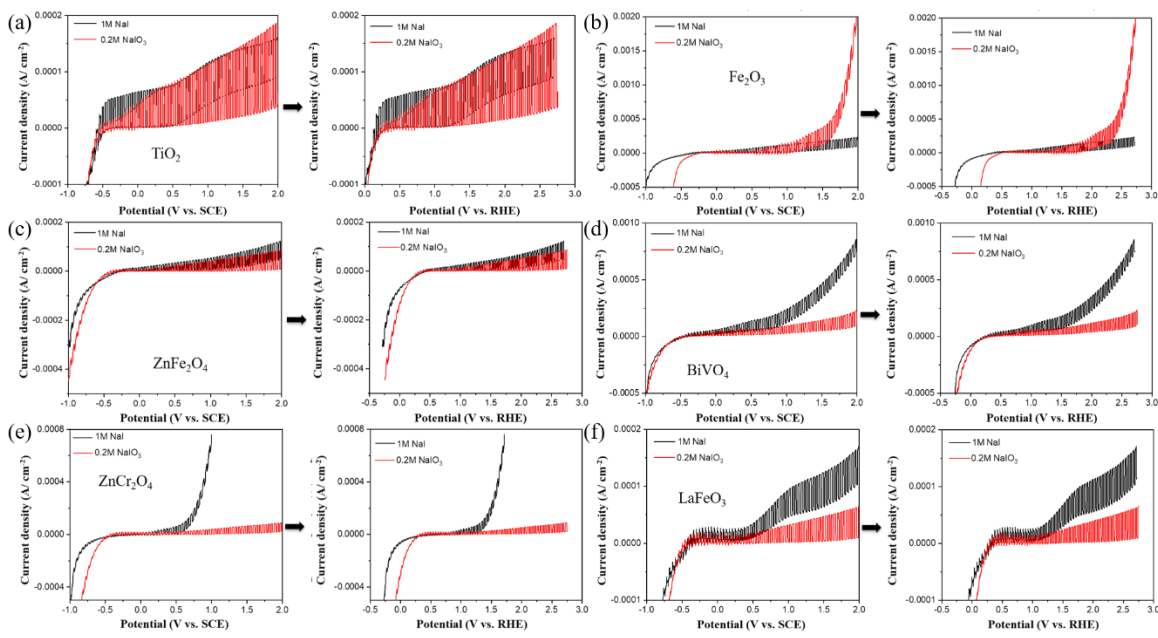


Fig. S5.9. Linear sweep voltammogram (LSV) curves of different photoanodes based on (a) TiO_2 , (b) Fe_2O_3 , (c) ZnFe_2O_4 , (d) BiVO_4 , (e) ZnCr_2O_4 and (f) LaFeO_3 using Na_2S and Na_2SO_3 as electrolyte.

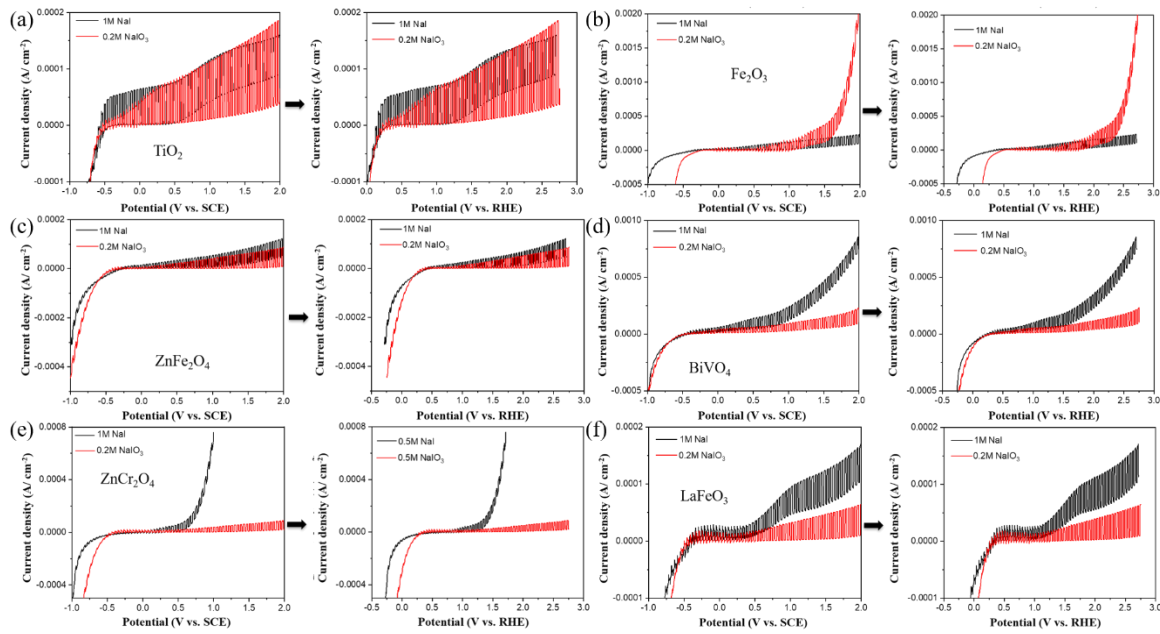


Fig. S5.10. Linear sweep voltammogram (LSV) curves of different photoanodes based on (a) TiO_2 , (b) Fe_2O_3 , (c) ZnFe_2O_4 , (d) BiVO_4 , (e) ZnCr_2O_4 and (f) LaFeO_3 using NaI and NaIO_3 as electrolyte.

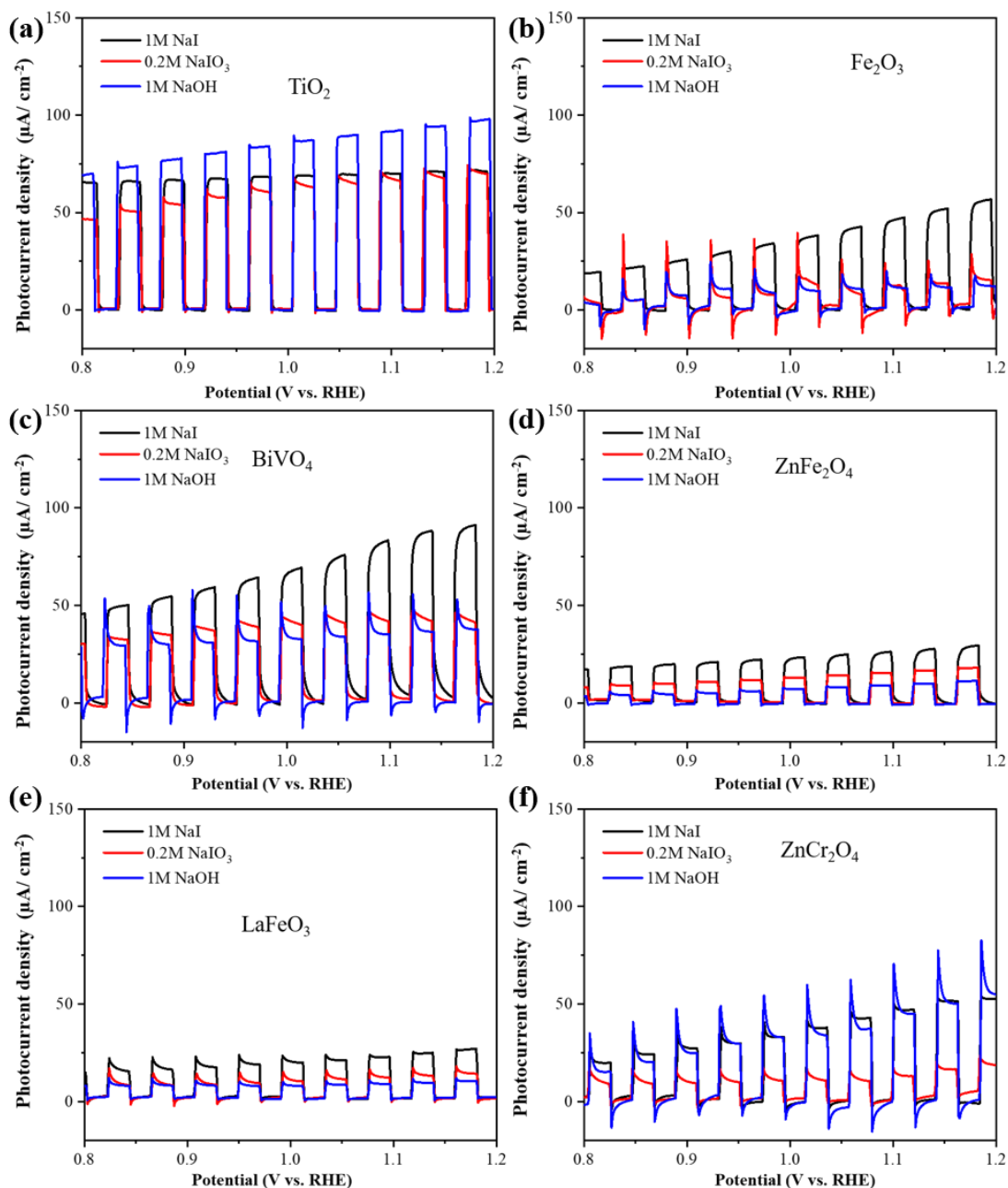


Fig. S5.11. Linear photocurrent density curves after subtracting current density under dark environment of different photoanodes based on (a) TiO_2 , (b) Fe_2O_3 , (c) BiVO_4 , (d) ZnFe_2O_4 , (e) LaFeO_3 and (f) ZnCr_2O_4 using NaI , NaIO_3 and NaOH as electrolyte.

Table S5.1. Precursors for preparing different MOFs thin films

MOS	Precursor (solvent: water)
TiO ₂	0.1 mol/L TiCl ₄ + 4% HCl
Fe ₂ O ₃	0.1 mol/L Fe(NO ₃) ₃
BiVO ₄	0.1 mol/L Bi(NO ₃) ₃ + 0.1 mol/L VOSO ₄ + 8% HCl
LaFeO ₃	0.1 mol/L Fe(NO ₃) ₃ + 0.1 mol/L LaCl ₃
ZnFe ₂ O ₄	0.1 mol/L Zn(NO ₃) ₃ + 0.2 mol/L Fe(NO ₃) ₃
ZnCr ₂ O ₄	0.1 mol/L Zn(NO ₃) ₃ + 0.2 mol/L Cr(NO ₃) ₃

Table S5.2. Applied Electrolytes

Electrolytes	PH value	Solvent
1 M LiOH	14	Water
1 M KOH	14	Water
1 M NaOH	14	Water
0.01 M KOH+0.99 M KCl	12	Water
0.0001 M KOH+0.999 M KCl	10	Water
1 M KCl	7	Water
1 M HCl	0	Water
0.01 M HCl +0.99 M KCl	2	Water
0.0001 M HCl +0.999 M KCl	4	Water
0.5 M Na ₂ S	13	Water
0.5 M Na ₂ SO ₃	8	Water
1 M NaI	8	Water
0.2 M NaIO ₃ +0.8 M KCl	9	Water
1 M KOH+ SRs	14	Methanol and Water (Volume ratio 1:4)
1 M KOH+ SRs	14	Methanol and Water (Volume ratio 1:2)

Table S5.3. Standard Thermodynamic Values

Formula	State of matter	Gibbs free energy (kJ/mol)	Splitting energy(eV)
H ₂ O	Water (l)	-237	1.23
CH ₃ OH	Methanol (l)	-167	0.84
CH ₃ CH ₂ OH	Ethanol (l)	-174	0.90
CH ₃ CH ₂ CH ₂ OH	1-Propanol (l)	-171	0.89
CH ₃ CH ₂ CHOHCH ₃	2-Butanol (l)	-177	0.92
CH ₃ (CH ₂) ₂ CH ₂ OH	1-Butanol (l)	-163	0.85
CH ₃ CH ₂ OCH ₂ CH ₃	Diethyl ether (l)	-117	0.61
H ₂ O ₂	Hydrogen peroxide (l)	-120	0.62
H ₂ S	(g)	-33	0.17

CHAPTER 6.

Conclusions and Perspectives

6.1 Conclusions

The main objective of this PhD thesis is thus to investigate the effect of doping, coating and electrolytic environment on the photocatalytic and photoelectrochemical activity of metal oxide semiconducting materials to improve the photocatalytic and photoelectrochemical performance of metal oxide semiconducting materials.

Carbon doping and coating can effectively enhance the photocatalytic activity of TiO_2 for PC/PEC hydrogen production from water splitting. The synergy of carbon coating and doping can further improve the photocatalytic activity of TiO_2 . The synergistic effect of carbon doping and coating in TiO_2 was further investigated and discussed. Meanwhile, $\text{Ti}_n\text{O}_{2n-1}$ which is known as Magnéli materials were successfully synthesized and composed with carbon. The formation mechanism and further application of Magnéli materials in PEC water splitting were discussed in detail. Besides, the electrolytic environments can also affect the PEC performance on different MOSSs including TiO_2 . Extending to other MOSSs such as WO_3 , Fe_2O_3 , BiVO_4 , LaFeO_3 and ZnFe_2O_4 , the impact of the electrolytic parameters such as electrolyte cations, pH values, temperature and additive sacrificial reagents on PEC performance was specifically discussed in detail. Based on these studies in thesis, some interesting results can be concluded as follows.

- 1) The “one pot” simultaneous carbon coating and doping of TiO_2 materials by the hydrolysis of TiCl_4 in fructose was successfully fabricated. The synergistic effect of carbon doping and coating of TiO_2 to significantly boost textural, optical and electronic properties and photocurrent of TiO_2 for high performance visible light H_2 production from water splitting has been comprehensively investigated. Carbon doping can significantly increase the thermal stability, thus inhibiting the phase transformation of the Titania material from anatase to rutile while carbon coating can suppress the grain aggregation of TiO_2 . The synergy of carbon doping and coating can not only ensure an enhanced narrowing effect of the electronic band gap of TiO_2 thus extending the absorption of photocatalysts to the visible regions, but also promote dramatically the separation of electron-hole pairs. Owing to these synergistic effects, the carbon coated and doped TiO_2 shows much superior photocatalytic activity for both degradation of organics and photocatalytic/photoelectrochemical (PEC) water splitting under simulated sunlight illumination. The photocatalytic activity of obtained materials can reach 5, 4 and 2 times higher than that of pristine TiO_2 , carbon doped TiO_2 and carbon coated TiO_2 , respectively in the degradation of organic pollutants. The carbon coated and doped TiO_2 materials exhibited

Conclusions & Perspectives

more than 37 times and hundreds of times photocurrent enhancement under simulated sunlight and visible light, respectively compared to that of pristine TiO₂. The present work providing new comprehensive understanding on carbon coating and doping effect could be very helpful for the development of advanced TiO₂ materials for a large series of applications.

2) A series carbon composed Ti_nO_{2n-1} with different n value ($3 \leq n \leq 9$) including Magnéli materials were prepared by a simple sintering of amorphous TiO₂ coated by polysaccharide derived from fructose under Ar. The higher concentration of fructose in precursor solution, prolonged calcination time and increased calcination temperature can result in Ti_nO_{2n-1} with lower n value. The formation mechanism supposed to be the reduction of TiO₂ by the reductive gases, H₂ and CO produced from the decomposition of polysaccharides. The 3D simulation of the crystallite structures of these Ti_nO_{2n-1} according to XRD results provides a comprehensive understanding of their unique crystallite structures. Owing to the oxygen deficiency in every layer of TiO₆ octahedrons, the Ti_nO_{2n-1} occupy the semiconductor-metal transition resulting in the inherent semiconductor-metal junction which facilitates the charge transfer and separation. However, the enhanced semiconductor-metal transition suppresses the carrier harvesting preventing photocatalytic reactions. With suitable semiconductor-metal junction in Magnéli phase, Magnéli materials show better PEC performance than TiO₂ and non-Magnéli Ti₃O₅. Thus, the Magnéli materials as a new type of photocatalysts might be superior in the application for PEC water splitting.

3) The ordered porous thin films of various metal-oxide-semiconductors (MOSSs) as photoanodes were synthesized by the template-based transferring method. The PEC performance in specific electrolytic environments over different photocatalysts were investigated with different electrolyte cations, pH values, temperature and sacrificial reagents. It is found that electrolyte temperature strongly influences the photocurrent density of binary MOSSs such as BiVO₄, ZnFe₂O₄ and LaFeO₃. For example, the photocurrent of LaFeO₃ operated at 60 °C (650 μA) is 16.3 times as that at 20 °C (40 μA) at 3 V_{RHE}. By using sacrificial electrolytes such as Na₂S and Na₂SO₃, the photocurrent of photoanodes based on various MOSSs was notably increased. For instance, the photocurrents of Fe₂O₃ in Na₂S (2250 μA) and Na₂SO₃ (730 μA) are 110 times and 35 times higher than that in NaOH (20 μA). Obviously, the electrolytic environment especially the temperature and sacrificial ions can significantly affect the PEC performance of MOSSs photoanodes. Comparing to developing new functional photoanodes materials, focusing on the effect of electrolytic environments on PEC behavior of

Conclusions & Perspectives

photoanodes might be more worthwhile for enhancing the efficiency of PEC water splitting.

6.2 Perspectives

- 1) The coated carbon can be observed by TEM and characterized by Raman which confirm the carbon coating directly. However, the direct observation or characterization for carbon doping is highly challenging. The carbon doping can only be proved by supporting clues from UV-Vis spectra, XPS as well as photocatalytic tests et al. comparing with pristine TiO₂. The carbon doping type (substitutional or interstitial type) in TiO₂, the resulted modification of the band gap structure of TiO₂ and the specific origin of visible-light response are still unclear and under debate. The HR-TEM is highly expected to observe the lattice distortion in TiO₂ caused by carbon doping or identify directly the doped carbon atoms in TiO₂ lattice providing the most convincing proof of carbon doping in TiO₂ and paving the path for the further analysis of specific carbon doping effect on the band gap structure of TiO₂. In this thesis, the investigation of the synergy of carbon doping and coating provides a comprehensive understanding on the effect of carbon on TiO₂ and serves an important contribution to area of photocatalytic / photoelectrochemical water splitting. The synergistic effect of carbon doping and coating plays a crucial role on the highly enhanced photocatalytic activity of TiO₂. More efforts should be devoted in the modification of carbon and other non-metals in TiO₂ and other metal oxides for the application in energy-related areas.
- 2) The large amount of carbon composed in Ti_nO_{2n-1} suppressed the photocatalytic activity of Ti_nO_{2n-1}. However, it is difficult to remove the carbon for example by calcination in air, gas plasma cleaning or sputtering techniques without phase changing of Ti_nO_{2n-1}. Meanwhile, the pure phase of Ti_nO_{2n-1} is also hard to obtain. Thus, it is challenging to determine and compare the photocatlaytic activity of pure Ti_nO_{2n-1} photocatalysts including pure Magnéli materials. Impacting parameters, concentration of fructose in precursor, calcination temperature and duration as well as the reductive atmosphere for calcination can be adjusted more strictly to control the n value and carbon loading amount more precisely. In this thesis, the titanium suboxides, Ti_nO_{2n-1} ($4 \leq n \leq 9$) known as Magnéli materials show good potential for photoelectrochemical water splitting, which is seldom reported. The semiconductor-metal transition in Magnéli phase might be vital to enhance the photocatalytic activity acting as semiconductor-metal junction. Actually, it would be very interesting to investigate the relationship between the unique crystalline structures of Magnéli materials with the photocatalytic activity. More research work should be done to explore the photoelectrochemical properties of Magnéli materials.

Conclusions & Perspectives

3) The electrolytic environments on PEC performance affect each type of metal oxide semiconductors (MOSSs) differently, the general commonalities of the impact of electrolytic environments on PEC performance of each type of MOSSs photoanodes can not be finalized and reached based on the present work. More other MOSSs and electrolytes except MOSSs and electrolyte mentioned in this thesis should be added in the blueprint. Meanwhile, the band bending effect which often occurs at the interface between semiconductor and electrolyte can significantly affect the electron-hole separation and the PEC performance. However, due to the difficulties of both observation and characterization of the band bending effect in different electrolytic environments, the practical experiments about impact of band bending on PEC performance of MOSSs photoanodes could not be carried out. The band bending effect on MOSSs is very fundamental research topic of electrochemistry and photoelectrochemistry. Considerable literatures reading on both theoretical and experimental are very necessary. In-situ characterization platform combined with the electrochemical or photoelectrochemical testing instruments are also in need. In this thesis, the dramatical influences of electrolytic environments on photoelectrochemical performances of various metals oxides semiconductors have been demonstrated in this thesis. The photocurrents of photoanodes based on binary metal oxides such as BiVO₄, LaFeO₃ and ZnFe₂O₄ were remarkably enhanced by increasing the electrolyte temperature. The improvement of photoelectrochemical performances of these binary metal oxides is closely related to the photothermal effect which combines the thermochemical and photochemical properties. The photothermal catalysis is a new sub-discipline of heterogeneous catalysis and still on its early stage. The fundamental mechanism behind the photothermal enhanced efficiency of hydrogen production from water splitting over these binary metal oxides is very complicated and worthwhile for investigation. Moreover, new photothermal materials are highly expected to be exploited. Except the binary metal oxides, BiVO₄, LaFeO₃ and ZnFe₂O₄, other binary metal oxides and multiple metal oxides should be investigated for the photothermal catalysis.

4) By adding sacrificial electrolyte, Na₂S and Na₂SO₃ to consume the holes, the recombination of photogenerated electron / hole pairs is successfully suppressed and the followed photocurrents of photoanodes based on various metal oxides increased significantly. Specially, Fe₂O₃ shows more than one hundred and thirty times enhancement of photocurrent in Na₂S and Na₂SO₃, respectively, than that in normal electrolyte like NaOH. The sensitivity of the photoelectrochemical performance of Fe₂O₃ to Na₂S might relate to sulfide modification including sulfur doping on the surface of Fe₂O₃. Slight phase changing from Fe₂O₃ to Fe₂S₃ or

Conclusions & Perspectives

FeS might also occur and enhance the conductivity of the photocatalyst system leading to enhanced photoelectrochemical performance. More characterization work should be projected for better understanding the fundamental mechanism behind the highly S-assisted photoelectrochemical performance. For better design the electrolytic environment to optimize the photoelectrochemical properties of metal oxides, more research about how sacrificial electrolyte such as Na₂S affect the photoelectrochemical performance on metal oxides should be carried out.

List of papers

1. Yingying Wang, Yan-Xin Chen, Tarek Barakat, Alain Krief, Bao-Lian Su, Synergistic effects of carbon doping and coating of TiO₂ with exceptional photocurrent enhancement for high performance H₂ production from water splitting, J. Energy Chem. DOI: 10.1016/j.jecchem.2020.08.002
2. Yingying Wang, Tarek Barakat, Alain Krief, Yanxin Chen, Bao-lian Su, Non-metal doped TiO₂ for photocatalytic / photoelectrochemical water splitting under solar light. Submitting.
3. Yingying Wang, Yanxin Chen, Tarek Barakat, Bao-lian Su, A novel synthesis of carbon composed two-dimensional Ti_nO_{2n-1} for PEC water splitting, Preparing.
4. Yingying Wang, Yanxin Chen, Bao-lian Su, Impact of electrolytic environments on PEC water splitting over different metal oxide semiconductors, Preparing.
5. Emile Haye, Nathalie Job, Yingying Wang, Laurent Houssiau, ZnO/Carbon xerogel photocatalysts by low-pressure plasma treatment, the role of the carbon substrate and its plasma functionalization, J. Colloid Interface Sci. 570 (2020) 312-321.

Acknowledgements

The research work mentioned above in this dissertation was finished under the full and proficient supervision of Prof. Bao-Lian SU at the Laboratory of Inorganic Materials Chemistry (CMI), University of Namur, Belgium since September, 2017. I feel honored to deliver my sincerely appreciation to Prof. SU for his patient, rigorous and enlightening guidance. I have learned a lot about both work and life from the talented scientist, Prof SU which will benefit my whole lifetime.

I would like to thank Prof. Alain Krief for his valuable and selfless guidance on my work. Although he has retired officially, he never stops chasing the truth of science personally inspiring every young researchers like me.

I also appreciate the committee professors. Prof. Olivier Deparis, Prof. Yujia Zeng and Prof. Alexandru Vlad for their constructive suggestions and comments on my thesis. Due to their contribution, the quality of my theis is highly improved.

It is also my great pleasure to thank my lovely, interesting, thoughtful and smart co-workers and friends, Mrs. Isabelle Virlet, Mrs. Valérie Charles, Dr. Tarek Barakat, Mr. Marvin Laboureur, Dr. Luca Fusaro, Mrs. Hongyan Li, Dr. Minghui Sun, Mrs. Myriam Neumann, Mr. Quentin Bizot, Mr. Benjamin Buysens, Mr. Yang Ding, Mr. Yao Shi, Mr. Pengcheng Xing, Mr. Domenico Grammatico, Mrs. Silvia Pugliese and Mr. Thomas Madanu. Specially, I would like to thank some colleagues I had worked with, Dr. Yanxin Chen, Dr. Chao Li, Dr. Li Wang and Dr. Chenxi Zhang, the F4 of Namur. I also thank previous colleagues, Dr. Cyrille Delneuville, Dr. Aizhong Jia and Mr. Lionel Weber. I really enjoy working with them and many thanks for their help and supports during these years.

I would like to thank my dear parents, my sisters and my nieces for their love in heart and great faith in me all the time even I have been absent from their lives for almost four years. Finally, thanks and best wishes to all my families, friends and colleagues!

Yingying Wang

July 15, 2020, Namur